An airbag for drops:

High speed interferometry studies of air film lubrication in drop impact

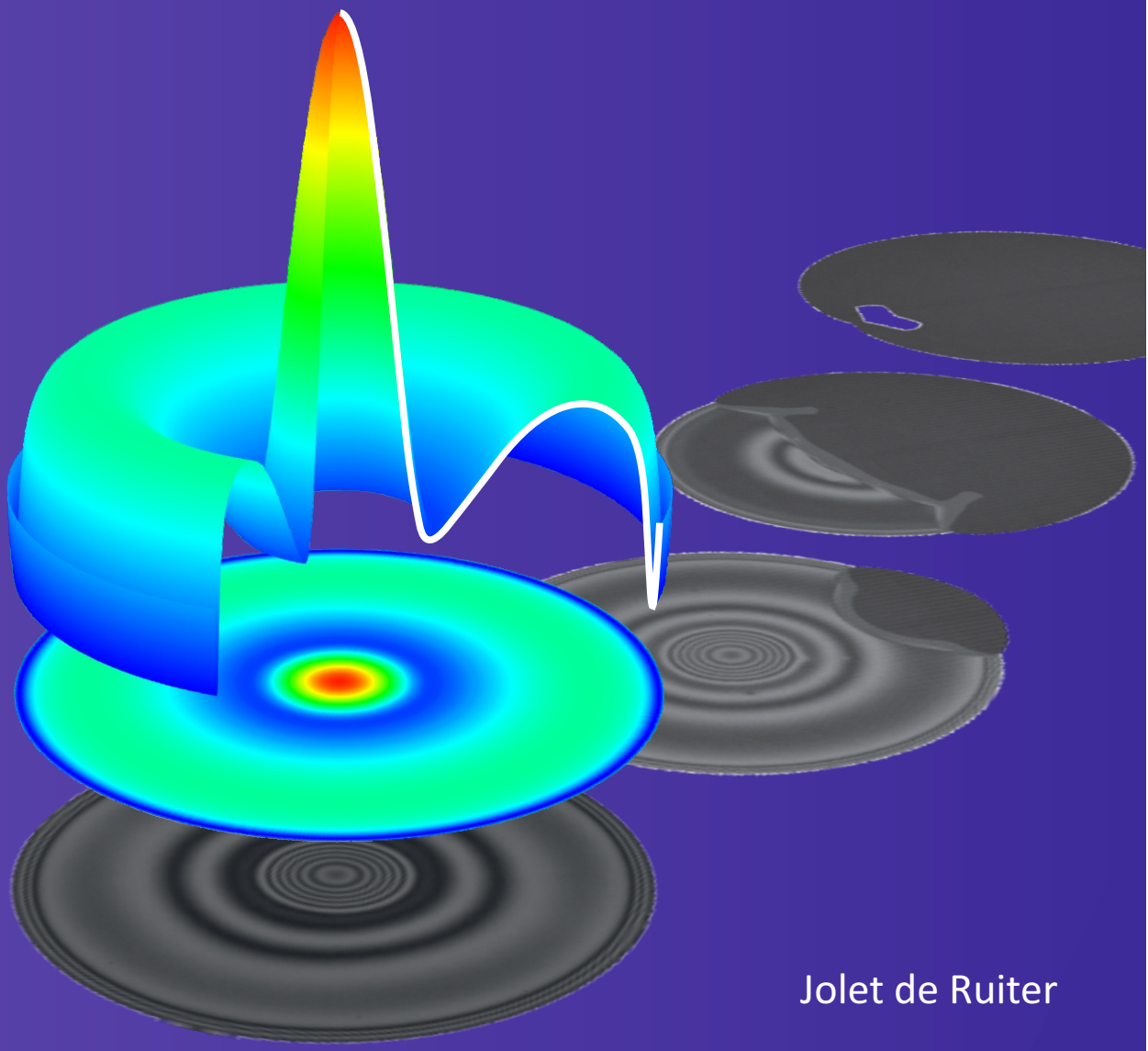

Jolet de Ruiter

An airbag for drops:

High speed interferometry studies of air film lubrication in drop impact

Jolet de Ruiter

Committee members:

Prof. dr. ir. J.W.M. Hilgenkamp	University of Twente, chairman
Prof. dr. F. Mugele	University of Twente, promotor
Dr. H.T.M. van den Ende	University of Twente, assistant promotor
Prof. D. Quéré	ESPCI ParisTech
Prof. N. Vandewalle	University of Liège
Prof. K.K. Varanasi	Massachusetts Institute of Technology
Dr. H. Wijshoff	Océ Technologies B.V.
Prof. dr. W.J. Briels	University of Twente
Prof. dr. S.J.G. Lemay	University of Twente

The research described in this thesis was performed at the Physics of Complex Fluids group within the MESA+ Institute for Nanotechnology and the Department of Science and Technology of the University of Twente. This work is part of the project “High Precision Inkjet Printing System (HIPRINS)” supported by the subsidy “Pieken in de Delta” of the Dutch Ministry of Economic Affairs. The project is co-sponsored by the Dutch provinces Overijssel, Limburg, and Noord-Brabant, and Samenwerkingsverband Regio Eindhoven (SRE), and the industrial partners: Holst Centre, Océ, Roth & Rau, Thales, and NTS.

Title:	An airbag for drops: High speed interferometry studies of air film lubrication in drop impact
Author:	Jolet de Ruiter
ISBN:	978-90-365-3638-7
DOI:	10.3990/1.9789036536387

Printed by Gildeprint Drukkerijen, Enschede.

AN AIRBAG FOR DROPS:

HIGH SPEED INTERFEROMETRY STUDIES OF AIR FILM LUBRICATION IN DROP IMPACT

PROEFSCHRIFT

ter verkrijging van
de graad doctor aan de Universiteit Twente,
op gezag van de rector magnificus,
prof. dr. H. Brinksma,
volgens besluit van het College voor Promoties
in het openbaar te verdedigen op
woensdag 26 maart 2014 om 16:45 uur

door

Jolet de Ruiter

geboren op 5 april 1985
te Tiel

This dissertation has been approved by:

Promotor:	Prof. dr. Frieder Mugele
Assistant promotor:	Dr. Dirk van den Ende

Table of Contents

Summary

The impact of droplets on substrates is of wide-spread practical relevance ranging from raindrop erosion, aerosol dispersion, and water-repellency of leaves, to industrial applications as pesticide spraying, fluid coating, and ink-jet printing. High-end applications of the latter require accurate positioning of picoliter droplets, and inspired the research described in this thesis.

The deposition of a droplet on a surface is a quite complicated process including the formation and spreading of an air layer between the droplet and the surface before the droplet actually touches the surface. This air-cushioning effect that can take a few milliseconds, guarantees a relatively soft landing or even prevents the impact altogether, similar to the protection by an airbag in a car accident. Here, the naturally present ambient air acts as the airbag since a lubrication pressure builds up in the air layer while it is being squeezed to a thickness of only a few micrometers. This not only decelerates the droplet to a small fraction of its initial impact speed, but also strongly deforms the droplet interface. The interfacial deformation has important consequences for entrapment of an air bubble below the droplet and the actual formation of liquid-solid contact, *i.e.* the 'deflation of the airbag'. In this thesis model droplets of millimeter size are studied while they impact at intermediate velocities of tens of centimeters per second onto a solid substrate. This corresponds to Weber numbers We around unity – indicating that both surface tension and inertia play a role on the impact dynamics. We study the evolution of the air film and its influence on further impact dynamics.

The evolution of the air film entrapped between the droplet and the substrate is studied using reflection interference microscopy (RIM) through the transparent substrate. **Chapter 3** describes how an absolute thickness measurement can be obtained using a combination of dual wavelength RIM with a finite spectral bandwidth to get a characteristic damping pattern of the interference intensity oscillations with air film thickness. This yields a depth of view of 8 μm, a height accuracy better than 30 nm and a time resolution that is only limited by the state-of-the-art of high-speed photography (we use 10-50 μs).

The squeezed air film has a width-to-height ratio of 10^3 and is simply flat - at first sight. However, the RIM technique reveals salient details of the complex shape evolution that prove to be critical for the impact dynamics. In **Chapter 2** we show that the air film

thickness develops an off-center local minimum. Yet, the descend of the droplet interface is stopped by the diverging capillary pressure at this 'kink' with increasing curvature. An equilibrium thickness is obtained in agreement with recent theoretical predictions, and the droplet 'skates' on the air film. For $We < 4$ we are able to observe the formation of a second - and possibly more - local minimum. **Chapter 4** explains this observation by continued liquid advection. Solid-liquid contact is formed from a critical air film thickness of 200 nm. Depending on We contact is either formed within microseconds at the first kink, leading to a ring impact and thus entrapment of a small air bubble ($We > 4$), or (temporarily) suppressed ($We < 4$). In the latter case we observe and describe the formation of a single contact point after a few milliseconds at the second kink. The subsequent spreading of liquid-solid contact follows an inertial-capillary scaling (**Chapter 2**), and its velocity is enhanced compared to early-time wetting of non-cushioned droplets (**Chapter 4**).

Remarkably, droplets can even bounce repeatedly on a persisting air film for $We < 4$. In **Chapter 5** we analyze both the droplet dynamics and interaction with the lubrication layer to characterize the role of the lubrication layer in bouncing. Of course, the absence of a contact line eliminates an important source of dissipation. However, this is not sufficient to allow repeated bouncing with a restitution coefficient larger than 0.9. In particular we find that an asymmetry in the spreading and contraction of the air layer is critical to obtain an efficient reversal of the momentum of the droplet. Careful analysis of the air film evolution shows that the net lubrication force on the droplet is repulsive during the full interaction phase with the substrate, even when the drop moves away from the substrate. Center of mass energy stored in internal modes during the interaction phase is thus almost fully recovered. The shape details of the droplet interface are thus not only critical for the dynamics of liquid-solid contact formation and air bubble inclusion, but also for the bouncing process.

We study the influence of a micro-textured substrate on the thinning of the squeezed air film in **Chapter 6**. For this we fabricate micro-structures with sharp vertical step edges, *i.e.* step edges and narrow ridges, using lithography. The edge only has a very local effect on the squeeze out of the air. The air film thickness has a minimum at the edge, and liquid-solid contact can be forced *at* the edge from a critical distance $\sim$ 60 nm provided that the micro-texture is sufficiently high or has a large height-to-width aspect ratio. We discuss implications for the elimination of bouncing and controlled wetting, and the incidental premature destabilization of the air layer by small dust particles or irregularities.

Finally, we can sketch a coherent picture of the scenarios following cushioning at Weber numbers around unity. Depending on the shape details of the air film evolution **Chapter 7** discusses the various possibilities regarding liquid-solid contact formation *vs.* droplet bouncing, and air bubble inclusion *vs.* (complete) squeeze out of the initially trapped air film. For inkjet droplets the same scenarios are expected, although at smaller air film thicknesses.

Samenvatting

De impact van druppels op oppervlakken heeft een wijdverbreide praktische relevantie voor zowel erosie door regendruppels, dispersie van aerosolen en waterafstoting door planten, als industriële toepassingen zoals het aanbrengen van pesticide-sprays en vloeistof coatings, en inkjet printen. Geavanceerde inkjet-toepassingen zijn sterk afhankelijk van een nauwkeurige depositie van picoliter druppels, en inspireerden het onderzoek beschreven in dit proefschrift.

De depositie van een druppel op een oppervlak is een gecompliceerd proces met onder andere de vorming en spreiding van een luchtlaag tussen de druppel en het oppervlak, vóórdat er daadwerkelijk contact wordt gemaakt tussen de vloeistof en het substraat. Dit luchtkusseneffect kan enkele milliseconden duren en zorgt ervoor dat een relatief zachte landing wordt verkregen of zelfs voorkómen, zoals de bescherming van een airbag in een auto-ongeluk. In dit geval gedraagt de aanwezige lucht onder de druppel zich als airbag zodra de lucht moet worden uitgeperst via een laag van slechts enkele micrometers en hierdoor een lubricatiedruk wordt opgebouwd. De druppel wordt dan niet alleen afgeremd tot een fractie van zijn initiële snelheid, maar ook wordt het druppeloppervlak sterk vervormd. Deze vervorming heeft belangrijke gevolgen voor de opsluiting van een luchtbel onder de druppel en de daadwerkelijke vorming van vloeistof-substraat contact, het 'leeglopen' van de airbag. In dit proefschrift bestuderen we modeldruppels van millimeter grootte die met een matige snelheid van enkele tientallen centimeters per seconde een vast substraat naderen. Dit komt overeen met een Weber getal We rond één – wat aangeeft dat zowel de oppervlaktespanning als de traagheid een belangrijke rol spelen in de dynamica van de impact. We bestuderen de ontwikkeling van de luchtlaag en haar invloed op de dynamica van de navolgende impact.

De ontwikkeling van de luchtlaag tussen de druppel en het substraat wordt bestudeerd met reflectie interferentie microscopie (RIM) dóór het transparante substraat heen. **Hoofdstuk 3** beschrijft hoe een absolute filmdiktebepaling wordt verkregen door een combinatie van dubbele-golflengte RIM en het gebruik van een eindige spectrale bandbreedte om een karakteristiek dempingspatroon te verkrijgen voor de oscillaties in lichtintensiteit versus luchtlaagdikte. Dit resulteert in een beelddiepte van 8 μm, een nauwkeurigheid in de filmdiktebepaling beter dan 30 nm en een tijdresolutie die enkel gelimiteerd wordt door de state-of-the-art in hogesnelheidsfotografie (wij gebruiken 10-50 μs).

De dunne luchtlaag heeft een breedte-tot-hoogte verhouding van 10^3 en is simpelweg vlak - op eerste gezicht. De RIM methode onthult echter saillante details van de complexe filmontwikkeling, die bepalend blijken te zijn voor de dynamica van de impact. In **Hoofdstuk 2** laten we zien dat de filmdikte een lokaal minimum ontwikkelt buiten het centrum van de impact. De daling van het druppeloppervlak wordt echter afgeremd door de divergerende capillaire druk op de positie van voorgenoemde 'kink' met toenemende kromming. Hier wordt een evenwichtsdikte bereikt die overeenkomt met recente theoretische voorspellingen. Vervolgens 'zweeft' de druppel op de luchtlaag. Voor $We < 4$ kunnen we een tweede lokaal minimum waarnemen - en soms meerdere. **Hoofdstuk 4** verklaart dit door verdere advectie van de vloeistof. Vloeistof-substraat contact wordt gevormd wanneer een kritieke luchtlaagdikte van 200 nm wordt bereikt. Afhankelijk van We wordt het contact binnen enkele microseconden gevormd onder de eerste kink, wat tot een ringvormige impact en de opsluiting van een kleine luchtbel leidt ($We > 4$), óf contact wordt (tijdelijk) onderdrukt ($We < 4$). In het laatste geval observeren en beschrijven we de vorming van een enkel contactpunt onder de tweede kink na een tijdspanne van enkele milliseconden. De navolgende uitbreiding van vloeistof-substraat contact volgt een inertia-capillaire schalingswet (**Hoofdstuk 2**), en de spreidsnelheid is verhoogd in vergelijking met de initiële bevochtigingssnelheid voor druppels zonder luchtkusseneffect (**Hoofdstuk 4**).

Het is opmerkelijk dat druppels voor $We < 4$ zelfs kunnen stuiteren op de luchtlaag zonder tussendoor contact te maken met het substraat. In **Hoofdstuk 5** analyseren we zowel de dynamica van de druppel als de interactie met de luchtlaag om de rol van de lubricatielaag in het stuiterproces te karakteriseren. Natuurlijk elimineert de afwezigheid van een contactlijn een belangrijke bron van dissipatie. Dit is echter niet voldoende om de druppel meerdere malen te laten stuiteren met een restitutiecoëfficiënt hoger dan 0.9. In het bijzonder kunnen we concluderen dat een asymmetrie in de spreiding en contractie van de luchtlaag beslissend is om een efficiënte omdraaiing van de druppelimpuls teweeg te brengen. Een nauwkeurige analyse van de ontwikkeling van de luchtlaag laat zien dat de netto lubricatiekracht op de druppel altijd positief is gedurende de interactiefase met het substraat, zelfs wanneer de druppel van het substraat af beweegt. De energie geassocieerd met het massacentrum van de druppel, die wordt opgeslagen in interne modi tijdens de interactiefase, wordt dus vrijwel geheel teruggewonnen. De details van de vorm van het druppeloppervlak zijn dus niet alleen beslissend voor de dynamica van contactvorming en opsluiting van luchtbellen, maar ook voor het stuiterproces.

We bestuderen de invloed van een micro-gestructureerd substraat op de uitpersing van de lucht in **Hoofdstuk 6**. Met gebruik van lithografie produceren we microstructuren met scherpe verticale kanten, namelijk plateaus met een enkele stap en smalle richels. Zo'n scherpe kant heeft alleen een zeer lokaal effect op de uitpersing van de lucht. De luchtlaagdikte heeft een minimum boven de rand van de microstructuur. Vloeistof-substraat contact wordt geforceerd op de rand wanneer de lokale luchtlaagdikte een kritieke waarde van $\sim$ 60 nm bereikt, mits de microstructuur hoog genoeg is of een grote hoogte-tot-breedte verhouding heeft. We bediscussiëren de implicaties voor de onderdrukking van stuiteren en gecontroleerde bevochtiging, en de incidentele voortijdige destabilisatie van de luchtlaag door de aanwezigheid van kleine stofdeeltjes of onregelmatigheden.

We sluiten af door een coherent overzicht te schetsen van de scenario's die kunnen optreden na het afremmen en vervormen van een druppel door de luchtlaag voor Weber getallen rond één. **Hoofdstuk 7** beschrijft de verschillende mogelijkheden betreffende vloeistof-substraat contactvorming versus stuiteren, en opsluiting van luchtbellen versus (volledige) uitpersing van de aanvankelijk ingesloten lucht - wat afhankelijk is van de details van de filmontwikkeling. Voor inkjet druppels verwachten we dezelfde scenario's hoewel de luchtlaagdikte kleiner is.

Chapter 1

Introduction

The impact of droplets on solid surfaces is of importance to wide-spread biological, environmental and industrial applications. The targeted outcome of the impact can be very different: sticking to the surface, completely spreading out, bouncing off, or fragmentation into many small droplets. For example in nature many animal integuments (skin, scales, feathers) and plant leaves have superhydrophobic properties such that rain droplets bounce off. This has distinct biological functions such as the self-cleaning 'lotus effect' to remove pathogens and dust particles [1, 2], the possibility of aquatic animals to respire under water [3], or the prevention of photosynthesis impairment by a thin water film [4]. Consequently, applying pesticides to crops is particularly difficult as the pesticide spray tends to be repelled, even break up in many small droplets. Since these so-called aerosols can be dispersed by the wind and thus pollute the environment, surfactants are added to the pesticide spray [5] or the viscosity is modified [6] to prevent drop fragmentation. On the other hand, fragmentation can be advantageous in other processes like spreading of fungus spores *via* splashing of raindrops [7], or atomization in combustion sprays [8]. In many industrial applications spreading of the droplet should be carefully controlled ranging from complete wetting into a continuous film (*e.g.* fluid coating) to partial spreading of the droplet to obtain discrete structures in inkjet-printing [9].

1.1. Motivation for droplet impact studies

The motivation for this thesis was inkjet-printing for high-end applications. While conventional graphic printing requires relatively 'large' droplets of about 100 picoliter volume (a diameter of 60 micron) to obtain a resolution sufficient to the human eye, printing of electronics has higher demands. Many efforts are made in this field to reduce the droplet size as to improve the resolution and reduce the consumption of - often expensive - materials. Simultaneously the droplets as small as 1 picoliter (a diameter of 10 micron) should be accurately positioned to still form connected lines in the electrical circuit. An illustrative example is a solar cell, as shown in Figure 1, that converts sunlight to electricity. Its semiconductor base consists of a monocrystalline silicon wafer decorated with a micro-texture to increase light absorption. The generated current is transported *via* a contact grid on top of the micro-textured wafer. To obtain a high energy conversion efficiency the width of the lines (so-called 'fingers') should be minimized, for which inkjet

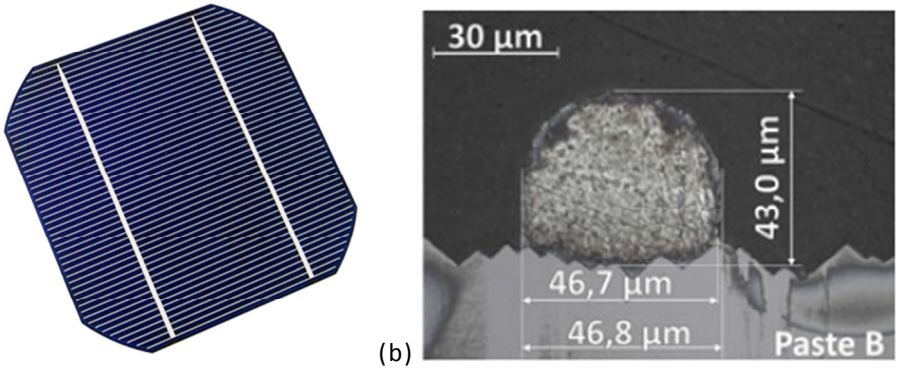

(a) (b)

Figure 1. Solar cell. (a) Picture showing the contact grid on a solar cell: two busbars with perpendicular fingers. (b) Cross-section of an inkjet-printed finger [10]. Silver paste is printed in a line on top of a silicon wafer with pyramidal micro-texture.

printing techniques are developed [10-12]. Aiming at line widths down to ~ 30 micrometer, this yields high demands not only to droplet size, but also printing accuracy and knowledge of the spreading dynamics on the micro-texture. In this thesis we describe droplet impact using a model system of millimeter-sized aqueous droplets. The larger length scale offers a good resolution to study the fundamentals of the impact. Yet, due to similarities in ratio between inertial and surface tension forces [9, 13] implications can be derived for the micron-sized inkjet droplets.

1.2. Droplet impact scenarios and surface properties

A liquid droplet impacting on a dry rigid substrate, liquid layer or deep liquid pool can show very different behaviors that can be narrowed down to either one of three: bouncing, spreading or coalescence, and splashing. For an extensive review, see Refs. [14, 15]. Impacts on liquid pools and dry rigid substrates have different complications. In case of a liquid pool, the flow can also penetrate into the bulk, *e.g.* a crater can be formed that ejects a so-called Worthington jet. During impact on a dry rigid substrate the substrate is undisturbed, but one has to consider the three-phase contact line. As a consequence the surface structure, *i.e.* its wettability and roughness, is a critical factor. Next to this, the outcome of the impact depends on impact velocity, droplet size, liquid properties (density, viscosity and Non-Newtonian effects), surface tension, and the properties of the surrounding air. We give a short description of how the various parameters influence droplet impact with a main focus on the substrate properties.

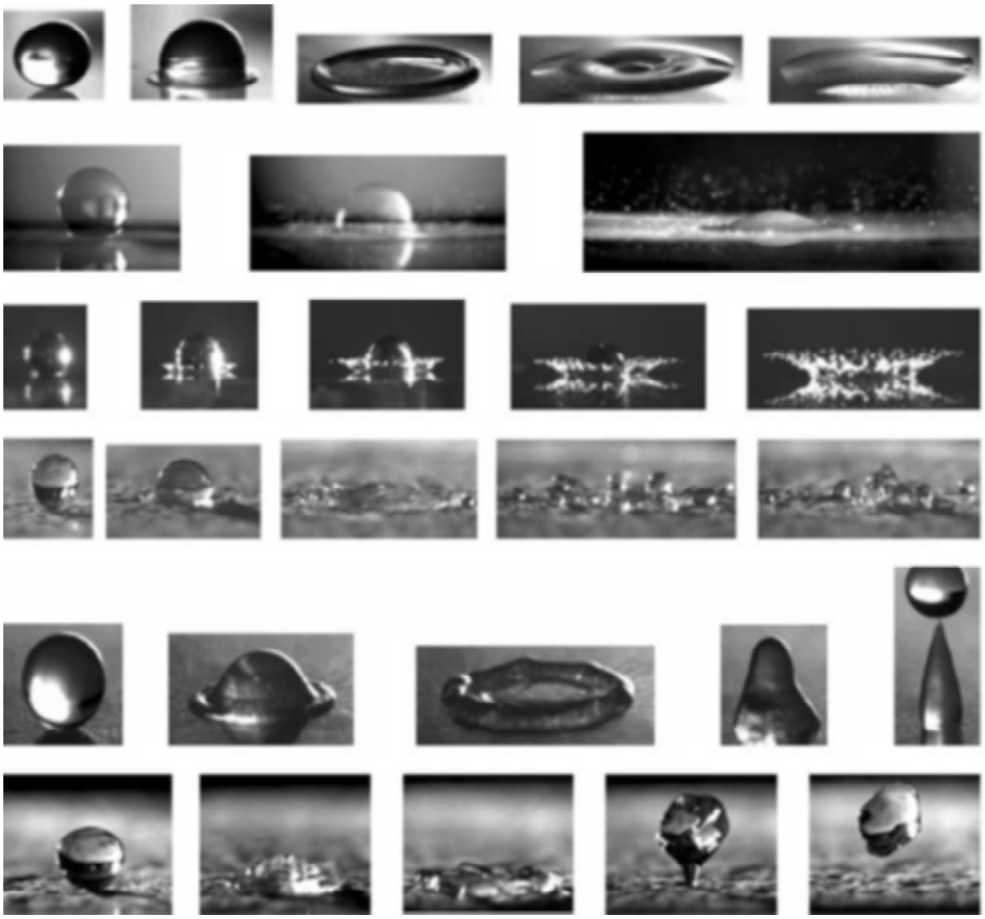

Figure 2. Droplet impact scenarios on a dry solid surface. Six cases are shown, from top to bottom: (1) deposition; (2) prompt splash; (3) corona splash; (4) receding break-up; (5) partial rebound; and (6) complete rebound. Picture taken from Ref. [16].

The impact scenarios defined by Rioboo *et al*. [16] shown in Figure 2 show a large variety in outcomes. Yet, the first stage is universal. It has been shown recently that the very early times of spreading $\lesssim 10$ μs (for a millimeter-sized droplet) are completely independent of substrate wettability [17]; the dynamics is determined by inertia and follows the universal law $r \sim t^{1/2}$ [18]. For slightly larger times $\lesssim 1$ ms the equilibrium contact angle comes into play and determines the exponent of the power-law for the remainder of the inertial regime [19]. Hereafter, a transition is observed to a regime where dissipation mechanisms start to play a role in the droplet spreading. Two main sources of dissipation are proposed

using the *hydrodynamic theory* [20-22] and the *molecular kinetic theory* [23] that are a macro- and microscopic approach respectively. The first ascribes the dissipation to viscous flows in the droplet, leading to Tanner's law for spreading of the droplet, $R{\sim}t^{1/10}$. Due to diverging shear rates at the contact line a cut-off value needs to be implemented assuming a certain amount of slip at the solid substrate, or assuming a precursor film in the completely wetting case [24]. The molecular kinetic theory ascribes the dissipation to absorption and desorption of fluid particles to the substrate in the vicinity of the advancing contact line, which leads to $R{\sim}t^{1/7}$ instead. Both theories have their limitations and combined theories were proposed to explain the experimental observations, *e.g.* [25]. In any case, the properties of the substrate start to become important in this phase, either through the contact angle or through the specific interaction between the liquid molecules and the substrate.

Whether or not a droplet splashes depends on impact velocity and surface tension, whose ratio is given by the Weber number, $We = \rho R_0 v^2/\sigma$: splashing is promoted by a high impact velocity and a low surface tension. A critical value We_c is often reported to define the splashing threshold, but this also depends crucially on other parameters such as surface roughness [14]. Roughness has been shown to either promote or inhibit splashing depending on the splashing mechanism [26]. Figure 2 shows the prompt splash (second line) and the corona or thin sheet splash (third line). During a prompt splash droplets are ejected at the contact line, which is promoted by roughness. For a thin-sheet splash, a thin ejecta sheet should be first lifted from the surface (requiring a low surface tension) and small satellites are subsequently ejected from this sheet. Roughness inhibits the detachment of the ejecta sheet and thus the thin sheet splash. Additionally, both the corona [27] and the prompt splash [26] can be suppressed by decreasing the pressure of the surrounding gas, which already exemplifies the important role of the surrounding air in droplet impact.

For lower velocity impacts, splashing is absent and the droplet continues to spread until its kinetic energy is converted to surface energy, and partly dissipated by viscous forces. The subsequent behavior depends largely of the contact angle hysteresis characterized by an advancing angle θ_{adv} and a receding angle θ_{rec}. If viscosity dissipates most of the energy the droplet slowly equilibrates to its equilibrium diameter leading to deposition (shown in the first line of Figure 2) [28, 29]. However if viscous dissipation is small, the droplet footprint overshoots its maximum diameter, obtaining a contact angle that is smaller than the receding one. Subsequently the contact line starts to recede. Whether the droplet equilibrates on the surface towards $\theta_{rec} < \theta < \theta_{adv}$ or bounces off, depends

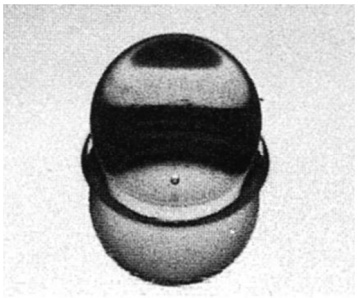

(a)

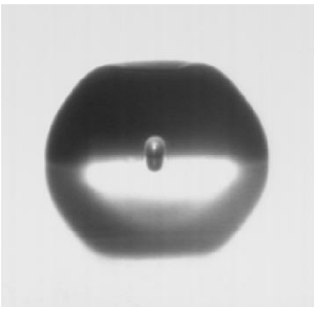

(b)

Figure 3. Air bubble entrapment. (a) Impact of an R = 0.71 mm n-heptane droplet at a velocity of 0.93 m/s ($We \sim 21$). Picture taken from Ref. [30]. (b) Impact of an R = 30 μm water droplet at a velocity of 0.74 m/s ($We \sim 0.23$). Picture taken from Ref. [9].

largely on the contact angle hysteresis of the substrate that originates from roughness or chemical heterogeneities [15]. When the stored surface energy gets fully dissipated at the contact line during the receding motion, the droplet gets pinned on the surface. On non-wettable surfaces the shrinking lamella may also break into a number of fingers (shown in the fourth line of Figure 2). In contrast when the contact angle hysteresis is low enough, the droplet can bounce off - either partially when a capillary instability is present or fully (shown in the fifth and bottom line of Figure 2).

In most studies described above the influence of the surrounding air is neglected, apart from the more recent splashing studies [9, 26, 27]. Earlier, experimental reports of tiny air bubbles being incorporated into drops [9, 30-32] did demonstrate the importance of expulsion of air in the impact process. These experiments showed an air disk captured in the impact zone that retracts into a spherical bubble shown in Figure 3. Universally, the formation of the air disk is explained by air entrapment; numerical simulations using a one-field volume of fluid method [33] show that divergence of the viscous pressure in the extremely thin gas layer forms a dimple in the droplet interface. From measurements of the air disk size and final bubble volume it follows that the average initial thickness of the assumedly flat disk is about 0.5 to 2 μm (for impact on a liquid pool [32]), and that the bubble size increases for lower impact speeds. However, the exact shape of the dimple interface could not be experimentally recovered. Some particular observations at low impact velocities thus remained unexplained, such as a large variation in bubble number, size and position [9, 32]. These studies however initiated more fundamental work - both numerical and experimental - to describe the role of the surrounding air in droplet impact.

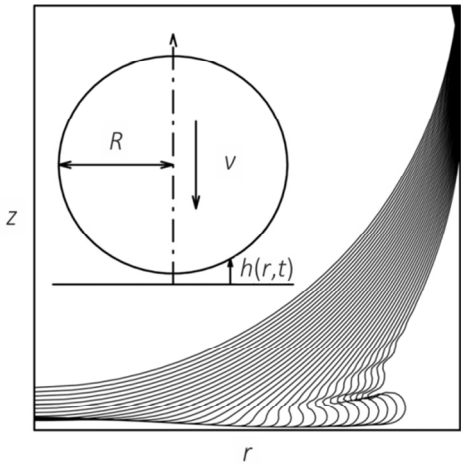

Figure 4. Sketch of the droplet impact. A liquid sheet (2D: jet) forms when the interface overturns. Figure adapted from Ref. [34].

1.3. Air lubrication in droplet impact

Based on the early model by Smith, Li and Wu [35] and motivated by the just described experimental observations, recently several authors have developed theoretical models to study the role of the surrounding air in droplet impact [34, 36-41]. The papers all originate from the period 2009-2013 in which this PhD project was executed, and they describe various extensions to the model that partly overlap as they were developed independently in the same time frame. In the following we will first explain the main theoretical concepts and then summarize the various extensions that have been considered, with the main focus on the version by Brenner *et al*. [36, 38, 39] that we use extensively throughout this thesis.

1.3.1. Main theoretical concepts

The impact of a droplet is sketched in the inset of Figure 4: a deformable water droplet of radius R is moving towards the solid substrate with velocity v such that the air gap between them gets smaller and smaller. We consider a two-dimensional model and neglect the effects of surface tension, compressibility and gravity. Due to a building air pressure the water motion and in particular the shape of the droplet interface are altered close to the air gap, to which we refer as ‘cushioning’. The central question is when and how cushioning by the surrounding air takes place.

We first consider the liquid motion. In a typical droplet impact event the Reynolds number balancing the inertial forces to viscous forces $Re = \rho UL/\mu$ is large. Here, ρ and μ are the density and the viscosity of the fluid, and U and L are the typical velocity and lengthscale. For a millimeter-sized water droplet impacting with a velocity between 0.1 and 10 m/s the Reynolds number is of order 10^2-10^4. The water motion can thus be treated inviscid during the approach, *i.e.* it is dominated by inertia of the fluid. The liquid motion and the air motion couple as follows: the dynamics of the air - yet unknown - are solved subject to the velocity conditions at the interface given by the water solution. The horizontal gas velocity is much higher than that in the liquid and its viscosity is much smaller, thus a no-slip boundary condition is employed for the gas dynamics. Subsequently, the water motion can be solved subject to the generated air pressure at the interface, and so on. When the droplet is far away from the substrate, the pressure build-up in the air is negligible due to its very low viscosity μ_{air}, thus the influence on the interfacial shape is insignificant. Ultimately a thin gap is created in which the air motion is either described by an inviscid or viscous (lubrication) layer. This depends on the local Reynolds number in the gap: dominance of viscosity is promoted by the small vertical length scale of the gap, while dominance of inertia is promoted by large horizontal gas velocities. An inviscid air response is only expected if the droplet Reynolds number is above 10^7. Thus, for a wide range of droplet experiments the lubrication approach is valid, *i.e.* significant air cushioning does not occur until the air layer is sufficiently thin. The full coupled liquid-air problem is thus described by an inviscid-lubrication balance.

Initially the pressure increase is strongest at the center of the droplet - where the gap is thinnest -, and the motion of the interface is locally strongly decelerated. This cushioning effect can be compared to the deceleration by an airbag in a crash, yet here it is the naturally present air that slows down the droplet to a small fraction of its initial impact speed. This causes the droplet interface to deform. The change of curvature sign leads to the formation of a so-called ‘dimple’ in the liquid interface as shown in Figure 5(a) for $t > 0$. The raised pressure in the middle creates a stagnation point in the fluid that tends to drive fluid to the sides as shown in Figure 6. As a result the fluid is collected in a rim or “kink” that moves down and outward, and is accompanied by a local pressure peak that increases and also moves outward as shown in Figure 5(b). When the liquid finally touches down at the two kinks - or in a ring in the axisymmetric case -, an air bubble is entrapped. It should be noted that the final stages are not incorporated in the model as other effects

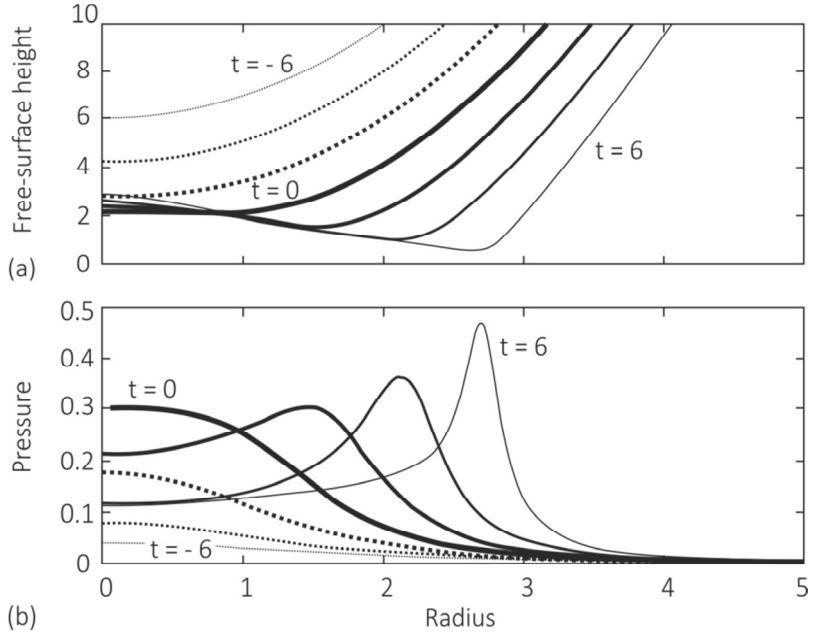

Figure 5. Evolution of the (a) interface shape, and (b) pressure as the droplet approaches the substrate. Profiles are axisymmetric and shown from t = -6 to t = 6 (touchdown). The thick solid lines indicates t = 0, when impact would occur without cushioning. Figure adapted from Ref. [37].

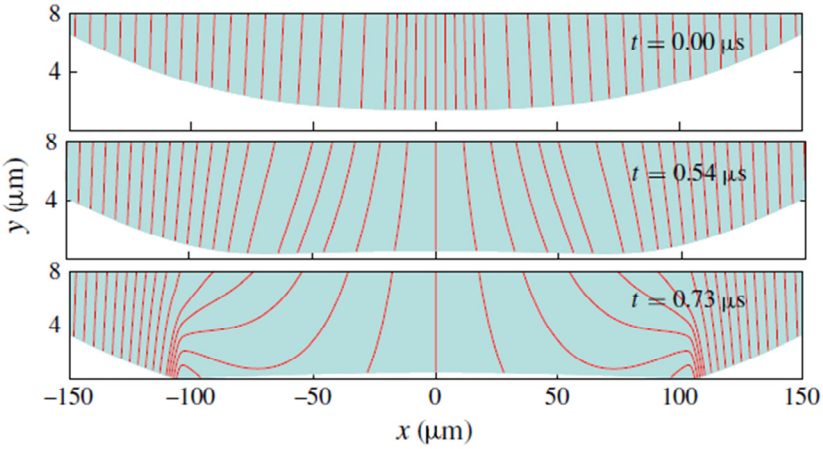

Figure 6. Stagnation point in the droplet, diverting fluid towards the rim. The curves show instantaneous streamlines of the flow, where the local liquid velocity is proportional to the density of streamlines. Figure adapted from Ref. [39].

start playing a role when the air layer thickness diminishes. These include the breakdown of lubrication theory, surface tension, non-linear inertia, liquid viscosity, Van der Waals forces between the liquid and the substrate, interface fluctuations, surface roughness, and non-continuum (rarefied gas) effects, some of which will be treated in the following section.

1.3.2. Recent theoretical studies and model extensions

Motivated by the air pressure-dependence of splashing observed in experiments by Xu *et al.* [27], Brenner and coworkers aim to explain the role of the surrounding air in the launch of the ejecta sheet that expels droplets in a corona splash (see third line of Figure 2) [36]. They pose the hypothesis that "the liquid [ejecta] sheet might originate due to the interaction of the liquid with the intervening gas layer *before* the droplet contacts the solid surface." Therefore they are in particular interested in what happens at the final moment of touchdown of the droplet. Although liquid inertia and gas pressure initially fully dominate the dynamics according to the model described above, the development of the kink holds the key for a change in dynamics. Owing to the divergence of liquid velocities, curvature and gas pressure at the kink, initially small terms in the governing equations grow rapidly and can take over the dynamics. In a sequence of three papers they unravel the touchdown dynamics. (In addition their model contains gas compressibility assuming isothermal or adiabatic behavior - which is of less interest to our low velocity experiments.) At low impact velocities, the kink singularity is inhibited by surface tension which causes the droplet to skate on an air film of constant thickness [36]. At higher impact velocities surface tension is negligible and other terms become important [38]. In particular, advection takes over the dynamics [39]: the large horizontal velocity component at the interface amplifies the interfacial slope of the kink, which can eventually lead to overturning of the interface and ejection of a sheet. When the drop contacts the surface the ejected sheet is a potential precursor to splashing due to development of a viscous boundary layer at the substrate, and launching of the sheet. This opens up the possibility of separation of dimple touchdown and splashing in time. It should be noted that contact formation itself is not included in the model as steepening of the interfacial slope finally leads to violation of the model assumptions, and contact is invoked by non-continuum effects or roughness of the interface.

Duchemin and Josserand ignore compressibility and use a curvilinear description of the interface [34] to be able to detect sheet formation instead of merely divergence of the

interfacial slope. In the presence of surface tension a thin sheet indeed emerges as shown in Figure 4. However, the air layer height below the sheet is of the order of a few angstrom under conditions of splashing impacts, so it is expected that the liquid touches the solid. In a second paper they study the non-continuum effects that come into play upon touchdown, *i.e.* when the air layer height is of the order of the mean free path length [40]. In this case, the no-slip condition does not hold any more for the rarefied gas and is replaced by a slip velocity at both interfaces. This changes the dynamics of the singularity, and even the dynamics of the initial interfacial dynamics if the gas pressure is reduced. The large mean free path then leads to a pressure-dependence of air bubble inclusion - and possibly ejecta sheet features.

Finally, Hicks and Purvis [37] extended the model to three dimensions allowing to predict the size of the trapped air bubble in terms of the droplet radius and impact velocity. These prediction show good agreement by direct comparison with the experimental observations in Refs. [9, 42]. In the most recent paper they investigate the role of gas compressibility taking into account both thermal diffusion and viscous dissipation [41] in contrast to Brenner's simplified approach of either isothermal or adiabatic behavior [38]. This yields additional information about the gas temperature and density profiles, and reveals a small dependence of the air bubble size on the air properties.

1.3.3. Recent experimental studies

The theoretical predictions gave rise to various independent experimental studies visualizing the cushioning process in a relatively short time period (2011-2012). Driscoll and Nagel [43] used reflection interference microscopy to show that the first indication of splashing, *i.e.* launching of the ejecta sheet, is separated in time and space from the cushioning air layer. The droplet has touched down (incorporating an air bubble) before interference fringes are observed at the edge of the spreading droplet. Their conclusion that gas flow at the edge is thus responsible for destabilizing the liquid - rather than the cushioning air film - might be premature as Brenner *et al.* [39] later showed that this separation of timescales is theoretically possible when advection dominates at the touchdown. Three papers followed that describe the evolution of the droplet interface in detail; our own study [44] described in Chapter 2 and the study by Van der Veen *et al*. [45] both use reflection interferometry, while the study by Kolinski *et al*. [46] uses total internal reflection. The latter focuses at higher impact velocities leading to splashing, while we focus at the regime of relatively low $We \sim 1$. Results from the other two papers will be discussed where applicable.

Other studies focused at the predicted air bubble inclusion: these include measurements of air bubble size as function of the impact velocity [47], and detailed characterizations of the contraction of the enclosed air film. The latter shows a characteristic toroidal bubble stage [48, 49], which is followed by daughter droplet inclusion and wettability-dependent bubble detachment as demonstrated with x-ray phase-contrast imaging [48].

1.4. Thesis outline

In this thesis we demonstrate the existence of a lubrication air film below an impacting droplet, and we describe its role on impact dynamics in the case of low droplet velocity. The droplet experiences an air-cushioning effect that guarantees a relatively soft landing, similar to the protection by an airbag in a crash. Using high-speed reflection interference microscopy to visualize the development of the air film, we not only confirm the predictions of the existing numerical simulations, but are also able to extend beyond their assumptions and characterize the air film in further stages of the impact process. For Weber numbers around unity the time evolution of the radial thickness profile depends critically on the surface tension effects. For $We \gtrsim 1$ the air film gets trapped as a small bubble below the droplet within microseconds, while for $We \lesssim 1$ the air film is expanding over the whole "contact" area, thereby delaying liquid-solid contact by milliseconds - or even preventing it altogether. The general phenomenon of droplet cushioning is presented in **Chapter 2**, where we show time-evolving radial thickness profiles of the air film for varying strength of the surface tension (We ~ 1 … 10). We also describe the dynamics of the triple contact line after liquid-solid contact has been formed.

After the description of the main phenomena, we focus on several facets in detail. **Chapter 3** explains the development of the Reflection Interference Microscopy (RIM) technique used to measure the air film thickness. With this technique we can look through the transparent substrate and directly measure the micrometric thickness of the squeezed film based on interference theory. A complication is the absence of a reference height; yet, we discuss our method to obtain an absolute height measurement with an accuracy better than 30 nm.

In **Chapter 4** we observe that the lubricating air layer develops several local minima in the film thickness. It is observed that more and more fluid is diverted into subsequent sharp kinks that approach the substrate while continuing to squeeze out air. We explain this by the effects of surface tension and advection. Eventually, solid-liquid contact is formed at

the kink that approaches the substrate within $\sim$ 200 nm. We characterize the early-times of spreading that are restricted to the cushioned region, and compare it to the reference case of spherical drop impact.

Remarkably, droplets can even bounce repeatedly on a persisting air layer below it. This is demonstrated in **Chapter 5** for $We < 4$ and when no irregularities are present in the impact zone. Since contact line hysteresis is strictly absent, the restitution of the bounce is determined exclusively by internal dissipation (in droplet oscillations) and dissipation in the squeezed air layer. Here, we analyze both the droplet dynamics and interaction with the lubrication layer to characterize the role of the lubrication layer in bouncing. We compare our approach to previous models in literature that neglect the lubrication effect, and find that the observed shape details of the air film are critical for bouncing.

In **Chapter 6** we show that liquid-solid contact can be actively induced by introducing a microstructure in the impact zone. In particular we show that a sharp vertical edge or pillar with large height-to-width aspect ratio “pierces” the air film and induces wetting. We measure the film thickness near the edge and use a simple interface description to predict the height of the edge needed to induce contact.

Finally, we present our overall conclusions and outlook in **Chapter 7**. Here, we discuss implication of the cushioning and sketch a coherent picture for the different scenarios following cushioning, *i.e.* wetting or bouncing.

References

[1] C. Neinhuis and W. Barthlott, Characterization and distribution of water-repellent, self-cleaning plant surfaces, *Ann. Bot.* **79** (1997), 667-677.

[2] W. Barthlott and C. Neinhuis, Purity of the sacred lotus, or escape from contamination in biological surfaces, *Planta* **202** (1997), 1-8.

[3] A. Balmert, H. Florian Bohn, P. Ditsche-Kuru and W. Barthlott, Dry under water: Comparative morphology and functional aspects of air-retaining insect surfaces, *Journal of Morphology* **272** (2011), 442-451.

[4] W. Smith and T. Mcclean, Adaptive relationship between leaf water repellency, stomatal distribution, and gas exchange, *Am. J. Bot.* (1989), 465-469.

[5] W. Wirth, S. Storp and W. Jacobsen, Mechanisms controlling leaf retention of agricultural spray solutions, *Pestic. Sci.* **33** (1991), 411-420.

[6] V. Bergeron, D. Bonn, J.Y. Martin and L. Vovelle, Controlling droplet deposition with polymer additives, *Nature* **405** (2000), 772-775.

[7] P. Gregory, E. Guthrie and M.E. Bunce, Experiments on splash dispersal of fungus spores, *J. Gen. Microbiol.* **20** (1959), 328-354.

[8] C. Mundo, M. Sommerfeld and C. Tropea, Droplet-wall collisions: experimental studies of the deformation and breakup process, *Int. J. Multiphase Flow* **21** (1995), 151-173.

[9] D. Van Dam and C. Le Clerc, Experimental study of the impact of an ink-jet printed droplet on a solid substrate, *Phys. Fluids* **16** (2004), 3403.

[10] M. Pospischil, J. Specht, H. Gentischer, M. König, M. Hörteis, C. Mohr, R. Zengerle, F. Clement and D. Biro, Correlations between finger geometry and dispensing paste rheology, *Proc. 27th Eur. Photovoltaic Solar Energy Conf. Exhib*, Frankfurt (2012).

[11] D.-Y. Shin, Y.-K. Cha, H.-H. Ryu and S.-H. Kim, Impact of effective volume ratio of a dispersant to silver nano-particles on silicon solar cell efficiency in direct ink-jet metallization, *J. Micromech. Microeng.* **22** (2012), 115007.

[12] D.-H. Kim, S.-S. Ryu, D. Shin, J.-H. Shin, J.-J. Jeong, H.-J. Kim and H.S. Chang, The fabrication of front electrodes of Si solar cell by dispensing printing, *Mater. Sci. Eng. B* **177** (2012), 217-222.

[13] H. Dong, W.W. Carr, D.G. Bucknall and J.F. Morris, Temporally-resolved inkjet drop impaction on surfaces, *AIChE Journal* **53** (2007), 2606-2617.

[14] M. Rein, Phenomena of liquid drop impact on solid and liquid surfaces, *Fluid Dyn. Res.* **12** (1993), 61-93.

[15] A. Yarin, Drop impact dynamics: splashing, spreading, receding, bouncing…, *Annu. Rev. Fluid Mech.* **38** (2006), 159-192.

[16] R. Rioboo, C. Tropea and M. Marengo, Outcomes from a drop impact on solid surfaces, *Atomization Spray* **11** (2001), 155-165.

[17] K.G. Winkels, J.H. Weijs, A. Eddi and J.H. Snoeijer, Initial spreading of low-viscosity drops on partially wetting surfaces, *Phys. Rev. E* **85** (2012), 055301(R).

[18] A.L. Biance, C. Clanet and D. Quere, First steps in the spreading of a liquid droplet, *Phys. Rev. E* **69** (2004), 016301.

[19] J.C. Bird, S. Mandre and H.A. Stone, Short-time dynamics of partial wetting, *Phys. Rev. Lett.* **100** (2008), 234501.

[20] C. Huh and L. Scriven, Hydrodynamic model of steady movement of a solid/liquid/fluid contact line, *Journal of Colloid and Interface Science* **35** (1971), 85-101.

[21] O. Voinov, Hydrodynamics of wetting, *Fluid Dynamics* **11** (1976), 714-721.

[22] R. Cox, The dynamics of the spreading of liquids on a solid surface. Part 1. Viscous flow, *J. Fluid Mech.* **168** (1986), 169-194.

[23] T. Blake and J. Haynes, Kinetics of liquid-liquid displacement, *Journal of Colloid and Interface Science* **30** (1969), 421-423.

[24] P.G. De Gennes, Wetting: statics and dynamics, *Rev. Mod. Phys.* **57** (1985), 827-863.

[25] M.J. De Ruijter, J. De Coninck and G. Oshanin, Droplet spreading: partial wetting regime revisited, *Langmuir* **15** (1999), 2209-2216.

[26] A. Latka, A. Strandburg-Peshkin, M.M. Driscoll, C.S. Stevens and S.R. Nagel, Creation of prompt and thin-sheet splashing by varying surface roughness or increasing air pressure, *Phys. Rev. Lett.* **109** (2012), 054501.

[27] L. Xu, W.W. Zhang and S.R. Nagel, Drop splashing on a dry smooth surface, *Phys. Rev. Lett.* **94** (2005), 184505.

[28] S. Schiaffino and A.A. Sonin, Molten droplet deposition and solidification at low Weber numbers, *Phys. Fluids* **9** (1997), 3172.

[29] R. Rioboo, M. Marengo and C. Tropea, Time evolution of liquid drop impact onto solid, dry surfaces, *Exp. Fluids* **33** (2002), 112-124.

[30] S. Chandra and C. Avedisian, On the collision of a droplet with a solid surface, *Proc. R. Soc. Lond. A* **432** (1991), 13-41.

[31] H. Fujimoto, H. Shiraishi and N. Hatta, Evolution of liquid/solid contact area of a drop impinging on a solid surface, *Int. J. Heat Mass Transfer* **43** (2000), 1673-1677.

[32] S.T. Thoroddsen, T.G. Etoh and K. Takehara, Air entrapment under an impacting drop, *J. Fluid Mech.* **478** (2003), 125-134.

[33] V. Mehdi-Nejad, J. Mostaghimi and S. Chandra, Air bubble entrapment under an impacting droplet, *Phys. Fluids* **15** (2003), 173.

[34] L. Duchemin and C. Josserand, Curvature singularity and film-skating during drop impact, *Phys. Fluids* **23** (2011), 091701.

[35] F.T. Smith, L. Li and G.X. Wu, Air cushioning with a lubrication/inviscid balance, *J. Fluid Mech.* **482** (2003), 291-318.

[36] S. Mandre, M. Mani and M.P. Brenner, Precursors to splashing of liquid droplets on a solid surface, *Phys. Rev. Lett.* **102** (2009), 134502.

[37] P.D. Hicks and R. Purvis, Air cushioning and bubble entrapment in three-dimensional droplet impacts, *J. Fluid Mech.* **649** (2010), 135-163.

[38] M. Mani, S. Mandre and M.P. Brenner, Events before droplet splashing on a solid surface, *J. Fluid Mech.* **647** (2010), 163-185.

[39] S. Mandre and M.P. Brenner, The mechanism of a splash on a dry solid surface, *J. Fluid Mech.* **690** (2012), 148-172.

[40] L. Duchemin and C. Josserand, Rarefied gas correction for the bubble entrapment singularity in drop impacts, *C. R. Mecanique* **340** (2012), 797-803.

[41] P.D. Hicks and R. Purvis, Liquid-solid impacts with compressible gas cushioning, *J. Fluid Mech.* **735** (2013), 120-149.

[42] S. Thoroddsen, T. Etoh, K. Takehara, N. Ootsuka and Y. Hatsuki, The air bubble entrapped under a drop impacting on a solid surface, *J. Fluid Mech.* **545** (2005), 203-212.

[43] M.M. Driscoll and S.R. Nagel, Ultrafast interference imaging of air in splashing dynamics, *Phys. Rev. Lett.* **107** (2011), 154502.

[44] J. De Ruiter, J.M. Oh, D. Van Den Ende and F. Mugele, Dynamics of collapse of air films in drop impact, *Phys. Rev. Lett.* **108** (2012), 074505.

[45] R.C. Van Der Veen, T. Tran, D. Lohse and C. Sun, Direct measurements of air layer profiles under impacting droplets using high-speed color interferometry, *Phys. Rev. E* **85** (2012), 026315.

[46] J.M. Kolinski, S.M. Rubinstein, S. Mandre, M.P. Brenner, D.A. Weitz and L. Mahadevan, Skating on a film of air: drops impacting on a surface, *Phys. Rev. Lett.* **108** (2012), 074503.

[47] W. Bouwhuis, R.C.A. Van Der Veen, T. Tran, D.L. Keij, K.G. Winkels, I.R. Peters, D. Van Der Meer, C. Sun, J.H. Snoeijer and D. Lohse, Maximal air bubble entrainment at liquid-drop impact, *Phys. Rev. Lett.* **109** (2012), 264501.

[48] J.S. Lee, B.M. Weon, J.H. Je and K. Fezzaa, How does an air film evolve into a bubble during drop impact?, *Phys. Rev. Lett.* **109** (2012), 204501.

[49] Y. Liu, P. Tan and L. Xu, Compressible air entrapment in high-speed drop impacts on solid surfaces, *J. Fluid Mech.* **716** (2013), R9.

Chapter 2

Dynamics of collapse of air films in drop impact

Liquid drops hitting solid surfaces deform substantially under the influence of the ambient air that needs to be squeezed out before the liquid actually touches the solid. Nanometer- and microsecond-resolved dual wavelength interferometry reveals a complex evolution of the interface between the drop and the gas layer underneath. For intermediate impact speeds ($We \sim 1$ … 10) the layer thickness can develop one or two local minima – reproduced in numerical calculations – that eventually lead to the nucleation of true solid-liquid contact at a We-dependent radial position. Solid-liquid contact spreads across the drop substrate interface at a speed involving capillarity, liquid viscosity and inertia.

This Chapter has been published as:

J. de Ruiter, J.M. Oh, H.T.M. van den Ende, F. Mugele. Dynamics of Collapse of Air Films in Drop Impact, *Phys. Rev. Lett.* **108** (2012), 074505.

Liquid drops deform substantially upon impact onto a solid surface. Depending on impact speed they rebound, get deposited on the surface, or disintegrate in a splash (for a review, see Ref. [1]). Following experimental reports of tiny air bubbles being incorporated into drops [2-5] as well as the suppression of splashing upon reducing the ambient air pressure [6] it became clear that the expulsion of the air that initially separates the drop from the solid plays an important role in the impact process. Several models were formulated that describe the drop impact primarily in terms of a balance between the inertia of the decelerating liquid and the excess pressure arising from the viscous squeeze-out of the thin air layer [7-9]. A local pressure maximum right under the drop leads to the formation of a "dimple", which should eventually evolve into the enclosed air bubble [9]. Using this model and including corrections due to capillary forces, it was shown that a thin air film of almost constant thickness should develop under the drop [10], and the formation of a thin liquid jet was observed using an axisymmetric, curvilinear description [11]. Mandre *et al*. [10] suggested that this air film plays an important role, *e.g.* for the splashing process, but recent experiments by Driscoll and Nagel [12] question this scenario: while the presence of interference fringes right under the drop indeed confirms the formation of a dimple, their measurements suggest that direct liquid-solid contact forms very quickly around the dimple, separating dimple from splashing dynamics. Whether air films do play an important role in other regimes of drop impact, how they collapse to establish direct liquid-solid contact, and to what extent the proposed visco-inertial models describe these processes remains unexplored at this stage.

In this Chapter, we address these issues by monitoring the evolution and the collapse of the air film for a wide range of liquid properties (interfacial tension σ, viscosity μ_l, density ρ_l) at moderate impact speeds. To do so, we develop an advanced high speed dual wavelength interferometry technique that allows us to extract full thickness profiles with an unprecedented resolution of ~ 10 nm and 50 μs. Focusing on impact speeds of millimeter-sized droplets where both inertial and capillary forces compete with the gas pressure, $We = R\rho_l v^2/\sigma \sim 1 \ldots 10$, we demonstrate the transient formation of an air layer with a thickness of a few 100 nm to a few μm and a life time of a few ms. We identify distinct scenarios for the evolution of the interface profiles, with one or two local minima at different radial positions, for variable impact speed. The visco-inertial model including capillary forces reproduces all salient features including the scaling of the film thickness up to the nucleation of liquid-solid contact. The latter is found to occur within less than 50 μs from a distance of 200-500 nm. The subsequent spreading of liquid-solid contact occurs within $\approx$ 1 ms.

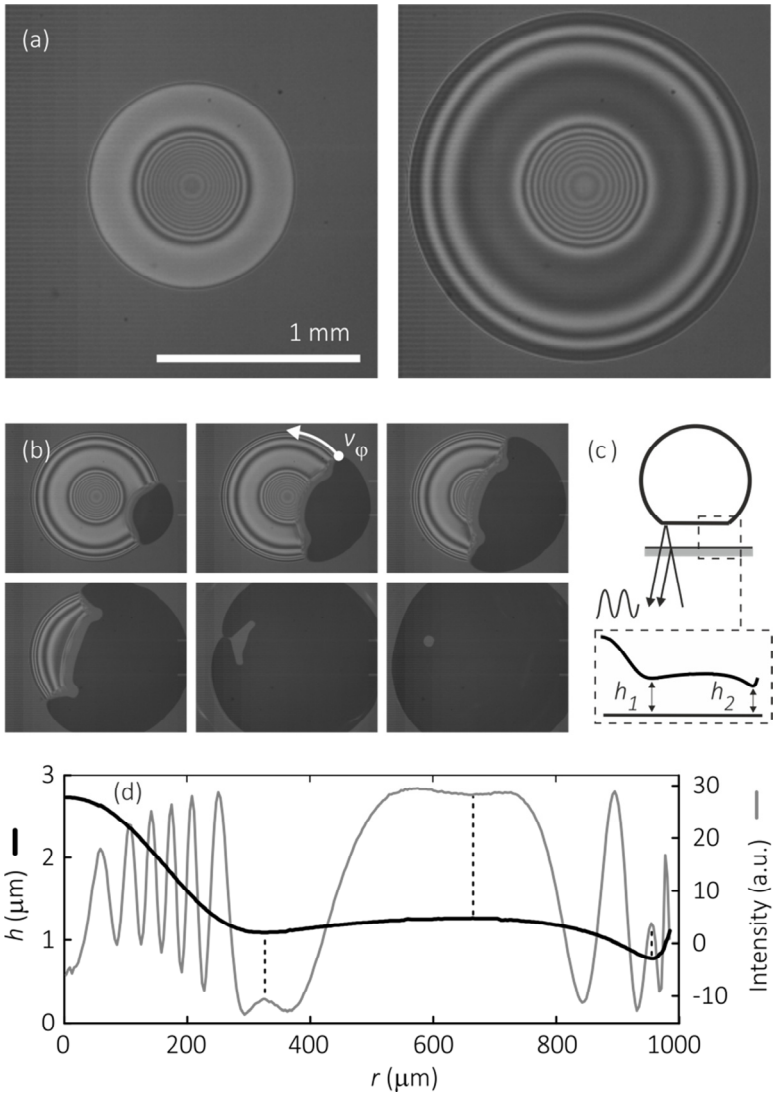

Figure 1. Droplet cushioning, and spreading of liquid-solid contact at moderate We impact. (a) Interference profile of the air film below a water droplet at (left) 4.1 and (right) 2.3 ms before nucleation of a liquid-solid contact. (b) Spreading of liquid-solid contact at 0.10, 0.21, 0.32, 0.49, 0.75, 1.05 ms after nucleation. v_φ: azimuthal spreading velocity. (c) Sketch of deformed drop indicating interference of light reflected from the solid/air and air/liquid interfaces. Inset: schematic dimple with local minima h_1 and h_1. (d) Characteristic radial intensity profile (thin grey line), and the corresponding interface profile (thick black line). Dotted lines indicate positions of local extrema in h.

Experiments are done with aqueous droplets, dispensed from a syringe pump to obtain a uniform radius of $R = 1.05$ mm. We vary the liquid properties using aqueous solutions of ethanol, glycerol, and $CaCl_2$, and obtain the following properties: $\sigma =$ 27-65 mN·m^{-1}, $\mu_l =$ 1-109 mPa·s, and $\rho_l =$ 997-1366 kg·m^{-3}. The droplets are impacting with a velocity v between 0.11 and 0.53 m/s onto carefully cleaned glass substrates (cover slip) with an rms surface roughness below 2 nm (measured with atomic force microscopy). Low concentrations of dye (rhodamin and fluorescein) are added to the liquids to suppress internal light reflections within the drop. The approach and impact are imaged in reflection mode through the transparent glass substrate by dual wavelength reflection interference microscopy (DW-RIM) at the 431 and 550 nm spectral lines (each with a bandwidth of $\sim$ 30 nm) of a mercury lamp. The separate interference signals are recorded with two synchronized high-speed cameras (Photron SA3 and SA5) at recording speeds up to 75000 fps. Figure 1(a) and Movie S1 [8] show typical interference patterns of the squeezed air film (for the 550 nm line). The non-monotonic spacing of the interference fringes indicates a rather complex thickness profile of the air layer with several inflection points. We extract absolute thickness profiles with an accuracy of $\approx$ 10 nm (see Figure 1(d)) by combining the information of the two wavelengths [13] and by interpolating between local maxima and minima of the intensity. Our optical model for the glass-air-water system shown in Figure 1(c) [8, 14] takes into account the finite aperture of the optics, the bandwidth of the light, as well as the spectral emission and sensitivity of the lamp and the cameras, respectively [15, 16].

We first analyze the time evolution of the liquid-air interface before liquid-solid contact (see Figure 2). When the drops enter our depth of view, they are already deformed and display a characteristic dimple profile with a central height of 4-5 µm. A “kink” of high local curvature at height h_1 marks the edge r_1 of the dimple. As time proceeds, this kink first approaches the substrate along with the central dimple. At some v-dependent value, both h_1 and r_1 saturate. As the drop spreads further, an air layer of approximately constant thickness is entrapped. For low impact speeds, see top profiles in Figure 2, the thickness of this layer eventually decreases and develops a second even sharper kink at r_2 as the drop approaches its maximum extension. The thickness h_2 at r_2 decreases linearly with time, see Figure 3(b), and eventually leads to the nucleation of liquid-solid contact. During this entire process, the film profile including h_1 remains essentially invariant in the range of $r \approx$ 200 … 700 µm. For somewhat higher impact speeds, see middle profiles in Figure 2, the overall thickness of the air layer decreases, and it develops a slight slope of $\approx$ 0.1°. Finally, a second kink develops and induces liquid-solid contact. For even higher

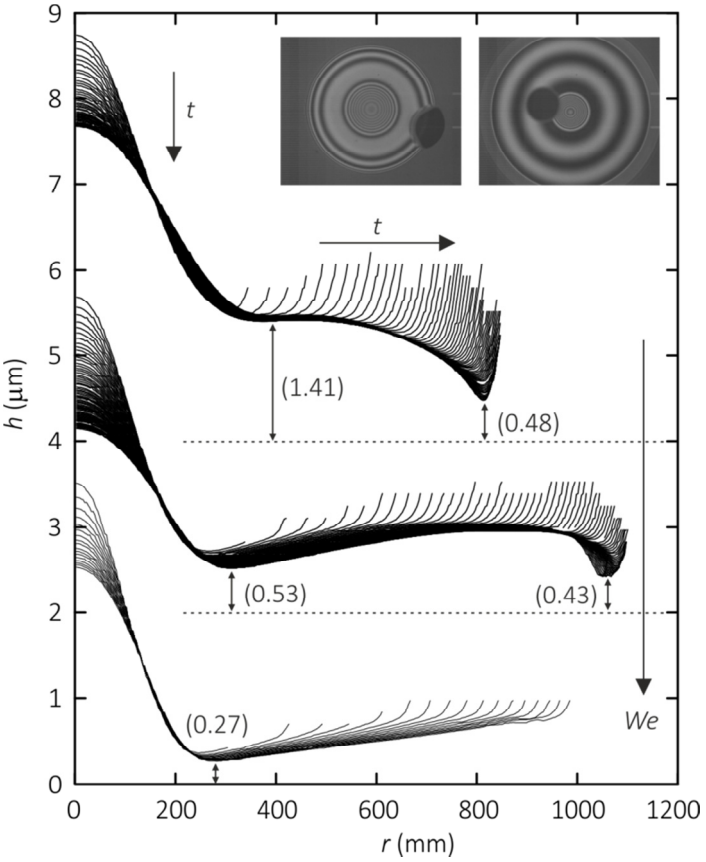

Figure 2. Time evolution of interface profiles for water drops with increasing impact velocities *v* (top to bottom: 0.24, 0.41, 0.52 m/s; corresponding We numbers: 0.9, 2.6, 4.2). Time step: 50 µs. Profiles for different v are shifted vertically for clarity. Note the different scales on the abscissa and the ordinate: maximum slope of interface $< 3°$. Numbers in parentheses indicate minimum heights in µm of h_1 and h_2. Inset: nucleation of solid-liquid contact at r_2 and r_1 for low (left) and high (right) We, respectively.

speeds, see bottom profile in Figure 2, however, no second kink is observed. Rather, h_1 becomes so small that nucleation of liquid-solid contact is observed before the drop reaches its maximum lateral extension, see inset of Figure 2. This transition from a two-kink scenario at low impact speeds to a single-kink scenario at higher v with liquid-solid contact nucleation at r_2 and at r_1, respectively, is consistently observed for all liquids. It occurs at $We \approx 1$ suggesting an important role of capillary forces in suppressing the kink at r_1 for low We.

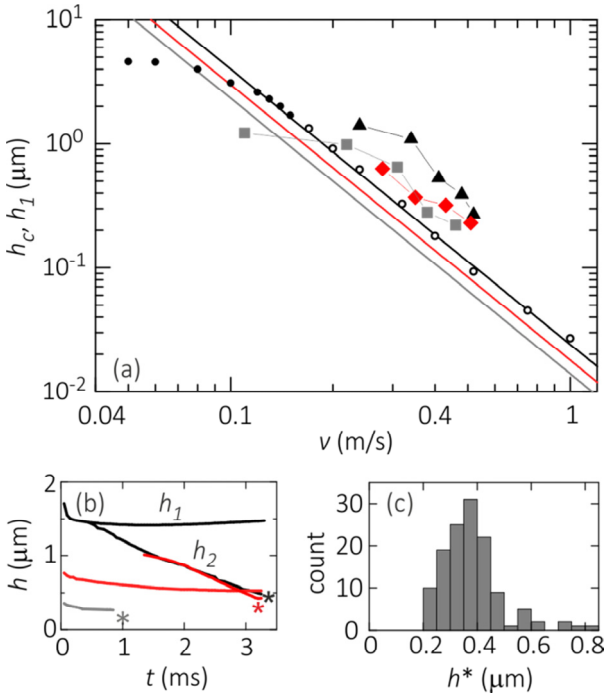

Figure 3. (Color online.) Temporal evolution of local minima, and their equilibrium and nucleation height. (a) Symbols: h_1 versus impact velocity v for experiments with water (black triangles), ethanol (red diamonds), and $CaCl_2$ (grey squares) drops. Solid lines: universal scaling law for h_c (colors according to experimental conditions). Dots: numerical values of h_1 for water; open dots: profiles with one local minimum, solid dots: two local minima. (b) h_1 and h_2 vs. time for the experiments shown in Figure 2. From top to bottom: $v = 0.24$, 0.41, and 0.52 m/s. The star indicates which of the two minima nucleates - at a height h^*. (c) Histogram showing the value of h^* in 128 experiments with various fluid properties (bin size 50 nm).

These results confirm the formation and subsequent evolution of the dimple including the existence of a thin transient air film of approximately constant sub-micrometer thickness, as predicted by the visco-inertial model including capillary forces [8, 10]. To achieve a more detailed comparison we calculated surface profiles for a wide range of We using this model. Indeed, we find transition from a regime involving two local minima to one local minimum around $We \approx 1$, see Figure S2 [8]. From these calculations, we extract a numerical value of h_1 as a function of v, see Figure 3(a). For $We > 0.23$ (here: $v > 0.12$ m/s), h_1 follows the universal scaling law for the crossover height $h_c = 2.54RSt^{14/9}Ca^{-2/3}$ at which capillary forces exceed the initially dominant gas pressure as resisting force at the location of the (first) kink due to the increasing local

curvature [10]. Here the Stokes number $St = \mu_g/(\rho_l v R)$ gives the ratio of viscous forces in the gas to inertial forces in the drop, and $Ca = \mu_g v/\sigma$ is the capillary number in the gas (with μ_g the gas viscosity). For $We < 0.23$, both the capillary pressure and the gas pressure remain low and in balance throughout the entire impact process. As a result, h_1 falls below h_c. Our experimental data agree with these predictions (see symbols in Figure 3(a)) – except for two aspects: (i) the absolute value of h_1 exceeds the expectation by a factor ≈ 3. This deviation is expected due to the difference between the two-dimensional calculations and the three-dimensional experiments. (ii) We never find values of h_1 (nor h_2) below 200 nm. Typically, liquid-solid contact can nucleate at any random moment within 50 µs as soon as either h_1 or h_2 decreases below ≈ 500 nm. Figure 3(c) shows a histogram of the 'nucleation height' h^* for a large number of drops. We find an average value of $h^* \approx 370$ nm. This value is remarkably large. Extensive AFM imaging of our glass surfaces shows that this value exceeds by far the roughness of our surfaces. At the same time, molecular forces such as attractive van der Waals forces between the liquid and the solid are negligible at these distances. We note, however, that h^* is only a few times the mean free path in the gas at ambient pressure. (Our numerical calculations indicate that the local gas density is not substantially enhanced for our experimental conditions.) At such distances rarefied gas effects begin to reduce the gas pressure [11, 17, 18] and thereby might promote the collapse of the air layer. Extrapolating to higher impact speeds, this suggests that the thin air layers predicted for the splashing regime [10] are probably unstable and hence not responsible for splashing – in line with the recent results by Driscoll and Nagel [12].

Finally, we analyze the spreading behavior of liquid-solid contact following nucleation. As shown in Figure 1(b), the liquid-solid contact area preferentially spreads in the azimuthal direction along the ring of minimum gas layer thickness, forming two characteristic cusps. The azimuthal spreading speed v_φ turns out to be constant in time, see Figure 4(a), with values of 0.2 to 4 m/s, depending on h^* as well as the properties of the fluid. If we neglect the effects of liquid viscosity, both Bernoulli's equation and conservation of momentum with v_φ the only dominant velocity component, $\rho_l \partial_t v_\varphi + \partial_x p = 0$, with $p \propto \sigma/h^*$ yield the scaling $v_\varphi \propto (\sigma/\rho_l h^*)^{1/2}$ that is independent of time. This is consistent with the capillarity-inertia controlled regime of drop spreading described earlier by Biance *et al*. [19] if adapted to the one-dimensional situation of our azimuthal spreading process. This inertial scaling was also found to be valid in the partial wetting regime when including a dependence on equilibrium contact angle [20]. Yet, this inertial description is incomplete.

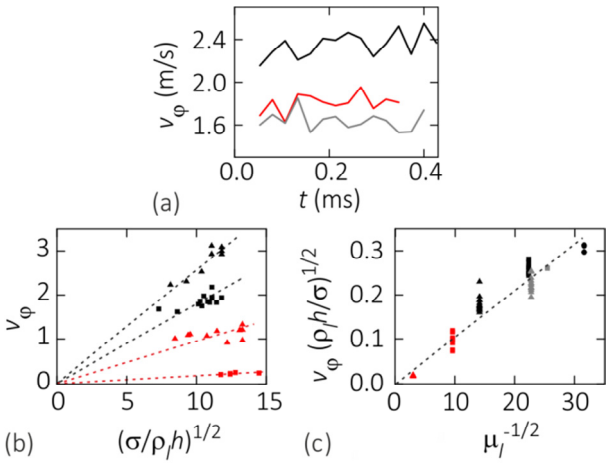

Figure 4. (Color online.) Spreading of liquid-solid contact. (a) Azimuthal velocity v_φ for $CaCl_2$ droplets with $h_1 = 0.23$, 0.57, and 0.74 μm (from top to bottom). (b) v_φ versus the inertial scaling for increasing viscosity (top to bottom). (c) v_φ, non-dimensionalised by the inertial scaling, versus $\mu_l^{-1/2}$ for experiments with seven fluids having viscosities ranging from 1 … 10^2 mPa·s. (The error in the determination of v_φ is typically 5%. All variables given in SI units.)

For aqueous drops of variable glycerol content, we find a clear decrease of v_φ with increasing viscosity, see Figure 4(b). Empirically, we find that the normalized azimuthal velocities for variable viscosity collapse if plotted *vs.* $\mu_l^{-1/2}$, see Figure 4(c). We do currently not have any explanation for this behavior. We note, however, that the spreading of the liquid-solid area involves a moving contact line, which is expected to produce substantial viscous friction [21]. One possibility to reconcile the apparent success of the capillarity-inertia model of spreading and the viscosity dependence observed here is to incorporate contact line friction in the form of a *dynamic* contact angle that modifies the shape of the liquid-vapor interface around the contact area. The adjacent liquid around the contact area would then be accelerated by a capillary pressure that scales as $\Delta p_L \propto \sigma \cos\theta_D / h^*$, where the dynamic contact angle θ_D depends on v_φ and $\mu_{l\varphi}$.

In summary, high speed dual wavelength interferometry provides the first experimental characterization of the evolution of the theoretically predicted gas layer and its role in drop impact. Our measurements reveal the formation of a dimple right under the impacting drop, which can be surrounded by a thin air layer depending on impact speeds. Nucleation of liquid-solid contact occurs from a surprisingly large distance of > 200 nm. The detailed time evolution of the interface provided here will enable quantitative

numerical studies to elucidate the role of rarefied gas effects for this process as well as the influence of viscous dissipation during the subsequent spreading of liquid-solid contact.

References

[1] A. Yarin, Drop impact dynamics: splashing, spreading, receding, bouncing…, *Annu. Rev. Fluid Mech.* **38** (2006), 159-192.

[2] H. Fujimoto, H. Shiraishi and N. Hatta, Evolution of liquid/solid contact area of a drop impinging on a solid surface, *Int. J. Heat Mass Transfer* **43** (2000), 1673-1677.

[3] V. Mehdi-Nejad, J. Mostaghimi and S. Chandra, Air bubble entrapment under an impacting droplet, *Phys. Fluids* **15** (2003), 173.

[4] S.T. Thoroddsen, T.G. Etoh and K. Takehara, Air entrapment under an impacting drop, *J. Fluid Mech.* **478** (2003), 125-134.

[5] D. Van Dam and C. Le Clerc, Experimental study of the impact of an ink-jet printed droplet on a solid substrate, *Phys. Fluids* **16** (2004), 3403.

[6] L. Xu, W.W. Zhang and S.R. Nagel, Drop splashing on a dry smooth surface, *Phys. Rev. Lett.* **94** (2005), 184505.

[7] F.T. Smith, L. Li and G.X. Wu, Air cushioning with a lubrication/inviscid balance, *J. Fluid Mech.* **482** (2003), 291-318.

[8] M. Mani, S. Mandre and M.P. Brenner, Events before droplet splashing on a solid surface, *J. Fluid Mech.* **647** (2010), 163-185.

[9] P.D. Hicks and R. Purvis, Air cushioning and bubble entrapment in three-dimensional droplet impacts, *J. Fluid Mech.* **649** (2010), 135-163.

[10] S. Mandre, M. Mani and M.P. Brenner, Precursors to splashing of liquid droplets on a solid surface, *Phys. Rev. Lett.* **102** (2009), 134502.

[11] L. Duchemin and C. Josserand, Curvature singularity and film-skating during drop impact, *Phys. Fluids* **23** (2011), 091701.

[12] M.M. Driscoll and S.R. Nagel, Ultrafast interference imaging of air in splashing dynamics, *Phys. Rev. Lett.* **107** (2011), 154502.

[13] J. Schilling, K. Sengupta, S. Goennenwein, A.R. Bausch and E. Sackmann, Absolute interfacial distance measurements by dual-wavelength reflection interference contrast microscopy, *Phys. Rev. E* **69** (2004), 021901.

[14] J. De Ruiter, D. Van Den Ende and F. Mugele, to be submitted.

[15] O. Theodoly, Z.H. Huang and M.P. Valignat, New modeling of reflection interference contrast microscopy including polarization and numerical aperture effects: Application to nanometric distance measurements and object profile reconstruction, *Langmuir* **26** (2009), 1940-1948.

[16] T. Becker and F. Mugele, Mechanical properties of molecularly thin lubricant layers: experimental methods and procedures, *J. Phys.: Condens. Matter* **17** (2005), S319.

[17] P. Zhang and C.K. Law, An analysis of head-on droplet collision with large deformation in gaseous medium, *Phys. Fluids* **23** (2011), 042102.

[18] A. Gopinath, S.B. Chen and D.L. Koch, Lubrication flows between spherical particles colliding in a compressible non-continuum gas, *J. Fluid Mech.* **344** (1997), 245-269.

[19] A.L. Biance, C. Clanet and D. Quere, First steps in the spreading of a liquid droplet, *Phys. Rev. E* **69** (2004), 016301.

[20] J.C. Bird, S. Mandre and H.A. Stone, Short-time dynamics of partial wetting, *Phys. Rev. Lett.* **100** (2008), 234501.

[21] O. Voinov, Hydrodynamics of wetting, *Fluid Dynamics* **11** (1976), 714-721.

Appendix 2.1 Supplemental Material

1. Reflection interference microscopy (RIM)

The idealized optical model for a single layer system (in our case: glass-air-water) and perfectly monochromatic light yields a simple periodic variation of the intensity of the reflected light with the layer thickness. In reality, this model has to be refined to reproduce the experimentally observed decrease of intensity extrema with layer thickness (see Figure 1(d) for radial positions of 0 … 200 μm). We incorporated the effect of (i) finite aperture of the optics [15], and, more importantly, (ii) finite bandwidth of the light. The total reflected intensity over the full spectrum is obtained by convoluting the numerically calculated reflection coefficient at each wavelength with the incident intensity at that wavelength [16]. To determine the incident intensity, we measured the spectral emission and sensitivity of the lamp and the cameras, respectively, using a monochromator to make 1 nm steps. The resulting intensity *vs.* air film thickness is shown in Figure S1 for air film thicknesses up to 10 μm. Below 4 μm the intensity difference between each subsequent interference maximum and minimum is obvious, as well as its overall decrease. Using dual wavelength information [13] the periodicity of the function can be solved, and the order of each experimental interference extremum can be unambiguously determined. Subsequently, the air film thickness corresponding to the measured intensity at each radial position is obtained by interpolating the function of intensity vs. air film thickness between the two surrounding interference extrema using the iterative bisection method.

2. Evolution of the interference signal during droplet approach

Movie S1 shows a typical interference signal upon droplet approach and nucleation of contact. In the early stages, the dimple flattens out, as observed by the increased spacing of interference fringes in the center. The fringe corresponding to the kink is clearly distinguished from the others, as it is no full 'black' or 'white' extremum. In time, more and more fringes appear outside of the initial kink. On closer inspection, a total of three inflection fringes is observed, corresponding to the development of local minima in the air layer thickness. Nucleation occurs at the position of minimum gas layer thickness, and the liquid-solid contact area preferentially spreads in the azimuthal direction along this ring of minimum thickness. Two characteristic cusps form, and a small bubble is enclosed after partial squeeze-out of the air.

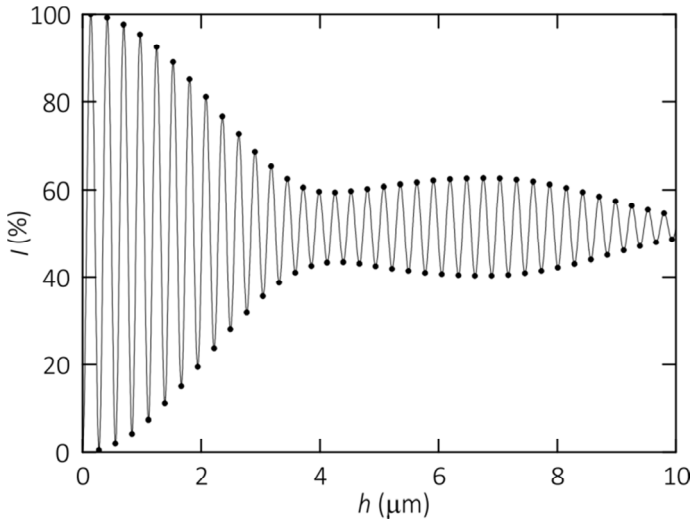

Figure S1. Modeled intensity I vs. air film thickness h for interference of light (550 nm spectral line of a mercury lamp with a bandwidth of ~ 30 nm) reflected from the glass-air and air-water interfaces. The solid line shows the full model, while the black dots indicate interference extrema.

[Movie S1 available at: http://prl.aps.org/supplemental/PRL/v108/i7/e074505]

Movie S1. Typical interference signal of an $R = 1.05$ mm water droplet approaching at $v = 0.24$ m/s. Time step is 13 μs, and total time is 6.8 ms. Total frame size is 2.1 × 1.8 mm. The bright rings outside the dimple area between 1.1 and 2.6 ms are caused by reflections from the upper liquid-air interface.

3. Numerical dimple profiles for $We \approx 1$

Figure S2 shows the dimple profiles obtained using the visco-inertial model including capillary forces. The calculations reproduce the transition from a regime involving two local minima to one local minimum upon increasing the impact speed from $We < 1$ to $We \approx 1$, see Figure S2(c) and (d). In particular, the evolution of the first kink from a shoulder (b), to a well-defined minimum (c), to being the inner edge of the layer of constant thickness (d) compares well to the experimental results described in Figure 2. Comparing the dynamic and the capillary pressure we can conclude that a transition exists between a predominantly inertia driven evolution at high We and an capillarity driven evolution at lower *We*, where the dominating Laplace pressure suppresses the formation

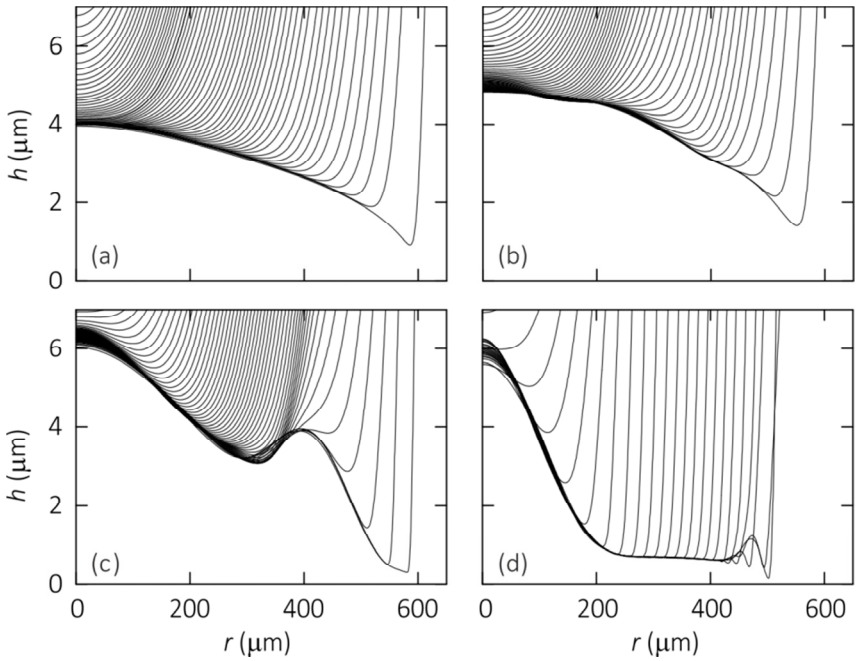

Figure S2. Numerical dimple profiles showing the transition from two to one local minimum upon increasing We. In the model [8] we used parameters equal to those in Figure 2. The respective We numbers (impact velocity in m/s) are (a) 0.015 (0.03), (b) 0.058 (0.05), (c) 0.16 (0.10), and 0.93 (0.24). The time step is 1 (a), 0.2 (b), and 0.1 ms (c-d).

of the first kink. For simulations at very low We, the first kink is completely suppressed (a) in line with experimental profiles for more viscous water-glycerol mixtures at low We (data not shown). Due to viscous losses that lower the available interfacial energy and thus kink curvature, water-glycerol droplets induce a lower overall film thickness. Nevertheless the overall scenario of film development is still captured by the model neglecting liquid viscosity. We conclude that the visco-inertial model including capillary forces indeed adequately describes the physics of drop impact in ambient air.

Dual wavelength reflection interference microscopy for high speed thin film measurements

Reflection interference contrast microscopy (RICM) is a widely used tool for the characterization of thin films of transparent media. Temporal and spatial resolution of the technique depends strongly on the reflectivity of the interfaces involved, on the intensity and bandwidth of the light, and on the sensitivity of the detector. Even for weakly reflecting interfaces, relative thickness variations of order nanometer are easily achieved, yet the absolute thickness is generally known only up to an additive constant a multiple of half of the wavelength.

Here we present an optical setup for measuring the absolute thickness of a thin air film transiently entrapped between a falling water drop and a solid substrate using a combination of standard Hg lamp for illumination, an optical microscope and three synchronized high-speed cameras to detect conventional side-view images as well as interferometric bottom view images at two different wavelengths. The combination of two different illumination wavelengths and finite coherence length set by the broad bandwidth of the optical filters allows for measuring the absolute thickness of the air films with a spatial resolution better than 30 nm at 50 µs time resolution with a maximum detectable films thickness of approximately 8 µm.

3.1. Introduction

Reflection interference contrast microscopy (RICM) has been used in many thin film problems; this technique is based on the determination of the film thickness from the interference of light, reflected from the two interfaces bounding the film. In various recent experiments with liquid droplets, RICM has been used to measure the thickness of a confined air film in various situations such as the air pocket shape between the pillars of a superhydrophobic surface during the Cassie-to-Wenzel transition under electrowetting [1], and the draining of air below a drop floating [2] or bouncing [3] on a liquid bath. In these cases no fully quantitative height analysis was used, with for example the latter detecting the minimum fringe density to indicate the maximal flattening of the air layer. The shape of the interstitial air film between a hot droplet and a cooled surface, stabilized by thermocapillary convection, was studied using the angle shift method [4]. Employing the increase in interference order variation with film thickness for a given angle shift, an absolute measurement could be made. However, the method requires static conditions and is thus not applicable to droplet impact experiments that involve interface deformations on timescales down to milliseconds or even microseconds.

Here, we are particularly interested in the squeeze out of air from below an impacting droplet and thus focus on films between a transparent planar substrate and a soft liquid-air interface. In this respect interesting insights are coming from vesicle-substrate adhesion experiments (for a review, see [5]) with the complexities of biological cells such as interface fluctuations and internal interfaces (membranes) leading to multi-reflections. It has been shown that the most simple RIM model that considers only normal illumination and reflection on only two parallel interfaces, has serious limitations in most experimental situations. To obtain an optimum description of the reflected light, it is necessary to take into account the effects of finite illumination numerical aperture (INA) [6, 7], multi reflections [8] and non-planar interfaces [7]. Moreover, decoherence caused by the finite bandwidth of 'monochromatic' light generated from a white-light source using optical filters has a strong impact on the decay of the interference pattern with increasing film thickness and hence on the maximum film thickness that can be determined. Another important problem is the measurement of the absolute film thickness. Single wavelength interferometry predicts in the film thickness up to an unknown multiple of $\lambda/2$, where λ is the wavelength of the light. The use of a second wavelength, provides an additional intensity curve *vs.* thickness with different spatial period. Combining the information from two wavelengths – so-called dual wavelength interferometry [9] – provides an optical signal with an overall periodicity of more than 1

μm. In combination with the decoherence-induced decay of the interference signal, this leads to a unique assignment of the interference order and hence to an absolute thickness measurement. The time resolution is only set by the recording rate of the high-speed camera(s) and the intensity of the available light. Currently frame rates of 100.000 fps can be reached by benefitting from the radial symmetry of (most) droplet impact problems and thus recording only a small stripe of the target area.

In this Chapter we describe how a non-monotonic and temporally changing thin film thickness can be determined from an interference pattern. In Section 3.2, we start with the most simple case of a single wavelength light beam entering at a single angle of incidence. Subsequently, we show that distributions in (1) the angle of incidence and (2) the wavelength spectrum that often occur in experiments (due to finite illumination numerical aperture (INA) and finite illumination bandwidth resp.) are useful tools rather than limitations. They induce a decay of the interference extrema with film thickness and thus provide additional information whether the film thickness is increasing or decreasing. In Section 3.3 we describe the optical set-up to record the interference pattern. Using a monotonic, static film (below a spherical lens) with known film thickness profile, we describe in Section 3.4 the analysis procedure and simultaneously verify our model. We here introduce dual wavelength interferometry to unambiguously determine the absolute film height, and consider interpolation between interference extrema to improve the resolution of the film thickness. Our final objective is to illustrate the use of our technique in more complex experimental situations where the film thickness is both spatially non-monotonic and temporally changing. As an example, we study low-velocity droplet impact onto a solid surface. The squeeze out of air from below the drop leads to a characteristic undulated liquid-air interface that slowly approaches the solid surface. In Section 3.5 we discuss how to analyze the spatio-temporal intensity information from the droplet impact experiments using representation in a so-called “dynamic interferogram”. With our RIM technique we are able to quantify the thickness evolution of the confined layer, which will be employed extensively in the following Chapters.

3.2. Reflection interference microscopy and thin film interference

3.2.1. Single wavelength, single angle of incidence

The reflection coefficient of a thin film squeezed between two half spaces depends on six parameters: its thickness d_1, its refractive index n_1 and that of adjacent layers (n_0 and n_2),

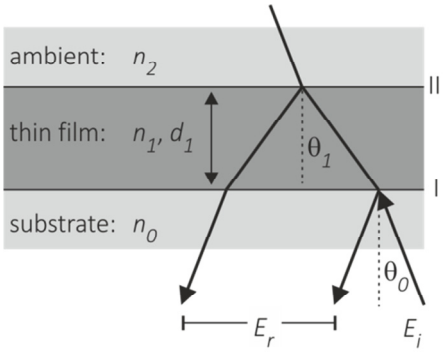

Figure 1. Schematic of the single thin film system (thickness d_1). The wave $\vec{E}_i$ enters with angle θ_0, and is reflected and transmitted at the thin film boundaries I and II. The refractive indices of the substrate, thin film, and ambient are denoted n_0, n_1 and n_2 respectively.

and the wavelength λ and angle of incidence θ_0 of the incoming light, see Figure 1. This can be derived in the most general way [10] by a characteristic matrix M that describes the relation between the electric ($\vec{E}$) and magnetic field ($\vec{H} = \sqrt{\varepsilon_0/\mu_0}\, n\vec{k} \times \vec{E}$, with ε_0 and μ_0 the electric and magnetic permittivity) at the two film boundaries I and II. Using field continuity at the film boundaries, and the phase shift $k_0 h_1 = k_0(\Lambda/2) = (2\pi/\lambda) \cdot n_1 d_1 \cos\theta_1$ associated with the optical path length difference Λ for the beams reflected at boundary I and II [10], we obtain at the film boundary:

$$\begin{bmatrix} E_I \\ H_I \end{bmatrix} = M \begin{bmatrix} E_{II} \\ H_{II} \end{bmatrix}$$

$$M = \begin{bmatrix} m_{1,1} & m_{1,2} \\ m_{2,1} & m_{2,2} \end{bmatrix} = \begin{bmatrix} \cos(k_0 h_1) & i\sin(k_0 h_1)/\Upsilon_1 \\ \Upsilon_1 i \sin(k_0 h_1) & \cos(k_0 h_1) \end{bmatrix} \quad (1)$$

where $E_I = E_{iI} + E_{rI} = E_{tI} + E_{rII} e^{-ik_0 h}$ and $E_{II} = E_{iI} + E_{rII} = E_{tII}$ the fields at both boundaries, and the subscripts i, r, t indicate the incident, reflected and transmitted components. The coefficient Υ_j depends on the polarization of the incoming beam and is given by $\Upsilon_j = \sqrt{\varepsilon_0/\mu_0}\, n_j \cdot cos\theta_j$ or $\Upsilon_j = \sqrt{\varepsilon_0/\mu_0}\, n_j/cos\theta_j$ for *s*- or *p*-polarization respectively. The angle of incidence in each subsequent layer $j = 0, 1, 2$ is given by Snell's law, $n_j \sin(\theta_j) = n_0 \sin(\theta_0)$.

It should be stressed that the transfer matrix for a thin film only depends on two properties of the thin film (refractive index and layer thickness) and three properties of the incoming light (angle of incidence, polarization and wavelength). In our experiments,

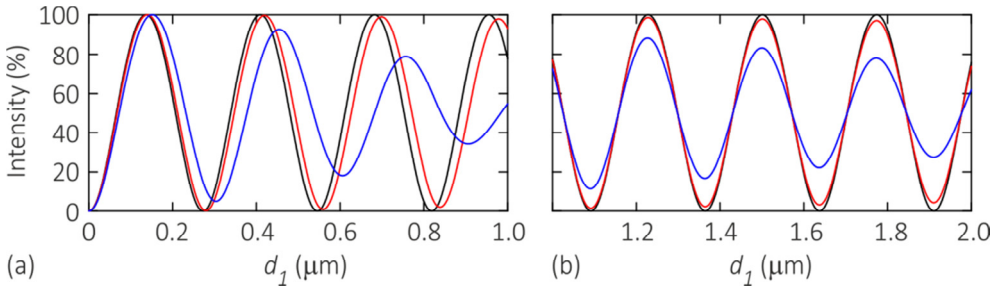

Figure 2. Reflection interference model for a single thin film. (a) Effect of non-zero INA. Reflected intensity versus film thickness d_1 for $INA = 0$ (normal incidence; black), 0.3 (red), and 0.6 (blue) for a single wavelength of $\lambda = 546$ nm. (b) Effect of non-zero bandwidth using (model) Gaussian wavelength distributions with $\mu = 546$ nm and $2\sigma = 0$ (reference; black), 10 (red), and 30 nm (blue) for $INA = 0$. For film thicknesses < 1 μm (not shown) the variations with bandwidth are small. The refractive indices are $n_0 = 1.517$, $n_1 = 1.0003$, and $n_2 = 1.333$.

the interface slopes with respect to the substrate are very small (< 3°), thus the corrections essential for non-planar interfaces as described by Wiegand *et al*. [7, 8] can be neglected. The reflection coefficient $r = E_{rI}/E_{iI}$ of the squeezed thin film is defined as the ratio of the total reflected field over the incident field that together form the field $E_I = E_{iI} + E_{rI}$ in the film at boundary I. It is obtained by expanding Equation (1) and shows an additional dependence on the refractive indices n_0 and n_2 of the adjacent layers (through the relationship between $\vec{E}$ and $\vec{H}$).

$$r = r(d_1, n_0, n_1, n_2, \lambda, \theta_0) = \frac{Y_0 m_{1,1} + Y_0 Y_2 m_{1,2} - m_{2,1} - Y_2 m_{2,2}}{Y_0 m_{1,1} + Y_0 Y_2 m_{1,2} + m_{2,1} + Y_2 m_{2,2}} \quad (2)$$

Assuming no *s/p* interference for an incoherent light source, the reflected intensity $I_{red} = I/I_0$ is proportional to the square of the reflection coefficient: $I_{red}(d_1, \lambda, \theta_0) \sim |r_s|^2 + |r_p|^2$ [7, 11]. Besides the film thickness dependence, we denote also explicitly the dependence on λ and θ_0 because experimentally, we need to consider their distributions (see below). The refractive indices however, are constant. In Figure 2(a) the black line shows the results for the simplest case of normal incidence, $\theta_0 = 0$, in a glass-air-water system. The intensity is normalized with respect to its minimum and maximum values: $(I_{red} - I_{min})/(I_{max} - I_{min})$. Interference maxima and minima are observed at regular intervals of film thickness. The total phase shift in the film is twice $k_0 h_1$ plus an additional shift of π radians when reflecting at an interface with a lower-index material at the incident side. This occurs once for an air film squeezed between two

higher-index ambient phases like glass or water. The total phase shift $\delta = (4\pi/\lambda)n_1 d_1 \cos\theta_1 + \pi$ leads to an interference maximum (minimum) if δ is an even (odd) multiple of π. Thus, interference maxima (minima) are obtained at equally spaced intervals with a spatial period $\Delta = 2\lambda/(4n_1 \cos\theta_1)$, see Figure 2(a). Maxima are obtained when $d_1 = (2m+1)(\Delta/2)$ and minima when $d_1 = (2m)(\Delta/2)$, with $m = 0,1,2,\ldots$. The phase order of these fringes will be denoted by $(2m+1) = 1,3,5,\ldots$ for the maxima, and $(2m) = 0,2,4,\ldots$ for the minima (even when the effects of finite illumination numerical aperture (INA) and bandwidth change the spatial period Δ).

3.2.2. Angle of incidence distribution (finite INA)

In experimental situations such as microscope illumination, a convergent light beam is focused at the focal plane, giving a distribution of incident angles. The resulting INA after passing the field-aperture opening is defined as $INA = n_0 \sin\theta_{0,max}$, with $\theta_{0,max}$ the half-angle of the incident cone in the first half-medium. For each incident angle θ_0, the reflection coefficient $r(d_1, \lambda, \theta_0)$ can be calculated independently using Equations (1-2). For the low spatial coherence of a mercury lamp, it can be assumed that only rays from a single point interfere [5, 7], and the total reflected intensity is obtained by integrating over the (assumedly homogeneous) incident illumination cone [11]:

$$I_{red}(d_1, \lambda) \sim \frac{1}{1-\cos\theta_{0,max}} \int_0^{\theta_{0,max}} \left(|r_s(d_1, \lambda, \theta_0)|^2 + |r_p(d_1, \lambda, \theta_0)|^2 \right) \sin\theta_0 \, d\theta_0 \quad (3)$$

The linear superposition of intensity responses with different spatial period ($\Delta \sim \cos^{-1}\theta_1$) modifies the intensity response in two ways, see Figure 2(a). For $INA > 0$ (red line: 0.3 and blue line: 0.6) the intensity oscillations decreases with film height, and the overall spatial period Δ is not perfectly constant. Also, Δ is larger as the separate contributions show a $1/\cos\theta_1$-increase for all non-normal angles in the incident cone.

3.2.3. Wavelength distribution (finite bandwidth)

When using a polychromatic light source with interference filters, or LED illumination, the full-width at half maximum $\Delta\lambda$ of the spectrum has a typical value of 20-40 nm. Monochromatic light can be obtained using a laser ($\Delta\lambda < 1$ nm), but its large coherence length results in unwanted reflections located deeper within the sample than the targeted thin film. At the other hand the finite bandwidth of our experiment will actually yield additional information about the local thin film thickness, and can be included in the RIM model. As different wavelengths do not interfere amongst each other, the total reflected

intensity $I_R(\lambda_{peak})$ for a given incident wavelength distribution $I_0(\lambda, \lambda_{peak})d\lambda$ centered around its peak wavelength λ_{peak} is obtained by convoluting the reflected intensity $I_{red}(\lambda)$ with $I_0(\lambda, \lambda_{peak})d\lambda$ [12]:

$$I_R(\lambda_{peak}) \sim \int_{\lambda} I_{red}(\lambda)\, I_0(\lambda, \lambda_{peak})d\lambda. \quad (4)$$

In Figure 2(b) the results are shown for model Gaussian incident wavelength distributions with $\lambda_{peak} = 546$ nm (green light) and $2\sigma = 0$ (reference), 10, or 30 nm (black, red, and blue lines respectively). With increasing bandwidth, the intensity oscillations are more damped with increasing film thickness, again due to linear superposition of intensity responses with different periodicity ($\Delta \sim \lambda$).

3.2.4. Damping of intensity oscillations as tool for film thickness measurements

How can the damping of the interference extrema with increasing film thickness be used to determine the latter? A well-known complication in reflection interference microscopy arises from the absolute phase which is unknown: the conventional model described in Equations (1-2) leads to a periodic fringe pattern, i.e. the reflected intensity is a function of film thickness, modulo a factor $\Delta = \lambda/2n_1$ (see Figure 2, black line for normal incidence). Thus quantitative thickness measurements are only possible if, either spatially or temporally, two conditions are fulfilled: firstly, the phase order should be known at a specific location (for example zero), and secondly, the film thickness should be known to increase or decrease monotonically. In many applications involving (sub)micron-thick wavy thin films - for example the (thermal) bending fluctuations of a membrane in cell adhesion [9], the dynamics of non-wetting drops under external forcing [13], and the squeeze out of air during drop impact - one or both conditions are not met. To overcome this ambiguity in film thickness, dual-wavelength (DW-RIM) has been used, where interference signals are recorded for two wavelengths independently. The additional periodicity of the second wavelength poses an additional boundary condition to the identified film thickness, thus increasing the repetition modulus [9] to a value of approximately 1 μm (depending on the choice of wavelengths).

The damping of the intensity oscillations (due to finite INA or bandwidth) can be used complementary to DW-RIM, as it gives direct information about the - spatial or temporal - change of film thickness: a decrease (increase) in extremum intensity corresponds to an increase (decrease) in film thickness, see Figure 2(a) and (b). It thus reveals the slope of

the interface. This is in particular useful for non-monotonic films as local thickness extrema are easily detected, without yet comparing the interference signals of two independent wavelengths as in DW-RIM. In absence of a reference height, dual wavelength information can be used subsequently to quantify the film thickness, while the interface slope is an already known boundary condition. The absolute height can be determined with more certainty because the spatial period Δ between extrema is not exactly constant and the decay of the intensity extrema is different for both wavelengths. Theoretically, it is even possible to determine the absolute film thickness from a single experiment only, by considering the amplitude ratio between successive intensity extrema. However, as possible inadequacies of the RIM model are primary reflected in the intensity decay of extrema (and not in their separation), and small experimental deviations - for example in the determination of the incident wavelength spectrum - cannot be fully eliminated, a combination with the dual wavelength technique is preferred.

3.3. Characterization of the experimental set-up

3.3.1. Optical set-up

The experimental set-up enables both high-speed and dual wavelength RIM (required for the dynamic drop impact experiments). As shown in Figure 3(a), it includes an incoherent light source (Nikon Intensilight with C-LHGF I Hg lamp), a Nikon Eclipse Ti inverted microscope, and three high-speed CCD cameras. From the mercury spectrum of the light source, the green (546 nm) and blue (436 nm) spectral lines are selected using a dual wavelength excitation filter (Chroma 51018x). The combined light beam is focused at the sample plane using an objective with numerical aperture $NA = 0.13$ (Nikon Plan Fluor 4x/0.13), and after reflection at the sample, the interference signal is split by a 460 nm long pass dichroic mirror (Chroma 460 DCLP) and a 500 nm short pass filter (Edmund Optics NT47-287) into two light beams with wavelengths around 546 and 436 nm. The 546 and 436 nm signals are separately recorded at 20.000 fps with two synchronized Photron-FASTCAM high-speed cameras, SA5 and SA3 respectively. A third high-speed camera (Photron-FASTCAM Ultima 512) is recording a synchronized side-view for the dynamic drop impact experiments. In a typical experiment, the recorded interference signals are corrected for the background intensity obtained in absence of the thin air film. In our experiments, the circular symmetry of the thin films can be exploited to smoothen the measured intensity profile, by averaging over a circular sector (with the midpoint obtained

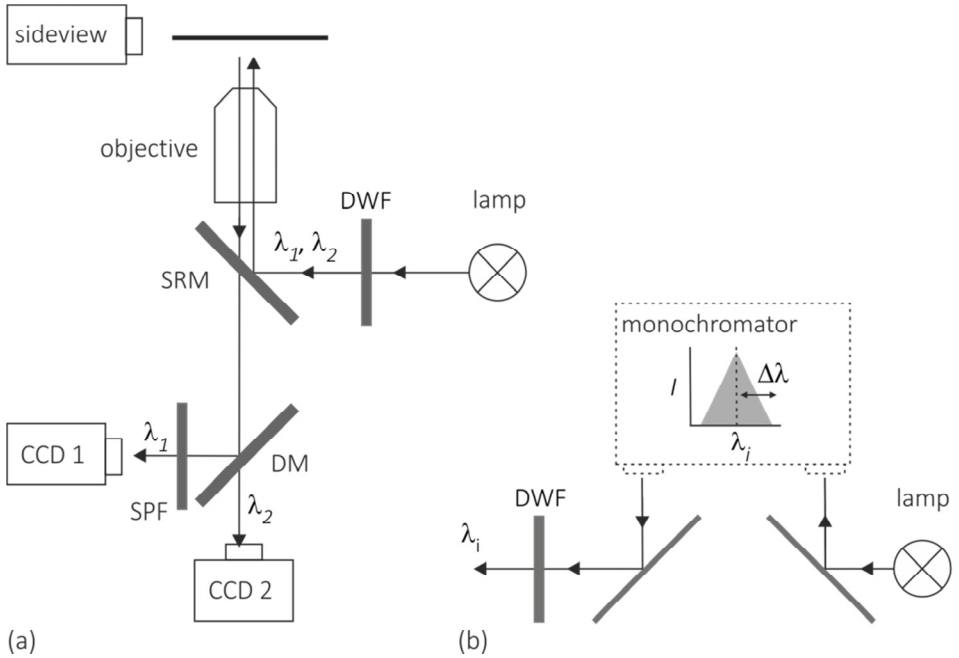

Figure 3. Schematic of the experimental set-up and light path for reflection interference microscopy. (a) The actual set-up; DWF: dual wavelength filter, SRM: semi reflecting mirror, DM: dichroic mirror, SPF: short pass filter, CCD 1 and CCD 2: CCD cameras. (b) A monochromator is inserted into the light path to measure the input spectrum of the assembly of lamp and filters.

by minimizing the sum of the standard deviation of the averaged signal). This yields a radial intensity profile.

3.3.2. Incident spectrum measurement

To obtain the film thickness from the reflected intensity profile, the wavelength spectrum of the incident light beam $I_0(\lambda)$ should be known, see Equation (4). We measured these spectra using a monochromator (Oriel 77233 with 1200 lines/mm) which was inserted in the light path between the mercury lamp and the excitation filter, see Figure 3(b). In steps of 1 nm a narrow wavelength band of 0.28 nm is selected, and the beam is focused at the object plane. The beam reflects back from a simple glass slide (identical to the glass substrate used in the experiments). The total intensity is measured on the respective CCD camera, after passing the excitation filter and dichroic mirror (plus short pass filter), as in

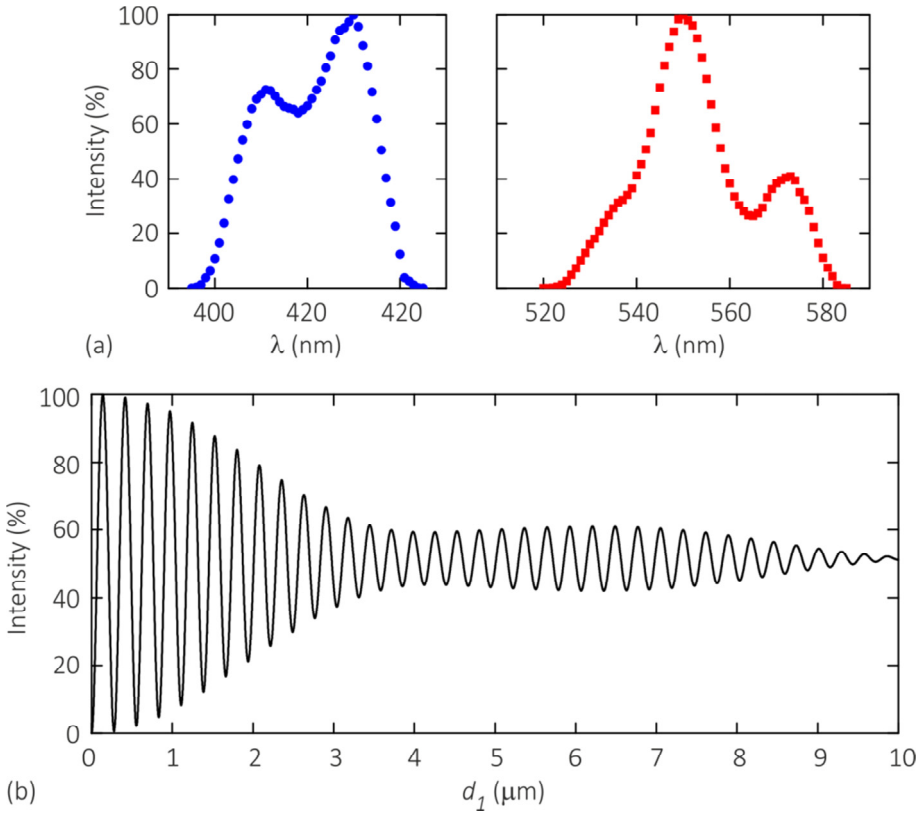

Figure 4. RIM model for the glass-air-water system. (a) Incident intensity with wavelength distribution $I_0(\lambda)$ for the 546 (right) and 436 nm (left) lines of the mercury lamp as measured on CCD 1 and CCD 2 respectively. (b) Calculated reflected intensity signal using as input: refractive indices $n_0 = 1.517$, $n_1 = 1.0003$, and $n_2 = 1.333$, finite $INA = 0.13$, and $I_0(\lambda)$ for the 546 line shown in (a).

the usual experimental set-up. In absence of a thin film, we assume this intensity distribution to be similar to the incident distribution as the reflection coefficient of the glass slide is independent of wavelength. The measured normalized distributions for the 546 and 436 nm line are shown in Figure 4(a). The 546 nm line (red) shows a distinctive peak at 550 nm with a smaller second peak at 573 nm, while the 436 nm line (blue) has a peak at 430 nm with a broad shoulder around 411 nm.

In the RIM model described above we take both the finite INA value and the incident wavelength distribution into account. Although the relatively small INA value (0.13) has a negligible effect on the damping of the intensity oscillations, see Figure 2(a), the incident

wavelength distribution leads to significant damping. Figure 4(b) displays the results of the RIM calculation for a glass-air-water system, including both effects for the 546 nm line. Due to these effects the amplitude is reduced to 20% within 4 μm. The envelope of the amplitude response shows a second local maximum which is caused by the double peaked wavelength distribution shown in the right panel of Figure 4(a). It should be noted that the damping pattern is sensitive to details in the incident wavelength distribution. Although measured carefully and reproducibly several times, in the actual set-up the mercury lamp is aligned differently (only part of the spot is illuminating the field of view), so slight variations in incident wavelength distribution, and thus amplitude damping, are to be expected. The initial amplitude damping for the 436 nm line (not shown) is stronger as a result of the broader wavelength distribution. Also, the overall intensity is lower due to the relative low transmittance (~ 60 vs. 85%) of the dual wavelength excitation filter for this wavelength. Therefore the 546 nm line is used as primary wavelength in our experiments, whereas the 436 nm line is used as reference in the dual wavelength technique.

3.4. Experimental approach and calibration procedure

3.4.1. Calibration with a lens

To illustrate the experimental approach and verify the RIM analysis, we measure the fringe pattern of a static thin film with known spatial thickness and compare this with the expected model intensity response. For this purpose we put an uncoated convex lens of borosilicate crown glass with radius of curvature $R = 39.38$ ($\pm$ 1%) mm (Edmund NT49-851) onto a Menzel microscope slide ($n_0 = n_2 = 1.517$) and measured the fringe pattern produced by the 546 nm line of the incident light beam. From this pattern the averaged radial intensity profile was calculated as shown in red in Figure 5(a) together with the profile, calculated from the RIM model in black. The fringe pattern itself is shown in the inset of Figure 5(b). As expected, the fringe pattern shows the typical damping of intensity oscillations with radial position - caused by the increasing air film thickness between the substrate and the convex lens. The fringe visibility is satisfactory up to a depth of view of 10 μm. In this calibration experiment, the film thickness is monotonously increasing from zero thickness at the center of the lens, thus subsequent extrema of the experimental intensity profile are assigned fringe orders 1,2,3,…, starting with the first maximum. The location of the extrema can be directly linked to the model film thickness d_1 using their

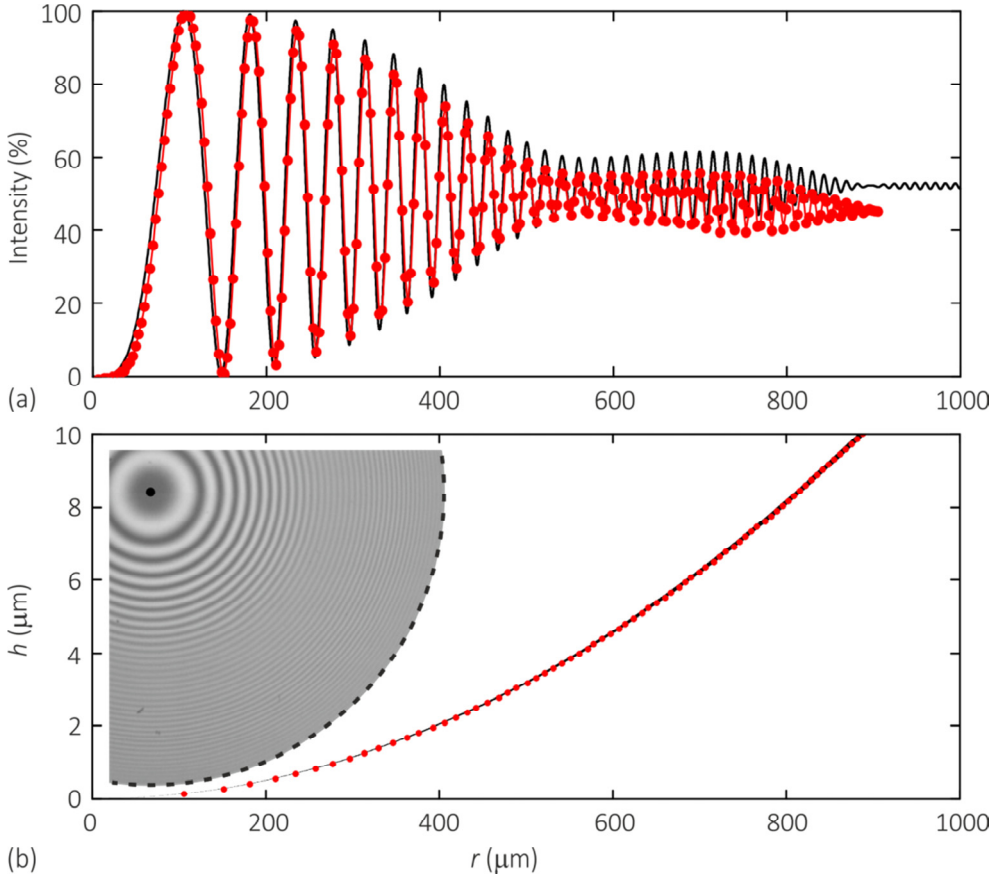

Figure 5. Verification of the RIM model, using the experimental fringe pattern - see inset of (b) - of an air film squeezed between a flat glass substrate and a lens of known curvature ($R = 39.38$ ($\pm$ 1%) mm). The wavelength distribution around 546 nm shown in the right panel of Figure 4(a) is used. (a) Averaged radial intensity profile (connected red dots), and model intensity response for a glass-air-glass system ($n_0 = n_2 = 1.517$, $n_1 = 1.0003$, $INA = 0.13$) rescaled to (I, r) with the known lens curvature (black continuous line). (b) Lens shape determined from the peaks in the intensity profile (red dots), compared to the specified lens curvature (black line with thickness indicating the $\pm$ 1% error interval).

assigned orders. The resulting lens profile $h(r)$ is plotted (red dots) in Figure 5(b) and directly compared with the lens shape (black line) as given by the specifications. Indeed, the determined profile agrees well with the given specifications, showing that the model predicts the spacing between fringes correctly. With this confirmed, the model intensity response (I, h) is rescaled with the lens specifications to an (I, r) response, and plotted in

Figure 5(a) for direct verification of the modeled intensity decay. The intensity decay predicted by the model shows a good correspondence with the experimental data. The depth of view of 10 μm (here obtained at a radial position of approximately 900 μm) is reproduced by the model, as is the typical decay pattern, including the local minimum in intensity amplitude at a film thickness of 4 μm ($r \sim 550$ μm). As mentioned before, small deviations between the absolute amplitude decay of the model and the experiment are to be expected. The experiment shows an additional overall intensity decrease for film thicknesses larger than 5 μm (outside the range considered in the drop impact experiments), which we attribute to experimental artifacts such as inhomogeneous illumination.

3.4.2. Absolute film thickness by dual wavelength technique

In the most generic case the film thickness should be derived exclusively from the interference pattern, as no reference point of previously known film thickness exists. In this case, the film thickness can only be derived up to an even shift in phase order. Although the absolute film thickness is unknown the shape of the film can be extracted from the intensity amplitude decay (see above), and from temporal information in dynamic experiments (as will be explained for the drop impact experiments later). To find the absolute film thickness, test film profiles are created shifting the profile upwards by increasing the phase order of all detected fringes simultaneously in steps of two. Similarly a family of profiles can be obtained at the second wavelength having a different spatial period. Minimizing the sum of squared errors for each pair of profiles yields a unique solution for the absolute film thickness and exact film shape.

As a check of the dual wavelength technique - which is obviously redundant here because a reference height is available from the contact point of the lens and the substrate -, we determine the (fictitious) higher order lens profiles, by assigning increasingly higher fringe orders 1,3,5,…,19 to the first intensity maximum. The same procedure is repeated for the second wavelength data (436 nm). The correspondence of each of the ten profiles obtained at 546 nm with each of those obtained at 436 nm is determined from the sum of squared errors (SSE). This sum is obtained by linear interpolation of one profile between two adjacent $h(r)$ values around r_i to be able to directly compare with the r_i value of the paired profile (due to the wavelength difference, the peaks are not located at identical r values), and vice versa. The resulting SSE is shown in Figure 6(a). The minimum $SSE = 0.03$ is correctly obtained at the lowest order solution, in other words when the lens is in

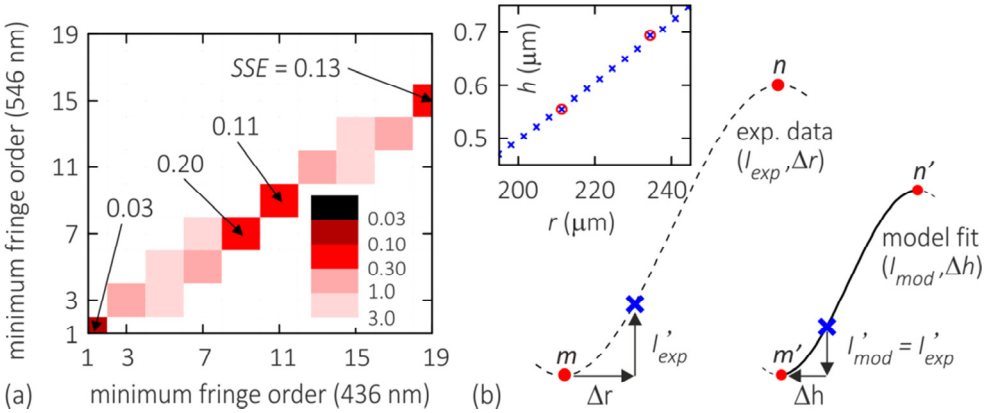

Figure 6. (a) Verification of the dual wavelength technique for an air film below a convex lens. For each pair of candidate profiles with increasing minimum fringe order (1,3,5,…,19) obtained from the 546 and 436 nm wavelength data, the SSE is indicated (increasing intensity for increasing SSE). (b) Interpolation of data between extrema. The experimental data is mapped onto the model curve between the corresponding extrema, i.e. $(I_{mod} - m')/(n' - m') = (I_{exp} - m)/(n - m)$, and the film thickness Δh is obtained by numerical enclosure on the (I, h) polynomial fit to the model. Inset: interpolated lens profile (section), with extrema (red circles) and interpolated data points (blue crosses).

contact with the surface. The second best solution, with the center of the lens hovering 1.1 µm above the substrate, has an SSE that is 4x higher.

3.4.3. Intermediate pixels

After determination of the absolute film thickness, the intensity values in between extrema are exploited to improve the lateral resolution. The experimental data from Figure 5(a) are cut into monotonic branches between each pair of subsequent extrema, yielding a $(I_{exp}, \Delta r)$ curve with Δr the distance with respect to the lower order extremum, see Figure 6(b). For each experimental branch, we select the corresponding branch of the model bounded by the same order extrema, and define Δh with respect to the lower order extremum. Now, the experimental relative intensity is mapped onto the model branch, and our goal is to find the corresponding Δh. As the model consists of discrete data points, we fit the selected model branch with an 8th order polynomial to the $(I_{mod}, \Delta h)$ data. Next, Δh is found by numerical enclosure on this curve, and the resulting $(\Delta r, \Delta h)$ is converted to absolute film thickness versus absolute radial position using the values at the extremum. The procedure is repeated for all branches to obtain the

complete interpolated film profile. An example for a small part of the lens profile is shown in the inset of Figure 6(b). It should be noted that at the inflection points of non-monotonic films, one of the extrema is not fully reached and its intensity is thus unknown at that time instance, see also Figure 7(b). Its intensity value is obtained from temporal information if available, otherwise by extrapolating the ratio between neighboring peak intensities using the model.

3.5. Analysis of dynamic drop experiments

To demonstrate the dynamic aspects of the film evolution we use the air film below a water droplet impacting on a substrate as an example. The water droplet with a radius of 1.05 mm is released from rest at a height of about 1 cm, resulting in an impact velocity of 0.41 m/s. More details of the experimental set-up can be found in Chapter 4 where the process of drop impact and air squeeze out will be studied in detail.

3.5.1. Temporal evolution of interference pattern: dynamic interferogram

Although the dynamic droplet experiments suffer from an unknown reference film thickness, the dimple shape can be determined - without using dual wavelength interferometry - from the decay of the intensity amplitude and the information embedded in the evolution of the intensity profile with time, as we discussed before. To capture the evolution of the fringe pattern, the averaged radial intensity profile is determined for each snapshot and plotted in a dynamic interferogram with the radial position along the horizontal axis and the time, with a time resolution of 50 μs, along the vertical axis, see Figure 7(a). For each line, also an (I, r) representation can be given in a single curve, as shown in Figure 7(b). The interferogram was introduced by van den Doel *et al*. [13] to characterize the dynamics of non-wetting drops under external forcing. It shows the time development of fringes; a constant-height fringe forms a connected segment in the (t, r) diagram (provided that temporal resolution is sufficient). Thus, the lateral shift of a fixed film thickness can be followed in time by following a connected fringe. We immediately observe a 'stagnation point' in film height at about 200 μm from the dimple center, separating an inner and outer region. In the inner region the constant-height fringes gradually move towards the dimple center and subsequently vanish in time.

Together with the increase in intensity amplitude away from the center as shown in Figure 7(b), we conclude that the center of the air film is convex and its thickness decreases in

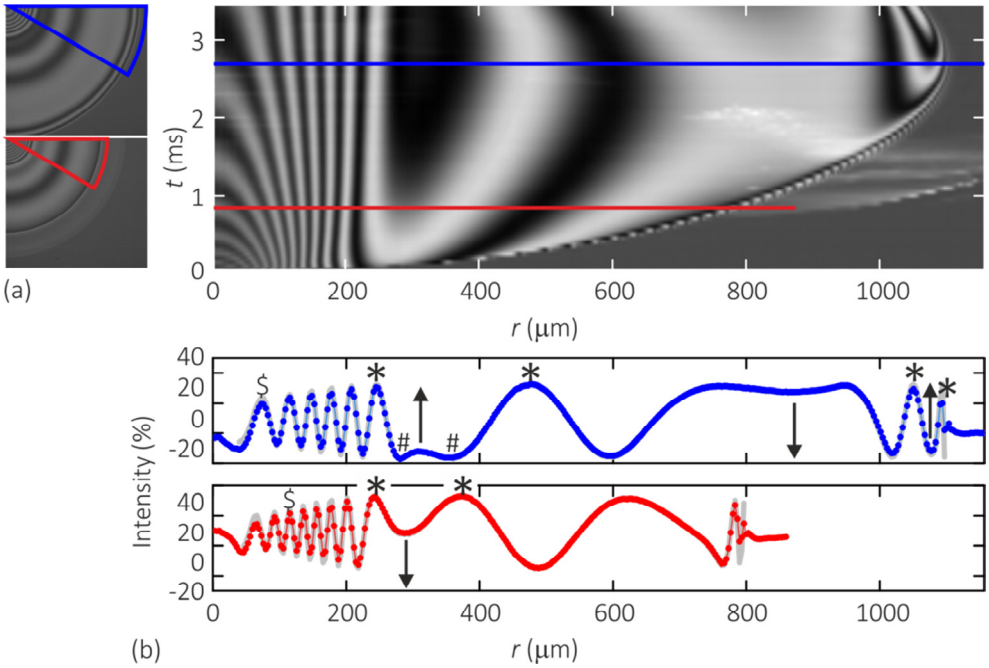

Figure 7. (a) Dynamic interferogram -capturing the time evolution of the $I(r)$ intensity curves that shows the connection between fringes of equal order- for the impact of a water droplet with a radius of 1.05 mm and an impact velocity of 0.41 m/s, as constructed from averaged radial intensity profiles (shown at the left for t = 0.80 and 2.75 ms). Time resolution is 50 μs. The bright spots appearing between $t = 1$ and 2 ms are unsuppressed reflections from the upper droplet interface. (b) Two examples of radial intensity profiles with indication of equal fringe orders (with equal symbols $, $*$ or #) and development of new fringes (indicated by the arrows) as follows from the dynamic interferogram. Grey lines: the model prediction for the intensity profile based on the determined interface shapes as shown in Figure 8.

time. The single intensity curves in Figure 7(b) quantify the intensity information, but lack the information of temporal connection between fringes: for example, the equality in height of the maximum indicated by $ is derived from the interferogram. In the outer region the air film shape is more complicated with several local minima and maxima in film thickness. Again, the formation of new fringes, indicated in the intensity scan of Figure 7(b) by black arrows, can most easily be observed in the interferogram by the onset of new fringes that are isolated in time. Finally, we observe that at $t = 2.8$ ms the squeezed air film is most expanded. Subsequently the interface retracts while the inner dimple profile remains almost stationary. The flattening inner dimple region, stagnation

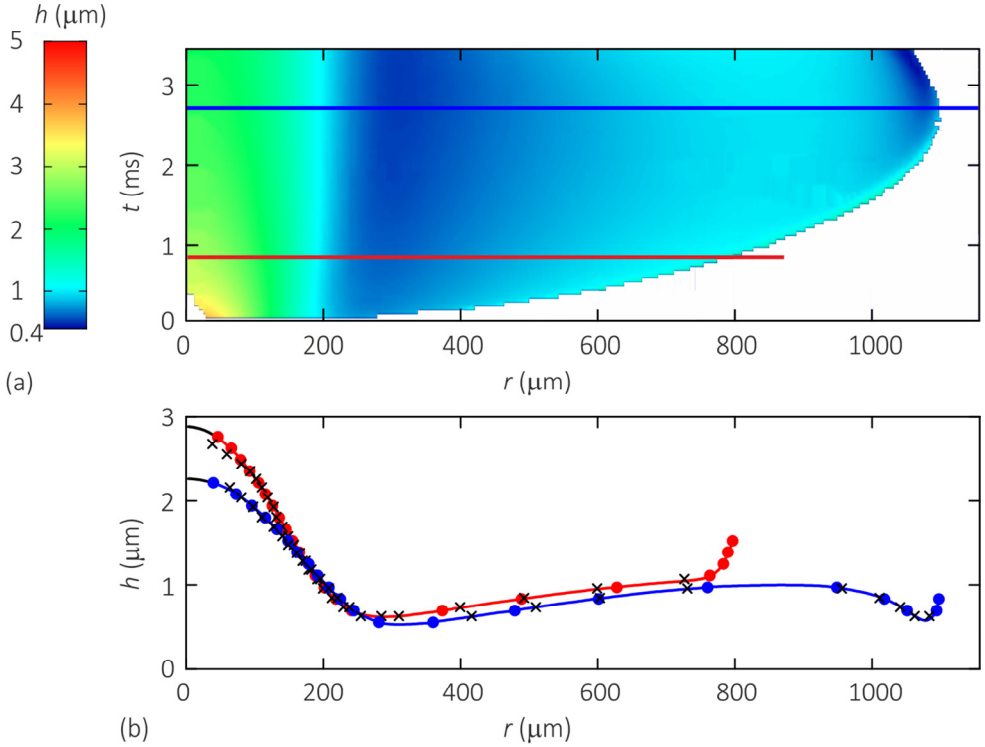

Figure 8. Time evolution of air film thickness determined from the dynamic intensity information shown in Figure 7. (a) Contour plot of film height as function of radial position and time. The color scale ranges from 0.4 to 5 μm (blue to red with 256 colors divided quadratically to obtain a finer color gradient in the low and shallow part of the film profile containing the local extrema). (b) Constructed dimple profiles for $t = 0.80$ (red) and 2.75 ms (blue), obtained from interference extrema (large dots), intermediary pixels (line), and interference extrema from the reference wavelength (black crosses).

point, and outer dimple region with several local extrema are common features observed in most droplet impact experiments.

3.5.2. Quantitative film thickness measurements

The film shape and its temporal evolution can be determined from the intensity extrema in the interferogram using the model described in Section 3.2. To obtain the absolute film thickness from DW-RIM (Section 3.4.2), we need to analyze only two snapshots of the reference wavelength (including the temporal connection between fringes from a similar

interferogram) and select the minimized-error solution. Next, the intermediate pixels are used to obtain continuous film profiles (Section 3.4.3). The two resulting profiles for $t =$ 0.80 (red curve) and 2.75 ms (blue curve) are shown in Figure 8(b) with separate symbols for the interference extrema (large dots), intermediate pixels (line), and interference extrema from the reference wavelength (black crosses). As a check, when the model intensity curve (I, h) is rescaled to (I, r) using the obtained film profile, and plotted together with the experimentally obtained intensity curves, the decay of intensity amplitude matches well, see Figure 7(b).

Although the quantitative film thickness is best represented at a single time t by the $h(r)$ profiles in Figure 8(b), the time evolution is better represented by a height plot $h(r, t)$ with height indicated by a color scale, see Figure 8(a). This gives a clear indication of the development of stagnation points and local extrema, even if their height or location is non-monotonic. Also the combined temporal and spatial information can be employed to interpolate film thicknesses where gaps exist in the film profile data due to experimental scatter in intensity or occasional unsuppressed reflections from the upper droplet interface (less than 5% of the available data).

3.6. Conclusion

We obtain a relative height resolution better than 30 nm according to the similarity between the known lens shape and the experimental results of either wavelength. The main sources of inaccuracies are the spectrum determination and experimental variations in intensity due to e.g. background light and unsuppressed reflections from the top droplet interface. The use of a finite bandwidth (here, the full-width at half maximum is roughly 30 nm) allows us, first, to determine the sign of the interface slope from the change in intensity oscillations and, second, to determine the absolute thickness of the film layer benefitting from the non-constant spatial period. At the same time, the depth of view is limited to circa 8 μm using the incident spectrum around 546 nm shown in the right panel of Figure 4(a), but this is sufficient to observe the full development of the air film. Finally, it can be noted that the refractive index of the air layer increases with air pressure: $dn/dp \sim 0.0003$ atm^{-1}. However, we estimate from our numerical simulations mentioned in Chapter 2 that for low-velocity impacts the increase of air pressure is smaller than 1 atm. Our RIM model shows that changes in the intensity response are negligible in that case. In particular, the first interference maximum in the modeled (I, h)

response shifts by only 1 nm (4 nm) for a significantly larger pressure increase to 10 atm (100 atm).

In summary, we have developed a high speed dual wavelength interferometry technique to characterize the dynamic behavior of thin films. With this technique the absolute thickness profiles can be measured with an accuracy of 30 nm and a time resolution of 50 μs, as demonstrated on a stationary air film between a solid spherical lens and a flat surface, see Figure 5, and a water drop impacting on a flat substrate, see Figure 8. With this technique we are able to study the complex evolution of the interface between a drop impacting on a flat surface and the air layer underneath.

References

[1] G. Manukyan, J.M. Oh, D. Van Den Ende, R.G.H. Lammertink and F. Mugele, Electrical switching of wetting states on superhydrophobic surfaces: A route towards reversible Cassie-to-Wenzel transitions, *Phys. Rev. Lett.* **106** (2011), 014501.

[2] Y. Couder, E. Fort, C.H. Gautier and A. Boudaoud, From bouncing to floating: Noncoalescence of drops on a fluid bath, *Phys. Rev. Lett.* **94** (2005), 177801.

[3] D. Terwagne, N. Vandewalle and S. Dorbolo, Lifetime of a bouncing droplet, *Phys. Rev. E* **76** (2007), 056311.

[4] P. Dell'aversana, V. Tontodonato and L. Carotenuto, Suppression of coalescence and of wetting: The shape of the interstitial film, *Phys. Fluids* **9** (1997), 2475-2485.

[5] L. Limozin and K. Sengupta, Quantitative reflection interference contrast microscopy (RICM) in soft matter and cell adhesion, *Chemphyschem* **10** (2009), 2752-2768.

[6] D. Gingell and I. Todd, Interference reflection microscopy - Quantitative theory for image interpretation and its application to cell-substratum separation measurement, *Biophysical Journal* **26** (1979), 507-526.

[7] G. Wiegand, K.R. Neumaier and E. Sackmann, Microinterferometry: three-dimensional reconstruction of surface microtopography for thin-film and wetting studies by reflection interference contrast microscopy (RICM), *Applied Optics* **37** (1998), 6892-6905.

[8] G. Wiegand, T. Jaworek, G. Wegner and E. Sackmann, Studies of structure and local wetting properties on heterogeneous, micropatterned solid surfaces by microinterferometry, *Journal of Colloid and Interface Science* **196** (1997), 299-312.

[9] J. Schilling, K. Sengupta, S. Goennenwein, A.R. Bausch and E. Sackmann, Absolute interfacial distance measurements by dual-wavelength reflection interference contrast microscopy, *Phys. Rev. E* **69** (2004), 021901.

[10] E. Hecht, *Optics*, Pearson Education, San Francisco (2002).

[11] O. Theodoly, Z.H. Huang and M.P. Valignat, New modeling of reflection interference contrast microscopy including polarization and numerical aperture effects: Application to nanometric distance measurements and object profile reconstruction, *Langmuir* **26** (2009), 1940-1948.

[12] T. Becker and F. Mugele, Mechanical properties of molecularly thin lubricant layers: experimental methods and procedures, *J. Phys.: Condens. Matter* **17** (2005), S319.

[13] L.R. Van Den Doel, P.T. Nagy, L.J. Van Vliet and P. Neitzel, Regularized phase tracker with isophase scanning strategy for analysis of dynamic interferograms of nonwetting droplets under excitation, *Applied Optics* **44** (2005), 2695-2704.

Chapter 4

An airbag for drops.
Characterization of the lubricating air film

A liquid drop approaching a solid surface deforms substantially under the influence of the ambient air that needs to be squeezed out before the liquid actually touches the solid. We use nanometer- and microsecond-resolved dual wavelength interferometry to reveal the complex spatial and temporal evolution of the squeezed air layer. In low-velocity droplet impact, *i.e.* the We number is of order unity, the confined air layer below the droplet develops two local minima in thickness. We quantitatively measure the evolution of the droplet bottom interface and find that surface tension determines the air film thickness below the first kink, after which fluid is diverted outward to form a second even sharper kink. Depending on We one of the two kinks approaches the surface more closely forming liquid-solid contact. The early-time spreading of liquid-solid contact is controlled by the capillary driving force and the inertia of the liquid. The cushioned air film geometry, *i.e.* a flat micrometer-thin gap, induces an increase of the spreading velocity; the contact area first spreads over the cushioned region, only then followed by radial spreading. This spreading mechanism can lead to the entrapment of one or more air bubbles.

4.1. Introduction

When a droplet approaches a solid surface in an impact, the separating air layer needs to be squeezed out and becomes thinner and thinner before the liquid touches the substrate. This leads to a strong deceleration of the droplet as if it is landing on an airbag. The importance of this air layer in the impact process has been recognized only recently, when analyzing the trapping of air bubbles into drops [1-4] during the impact, as well as the suppression of splashing upon reducing the ambient air pressure [5]. To explain these observations several models [6-12] were formulated to describe the air dynamics. Smith, Li and Wu [13] presented a lubrication model in which the inertia of the decelerating liquid is balanced against the excess pressure arising from the viscous squeeze-out of the thin air layer. A local pressure maximum right under the drop leads to the formation of a "dimple", diverting to the sides fluid that accumulates in a kink. The kink singularity, *i.e.* touchdown, can be inhibited completely in the models by introducing surface tension [6] which regularizes the curvature divergence and causes the droplet to skate on an air film of constant thickness [7]. Most theories focus on the splashing transition and incorporate either gas compressibility [7, 8, 11] or rarefied gas effects in the nanometer thick layer [11, 12] to explain the air pressure-dependence of splashing as observed in the experiments of Xu, Zhang and Nagel [5]. It has been shown that from the kink emerges a thin liquid that expands on the air film. However, it eventually touches the solid when the air film thickness decreases below the mean free path length, which is characteristic for impacts in the splashing regime [10]. Mandre and Brenner [11] demonstrated that the ejection is caused by advection, and the sheet is a potential precursor to splashing due to viscous drag *after* liquid-solid contact formation, provided the kink is not first regularized (flattened) by surface tension. Yet sheet ejection is initiated *before* touchdown of the droplet, so they hypothesize that the air cushioning can affect splashing although droplet touchdown and splashing are separated in time, as was shown experimentally using interferometry visualization [14]. Other experiments were also focused on the high-velocity impact regime, typically 1 m/s, measuring the air film thickness and its rupture [15], and the air bubble inclusion predicted by Hicks and Purvis [9]: these include measurements of air bubble size [16], and detailed characterizations of the (enclosed) air film retraction *via* a toroidal bubble stage [17, 18], followed by daughter droplet inclusion and wettability-dependent bubble detachment as demonstrated with x-ray phase-contrast imaging [17].

In our experiments we are particularly interested in the role of inertia and capillarity because they give rise to characteristic undulations of the liquid-air interface below the

drop as shown in Chapter 2. Therefore we study the low-velocity impact regime around 0.1 m/s, that is the Weber number regime around unity up to $We \sim 5$ ($We = R\rho_l v^2/\sigma$, the Weber number gives the ratio between inertial and capillary forces). In this regime, the film remains a few hundred nanometers to a few micrometers thick, allowing for the development of complex dimple shapes. Liquid-solid contact is formed from a single location such that the air film is not disconnected from the ambient at once and the air can be completely squeezed out. At higher We the air film thins faster, and early liquid-solid contact formation restricts both the complexity and lifetime of the film, with the possibility of splashing [11]. To observe the development of such a dimple at low We, reflection interference microscopy (RIM) is a very suitable technique [19, 20]. The details of our technique are explained in Chapter 3. After describing the experimental set-up, we first describe the overall deformation of the droplet. Next, we focus on the deformation of the lower side of the droplet, where we identify several stages: a fast initial deformation due to the steep increase in gas pressure when the droplet approaches the substrate, followed by a gradually squeeze out of the air layer and - finally - the collapse leading to formation and growth of liquid-solid contact. Finally we address two specific topics: the combined action of inertia and capillarity on the evolution of the film profile and the propagation of the contact line after formation of liquid-solid contact.

4.2. Experimental set-up for impacting drops

Experiments are performed with aqueous droplets. To probe the influence of the liquid properties upon impact, these droplets contain varying concentrations of ethanol, glycerol and calcium chloride. The interfacial tension σ of the solutions ranges from 27 to 65 mN·m^{-1} (as measured by pendant drop tensiometry), the density ρ_l from 997 to 1366 kg·m^{-3} (pycnometer), and the viscosity μ_l from 1 to 109 mPa·s (derived from literature using density data), see Table 1. The refractive indices are measured with an Abbe refractometer, and used as input (n_2) for the RIM model. Low concentrations of dye are added to the aqueous solutions to suppress internal light reflections within the droplet from the upper droplet interface. We use 0.01% wt. of both rhodamin and fluorescein-sodium, which strongly absorb light around 546 and 436 nm, respectively. The droplets are quasistatically dispensed from a syringe pump and detached by their own weight, to obtain a uniform radius that depends only on liquid properties. The impact velocity is varied between 0.11 and 0.53 m/s, by changing the height of the needle above the glass substrate. We perform 5-10 experiments for each condition to guarantee reproducibility.

Aqueous solution	σ (mN·m^{-1})	ρ_l (kg·m^{-3})	μ_l (mPa·s)	n (-)	R (mm)
water	64.6	996.9	1	1.3336	1.05/ 1.02
60% wt. glycerol	65.1	1150.8	10.8	1.4127	1.04
85% wt. glycerol	63.9	1219.4	109	1.4510	0.98
30% wt. calcium chloride	62.1	1203.2	2	1.3910	1.05
50% wt. calcium chloride	59.0	1366.4	5	1.4350	1.03
10% wt. ethanol	49.3	980.5	1.538	1.3398	0.98
60% wt. ethanol	27.3	899.2	1.93	1.3631	0.84

Table 1. Composition and liquid properties of the used aqueous solutions. The viscosity is derived from literature tables using liquid density [21, 22].

Microscope cover slips are used with an rms surface roughness below 2 nm (measured with atomic force microscopy), and - in a second experiment with water droplets - a polished glass wafer with a roughness below 3 nm. A small glass cuvette is placed around the substrate and needle, and closed at the top by Parafilm® M to prevent disturbances from the surrounding air and settling of dust particles. The radius of the droplet and the velocity of its center of mass just before impact are measured from the side view camera (recording at 4.000 fps) by fitting an ellipse to the droplet image. The 546 and 436nm interference signals reflecting from the squeezed air layer beneath the droplet are recorded separately with two synchronized high-speed cameras (Photron SA5 and SA3 respectively) at a recording speed of 20.000 fps. In a second experiment with water droplets we scanned the same velocity range in smaller steps. Here, the correspondence with the previous measurement allowed to omit the dual wavelength confirmation.

4.3. Macroscopic drop deformation

In the low We number regime, the typical impact speed of millimetric droplets is in the order of tens of centimeters per seconds. Figure 1(a) shows a time series of the impact of a water droplet with velocity $v = 0.22$ m/s. When approaching the solid substrate within a few micrometers, the sharply increasing air pressure below the droplet strongly

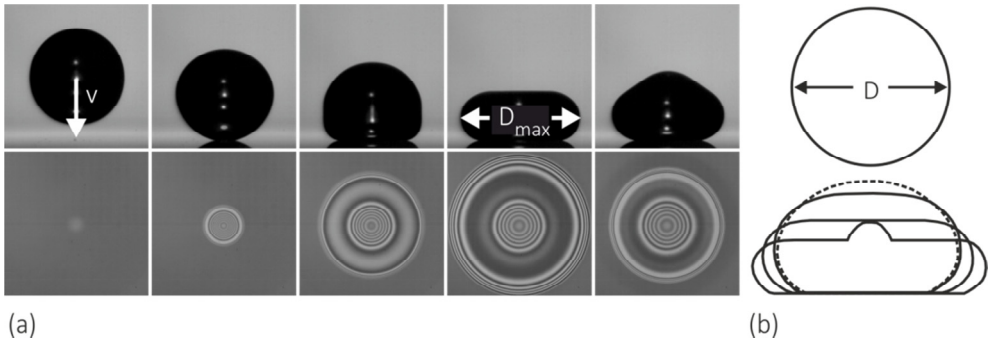

Figure 1. Macroscopic drop deformation upon droplet impact. (a) Water droplet ($R = 1.02$ mm) impacting with a velocity $v = 0.22$ m/s ($We \sim 0.7$) onto a hydrophilic wafer. Upper: side view images, lower: bottom view interference signal, obtained at -1.5, 0.2, 1.4, 3.9 and 5.7 ms with respect to cushioning. (b) Maximal deformations for $We = 0.29$, 1.9 and 4.4 (increasing deformation); dotted line: $We = 0.42$ for 85% wt. glycerol.

decelerates the bottom droplet interface [7]. The air is squeezed out from the confined film; this process can be observed *via* the interference signal (lower sequence) that yields a quantitative measurement of the air film thickness. Simultaneously, the droplet is deformed due to the continuing motion of the center of mass of the droplet. As long as the air film is sustained and liquid-solid contact is avoided, the droplet deformation is similar to that of droplets impacting on a superhydrophobic substrate with a contact angle close to 180°. The deformations we observe range from ellipsoidal to puddle-like, but remain small with the deformation D_{max}/D having a maximum value of 1.5 for the highest We impacts (puddles). In case of glycerol droplets the deformation is even smaller due to viscous dissipation in the droplet. Our observations in the $We \sim 1$ regime are at the transition between low and high We number. For $We \ll 1$ the deformation can be estimated considering the conversion from kinetic to elastic energy of an oblate ellipsoid. Writing the long axis as $R + x$, one obtains for $x \ll R$ a deformation $x/R = \sqrt{5/48}\, We^{1/2}$ [23], which is 3% for $We = 0.01$. For $We \gg 1$ the droplet experiences a deceleration $\gamma = v^2/D \gg g$ which creates a reinforced gravity field leading to a gravity puddle shape with characteristic thickness $\sqrt{\sigma/(\rho\gamma)}$ [24]. Here, the deformation scales as $D_{max}/D \sim We^{1/4}$ while the dominant energy transfer is from center of mass to internal kinetic energy. Figure 1(b) shows the range of observed droplet deformations for $We \sim 1$ from ellipsoidal to puddle-like. It should be noted that the predicted maximum diameter is in this case only characteristic for the no-contact stage and is thus not always obtained.

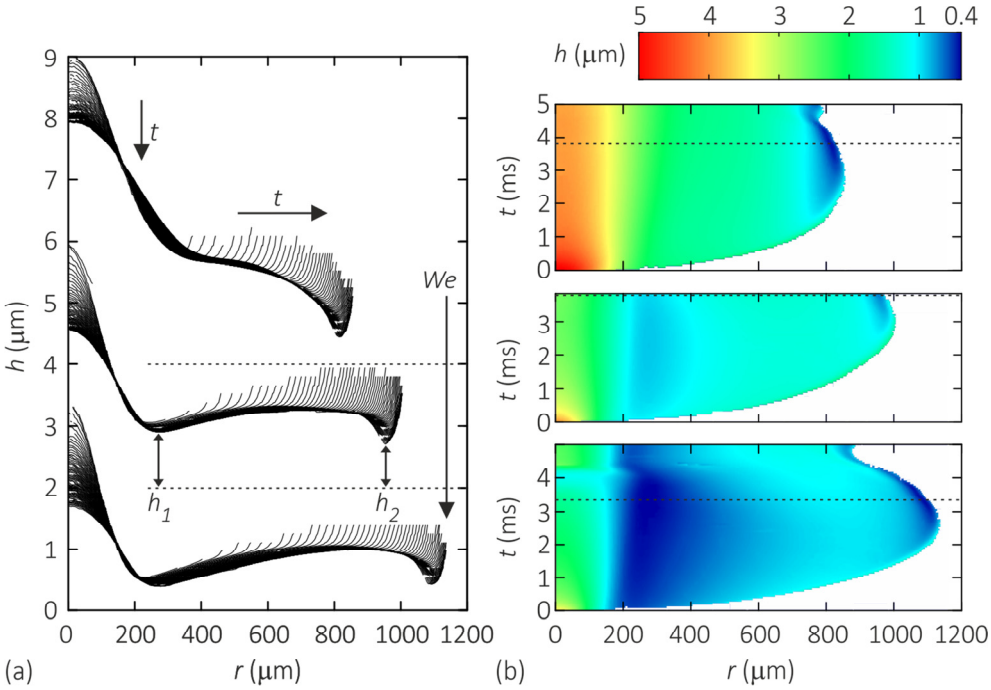

Figure 2. Time evolution of droplet-film interface profiles for water droplets with increasing We number: 0.83, 1.82, 3.19. Time step: 50 μs. (a) Superimposed interface profiles showing the minimum heights h_1 and h_2. The interface evolution is shown until h_2 reaches its minimum value, indicated by the dotted lines in (b). Profiles are shifted vertically 2 μm for clarity. (b) Corresponding contour plots of film height as function of radial position and time.

When the air film collapses and liquid-solid contact is made - possibly before reaching the maximum diameter - the droplet spreads on the surface in an almost completely wetting state with much larger diameter. We come back to this $D_{max}(We)$ dependence further on in Figure 6(d) where R_{max} is discussed in relation to the radius of the contact area under the droplet as reflected in the microscopic measurements of the air film dimensions and its evolution in time.

4.4. Droplet cushioning and film evolution

By analyzing the interference pictures like given in Figure 1(a), the transient air layer between droplet and substrate can be studied in detail. We construct a dynamic interferogram as demonstrated in Figure 7 in Chapter 3, and subsequently extract the air film thickness using the optical analysis described in Chapter 3. Figure 2(a) shows the film

thickness profiles for water droplet impact at three *We* numbers (from top to bottom: $We = 0.83$, 1.82, and 3.19), superimposed in time until the minimum film thickness is obtained. Note the different scales on the abscissa and the ordinate, the maximal slope of the interface is always smaller than 3°. Corresponding height plots $h(r,t)$ in Figure 2(b) extend further in time until the moment of liquid-solid contact, showing the successive contraction of the air layer, and the time evolution of local minima and maxima. Figure 2 reveals the different stages of the air film development, which will be discussed in the next subsections.

4.4.1. Initial drop deceleration

The deceleration of the droplet interface near the substrate is abrupt. Within our time resolution of 50 μs the interface falls from a distance > 8 μm (*i.e.* outside our depth of view as shown in Figure 4(b) in Chapter 3) into our field of view enclosing a film with a central thickness of 2-5 μm, see the lower left corners of the diagrams in Figure 2(b). This implies that the approach velocity just before cushioning is still of the same order as the impact velocity, about 0.1 m/s. The velocity of the interface is subsequently decelerated within our time resolution by 2 to 3 orders of magnitude, *i.e.* the transition to squeeze out is sharp. Next, the central part of the liquid-air interface has a residual vertical velocity less than 1 mm/s while squeezing out the air layer.

The interface deceleration is due to an increase of the opposing gas (lubrication) pressure when the droplet approaches the surface. Sufficiently far away from the surface the gas pressure can be neglected, but it steeply increases at small air film thickness H, leading to the observed abrupt deceleration. The opposing force is acting locally on the fluid mass in a region with a typical length scale $L \sim \sqrt{RH}$, set by the geometry of the impact; thus the lubrication pressure is given by $\sim\left(\mu_g R^2 v/H\right)/L^2 \sim \mu_g R v/H^2$ [7]. The strong local deceleration in a time scale $\tau \sim H/v$ comes along with a deformation of the initially spherical interface, leading to an air film thickness H. The pressure needed to decelerate the liquid mass of volume L^3 is given by $\sim\left(\rho_l L^3 (v/\tau)\right)/L^2 \sim \rho_l v^2 \sqrt{R/H}$. Balancing the lubrication and inertial pressures yields the length scale for the height of the air film where the droplet starts to deform [7], $H^*/R \sim St^{2/3}$ with $St = \mu_g/(\rho_l v R)$ the Stokes number giving the ratio of viscous forces in the gas to inertial forces in the droplet (here: $10^{-5} - 10^{-4}$).

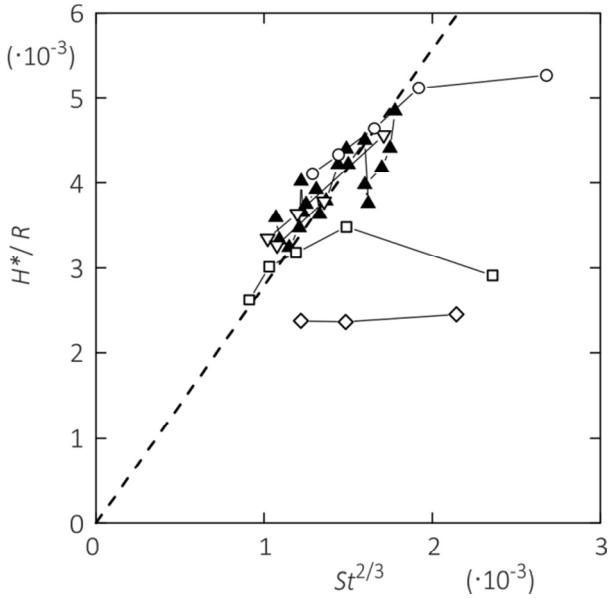

Figure 3. Scaling of H^*/R with $St^{2/3}$ [17]. The symbols show the experimental data: droplets of water (solid triangles and open triangles for a duplicate series), 60% wt. ethanol (open circles), 50% wt. $CaCl_2$ (open squares) and 85% wt. glycerol (open diamonds). The broken line indicates the best linear zero-offset fit to the data, yielding a slope 2.8 (excluding large fluid viscosity and impacts outside the two-kink regime).

Experimentally, we measure the first observable central dimple height and find that it follows the scaling with $St^{2/3}$, see Figure 3. (Note that one could argue that the decelerated volume is L^2H which leads to $H^*/R \sim St^{1/2}$. This scaling is equally compatible within our experimental data range.) The inertial-lubrication balance is violated [11] for large fluid viscosity - here: $Re \sim 1$ for the 85% glycerol aqueous solution - as a viscous stress rather than inertial pressure resists the interfacial deformation. Also, at sufficiently low impact velocities surface tension is not initially negligible; for our lowest Weber number impacts we have observed in Chapter 2 that the capillary pressure and the gas pressure remain low and in balance throughout the entire impact process. Indeed, Bouwhuis *et al*. [16] have shown that in the limit of low impact velocity a balance of the gas pressure with the Laplace pressure $\sim \sigma/R$ leads to a $H^*/R \sim St^{-1/2}$ dependence that leads to an maximum for H^* for intermediate impact speed.

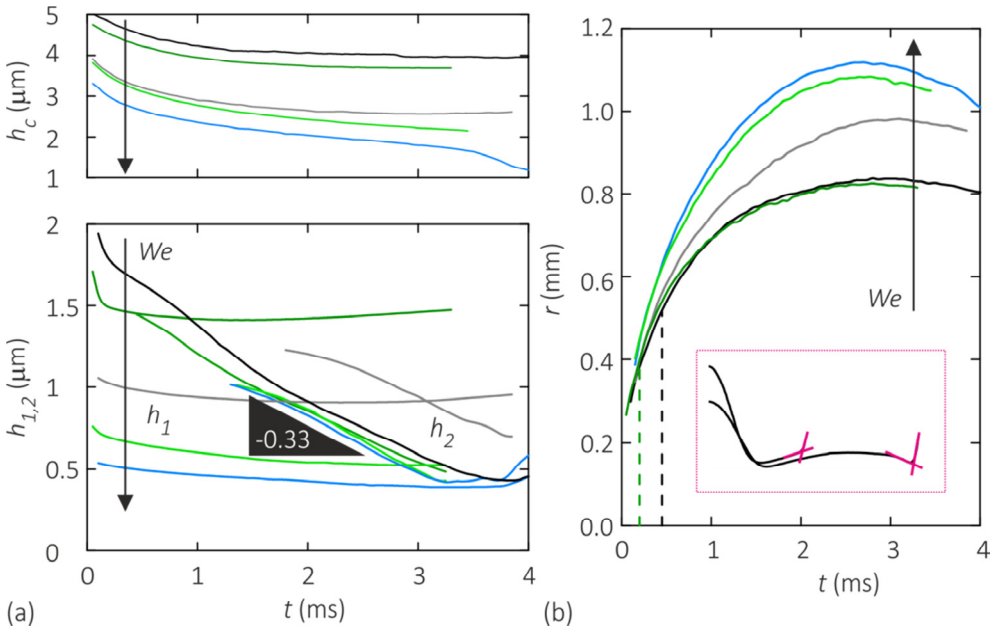

Figure 4. (a) Time evolution of the central dimple height h_c and kink heights $h_1$and h_2 for water droplets with increasing $We = 0.83$ (black), 0.93 (green), 1.82 (grey), 2.72 (light green), and 3.19 (light blue). (b) Time evolution of the dimple extension; for low We the broken lines indicate the start of continued spreading after the first kink. Inset: determination of dimple radius.

4.4.2. Gradual expansion of the film

Once the center of the droplet-air film interface is decelerated the drop starts to spread while a dimple is formed. A "kink" of high local curvature with height h_1 initially marks the edge of the dimple, see Figure 2(a). As time proceeds, this kink and the interface part bounded by the kink come closer and closer to the substrate. At some point, both h_1 and its lateral position r_1 reach a stationary We-dependent value. Continued spreading of the drop leads to the development of a second even sharper kink with a height h_2 before the droplet reaches its maximum extension. The corresponding lateral position of this second kink increases with We, as can be concluded from Figure 4, in which the time evolution of h_1, h_2 and the central dimple height h_c have been plotted for several We values in panel (a) together with the evolution of the dimple radius in panel (b).

This two-kink scenario is consistently observed for all liquids around $We \sim 1$, suggesting an important role of capillary forces in stopping the approach of the first kink towards the substrate. Indeed, the equilibrium film thickness h_1 at the position of the first kink decreases with increasing We as well as the central dimple height h_c, see Figure 4(a). This sets limits for the two-kink scenario: for We numbers of order 10, the formation of a second kink is limited by the formation of liquid-solid contact at the position of the first kink. At the lower limit, $We < 1$, the first kink is completely suppressed by surface tension, as can be observed from the black line in Figure 4(a).

In absence of surface irregularities, the air film is stable against collapse for $We \sim 1$. After reaching its maximum radial extension, the confined region contracts as can be observed from the contour of the $h(r,t)$ plots in Figure 4(b). The air film *does* eventually collapse if the minimum air film thickness reaches a critical value of a few 100 nm. The exact value depends on the presence (and size) of surface irregularities, or - in absence thereof – amongst others on the mean free path length of the gas, in which case effects of gas rarefaction need to be considered [10-12]. Our numerical calculations in Chapter 2 show that the gas density is not substantially enhanced and thus significant mean free path reductions from ambient ($\sim$ 60 nm) are not expected. Thus we believe that with the thinnest equilibrated films that we measured, 220 nm, we are at least probing the range where gas rarefaction becomes important.

To explain the observed two-kink scenario, we compare our experiments with a recent theoretical analysis by Mandre and Brenner [11] assuming inviscid flow inside the droplet, and lubrication in the gas layer. Although liquid inertia and gas pressure initially fully dominate the dynamics, the development of a kink (or 'rim') holds the key for a change in dynamics. The kink develops since a stagnation point forms near the impact center of the droplet and fluid is diverted outwards (see Figure 6 in Chapter 1). The additional fluid flux leads to a divergence in liquid velocities, curvature and gas pressure to balance the enhanced liquid momentum. Owing to this divergence at the kink, initially small terms in the governing equations grow rapidly and can take over the dynamics; in particular it has been shown that the divergence can be regularized by either surface tension or advection. The capillary pressure relative to the global lubrication pressure is expressed by $\delta = \left(\sigma/\mu_g v\right) St^{4/3}$ (here: 10^{-2} – 10^{-1}). Now, for $St \ll \delta$ surface tension dominates the dynamics after kink formation, and stops the approach of the kink toward the surface. The drops spreads on an air layer with thickness $h_c = 5R\delta^{2/3}St^{2/3}$, the height at which the locally diverging capillary force at the kink starts to exceed the maximum gas pressure at

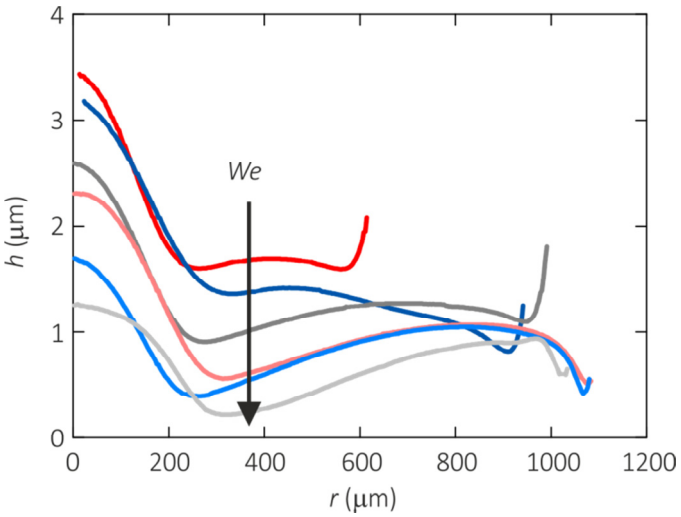

Figure 5. We-influence on the behavior of the first kink. Shown are the interface profiles at the moment h_1 obtains its minimum value; for water droplets with increasing $We = 1.06$ (red), 1.23 (dark blue), 1.82 (grey), 2.39 (pink), 3.19 (light blue), and 3.86 (light grey).

the kink. For $\delta \ll St$ advection dominates: the large horizontal velocity component at the interface amplifies the interfacial slope, which can eventually lead to overturning of the interface and ejection of a sheet. The drop contacts the surface and the ejected sheet is a potential precursor to splashing. In our experiments $St/\delta \sim (1\ldots6)\cdot10^{-3}$ and thus they provide an experimental illustration of the regime where surface tension regularizes the kink. Yet, eventually advection will cause delayed overturning and sheet ejection, although the residual air layer and the zero velocity of the kink prevent splashing [11]. In the following we describe the evolution of the droplet interface in the surface tension-dominated regime as a function of the Weber number, which relates as $We = (St/\delta)^3 Ca^{-2}$ with $Ca = \mu_g v/\sigma$ the capillary number.

4.4.3. Behavior of the first kink

We observed the formation of a first kink at the position r_1. From the interface profiles in Figure 2(a) we extract the temporal evolution of the film thickness at this position. As shown in Figure 4(a) the height of this kink h_1 quickly stabilizes in a time much less than 1 ms, keeping an approximately constant value during most of the spreading stage. This is characteristic for the $We \sim 1$ regime in which surface tension plays an important role (along with inertia). We define the steady state thickness of h_1 as the minimum of this

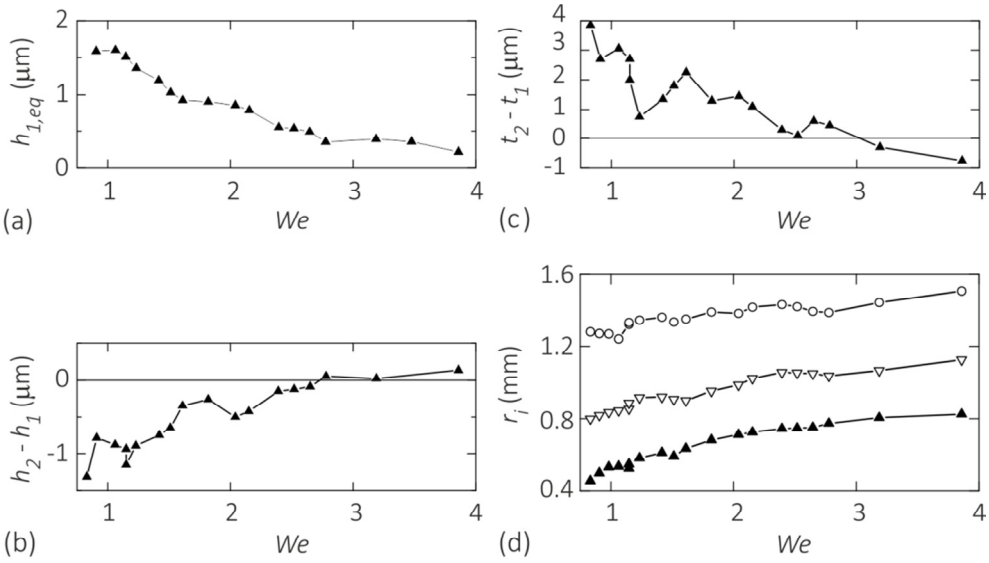

Figure 6. We-influence on kink parameters: (a) equilibrium height of the first kink $h_{1,eq}$; (b) relative height of the second kink $h_2 - h_1$ when h_2 is minimum; (c) difference in time between the minimum of the second and first kink $t_2 - t_1$; and (d) lateral scales: (open circles) maximum droplet extension R_{max}, and (open and closed triangles resp.) r_2 and $r_2 - r_1$ when h_2 is minimum.

curve. Figure 5 shows a family of interface profiles obtained at varying We for impacting water droplets, all collected at the instant that h_1 reaches its minimum value. We note that the steady state thickness h_1 decreases with We. Figure 6(a) shows the decrease of h_1 with We for a large series of impacting droplets, from a thickness of 1.6 μm at $We =$ 0.91 to 220 nm at $We = 3.9$. This represents the complete We range for which a steady state for h_1 is obtained: for higher We liquid-solid contact is formed and for lower We no clear kink is present.

We compare our experimental results to the model by Mandre and Brenner [11] by identifying h_1 as the crossover height h_c at which the locally diverging capillary force at the kink exceeds the maximum gas pressure at the kink. Indeed, in steady state h_1 follows the proposed scaling law, up to a pre-factor of approximately 1.5, very well, see Figure 7. (Please note that the agreement with the theory is better than in Chapter 2 as the numerical prefactor changed due to an improved model in Ref. [11].) This shows that capillary forces indeed strongly decelerate the local droplet velocity, and stop the squeeze out of air. For lower $We \sim 0.1$ we have shown before in Chapter 2 using the numerical

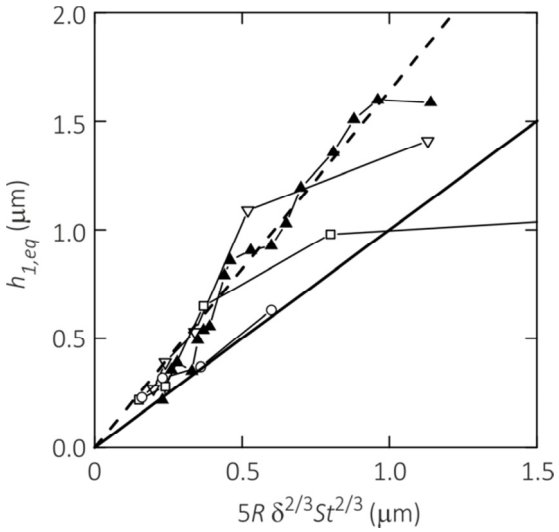

Figure 7. Scaling of $h_{1,eq}$ as the crossover height h_c proposed by Mandre *et al*. [21]. The symbols show the experimental data: droplets of water (solid triangles for the series shown in Figure 5, and open triangles for a duplicate series), 60% wt. ethanol (open circles), and 50% wt. $CaCl_2$ (open squares). The solid line indicates parity, and the broken line the best linear zero-offset fit to the data obtained for the two-kink regime.

model for $St \to 0$ [8] that both the capillary pressure and the gas pressure remain low and in balance throughout the entire impact process. As a consequence, the equilibrium height of the first kink falls below h_c (observed for the low v impacts); and eventually the kink is fully suppressed for $We \sim 0.01$ (see Figure S2 in Chapter 2).

After identification of h_1 as the "skating layer thickness" we note that the evolution of the interface does not stop here. Rather, the spreading continues and a second even sharper kink is formed as was shown in Figure 2(a). We believe this is the result of continuing advection outside the stationary inner fluid region.

4.4.4. Behavior of the second kink

Figure 8 shows the extended dimple profiles after continued spreading for different Weber numbers, all collected at the instant that h_2 reaches its minimum value. At this time all profiles exhibit a distinct second kink with a relatively high radius of curvature. However, the spreading interface first develops a slight positive slope of $\sim 0.1°$ thus at earlier times the kink is merely a transition between small and large positive slope (and

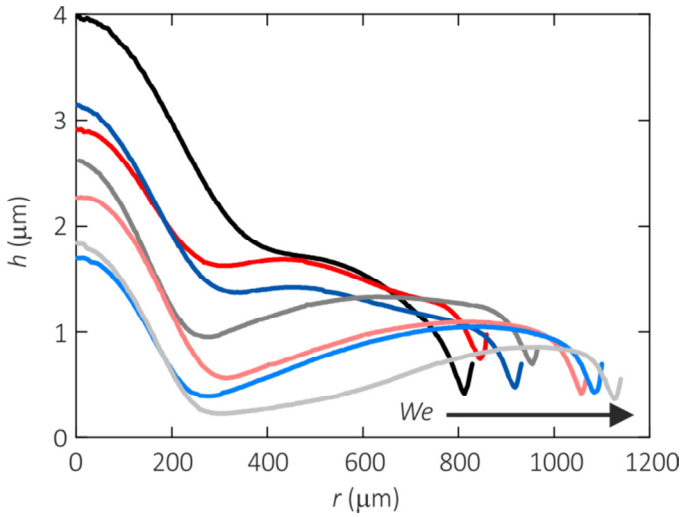

Figure 8. We-influence on the behavior of the second kink. Shown are the interface profiles at the moment h_2 obtains its minimum value; for water droplets with increasing $We = 0.83$ (black), 1.06 (red), 1.23 (dark blue), 1.82 (grey), 2.39 (pink), 3.19 (light blue), and 3.86 (light grey).

not a local minimum in thickness), as observed for the intermediate times in Figure 2(a). We determine the position of the leading edge of the spreading interface by the intersection of two linear fits to the interface profile; one just outside the edge with steep positive slope, and one just inside the edge, see the inset of Figure 4(b). For late-time nearly symmetrical kinks this yields exactly the position of the second kink. Figure 4(b) itself shows the results for different We numbers. The radius of the squeezed air layer grows to a maximum value, followed by contraction. This maximum increases with We from 0.8 to 1.2 mm ($We = 1…4$) as expected if advection sets the spreading. It shows the same, weakly undulating, time behavior as r_1 and the macroscopic maximum drop extension R_{max}, see Figure 6(d).

Finally, we focus at the height under the second kink, h_2. It is measured from the instance that the leading edge evolves into a local minimum. Figure 4(a) shows h_2 versus t for several We values (the curves are cut off after 4 ms or when liquid-solid contact is formed). After the second kink is formed, h_2 decreases almost linearly with t with a typical slope of -0.33 mm/s, independent of We in the two-kink regime. Only at the end the vertical kink velocity slows down, before the interface starts retracting again. Comparing h_2 with h_1 of the first kink, we observe that for $We \sim 1$, the second kink develops from

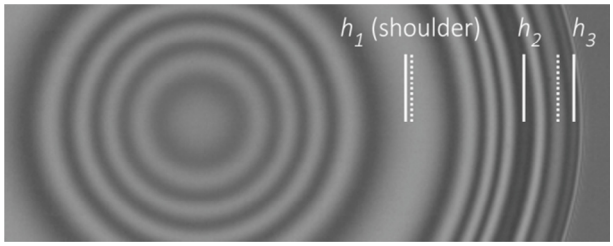

Figure 9. Formation of three subsequent kinks at $We = 0.44$: solid lines indicate the kinks, dotted lines the crests.

the leading edge after it moves away from the first kink in a slight upward direction, thus the second kink develops at larger height with respect to the first one. In time the second kink approaches the surface while the first kink keeps its steady state value, and thereby decreases below the height of the first kink. For the highest We this crossing does not occur and $h_2 > h_1$ at any time, see Figure 6(b). Hence, at low We number liquid-solid contact (if any) will be formed at the position of second kink whereas at high We number contact will be formed under the first kink.

For low We values the first kink is strongly suppressed and the second kink develops directly from the first one, see the black line for $We = 0.83$ in Figure 4(a). With strong interfacial tension effects, *i.e.* $We \ll 1$, the fluid is diverted further outward, leading to the subsequent development of more (small) kinks as shown in Figure 9. Numerical simulations for *e.g.* $We = 0.058$ (see Figure S2 in Chapter 2) show that a wavy interface is formed that marks the transition to full kink suppression expected at even lower We ($We = 0.015$ in the same simulation). We adopt the convention of naming the height of the outer kink 'h_2' even if other local minima are formed (and often subsequently suppressed) in between.

4.5. Collapse and contact line propagation

On a flat (hydrophobic or hydrophilic) surface, collapse of the air layer, *i.e.* sudden appearance of liquid-solid contact, is induced when the film thickness decreases below ~ 200 nm. For high *We* ~ 10 the air film collapses at the position r_1 close to the dimple center, limiting the squeeze-out stage to $\lesssim$ 0.1 millisecond. As shown in Chapter 2, for lower *We* collapse can occur at one or a few isolated locations under the outer kink at a radius r_2. The squeeze-out stage then takes several milliseconds. The final collapse

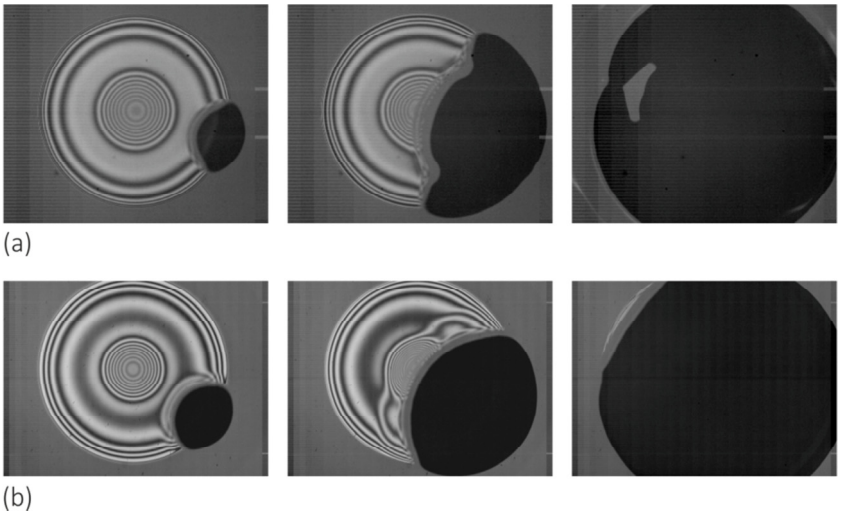

Figure 10. Propagation of air-liquid-solid contact line. Preferential spreading in tangential direction leading to (a) bubble inclusion or (b) complete squeeze out of the air layer. Snapshots are taken 0.1, 0.3 and 0.8 ms after contact. The scenario depicted in (a), *i.e.* cusp formation, is observed for hydrophobic surfaces (e.g. C_4F_8-coated) while the scenario depicted in (b) is observed for fully wettable surfaces.

happens within our time resolution (tens of microseconds); this implies a local vertical interface velocity of order 10 mm/s which is significantly increased with respect to the cushioned - and almost static - interface. The formation of liquid-solid contact is followed by propagation of the three-phase contact line. For high *We* numbers contact at r_1 often is a ring impact [14]. Our high-speed imaging in the moderate *We* regime shows that this ring originates from a large number of isolated contact points that merge together (see also [15]). The ring impact at high *We* leads to inclusion of a small air bubble that is smaller in size with higher impact velocity [9]. At the (sudden) transition towards collapse under the outer kink at r_2, when h_2 becomes smaller than h_1, see Figure 4(a), the air volume available for the air bubble is much larger because of the formation process of the second kink as described in the previous section. While further reducing the impact velocity the air film expansion decreases, leading to a maximum in the trapped volume [16]. However, the 'trapped' air not necessarily evolves into a bubble: rather, in the low *We* regime only isolated contact points are formed and the air accumulates in a thick rim preceding the contact line as can be observed from Figure 10, see also [15, 18]. So most of the air can be squeezed out from below the droplet and, depending on the spreading details such as the presence of multiple nucleation points or fast spreading in the

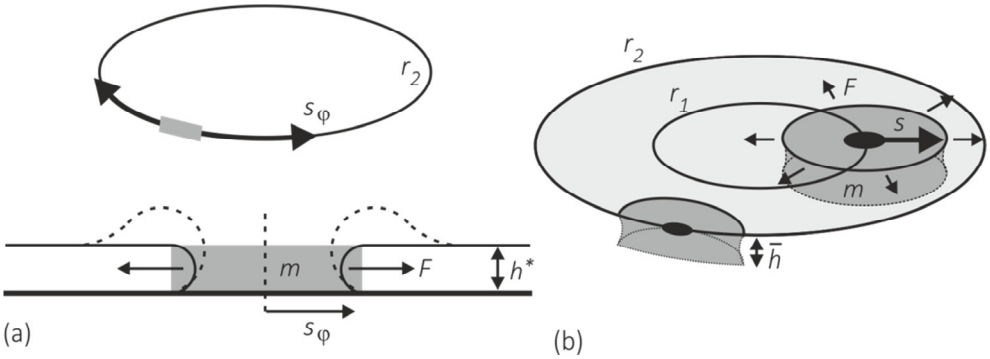

Figure 11. Models for spreading in the cushioned region. (a) One-dimensional spreading along the rim of minimum film thickness h^*, and (b) two-dimensional spreading assuming constant height $\bar{h}$ in the cushioned region. The capillary force F acts on a mass m (dark grey). The dashed line in (a) indicates rim formation, which is observed in *e.g.* Figure 10 as the grey blur preceding the contact line.

azimuthal direction, only a small fraction of air can be trapped into one or multiple bubbles. In Figure 10(a) we observe the formation of two distinct 'cusps' by strong preferential spreading in the azimuthal direction. This is observed on hydrophobic substrates, but fully eliminated, see panel (b), on fully wettable substrates.

To analyze the spreading of the contact line we consider a single contact point under the kink. It is important to note that the geometry of the cushioned region is distinctly different from that of a spherical droplet in its (early time) inertial wetting stage [25-27]. Here, the interface is flattened with small local slopes and small height above the substrate. This leads to faster and more local spreading: we observe in Figure 10 that the contact area *first* spreads over the cushioned region, while significant outward radial propagation happens on larger timescales only when the confined air layer has been squeezed out completely. The shape of the contact region is rather complex depending on the substrate wettability as shown in Figure 10 and the exact interface shape. We approach this in two ways. First we restrict spreading to a completely flat region with average height $\bar{h}$, leading to the two-dimensional spreading sketched in Figure 11(b). Second, we can make further restrictions stating that the contact line will spread much faster in the azimuthal direction because the local initial height goes through a clear minimum in the radial direction. Therefore we can also consider a one-dimensional

situation as depicted in Figure 11(a), where we denote the spreading distance in the azimuthal direction as s_φ. Both approaches will be followed and compared.

Biance *et al*. discussed this problem for a spherical droplet approach [25]. We will follow their argument but now for the case of cushioning. The bulk of the droplet remains immobile in the early times of spreading. When spreading is dominant in the azimuthal direction as shown in Figure 11(a), *i.e.* one-dimensional, the mass involved in the spreading can be estimated as $m = \rho w h^* s_\varphi$ where h^* is the local film thickness and w is the width of the kink, while the capillary force $F = 2w\sigma$ is constant in time. Neglecting the role of viscosity, the equation of motion is given by $F = \frac{d}{dt}\left(m\frac{ds_\varphi}{dt}\right)$ which reduces to $\frac{d}{dt}\left(s_\varphi\frac{ds_\varphi}{dt}\right) = 2\sigma/\rho h^*$. The solution:

$$s_\varphi \sim (2\sigma/\rho h^*)^{1/2} t \tag{1}$$

shows that the spreading velocity $v_\varphi \sim (2\sigma/\rho h^*)^{1/2}$ in the azimuthal direction is constant in time. Experimentally we also observe a spreading of the contact region in the inward radial direction, see Figure 10, because the increase of film thickness in this direction is only small, *i.e.* limited to the thickness of the dimple center (in contrast to the region outside the confined air layer where the slope diverges). Assuming a constant mean film thickness $\bar{h}$ we can model the equivalent spreading radius $s = \sqrt{A/\pi}$ of the contact area A. This description is particularly useful if liquid-solid contact is formed at the inner kink position r_1 and the surrounding film height is $\bar{h}$ in all radial directions, see Figure 11(b). The spreading problem is now two-dimensional and the scaling is as follows: the fluid mass scales with $\rho\bar{h}A$ and it is driven by a capillary force that scales with $4\pi\sigma s$. The solution,

$$s \sim \left(4\sigma/\rho\bar{h}\right)^{1/2} t \tag{2}$$

is very similar to Equation (1) but allows to compare the initial spreading with that of a droplet that approaches quasistatically, i.e. not flattened by air cushioning [25]. Here, we neglect the details of the non-circular spreading region as shown in Figure 10. A similar scaling law was proposed for coalescence of two low-viscosity droplets at small time-scales [28] where a flattened geometry was assumed to explain the observed initial linear increase of neck radius.

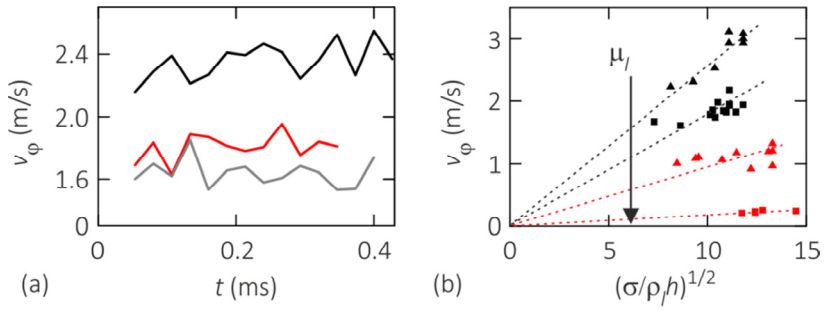

Figure 12. Azimuthal spreading of liquid-solid contact. (a) Azimuthal velocity v_φ for $CaCl_2$ droplets with $h^* = 0.23$ (black), 0.57 (red) and 0.74 μm (gray). (b) The constant value of v_φ versus the inertial scaling for droplets with increasing viscosity (from top to bottom).

We measured the azimuthal spreading velocity for experiments where two distinct cusps are formed. Figure 12(a) shows v_φ at the outer kink for 3 different heights h^*. Indeed the spreading velocity is constant in time within the experimental accuracy. It is larger for lower film heights, in full agreement with the simple balance between inertial and capillary forces, given above in Equation (1). In Figure 12(b) we verify this dependence for several fluids by plotting v_φ versus the scaling in Equation (1). Yet, the inertial description is incomplete: the plot also reveals a clear trend with viscosity of the fluid. Empirically, we find that the normalized azimuthal velocities collapse if plotted *vs.* $\mu_l^{-1/2}$ as shown before in Chapter 2. There it was suggested that the viscosity dependence might come into play *via* a dynamic contact angle that modifies the boundary condition for the shape of the liquid-air interface near the contact area.

The second approach using the wetted area-equivalent radius s shows that spreading in the cushioned case is much faster than the early-time spreading for a quasistatically approaching (*i.e.* non-cushioned) droplet. We observed the latter in our experiments when liquid-solid contact is formed in a very late stage after the confined air film is completely contracted and the droplet is about to lift off. The blue data in Figure 13(a) show that it follows the classic square root behavior in time for a spherical droplet approach, $s \sim (\sigma R/\rho)^{1/4} t^{1/2}$ [25]. When liquid-solid contact is formed at the inner kink position r_1 (black data) the spreading radius follows a distinctly different behavior, *i.e.* the linear time behavior of Equation (2). The velocity is constant in contrast to the spherical approach case where more and more moving liquid is entrained with respect to the driving force [25]. When the normalized radius s/R_0 is plotted versus the scaling $t/(c_1\tau)$

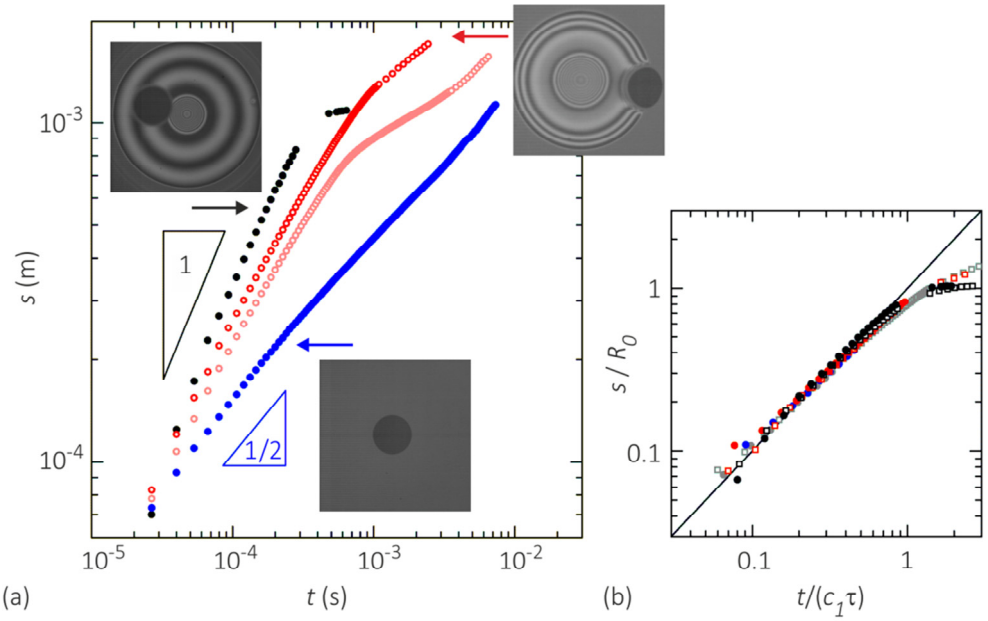

Figure 13. Overall spreading of liquid-solid contact. (a) Wetted area-equivalent radius s versus time for contact formation in the (blue) non-cushioned case or cushioned case at (black) r_1 and (red, pink) r_2. (b) Scaling for the spreading at r_1, *i.e.* the black data in (a), using various fluids.

with $\tau \sim \sqrt{\rho \bar{h} R_0^2/(4\sigma)}$ and $\bar{h}$ the volume-averaged dimple height, we observe a collapse for various liquids using a prefactor c_1 that varies between 0.13 to 0.18, see Figure 13(b). The equivalent spreading radius starts to deviate from linear when the contact region approaches the edge of the confined air film. As an extreme example of this, in panel (a) we also plotted the spreading velocity for liquid-solid contact formation at the outer kink position r_2 (red, pink). Radially inward the triple contact line advances within the confined region with approximately $s \sim t$ whereas radially outward a strong interfacial slope is present and the $t^{1/2}$ behavior is retrieved. The resulting equivalent radius of the contact area is in between the two limiting cases. The experiment shown in pink has a larger $\bar{h}$ and smaller confined area, leading to slower spreading and an earlier transition to another spreading regime, respectively. For contact formation at position r_2 a comparison between the azimuthal and radial inward velocity shows that bubble formation depends only on the ratio $\bar{h}/h^*$ and thus the typical dimple shape. If it is larger than a critical value, *i.e.* the dimple is relatively steep, a bubble should be entrapped as the azimuthal ring

closes first. This is only a very rough estimation as the azimuthal and radial spreading direction lose their independence as soon as the contact line approaches on itself.

4.6. Conclusion

We have experimentally studied the complex film height evolution of the squeezed air between an impacting droplet and a solid substrate, using the reflection interference microscopy technique developed in Chapter 3. We not only confirm the predictions of the existing numerical simulations, but are also able to extend beyond their assumptions and characterize the air film in further stages of the impact process. The initial height of the central part of the dimple scales with the Stokes number at impact as $H^*/R \sim St^{2/3}$, confirming that the balance between lubrication and inertial pressures sets the deformation of the droplet interface [7]. We subsequently observe the formation of a kink in the droplet interface that spreads outward while the central part of the dimple is almost stationary. As time proceeds this kink comes closer and closer to the substrate, ultimately reaching a stationary value that scales as $h_c \sim R\delta^{2/3}St^{2/3}$. This scaling shows that the kink is regularized by surface tension [7], as is expected for the low $We \sim 1$ regime that is studied here. Continued advection leads to the development of a second (and more) even sharper kink with a height h_2 before the droplet reaches its maximum extension. This was not studied before within the existing theoretical descriptions. Initially $h_2 > h_1$ but h_2 decreases almost linearly with t (with a typical slope of -0.33 mm/s). For low We numbers h_2 decreases below the height of the first kink and liquid-solid contact (if any) will be formed at the position of the second kink whereas at higher $We \gtrsim 5$ no crossing occurs and contact will be formed under the first kink. When the minimum film thickness becomes of the order of 200 nm eventually liquid-solid contact is formed, followed by spreading of the three phase contact line. The early time spreading is controlled by the capillary driving force and the inertia of the liquid, while the thin gap geometry increases the spreading rate compared to spherical droplet approach [25], *i.e.* the contact area first spreads over the cushioned region. The spreading velocity is constant in time, inversely proportional with the local film thickness just before nucleation, and the fastest along the azimuthal direction if contact is formed at r_2. The final entrapment of an air bubble then depends on the azimuthal and radial spreading velocities, but also on the shape of the dimple, and the number of contact points.

References

[1] H. Fujimoto, H. Shiraishi and N. Hatta, Evolution of liquid/solid contact area of a drop impinging on a solid surface, *Int. J. Heat Mass Transfer* **43** (2000), 1673-1677.

[2] V. Mehdi-Nejad, J. Mostaghimi and S. Chandra, Air bubble entrapment under an impacting droplet, *Phys. Fluids* **15** (2003), 173.

[3] S.T. Thoroddsen, T.G. Etoh and K. Takehara, Air entrapment under an impacting drop, *J. Fluid Mech.* **478** (2003), 125-134.

[4] D. Van Dam and C. Le Clerc, Experimental study of the impact of an ink-jet printed droplet on a solid substrate, *Phys. Fluids* **16** (2004), 3403.

[5] L. Xu, W.W. Zhang and S.R. Nagel, Drop splashing on a dry smooth surface, *Phys. Rev. Lett.* **94** (2005), 184505.

[6] R. Purvis and F.T. Smith, Air-water interactions near droplet impact, *European Journal of Applied Mathematics* **15** (2004), 853-871.

[7] S. Mandre, M. Mani and M.P. Brenner, Precursors to splashing of liquid droplets on a solid surface, *Phys. Rev. Lett.* **102** (2009), 134502.

[8] M. Mani, S. Mandre and M.P. Brenner, Events before droplet splashing on a solid surface, *J. Fluid Mech.* **647** (2010), 163-185.

[9] P.D. Hicks and R. Purvis, Air cushioning and bubble entrapment in three-dimensional droplet impacts, *J. Fluid Mech.* **649** (2010), 135-163.

[10] L. Duchemin and C. Josserand, Curvature singularity and film-skating during drop impact, *Phys. Fluids* **23** (2011), 091701.

[11] S. Mandre and M.P. Brenner, The mechanism of a splash on a dry solid surface, *J. Fluid Mech.* **690** (2012), 148-172.

[12] L. Duchemin and C. Josserand, Rarefied gas correction for the bubble entrapment singularity in drop impacts, *C. R. Mecanique* **340** (2012), 797-803.

[13] F.T. Smith, L. Li and G.X. Wu, Air cushioning with a lubrication/inviscid balance, *J. Fluid Mech.* **482** (2003), 291-318.

[14] M.M. Driscoll and S.R. Nagel, Ultrafast interference imaging of air in splashing dynamics, *Phys. Rev. Lett.* **107** (2011), 154502.

[15] J.M. Kolinski, S.M. Rubinstein, S. Mandre, M.P. Brenner, D.A. Weitz and L. Mahadevan, Skating on a film of air: drops impacting on a surface, *Phys. Rev. Lett.* **108** (2012), 074503.

[16] W. Bouwhuis, R.C.A. Van Der Veen, T. Tran, D.L. Keij, K.G. Winkels, I.R. Peters, D. Van Der Meer, C. Sun, J.H. Snoeijer and D. Lohse, Maximal air bubble entrainment at liquid-drop impact, *Phys. Rev. Lett.* **109** (2012), 264501.

[17] J.S. Lee, B.M. Weon, J.H. Je and K. Fezzaa, How does an air film evolve into a bubble during drop impact?, *Phys. Rev. Lett.* **109** (2012), 204501.

[18] Y. Liu, P. Tan and L. Xu, Compressible air entrapment in high-speed drop impacts on solid surfaces, *J. Fluid Mech.* **716** (2013), R9.

[19] J. De Ruiter, J.M. Oh, D. Van Den Ende and F. Mugele, Dynamics of collapse of air films in drop impact, *Phys. Rev. Lett.* **108** (2012), 074505.

[20] R.C. Van Der Veen, T. Tran, D. Lohse and C. Sun, Direct measurements of air layer profiles under impacting droplets using high-speed color interferometry, *Phys. Rev. E* **85** (2012), 026315.

[21] J.B. Segur and H.E. Oberstar, Viscosity of glycerol and its aqueous solutions, *Ind. Eng. Chem.* **43** (1951), 2117-2120.

[22] S. Mikhail and W. Kimel, Densities and viscosities of 1-propanol-water mixtures, *J. Chem. Eng. Data* **8** (1963), 323-328.

[23] D. Richard and D. Quere, Bouncing water drops, *Europhysics Letters* **50** (2000), 769-775.

[24] C. Clanet, C. Beguin, D. Richard and D. Quere, Maximal deformation of an impacting drop, *J. Fluid Mech.* **517** (2004), 199-208.

[25] A.L. Biance, C. Clanet and D. Quere, First steps in the spreading of a liquid droplet, *Phys. Rev. E* **69** (2004), 016301.

[26] J.C. Bird, S. Mandre and H.A. Stone, Short-time dynamics of partial wetting, *Phys. Rev. Lett.* **100** (2008), 234501.

[27] K.G. Winkels, J.H. Weijs, A. Eddi and J.H. Snoeijer, Initial spreading of low-viscosity drops on partially wetting surfaces, *Phys. Rev. E* **85** (2012), 055301(R).

[28] S.C. Case and S.R. Nagel, Coalescence in low-viscosity liquids, *Phys. Rev. Lett.* **100** (2008), 084503.

Bouncing on thin air. Squeeze force and film dissipation in a non-wetting bounce

Millimeter-sized liquid droplets are able to bounce multiple times on flat solid substrates - independent of the wettability - provided that a micrometer-thick air layer is sustained below the droplet, i.e. for $0.006 < We < 4$. For $We < 1$, the restitution coefficient is > 0.9. We analyze the motion of the drop and decompose its shape into eigen modes to study the conversion of energy between center of mass energy and internal (oscillation) energy during a series of bouncing processes. During the bounce internal modes are excited. Subsequent internal dissipation during the flight phase accounts for no more than 20% of the total energy loss. Hence, 80% of the energy is dissipated during the actual bouncing process, despite the continuous presence of a lubricating air film. Our analysis suggests that only a fraction of this energy loss is due to viscous dissipation within the drop. The rest is dissipated within the air film. Reflection interference microscopy yields the time evolution of the squeezed air film below the droplet with a 0.1 ms time resolution. Our measurements reveal a strong asymmetry in the air film profiles between the spreading and receding phase of the bouncing process. This asymmetry is found to be crucial in a simple model of the bouncing process for reproducing the large number of bounces and the high restitution coefficient found experimentally.

5.1. Introduction

The intriguing phenomenon of droplets bouncing on a liquid or solid substrate has drawn quite some attention during the last decade. Using droplets bouncing on a vertically vibrated bath it was shown that the continuous resupply of an air film below the droplet allows for an unlimited bouncing series [1]. We are interested in bouncing on solid substrates, where the creation of liquid-solid contact has large consequences for the recoil. Contact angle hysteresis is the main dissipation mechanism in the receding motion, and is able to inhibit a bounce [2]. Yet, the influence of contact angle hysteresis can be fully eliminated by creating a non-wetting impact (as in the vibrated-bath case), in which a thin layer of air is squeezed between the droplet and the substrate. Herewith the main source of dissipation is eliminated thus allowing the droplet to bounce. During lift-off energy is transferred to vibrational modes causing the droplet to oscillate. This is especially prominent at large impact velocity and leads to a low restitution of the bounce [3]. Instead we focus here at $We < 1$ where the exited oscillations are moderate and repeated quasi-elastic bouncing can be observed; moreover, the oscillation behavior can then be described by linear theory. The non-wetting state can be obtained either by using a superhydrophobic substrate to minimize the contact area (quasi non-wetting) [4], or actively maintain an thin layer of air or vapor below the droplet. The latter is generally obtained through evaporation exploiting the Leidenfrost effect on a heated surface [3, 5, 6]. The squeezed layer then exists of the vapor of the droplet phase. Recently, the reversed experiment on a sublimating substrate of dry ice also proved to support bouncing [7]. A way to maintain the air layer without creating a vapor phase is to oscillate the substrate, then often a liquid, *i.e.* a bath [1, 8, 9] or soap film [10]. In both cases, energy of the substrate is transferred via the squeezed film to the droplet.

Here we are interested in role of the air film in the bouncing mechanism. In many studies the presence of an air film is suggested merely to sustain non-wetting and thus explain in experiments [3, 4] or justify in simulations [11, 12] the absence of contact angle hysteresis. When exploiting the Leidenfrost effect the air film is relatively thick (~ 100 μm) and air film dissipation is indeed negligible, leading up to 1000 successive bounces [3]. However, for small air film thicknesses the role of the squeezed layer as a source of dissipation or as a force actor might not be negligible. For a droplet bouncing on a viscous bath Gilet *et al*. [9] have developed a theoretical description involving a squeeze force and dissipation in the air film. According to their description, an internal droplet motion must have a significant influence on the film drainage to observe a positive momentum transfer and thus permanent bouncing. The model is supported by interference measurements of

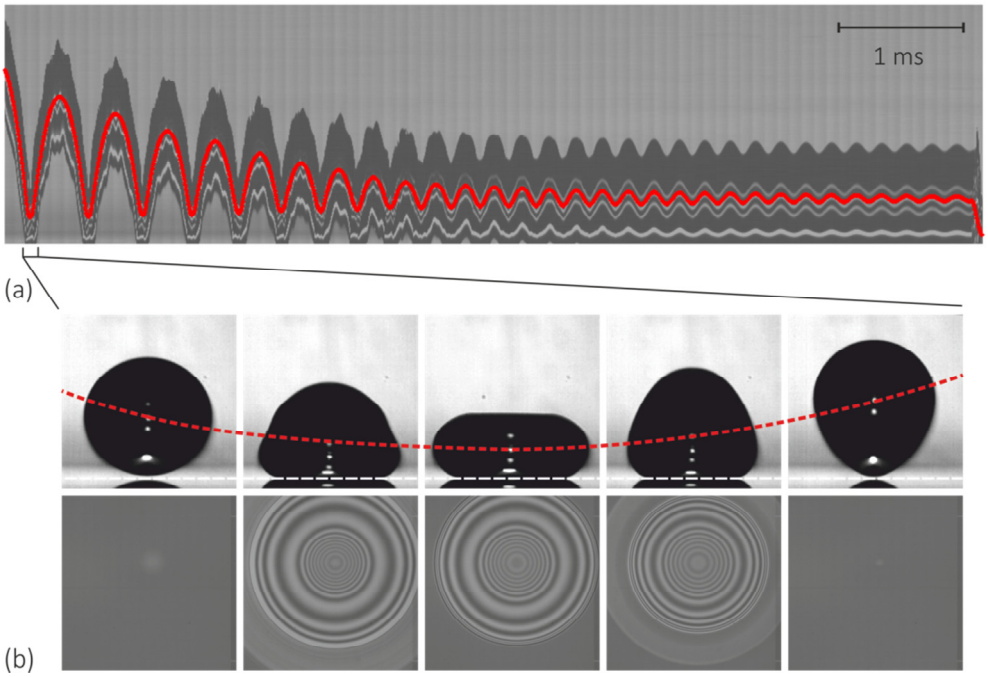

Figure 1. Bouncing series of an $R_0 = 1.03$ mm droplet impacting on a flat glass substrate with an initial velocity of 0.22 m/s. (a) Time sequence showing the vertical centerline of the droplet. Wetting occurs rapidly when solid-liquid contact is finally formed after 0.79 s. The white lines are reflections from the droplet surface. (b) The snapshots show a selection of (upper row) side-view images and (bottom row) the corresponding reflection interference pictures ($\Delta t =$ 2.4 ms) during the first bounce.

the film, that yield an average 'flat' film height in time [13]. The question arises whether the assumption of a flat air film is correctly explaining the momentum transfer *via* the air film to the bouncing droplet.

To address these questions, we study millimeter sized aqueous droplets impacting onto a rigid, stationary and hydrophilic substrate. Herewith we exclude any forcing or replenishment of the air film - except for the falling droplet motion. The experiments in Chapter 2 and 4 show the start of air film contraction after its spreading, suggesting that a full bounce can be observed under the proper conditions. Exploiting this idea is the key question in this Chapter. Indeed, when released from a typical height of 4-14 mm the droplet bounces repeatedly before an abrupt transition to wetting is observed. Figure 1(a) shows the time evolution of the center of mass of a typical bouncing series. During the

"bounce" *i.e.* when the linear momentum is reversed due to interaction with the substrate, the droplet is flattening on the substrate, but maintains a contact angle of virtually 180^{o}, as shown in the upper row of panel (b). To sustain this non-wetting situation, even on a hydrophilic substrate, a finite air layer should exist between the droplet and the substrate, which is confirmed by reflection interference microscopy; the interference signal is permanently observed during the bounce, see the bottom row of panel (b). This means that the bouncing phenomenon should be independent of substrate wettability. In absence of a contact line the dissipation during the bounce can be small. This leads to a remarkable high restitution coefficient of 0.96 ± 0.04 and up to 16 subsequent bounces, followed by another 14 shape oscillations while the drop is hovering on the air film, before eventually the liquid-solid contact is established. But, how can a drop bounce on air? At first glance one can think the air film is elastically compressed resulting in a reaction force which is permanently oriented upwards to reverse the droplet momentum. However, because all velocities involved are much smaller than the speed of sound, certainly during the last bounces, the Mach number is smaller than one and the air flow in the film must be considered as incompressible. This makes the reaction force purely dissipative and thus directed against the velocity direction of the liquid-air interface, i.e. presumably downwards in the second half of the bounce. So, *how can a drop bounce on air?*

We analyze this process in terms of an energy picture *e.g.* the conversion from center of mass energy to internal energy and backwards, using the side view recordings as a guidance. The role of the force exerted by the air film onto the drop, necessary to reverse the linear momentum of the drop in a bounce, is investigated by analyzing the evolution of the droplet-air film interface from the bottom view interferometric data. In section 5.2 we present our experimental approach, while in section 5.3 the analysis of the recorded data is discussed as well as how to obtain the kinetic and potential energy from the droplet shape evolution. Here we will also sketch how the evolution of the film profile is used to obtain the dissipation and the squeeze force in the air layer. In section 5.4 the results of the bouncing and squeeze out analysis are discussed. Moreover, a simple "single oscillation mode" model will be presented to explain the bouncing on a purely dissipative force. We conclude our findings in section 5.5.

5.2. Experiments

The droplets are quasistatically dispensed from a syringe needle and detached by their own weight to obtain a uniform radius that depends only on liquid properties and outer needle diameter. The height of the needle above the substrate is varied between 5 and 15 mm, leading to initial impact velocities between 0.22 and 0.49 m/s. We use three types of substrate to test the influence of surface wettability: fully wettable polished glass wafers (with a roughness below 3 nm as verified by atomic force microscopy), glass wafers hydrophobized with a UV-cured silicon oil layer [14], having a contact angle of approximately 90°, and a series of (super)hydrophobic substrates with an RMS roughness varying between 8 and 100 nm. The latter are produced by oxygen plasma etching of a ~ 5 μm SU-8 photoresist layer on a glass wafer, which is subsequently coated with a C_4F_8 layer to obtain an advancing contact angle of 155° and a roughness-dependent receding contact angle of 120-150° (for the method, see Ref. [15]). All substrates are rigorously cleaned to prevent premature formation of contact due to any irregularities. The glass wafers are first cleaned ultrasonically in subsequent steps with soap solution, water and isopropanol, and then exposed to a plasma treatment. The rinsed substrates are transferred to the cuvette in which the impact experiments are performed, shortly before the experiments take place to avoid the settlement of dust particles from the air.

We also vary the fluid properties of the droplet, being the liquid density ρ, the viscosity μ, and the surface tension σ. Together with the droplet size R_0 and its impact velocity v, this leads to three non-dimensional numbers with which the bouncing dynamics can be captured, *i.e.* Weber number $We = \rho R_0 v^2/\sigma$, Ohnesorge number $Oh = \mu(\sigma\rho R_0)^{-1/2}$ and Bond number $Bo = \rho g R_0^2/\sigma$, that give the ratio of inertia, viscosity and gravity to surface tension, respectively. For a millimeter sized aqueous drop the *Oh* number is typically 0.004 << 1, so droplet viscosity will play a minor role, while the *Bo* number, of order 0.1, will mainly determine the drop shape in the hovering state. However, the initial We number in the bouncing regime will vary between 0.1 and 5 indicating that the process is controlled by the competition between inertia and surface tension. For higher We numbers direct liquid-solid contact is initiated in the bounce (see [9] and Chapters 2 and 4). During the bouncing series, the *We* number gradually decreases with each bounce until the squeeze force prevents the rebound. To investigate the (minor) role of *Bo* and *Oh* number, we also use 90% wt. propanol droplets with two different sizes, using needles with different diameter, and 85% wt. glycerol droplets, respectively. A full overview of the used liquids in shown in Table 1.

Aqueous solution	R_0 (mm)	σ (mN·m^{-1})	ρ (kg·m^{-3})	μ (mPa·s)	Bo (-)	Oh (-)
water	1.03	64.6	996.9	1.0	0.16	0.004
90% wt. propanol	0.79	28.7	825.2	2.2	0.17	0.016
90% wt. propanol	1.04	28.7	825.2	2.2	0.31	0.014
85% wt. glycerol	0.95	63.9	1219.4	109	0.17	0.401

Table 1. Composition and liquid properties of the used aqueous solutions. All solutions contain 0.01% wt. rhodamin to suppress reflections at the 546 nm interference signal. The viscosities are derived from literature using the measured liquid density [16, 17].

The experiments are performed at room temperature and under ambient pressure and recorded with three synchronized high-speed cameras to obtain side-view contour images and a bottom-view interferometry images. The full bouncing sequence is recorded from the side at 4.000 fps (Photron-FASTCAM Ultima 512). In addition the air film is imaged using dual wavelength reflection interference microscopy, of which the two signals are recorded separately at 20.000 fps with two high-speed cameras (Photron SA3 and SA5), see Chapter 3.

5.3. Analysis of the recorded data

5.3.1. Side-view

From the side-view images as shown in Figure 1 we extract the droplet contour as a function of time, using a Laplacian edge detection, in order to study the center of mass motion and the shape oscillations. Therefore, the droplet contour $R(t,\theta)$ measured from the center of the drop, is decomposed in spherical harmonics using Legendre polynomials [18, 19]:

$$R(t,\theta) = R_0 + \sum_{n=0}^{\infty} c_n(t) P_n(x) \qquad (c_1 = 0) \qquad (1)$$

where $P_n(x)$ is the Legendre polynomial of order n and $x = \cos\theta$. The zeroth-order coefficient c_0 gives the deviation from the radius R_0 of the unperturbed sphere. For small coefficients c_n ($n > 1$), c_0 will be zero. The height of the center of the drop above the substrate is given by y_0. The first-order coefficient c_1 indicates the deviation between this

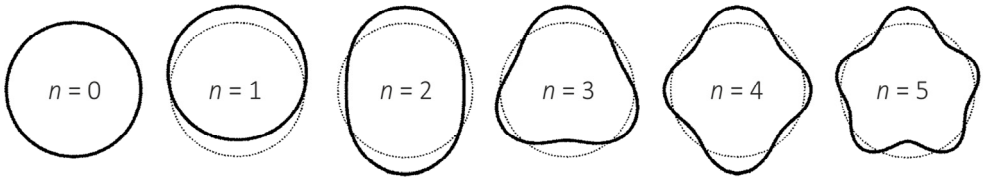

Figure 2. Shape modes for a spherical decomposition of an interface. The sequence shows the modes up to order $n = 5$. The higher modes are imposed onto the undisturbed droplet: $R(\theta) = R_0[1 + 0.25P_n(x)]$.

center height and the initial guess for y_0 (taken from the center of mass position) and is used to optimize the value of y_0. The higher order coefficients $c_2 \ldots c_\infty$ give the contributions of the successive shape modes. As visualization the modes up to $n = 5$ are shown in Figure 2 with a positive amplitude $c_0/4$. Using the orthogonality of the Legendre polynomials, $\int_{-1}^{1} P_n(x)P_m(x)dx = 2\delta_{nm}/(2n+1)$, the coefficients c_n can be calculated from the drop profile $R(t,\theta)$ [18, 19]:

$$c_n(t) = \frac{2n+1}{2}\int_{-1}^{1}\{R(t,\theta) - R_0\}\, P_n(x)dx\,. \qquad (2)$$

To this end the following procedure has been used: for each time frame the drop contour (x_i, y_i) is obtained from the edge detection procedure, where x and y are the Cartesian coordinates, and mirrored with respect to their vertical symmetry axis, $x = x_0$; the mirror points are added to the (x_i, y_i) list. Using an initial estimate y_0 the $R(t,\theta)$ profile is obtained from the (x_i, y_i) values, with a step size in the cosine of the polar angle $\Delta\cos\theta = 10^{-3}$ over the interval $-1 \le \cos\theta \le 1$. The c_n are iteratively obtained by numeric integration of Equation (2), updating the center height y_0 and the $R(t,\theta)$ profile, to obtain $c_1 = 0$. Legendre polynomials up to order 10 are included to obtain a sufficiently flat bottom when the droplet is interacting with the substrate. Figure 3 shows the shape decomposition for a large deformation ('worst-case') obtained during the bounce phase. Including modes up to $n = 4$ yields already a reasonable fit, but modes up to $n = 10$ are included to obtain a flat bottom interface within the pixel resolution.

The evolution of the droplet shape is now fully characterized by the coefficients $c_0(t), c_2(t) \ldots c_{10}(t)$, while the center of mass motion is determined by $y_{CM}(t) = y_0(t) + \int_{-1}^{1} xR^4(t,\theta)dx \,/\, \int_{-1}^{1} R^3(t,\theta)dx$. The latter term is the correction for the center of mass height with respect to y_0, which is zero for small c_n values. During the bounce, however,

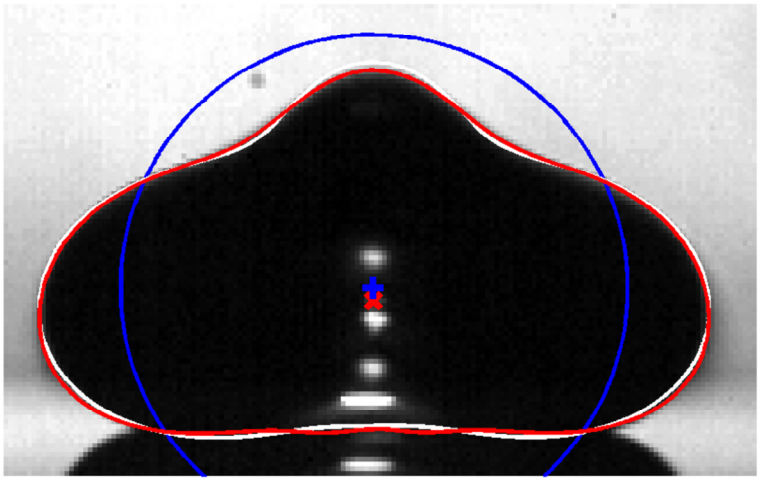

Figure 3. Side-view analysis: shape mode decomposition of the droplet interface, during the bounce. The spherical decomposition is shown for the $n = 0$ mode (blue), and superpositions up to order $n \leq 4$ (white) and $n \leq 10$ (red). Also the center of decomposition y_0 and the center of mass y_{cm} are indicated by the blue + and red ×, respectively.

this term cannot be neglected. The center of mass trajectory during the flight can be fitted with a parabola, from which we can accurate calibrate the pixel size (17.96 μm/pixel) knowing the acceleration $g = 9.81$ m/s^2. This pixel size is used for calibration of the length scale in the recorded pictures. The velocity $\dot{y}_{CM}$ and acceleration $\ddot{y}_{CM}$ of the center of mass are determined by fitting a second order polynomial to the $y_{CM}(t)$ data over the interval $[t - 2\Delta t, t - \Delta t, t, t + \Delta t, t + 2\Delta t]$, where $\Delta t = 0.25$ ms, from which the slope and second derivative in the central point is obtained. An example of the CM trajectory and the first 4 modes of the shape decomposition are shown later in the results section in Figure 7 and Figure 13 respectively.

As we will discuss the repeated bouncing of the impacting droplet in terms of an energy analysis, we calculate the potential and the kinetic energy of the center of mass motion from the values of y_{CM}, $\dot{y}_{CM}$, and $\ddot{y}_{CM}$ as:

$$U_{CM} = \rho V g y_{CM} \tag{3}$$

$$K_{CM} = \frac{1}{2}\rho V \dot{y}_{CM}{}^2 \tag{4}$$

Moreover, the drop-substrate interaction force F_s is the only external force, besides gravity, that acts on the drop. It is given by:

$$F_s = \rho V(\ddot{y}_{CM} + g)\,. \tag{5}$$

The time evolution of the drop shape is characterized by the time derivatives $\dot{c}_n$ and $\ddot{c}_n$, which are determined in the same way as the time derivatives of y_{CM}.

Next we consider the internal potential and kinetic energy involved in the droplet shape variation. The potential energy is given by the surface energy of the deformed droplet: $U_{int} = \sigma A_{surf}$ which is linear in the area:

$$U_{int} = 2\pi\sigma \int_0^{\pi} R \sin\theta \sqrt{R^2 + (\partial_\theta R)^2}\, d\theta \tag{6}$$

with R the angle-dependent radius of the droplet. In the limit of small deformations this expression reduces to $U_{int} \simeq 2\pi\sigma \int_{-1}^{1} \left\{R^2 + \frac{1}{2}(\partial_\theta R)^2\right\} dx$, where $x = \cos\theta$. Using the shape decomposition as given by Equation (1) one finally obtains for the potential energy up to second order in the coefficients c_n (see Appendix 5.1 for details):

$$U_{int} = 2\pi\sigma \sum_{n=2}^{\infty} \frac{(n-1)(n+2)}{2n+1} c_n^2 \tag{7}$$

The potential energy can be written in the usual form as $U_{int} = \sum_{n=2}^{\infty} \frac{1}{2} k_{eff,n} c_n^2$ with the effective spring constant $k_{eff,n} = 4\pi\sigma(n-1)(n+2)/(2n+1)$ which quickly converges to $k_{eff,n} = 2n\pi\sigma$ for $n \geq 2$. Thus $k_{eff,n}$ increases about linearly with mode number. Higher frequency modes are stiffer as their creation causes a large increase of surface area.

The kinetic energy is determined by the flow inside the droplet. As we expect that the droplet viscosity plays a minor role in the bouncing process we assume potential flow: $\underline{v} = \nabla\varphi$. Due to incompressibility the velocity potential should satisfy Laplace's equation: $\nabla^2\varphi = 0$. The solution of this equation is given in spherical coordinates by:

$$\varphi(r,\theta) = \sum_{n=2}^{\infty} A_n r^n P_n(x) \tag{8}$$

where $P_n(x)$ is the Legendre polynomial of order n and A_n is the strength of mode n. The corresponding radial and tangential velocities are given by $u_r(r,\theta) = \partial_r\varphi(r,\theta)$ and $u_\theta(r,\theta) = r^{-1}\partial_\theta\varphi(r,\theta)$, respectively. For small deformations the normal vector $\underline{n}$ can be

replaced by the radial unit vector $\hat{e}_r$ and we obtain for the displacement at the interface ($r = R_0$):

$$\partial_t R(\theta) = u_r(R_0, \theta) = \sum_{n=2}^{\infty} n A_n {R_0}^{n-1} P_n(x) \tag{9}$$

Comparing this with our shape decomposition in Equation (1), we find

$$\dot{c}_n = n A_n R_0^{n-1} \tag{10}$$

where $n > 1$ so in the limit of small deformations, c_0 should be zero. However, for large amplitudes of the fundamental mode $c_2 > 0.1R_0$ (*i.e.* during each bounce phase except the very last hover oscillations) the relation between c_n and A_n becomes very complicated as energy is transferred between modes which leads to non-linear coupling. For example, Becker, Hiller and Kowalewski [20] have formulated a non-linear inviscid model that evaluates the kinematic and normal stress boundary conditions at the deformed droplet surface $R(\theta, t)$ instead of the equilibrium spherical droplet. Here, we will restrict ourselves to the linear approximation using the c_n values during the bouncing phase as an estimate of the flow field.

Given the velocity potential, Equation (8), we calculate the kinetic energy $K_{int} = \frac{1}{2}\rho \int \nabla\phi \cdot \nabla\phi \, dV$. Using the relation $\nabla \cdot (\phi\nabla\phi) = \nabla\phi \cdot \nabla\phi + \phi\nabla^2\phi = \nabla\phi \cdot \nabla\phi$ and the divergence theorem, the integral over the volume of the droplet is converted to a surface integral $K_{int} = \frac{1}{2}\rho \int \phi\left(\underline{\mathrm{n}} \cdot \nabla\phi\right) dA$. In the small deformation limit this expression reads $K_{int} = \pi\rho R_0^2 \int_0^{\pi} (\varphi \, \partial_r \varphi)|_{R_0} \sin\theta \, d\theta$. Evaluating it yields (see again Appendix 5.1 for details):

$$K_{int} = 2\pi\rho R_0^3 \sum_{n=2}^{\infty} \frac{1}{n(2n+1)} \dot{c}_n^2 \tag{11}$$

The kinetic energy can be written in the usual form as $K_{int} = \sum_{n=2}^{\infty} \frac{1}{2} m_{eff,n} \dot{c}_n^2$ with the effective mass for oscillation given by $m_{eff,n} = 3M/(2n^2 + n)$ where *M* is the total mass of the droplet. The effective mass decreases with increasing mode number as the flow field gets more localized towards the surface region for higher frequency oscillations.

Although potential flow assumes that the fluid is inviscid, we can calculate the dissipation in the flow field in the limit of low fluid viscosity, i.e. small Oh number. The internal dissipation rate is given in terms of the rate of strain tensor $\overline{\overline{D}}$ by $\dot{W}_{drop} = \int \left(2\mu \overline{\overline{D}} : \overline{\overline{D}}\right) dV$ where $\overline{\overline{D}}$ in case of rotational symmetry is given by:

$$\overline{\overline{D}} = (\partial_r u_r)\hat{e}_r\hat{e}_r + \left(\frac{1}{r}\partial_\theta u_\theta + \frac{u_r}{r}\right)\hat{e}_\theta\hat{e}_\theta + \left(\frac{u_r}{r} + \cot\theta\,\frac{u_\theta}{r}\right)\hat{e}_\phi\hat{e}_\phi$$

$$+\frac{1}{2}\left(r\partial_r\left(\frac{u_\theta}{r}\right) + \frac{1}{r}\partial_\theta u_r\right)(\hat{e}_r\hat{e}_\theta + \hat{e}_\theta\hat{e}_r)$$

It can be derived that [11]:

$$\dot{W}_{drop} = 8\pi\mu R_0 \sum_n \frac{n-1}{n}\dot{c}_n^2 \tag{13}$$

These expressions for the energy and the dissipation will be used in section 5.4 to analyze the bouncing process. Moreover, from Equations (7) and (11) we obtain the Rayleigh frequencies for an freely oscillating droplet by evaluating $\partial_t(K_{int} + U_{int}) = 0$:

$$\omega_n = (\sigma/\rho R_0^3)^{1/2}\sqrt{n(n-1)(n+2)} \tag{14}$$

5.3.2. Bottom view

In bottom-view the development of the air film during the bounce can be observed. The film is imaged in reflection mode through the transparent substrate by dual wavelength reflection interference microscopy (DW-RIM) at the 436 and 546 nm spectral lines (each with a bandwidth of ~ 30 nm) of a mercury lamp, see Figure 4(a). The non-monotonic spacing of the interference fringes, shown in Figure 4(b), indicates a rather complex thickness profile of the air layer with several inflection points. We extract absolute thickness profiles with an absolute accuracy of approximately 30 nm, by taking into account the finite aperture of the optics, as well as the wavelength distribution of the lamp and the spectral sensitivity of the cameras.

The experimental set-up and analysis procedure are described in detail in Chapter 3. The resulting film thickness profile $h(r,t)$ of the so-called “dimple” is plotted in Figure 4(c). We analyzed the 20.000 fps recordings with a time step between 0.1 and 0.25 ms to obtain about hundred interface profiles per bounce. From Figure 4 it is clear that the film can only be observed over a finite radial extent. Outside the kink the interference pattern quickly vanishes. This is not caused by the finite depth of view of 8 μm, but rather by the steepening of the interfacial slope that becomes too large for the lateral resolution when it is larger than $3°$. Because of this steepening we assume that both the build-up of pressure and the dissipation are essentially restricted to the observable region of the air layer.

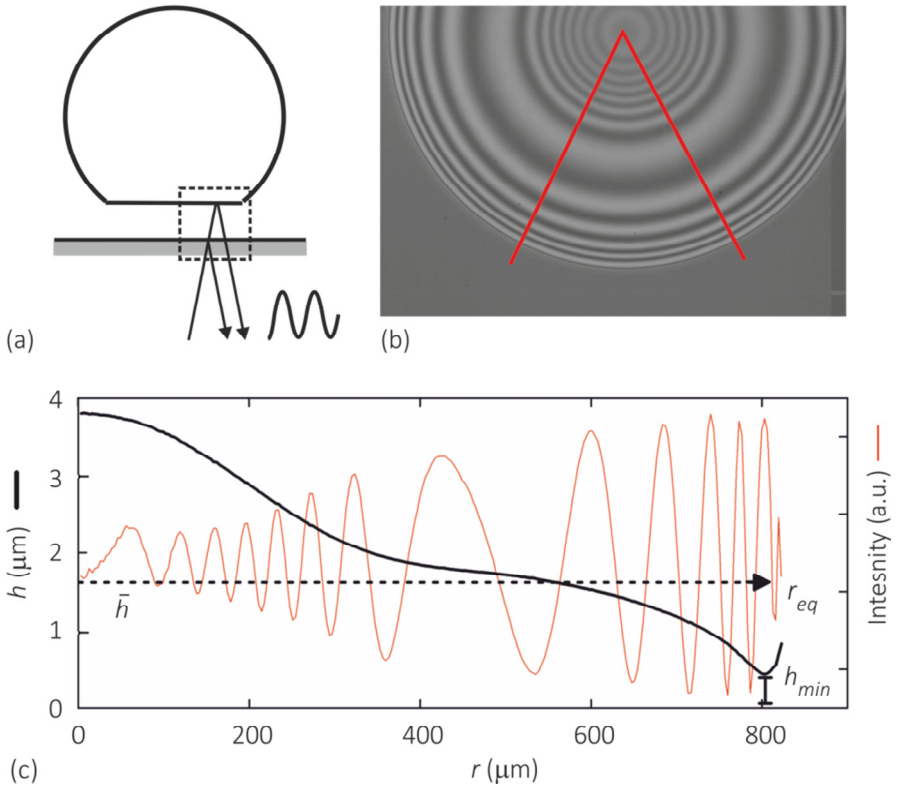

Figure 4. Bottom-view analysis: air film thickness during the bounce phase. (a) Sketch of the thin film interference. (b) Typical interference profile of the air film below a water droplet. (c) The radial intensity profile (thin red line) and the corresponding interface profile (thick black line). Indicated are the dimple radius r_{sq}, the minimum film thickness h_{min}, and the volume-averaged film thickness $\bar{h}$ (dashed line).

In Chapter 4 it was shown that the droplet interface rapidly decelerates when approaching the substrate; thus the timespan over which the interference pattern can be observed agrees within 10^{-4} seconds with the timespan over which interaction with the squeezed air layer induces flattening of the bottom droplet interface. In absence of real liquid-solid contact we instead use this interaction time as 'contact' time. Below a critical We number the air film remains continuously squeezed to a micrometric layer: it remains visible throughout the entire oscillation period (also eliminating the characteristic deceleration stage upon approach). This stage will be denoted "hovering" instead of "bouncing".

From the dimple profile evolution $h(r,t)$ during the interaction phase we determine the time derivative $\dot{h}(r,t)$ to describe the dynamics of squeeze out, using a central difference

method. In addition, we calculate the time dependence of some characteristic quantities of the air film, see Figure 4(c), namely the film radius r_{sq}, the film volume V_{sq}, the average height $\bar{h}$ and minimum height h_{min}. The radius $r_{sq}(t)$ of the squeezed air layer was previously defined in Chapter 4 and its volume is $V_{sq}(t) = \int_0^{r_{sq}(t)} h(r) 2\pi r dr$. Two characteristic height measurements can be made: the average height $\bar{h}(t) = V_{sq}/(\pi r_{sq}^2)$, and the minimum film thickness $h_{min}(t)$ at its position $r_{min}(t)$ that is critical for the stability of the film.

As stated before, when the droplet comes close to the substrate the air in between droplet and substrate forms a thin film. Due to the thinning of this film, the gas pressure in this layer increases as well as the outward gas velocity. The build-up of pressure leads to an upward force that decelerates the droplet, while the associated shear within the gas flow leads to dissipation of energy. This squeeze force should provide the impulse to let the droplet bounce, *i.e.* the droplet velocity should be reversed before the air film thins so much that solid-liquid contact is formed. At the same time we are interested in the dissipation during this process as it will limit the restitution in the bounce. Therefore we look for expressions for the squeeze force and dissipation in terms of the evolution of the droplet interface $h(r,t)$.

The flow in the squeezed air layer can be described in the lubrication limit because the layer has a thickness $h \approx 1$ μm while its radius r varies from 10^2 to 10^3 μm. Moreover, because the Mach number is smaller than one, the gas film can be considered as incompressible. In that case the continuity relation leads to a simple relation between the interface profile $h(r,t)$ and the radial volumetric flow rate $\dot{Q}(r)$: that is, $d\dot{Q}(r)/dr = -2\pi r\dot{h}(r)$, see Figure 5(b). Hence:

$$\dot{Q}(r) = -2\pi \int_0^r s\dot{h}(s)ds \tag{15}$$

The axial dependence of the velocity field can be obtained from the reduced Stokes equations:

$$\partial_r p = \mu \partial_z^2 v \tag{16}$$

$$\partial_z p = 0 \tag{17}$$

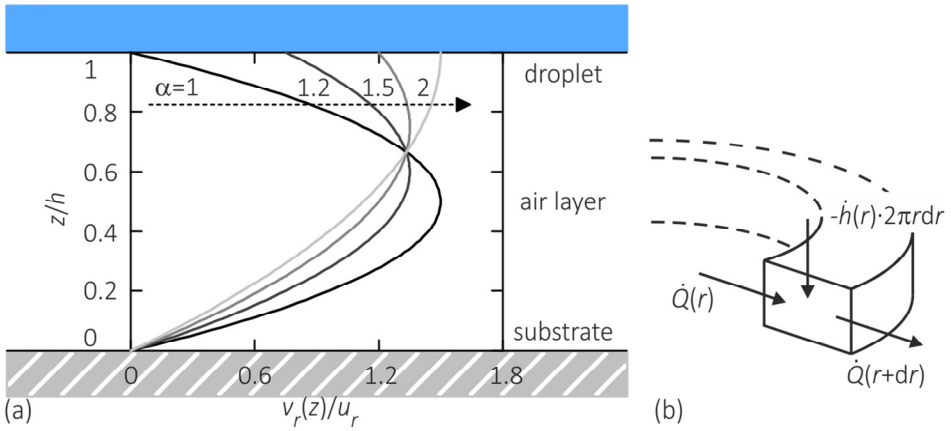

Figure 5. (a) Parabolic flow profile in the squeezed air layer for various slip coefficients from no-slip to full slip: $\alpha = 1$, 1.2, 1.5 and 2. (b) A single cylindrical shell with arrows indicating the in- and outflow and the volume (height) change, where $\dot{Q}(r) = 2\pi r h(r)\bar{v}(r)$.

where $\partial_a A$ stands for $\partial A/\partial a$. Integration of Equation (16) yields an expression for $v(r,z)$ that is quadratic in z, resulting in a parabolic flow profile. The exact shape of the profile is determined by the boundary conditions: we assume a no-slip condition at the gas-substrate interface, i.e. $v(r,0) = 0$, while we consider partial slip at the gas-droplet interface, i.e. at $z = h(r)$, depending on the mobility of the droplet interface. It has been shown that a liquid interface with impurities has a finite mobility that allows the gas to slip along the interface and have a finite velocity at the boundary [21]. For a fully mobile interface we assume $(\partial_z v)_h = 0$, for a fully immobile interface $v(r,h) = 0$. To interpolate between these limiting cases we introduce a coefficient $1 \le \alpha \le 2$ ($\alpha = 1$: no slip, $\alpha = 2$: full slip, see Figure 5(a)). The resulting velocity profile is given by:

$$v(r,z) = \frac{\beta(\alpha)\dot{Q}(r)}{2\pi r h(r)}\left\{\left(\frac{z}{\alpha h(r)}\right) - \left(\frac{z}{\alpha h(r)}\right)^2\right\} \tag{18}$$

where the normalization factor is given by $\beta(\alpha) = 6\alpha^2/(3\alpha - 2)$ to assure that the height-integrated velocity profile is equal to the total height times the average velocity $\bar{v}(r) = \dot{Q}(r)/(2\pi r h(r))$, thus $\int_0^{h(r)} v_r(r,z)dz = h(r)\bar{v}(r)$.

The local dissipation in the film is given by $\dot{\varepsilon}(r,z) = 2\mu\bar{\bar{D}}:\bar{\bar{D}} = \mu(\partial_z v)^2$, where $\bar{\bar{D}} = \frac{1}{2}\partial_z v\,(\hat{e}_r\hat{e}_z + \hat{e}_z\hat{e}_r)$ is the rate of strain tensor. So the total dissipation rate $\dot{W}_{sq} = \int \dot{\varepsilon}(r,z)dV$ is given by (see Appendix 5.2):

$$\dot{W}_{sq} = \frac{6\mu}{\pi}\left[\frac{3\alpha^2-6\alpha+4}{(3\alpha-2)^2}\right]\int_0^{R_{max}} \frac{\dot{Q}^2(r)}{rh^3(r)}dr \quad (19)$$

where the film extends over a lateral distance R_{max}. For a parallel plate geometry $\partial_r \dot{h} = 0$ with no-slip condition this reduces to the classical solution for the total dissipation rate $\dot{W}_{sq} = (3/2)\pi\mu\dot{h}^2h^{-3}R^4$.

Equivalently, we can calculate the pressure field in the squeeze flow and determine the squeeze force. For details see Appendix 5.2. By substitution of Equation (18) in Equation (16) we find the pressure gradient, which is integrated to obtain the excess pressure in the air film:

$$\Delta p(r) = p(r) - p_\infty = \frac{6\mu}{\pi(3\alpha-2)}\int_r^\infty \frac{\dot{Q}(s)}{sh^3(s)}ds \quad (20)$$

where p_∞ is the ambient pressure outside the squeezed layer. The squeeze force can be determined by integrating the pressure over the film area:

$$F_{sq} = \int_0^\infty 2\pi r\Delta p(r)dr = \frac{6\mu}{(3\alpha-2)}\int_0^\infty \frac{s\dot{Q}(s)}{h^3(s)}ds \quad (21)$$

The partial slip pre-factor decreases from 1 to 1/4 when the boundary condition changes from no-slip to full slip at the droplet interface. For the analysis of our experiments we use the no-slip condition in line with the previous numerical work [22-24].

5.4. Results and discussion

Non-contact bouncing of a liquid droplet on a rigid substrate is restricted to intermediate Weber numbers of the order 0.001 to 1, simply because the squeezed air film should be stable. These limits are set by the formation of solid-liquid contact at both high We (fast squeeze-out, see Chapter 4) and low We (gradual squeeze-out). It should be noted that for the initial We number the lower limit is 10x higher. It is impossible to obtain $We <$ 0.01 upon detachment of millimetric droplets from the needle as it requires releasing a spherical droplet from a height of several tens of micrometers above the substrate. Upon detachment from the needle the droplet elongates, thus forming a liquid bridge between the needle and the substrate for too low release heights. If this initial condition is fulfilled, the droplet will bounce a number of times until We drops below 0.006.

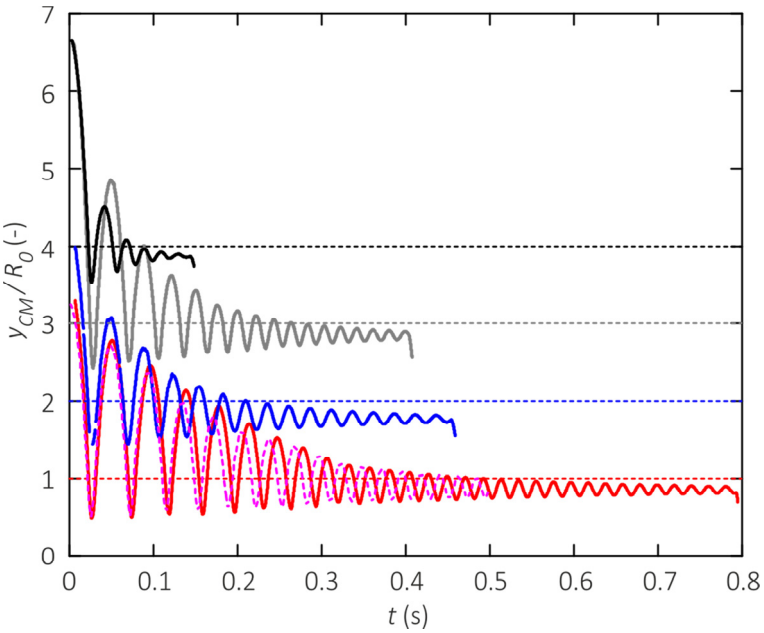

Figure 6. Millimeter-sized droplets bouncing on a smooth glass wafer: influence of wettability and liquid properties. The center of mass height is shown as a function of time. An $R_0 = 1.03$ mm water droplet impacts (red) on a hydrophilic wafer with impact velocity of at 0.22 m/s, or (magenta dashed) on a hydrophobic wafer (UV-cured silicon oil layer) with 0.20 m/s. Subsequently, by 1 unit off-set each are shown: (blue) an $R_0 = 1.04$ mm 90% wt. propanol droplet, (grey) an $R_0 = 0.79$ mm 90% wt. propanol droplet, and (black) an $R_0 = 0.95$ mm 85% wt. glycerol droplet.

All droplets irrespective of liquid properties or size exhibit bouncing in the same We regime, but the number of bounces (and subsequent hovers) does depend on properties and size, see Figure 6. The longest series of 16 bounces is observed for $R_0 = 1.02$ mm water droplets ($Bo = 0.16$ and $Oh = 0.004$). The number of bounces decreases to 9 for 'small' ($R_0 = 0.79$ mm) and 5 for 'large' ($R_0 = 1.04$ mm) 90% wt. propanol droplets. 85% wt. glycerol droplets with $R_0 = 0.95$ mm bounce only twice. All droplets have similar Bo as they are formed at the same needle, except the large propanol droplets that are formed at a needle with larger outer diameter. They have significantly higher $Bo = 0.31$ indicating that they are more deformed in the quasi equilibrium, just before formation of contact, as can be observed from Figure 6 (blue line). The highly viscous glycerol droplets ($Oh = 0.40$) obviously have a much lower restitution coefficient, due to a higher dissipation, both in the drop itself and in the gas layer (as will be shown later) as result of

a more stiff interface on short time scales due to the higher drop viscosity. As the bouncing phenomena are most clearly visible for water droplets, we will discuss them in detail and describe the differences with other drop composition when relevant.

On a fully wettable substrate the droplet shows in the bouncing process an abrupt transition between a non-wetting state supported by an air layer (a contact angle of 180°), and fast and complete wetting as soon as solid-liquid contact is made (a contact angle of 0°). Thus the presence of a non-wetting state is most convincingly demonstrated when using a fully wettable polished glass wafer. However, as no contact is made, the bouncing behavior should be independent of wettability, thus resulting in the same bouncing trajectories for more hydrophobic surfaces. When repeating the experiment with hydrophobized glass substrates with a contact angle of $\sim 90^\circ$ or a (super)hydrophobic substrate with an advancing contact angle of 155^o, indeed very similar bouncing dynamics is observed. The first is plotted in Figure 6 (magenta dashed line) together with the bouncing series on a hydrophilic substrate. Again 16 bounces are observed, and the CM height decays to the same pattern. Small deviations are attributed to a 10% difference in initial impact velocity. For a superhydrophobic substrate the following should be noted: as soon as the bottom-view shows that microscopic liquid-solid contact is formed on the tops of the nanostructured surfaces, the droplet subsequently sticks for a moment to the substrate due to residual contact angle hysteresis and the restitution of the bounce is decreased. In this work we focus on those cases where an air layer of finite thickness remains present at any time during each bounce. We describe the droplet dynamics during the bouncing using the side-view analysis from section 5.4.2, while the interaction with the squeezed air layer and the resulting momentum transfer is discussed using the bottom-view analysis from section 5.4.3.

5.4.2. Shape dynamics of the droplet during the bouncing

The bouncing series of a water droplet with $R_0 = 1.03$ mm, obtained from the side view camera, is shown in Figure 7. The center of mass of the droplet is released from $h_{0,eff} =$ 3.61 mm resulting in an initial impact velocity of 0.22 m/s, *i.e.* $We = 0.76$. The red line shows the height of the center of mass obtained from the shape mode analysis. The full series takes less than one second, during which the droplet bounces 16 times on the substrate, followed by a hovering stage with 15 oscillations. The air film thickness below the center of the droplet (grey), i.e. $h_c(t) = y_0(t) - \sum_{n=0}^{\infty} c_n(t) P_n(-1)$, approaches zero during each bounce, but the remaining thickness, which is clearly visible in the bottom

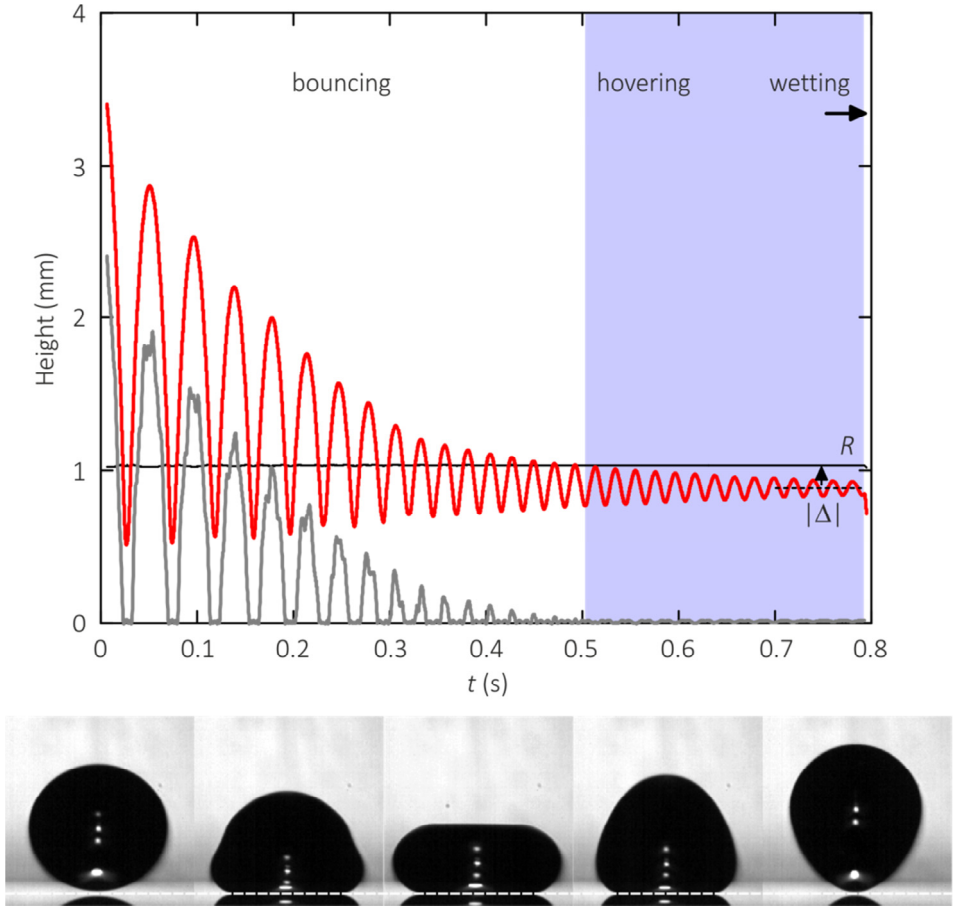

Figure 7. Bouncing series of a $R_0 = 1.03$ mm droplet impacting on a flat glass substrate with an initial velocity of 0.22 m/s. Time evolution of the center of mass height (red) and macroscopic air layer thickness (grey) obtained from the side view images. The bouncing series can be subdivided into a bouncing phase and a hovering phase (shaded blue) that shows an equilibrium sag $|\Delta|$, followed by wetting. Snapshots: selection of side-view images $\Delta t = 2.4$ ms) from the first bounce.

view (see next section), cannot be resolved from the side view. (This is due to the limited lateral resolution and some artificial oscillations from the shape decomposition when the interface is almost flat.) The maximum flight height decreases with each bounce, and thus We decreases. In the final hover oscillation, before solid-liquid contact is established and the droplet wets the substrate, it is only 0.0028.

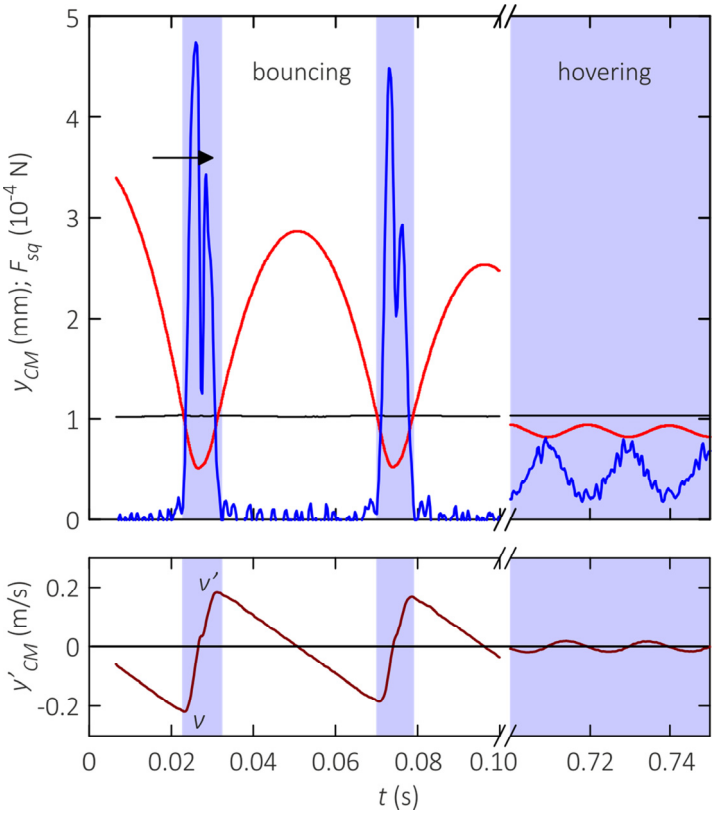

Figure 8. Velocity and estimated interaction force for the experiment shown in Figure 7. Top: time evolution of the center of mass height (red) and interaction force (blue) derived from the center of mass acceleration. Bottom: center of mass velocity (dark red). The first two bounces are shown ($t < 0.10$), as well as a few hovers ($0.70 < t < 0.75$). The blue shaded area indicates interaction with the substrate.

5.4.2.1. Center of mass analysis

For each single bounce the center of mass (CM) motion can be subdivided in two phases, a free flight and the actual bounce, see Figure 8. During the flight the interaction force is zero and the CM motion is fully decoupled from the droplet oscillation; the trajectory is parabolic with a constant gravitational acceleration of 9.81 m/s^2, so the speed increases linearly in time upon approaching the substrate. In contrast, during the bounce phase when the droplet interacts via the squeezed air layer with the substrate (*i.e.* the grey line in Figure 7 is practically zero), the motion of the CM is directly linked to the droplet deformation. The droplet can be viewed as a liquid spring that converts energy of the CM

into elastic surface energy. The droplet stretches laterally while the CM height decreases down to about half the droplet radius for the first bounce, see the middle snapshot in Figure 7. The maximum speed $v = |\min(\dot{y}_{CM})|$ is reached at the end of the flight phase and defines the We number of the impact, see Figure 8. During the deformation, the CM velocity decreases to zero. Subsequently the velocity is reversed and the droplet bounces off with a velocity $v' = \max(\dot{y}_{CM})$. During the bounce the droplet thus experiences a strong acceleration that must be caused by the interaction with the air film. The blue line in Figure 8 shows the interaction force during the bounce with a time resolution of about 1 ms, as calculated with Equation (5). The force is double (sometimes single) peaked and is always positive as would be the case for a normal force in case of real contact. We will discuss this observation when analyzing the nature of the force in a later section.

What happens during the subsequent bounces? In the bounce energy is not only transferred towards internal modes and backwards but also partially dissipated, with the result that the droplet bounces back to a smaller height in the next flight phase, as can be observed from Figures 7 and 8. Simultaneously the impact velocity decreases and the minimum CM height increases while the droplet stretches less in lateral direction. Ultimately the free flight phase is eliminated when the CM height remains smaller than the droplet radius. This roughly coincides with the start of the hover phase where the air layer keeps its micrometric thickness throughout. Thus in the hover phase the motion of the CM is permanently linked to the shape oscillations. The interaction force does not decrease to zero any more as the droplet is in continuous 'contact' with the substrate via the air film. Instead, the force converges to the gravitational force when the droplet approaches its equilibrium shape.

The overall bouncing behavior can be described by the restitution coefficient ε and the interaction time t_c. The restitution coefficient is defined as the ratio between maximum velocities after and before the bounce: $\varepsilon = v'/v = \sqrt{We'/We}$, see Figure 8. It has been plotted in Figure 9 as function of We for three different initial impact speeds. For a water droplet with $R = 1.03$ mm it is approximately constant over most of the We range and has a value of 0.96 ± 0.04 which is similar to the restitution coefficient found by Richard and Quéré [4], for bouncing on a superhydrophobic substrate. We find that the restitution coefficient dramatically decreases on superhydrophobic substrates, when microscopic contacts are formed (as we can verify from the bottom view), thus we expect that also in their experiments a squeezed air layer was present. The restitution coefficient in Figure 9 shows characteristic 'oscillations' as a function of We that are remarkably independent of

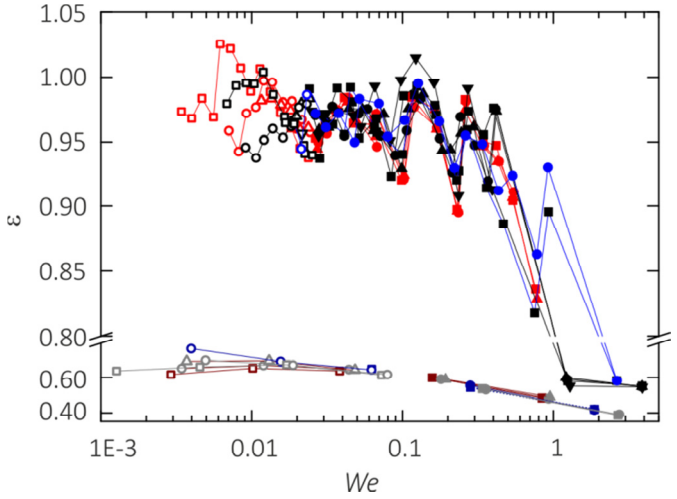

Figure 9. The dependence of restitution coefficient ε on impact We for experiments with 1.03 mm water droplets (released from various initial heights: red, blue and black data set) and 0.95 mm glycerol droplets (dark red, dark blue and grey data set). Solid symbols denote the bouncing phase, while open symbols denote the hovering phase.

the initial fall height. We expect that this is caused by the phase of the droplet with respect to the impact; the restitution is optimal when the droplet is spherical upon impact while stretching towards oblate since the bottom interface velocity is then minimized [3].

At the low We end the restitution coefficient stays constant before it suddenly drops to zero when liquid-solid contact is made (in contrast to the model in *e.g.* Ref. [11] that assumes persisting non-wetting and yields a gradual decrease of ε). At the other limit of $We \sim 1$ the restitution coefficient does not vanish, but decreases significantly to about 0.6. This can be explained by the large droplet deformation: at higher impact velocity the restitution coefficient is largely determined by the transfer of energy to (large amplitude) oscillations rather than dissipation in the liquid or the squeeze layer. With a simple liquid spring free of dissipation Biance *et al*. [3] showed that for $We > 1$ the speed after take-off, $v' \sim \sqrt{\sigma/(\rho R)}$, does not depend on the impact speed nor the compression of the spring. It can be easily shown that this leads to $We' \sim 1$ and the water droplet rises to about 3.5 mm independent of the impact speed. We indeed observe a jump to $We \sim 1$ for the second bounce of each experiment, see Figure 9. Then, the droplet falls into the same trajectory as shown in Figure 7 as soon as $We < 1$. As a result the number of bounces remains remarkably constant (16-18) for water droplets impacting at higher initial impact

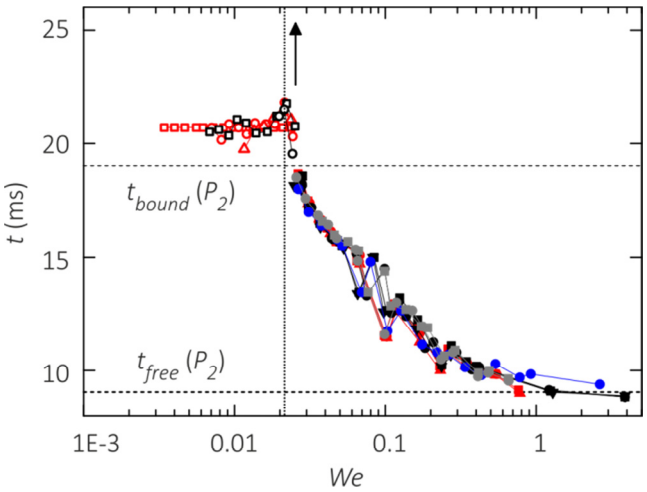

Figure 10. The dependence of interaction time on We for experiments with 1.03 mm water droplets. The droplet is released from various initial heights (red, blue and black data set) onto a glass substrate, or a hydrophobic cured silicon oil layer (grey). In the bouncing state the interaction time of individual bounces can be obtained (closed symbols), while in the hovering state the interaction time diverges (see dotted line and arrow) and we rather measure the oscillation time (open symbols). The dashed horizontal lines indicates the free P_2 mode (Rayleigh) and the bound P_2 mode.

velocities up to $We \sim 4$. Moreover, from Figure 9 we observe that the restitution coefficient and thus the number of bounces depends on the droplet viscosity: the restitution coefficient of highly viscous glycerol droplets is about 0.7, which leads to only 2 bounces.

The interaction time t_c is defined as the time the interaction force during the bounce is non-zero. This time is, within the time resolution of the experiments, equal to the time the interference pattern of the air film is visible. The results for the impact of an 1.03 mm water droplet are shown in Figure 10: for the subsequent bounces the interaction time increases while We decreases. Again, the results from the various experiments at different initial impact velocity collapse perfectly. Also for hydrophilic and hydrophobic substrates we observe no difference. The interaction time converges to approximately 9.1 ms (the Rayleigh P_2 mode described in Equation (14)) for the bounces at $We \sim 1$ and increases towards 18.5 ms for the last bounce. Subsequently, the interaction time diverges at $We \sim 0.02$ as the droplet interface remains continuously dimpled in the hover

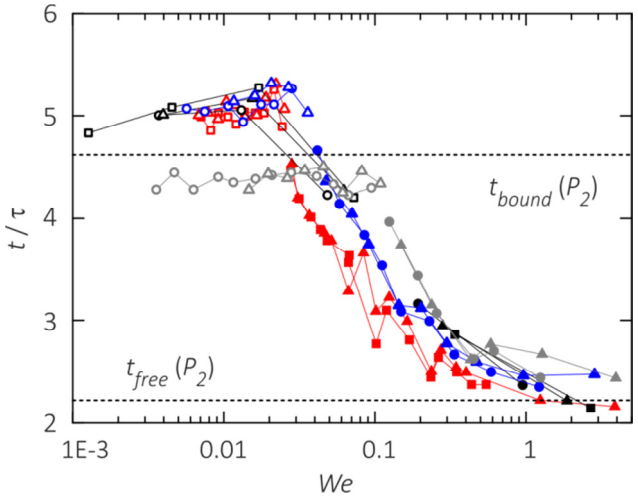

Figure 11. The dependence of interaction time normalized by $\tau = (\rho R_0^3/\sigma)^{1/2}$ on We for experiments with droplets of water (red), glycerol (black), and propanol (small droplets: blue, large droplets: grey). The dashed horizontal lines indicates the free P_2 mode (Rayleigh) and the bound P_2 mode.

stage. During the hover stage we can instead measure the oscillation time of the droplet (and the dimple) which is 20.7 ms.

In Figure 11 the results for all impact experiments are shown by scaling t_c on the characteristic oscillation time $\tau = (\rho R_0^3/\sigma)^{1/2}$. It has been shown previously that the contact time scales as $t_c \approx A\tau$ where $A = A(Bo, We, Oh)$ reduces to $A \approx A(We)$ if the effects of gravity ($We \gg Bo^2$) and viscosity ($Oh \ll 1$) can be neglected [11, 25]. In the bouncing phase we indeed observe reasonable collapse of all impact experiments. At high We the interaction time is given by the Rayleigh time of the dominant $n = 2$ mode: $t_{\text{free}} = 2\pi\,\tau/\sqrt{8} \sim 2.22\tau$, see Equation (14). For small We gravity starts to play a role and in the hover phase all droplets with the same Bo collapse to the same oscillation time of $\sim 5\tau$. The larger drops with a higher Bo number, which are more deformed by gravity, show a lower oscillation time: $\sim 4.3\tau$. The observed oscillation times approach the oscillation time that can be calculated for a spheroid droplet (P_2 mode) that is fixed at one side, *i.e.* it has a CM motion that is directly linked to the change in its half thickness. This 'bound' oscillation time is $t_{\text{bound}} = 2\pi\,\tau/\sqrt{24/13} \sim 4.62\tau$.

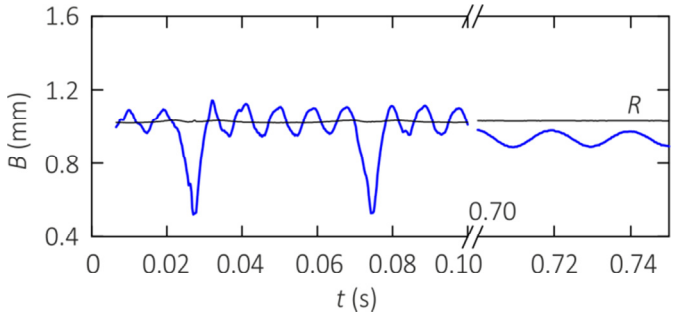

Figure 12. Droplet deformations during a bouncing series. Time evolution of the half droplet height for the bouncing series shown in Figure 7. The first two bounces are shown ($t < 0.10$), as well as a few hovers with equilibrated gravitational sag ($0.70 < t < 0.75$).

5.4.2.2. Droplet oscillations

So far we mainly considered the CM motion of the droplet. During the bounce, when the CM height drops below the droplet radius R_0, the droplet gets deformed to buffer the energy needed for recoil, and since not all energy is transferred back to the CM, it subsequently oscillates during the flight. The magnitude of the oscillation depends on impact velocity and droplet properties such as size, surface tension and viscosity. Let us consider the oscillations associated with the trajectory of an $R_0 = 1.03$ mm water droplet impacting at 0.22 m/s as in Figure 7. The half droplet height B is shown in Figure 12 for the first two bounces and the last few hover oscillations, where the half droplet height $B = \sum_{n=0}^{\infty} c_n(t)\,[P_n(1) + P_n(-1)]/2$ has been calculated from the mode decomposition as discussed in section 5.3.1. (Note that the presence of odd shape modes implies that the droplet is generally not symmetric with respect to a horizontal plane.) During the first few bounces, the droplet deforms in vertical direction to about half its original size, while the oscillations during the intermediary free flight phase are significantly smaller. They also show a slight decay due to viscous dissipation in the droplet. During the successive bounces the We number decreases and so does the droplet deformation. Also the intermediate flight time gets shorter and the bouncing pattern gradually transforms (see also Appendix 5.4) into the single oscillation pattern that can be observed in the hover phase (Figure 12). Due to gravity the droplet does not recover its spherical shape. Instead, the droplet oscillates with decreasing amplitude around a flattened equilibrium shape which is the result of the minimization of the total potential energy, *i.e.* gravity versus surface tension. Denoting Δ the distortion of the CM from spherical, we observe from the experiments in Figure 7 that $|\Delta|/R = 0.15$. Minimizing the total potential energy

$\partial_\Delta \left(mg\Delta + \frac{1}{2} k\Delta^2 \right) = 0$ yields that $|\Delta|/R \approx g/(R\omega_{0,b}^2) \approx 0.10$ in approximate agreement with the experimental observation.

In Figure 12 we also plot the radius $R(t) = (3V/(4\pi))^{1/3}$ of the undeformed droplet, which is not perfectly constant. To check for volume conservation, we calculated $V(t) = \frac{2}{3}\pi \int_0^\pi R^3(t,\theta) \sin\theta \, d\theta$ using Equation (1) for $R(t,\theta)$. The calculated volume is conserved within an accuracy of 1% . The small variation in the apparent volume is related with the position of the droplet in the field of view and can be explained by inaccuracies in the image analysis due to an uneven background illumination and determination of the $y = 0$ baseline. Hence, we take as the radius of the droplet $R_0 = (3V/(4\pi))^{1/3}$, where V is the time average of $V(t)$. The accuracy of $0.01\ R_0$ can be considered as an estimate of the accuracy of the coefficients c_n.

The most significant coefficients c_n up to $n = 4$ are shown in Figure 13, see Appendix 5.4 for more information on the coefficients c_n and their time derivatives. During the bounce phase the decrease of the mean radius $R_0 + c_0$ shows that the small amplitude approximation is not valid here. Thus we need some caution in using the c_n values to describe the potential flow inside the droplet. For now, we look at the surface decomposition itself. Amongst the orders ≥ 2, the dominant mode is $n = 2$: it has the largest amplitude and defines the free oscillation time of 9.1 ms ($\pm$ 0.1) also observed in the overall dynamics of Figure 12. The other oscillation times are 4.7 and 3.0 ms for the $n = 3$ and 4 modes; and all show perfect agreement with their respective Rayleigh frequencies, Equation (14). This only holds for the free flight phases; during the bounce phase all modes up to $n = 4$ are abruptly forced to the same phase as the droplet gets deformed by interaction with the squeezed air layer. The result is a single peak for the $n = 2$ mode and a double peak for the $n = 3$ mode. With the repeated bouncing, as We decreases, also the amplitude of the different modes during the bounce decrease, see Appendix 5.4 for illustration. Gradually the frequency of the modes change such that in the hover phase all modes are synchronized with the motion of the center of mass. The transition is most clear for the $n = 3$ mode that initially shows two peaks during a bounce, which are gradually merged to one. For the $n = 2$ mode the characteristic time for 'contact' merely increases. In the final hover stage shown in Figure 13 the synchronized oscillation time is 20.7 ms.

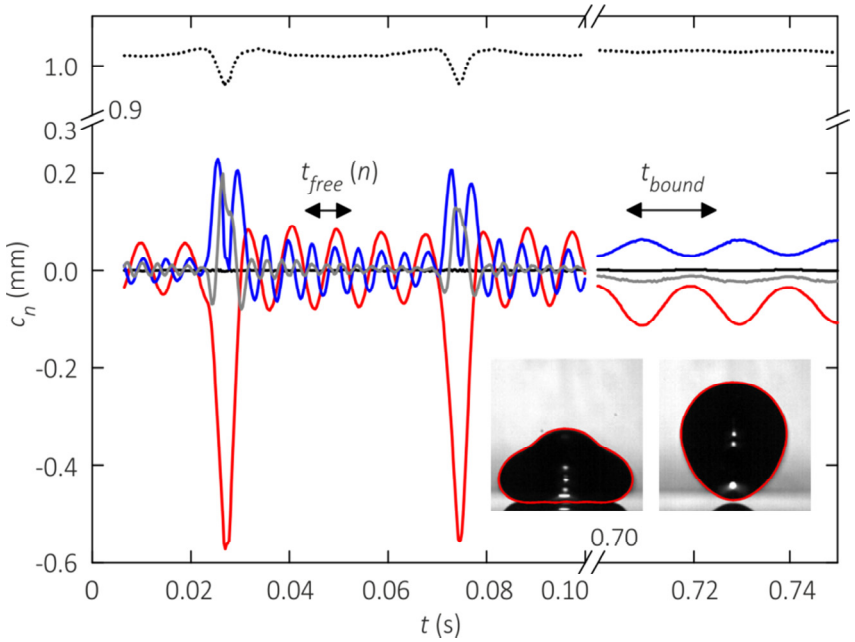

Figure 13. Shape mode decomposition using Legendre polynomials for the bouncing series shown in Figure 7, for $n = 0$ (black dotted line; shifted by R_0), $n = 1$ (black solid), $n = 2$ (red), $n = 3$ (blue), and $n = 4$ (grey) versus time. The first two bounces are shown, as well as a few hovers. The free oscillation time depends on the mode, $t_{free} = 9.1$, 4.7, 3.0 ms for $n = 2$ … 4, whereas during hovering the modes are synchronized, $t_{bound} = 20.7$ ms. Inset: modes up to order 10 are included to describe the shape sufficiently accurate. Left: during the stretch; right: moment of lift-off after the first bounce.

It is important to note that the higher oscillation modes are critical for the bouncing dynamics. The right inset of Figure 13 shows the lift-off after the first bounce. Near the contact point the droplet interface has a high curvature due to a favorable superposition of positive even modes $n = 2$ and 4 and negative odd mode $n = 3$. Thus, the superposition of higher modes can lead to a significant decrease of the 'contact' area that is critical during lift-off. Also, the higher modes have a significant contribution to the storage and dissipation of energy, as discussed later on.

5.4.2.3. Energy and dissipation

The transfer during the bounce of CM energy to internal energy (i.e. oscillations) and subsequent loss of internal energy have previously been described as the main source of dissipation in non-contact bouncing of droplets [4]. The relatively long flight time compared to the 'contact' time suggests that internal dissipation during the flight phase is

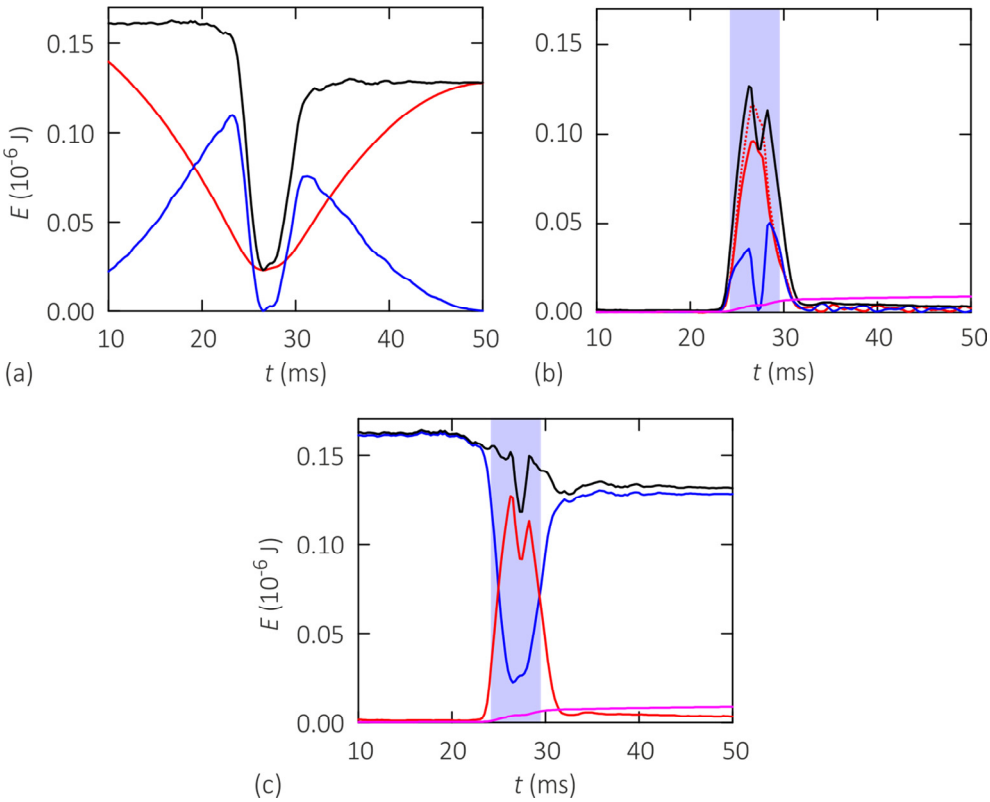

Figure 14. Energy conversions during the first bounce: (a) CM energy, (b) internal energy, and (c) total energy. In (a, b): red: potential energy (dotted: linear approximation), blue: kinetic, and black: total energy. In (c): red: internal energy, blue: CM energy, and black: total energy. Pink: internal dissipation. Experiment from Figure 7. The shaded region indicates when $c_2 > 0.1R_0$.

important. However, in our experiments the amplitude of the free oscillations is small, and the weak decay of the half droplet height B and c_n in Figure 12 and 13 respectively shows that there is little dissipation during the flight. Thus, we aim to quantify the dissipation during the bounce, which potentially includes internal dissipation in the fluid motion, but also viscous dissipation in the squeezed air layer. First, we consider the internal dissipation during the flight and the bounce.

Figure 14 shows the energy diagrams during the first bounce. Panel (a) shows the CM energy as calculated with the expressions given in section 5.3.1. During the flight no coupling with the oscillatory motion exists, so the conversion from gravitational to kinetic

energy is complete and the total CM energy is constant, $0.115 \cdot 10^{-6}$ J, with a very small scatter because of the inaccuracy in the position determination of the CM. During the bounce the total CM energy is buffered into internal energy as shown in panel (b) and gets partially restored again as the droplet is strongly de- and accelerated. In the subsequent flight phase the CM energy is again constant but has decreased to $0.082 \cdot 10^{-6}$ J.

The data in panel (b) are obtained from the analysis given in section 5.3.1. The kinetic energy and dissipation in the potential flow description are only valid in the small amplitude approximation. Since we can calculate the potential energy exactly with Equation (6) and in the linear approximation with Equation (7), we use the relative difference between both values as an estimate of the accuracy of the approximation. Figure 14(b) shows the result: the linear approximation significantly overestimates the potential energy during the bounce phase where also $c_2 > 0.1R_0$**.** The maximum deviation in the potential energy is 20% for the first bounce, but decreases to only 2% for the last bounce, showing that the approximation significantly improves during the bouncing series.

Figure 14(b) shows that during the bounce the potential energy increases and next decreases while the droplet deforms laterally. The kinetic energy in the flow field has two maxima, one before and one after the maximum deformation of the droplet, and is almost zero when the flow reverses. In the transition to the subsequent flight phase the internal energy does not reduce completely to zero: the droplet oscillates, continuously converting kinetic and potential energy. The internal energy at the start of the flight phase is $0.57 \cdot 10^{-8}$ J and slowly decreases in time. This is due to internal dissipation in the flow field as indicated by the pink line which is calculated by integrating Equation (13).

Finally panel (c) of Figure 14 shows the total CM energy E_{CM} (blue) and internal energy E_{int} (red), as well as the sum of the two, E_{tot} (black) for the first bounce. Also the internal dissipation (pink) has been shown again. In the shaded region the values of the kinetic internal energy and dissipation rate are quantitative less reliable leading to unphysical undulations in the total energy. Still, we can draw some clear conclusions. During the flight phase no coupling exists between the CM and the internal energy as expected. The slight decrease of internal energy in this phase is fully attributed to viscous dissipation in the droplet, as the slopes of both lines are exactly opposite. The internal dissipation rate during the bounce is much more pronounced, but still does not fully account for the energy loss (only $<$ 30% for the first bounce). This suggests that a considerable part is dissipated in the air film.

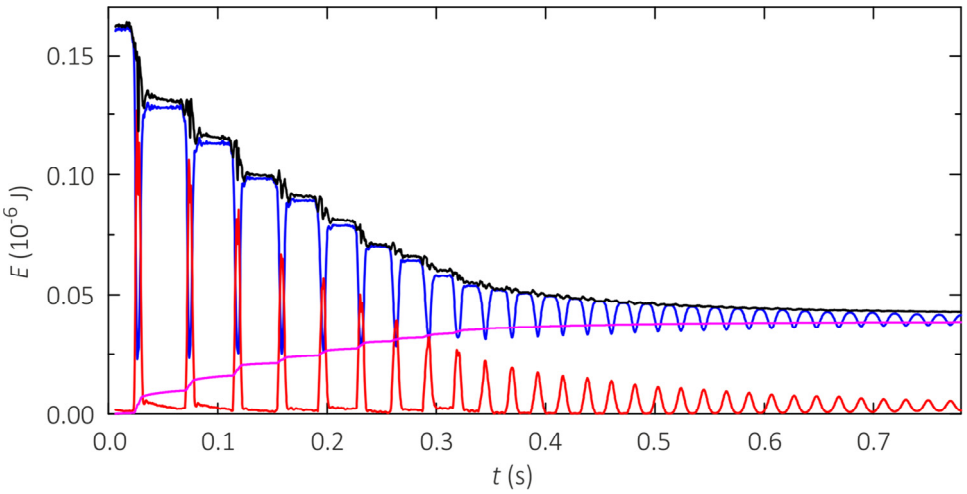

Figure 15. Energy conversion (center of mass vs. internal) and dissipation for the full series of Figure 7. Blue: the center of mass energy, red: the internal energy, and black: the total energy. Pink: the internal energy loss.

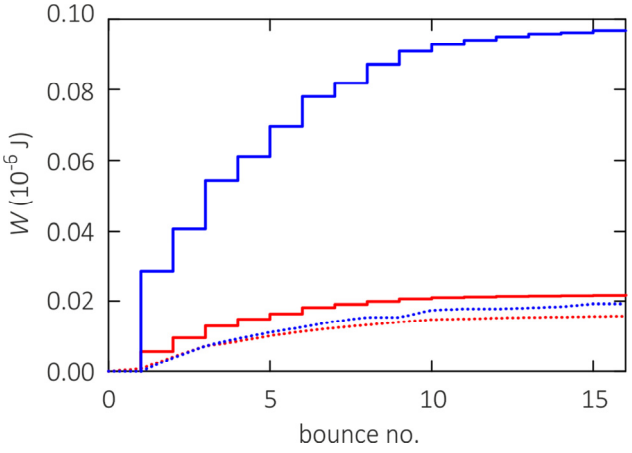

Figure 16. Cumulative energy loss and internal dissipation during the bouncing series shown in Figure 7. Both the energy loss (blue) and the calculated internal (drop) dissipation (red) are plotted as function of the bounce number, separated to their contributions during the flight (dotted) and bounce (solid).

Figure 15 shows the decrease of the total energy together with the internal dissipation during the whole series. During each bounce, CM energy gets (temporarily) converted into internal energy. At the end of the bounce only a small amount of internal energy is stored

in free oscillations while the CM energy has decreased by a significantly larger amount. In absence of an accurate quantitative description of the internal (kinetic) energy, only the total dissipation over the full bounce can be determined (as measured by the step decrease between the subsequent 'plateaus'). To get a clear picture of the energy loss and dissipation during the separate phases of bounce and flight, we plot both cumulatively as a function of bounce number in Figure 16. (The hover stage - with negligible energy loss - has been neglected here.) During the flight phase (dotted lines) energy loss and internal viscous dissipation agree rather well. Yet, the amount of energy dissipated during the flight phase amounts to less than 20% of the dissipated energy during the bouncing events (solid blue line). Most of the energy is thus dissipated during the short 'contact' time between the drop and the lubricating air film on the substrate.

The solid red line denotes the cumulative viscous dissipation within the drop through all the bounces based on the linear approximation, Equation (13). While very successful during the flight phase (dotted lines), the model dramatically underestimates the dissipation during the contact phase. Inaccuracies of the linear approximation during the bouncing, as suggested by the reductions in $R_0 + c_0$ in Figure 13, are expected to cause some deviations, yet, the amount of disagreement shown in Figure 16 suggests that a completely different additional dissipation channel may be needed. In the follow section, we therefore analyze in more detail the role of the air film in providing the force required to reverse the momentum of the drop and the dissipation with this thin film.

5.4.3. Air film dynamics during bouncing

5.4.3.2. Interface shape

The interaction of the droplet with the squeezed air layer during the bounce can be analyzed from the height profiles as obtained from the interferometry images, taken in the bottom view. As an example, Figure 17 shows the evolution of the air film for the first impact of a bouncing series: an $R = 1.01$ mm water droplet with a velocity of 0.22 m/s leading to $We = 0.75$. The evolution of the film shape is depicted in the contour plot in panel (a) and the height profiles are plotted in two separate figures: panel (b1) shows the spreading of the confined film up to the maximum lateral extension, while panel (b2) shows the contraction phase. The spreading phase has been described intensively in Chapter 4. The transient layer has a typical height of 1 μm while the lateral extension is typically 1 mm, giving a $\mathcal{O}(10^{-3})$ h/r aspect ratio. Again the two-kink scenario is observed, although the first kink is almost suppressed. In particular, the upper We limit for the two-kink scenario described in Chapter 4 also sets the limit for the bouncing phenomenon. The

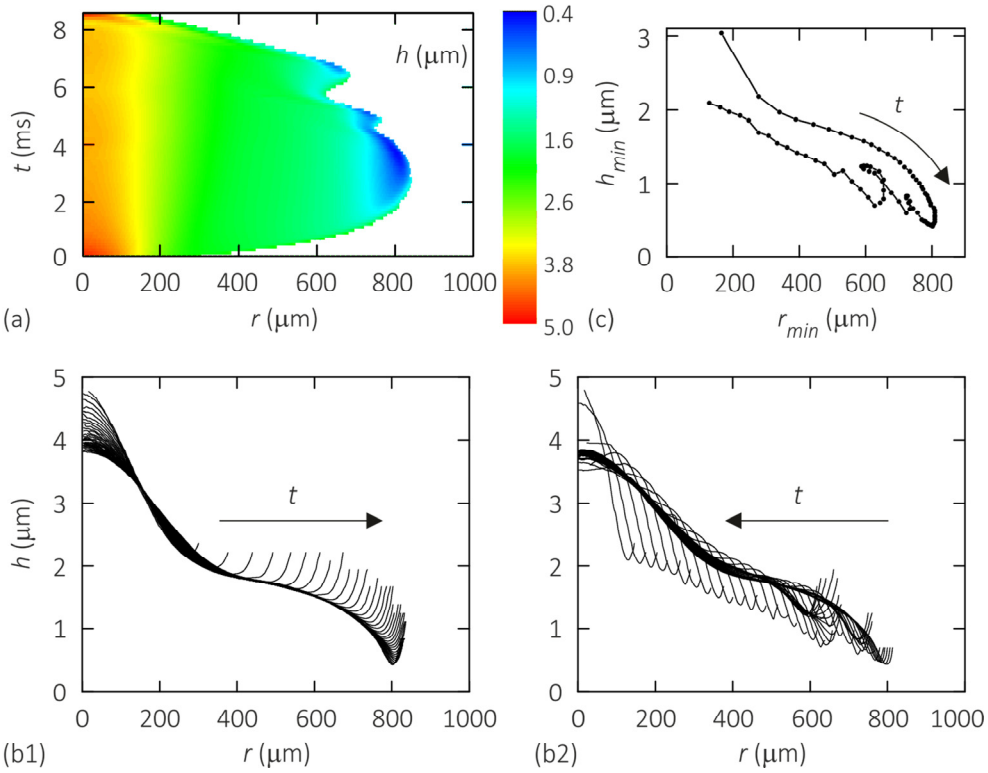

Figure 17. Time evolution of the squeezed air film during the first bounce phase for an $R_0 =$ 1.01 mm water droplet impacting with an initial velocity of 0.22 m/s, see Figure 19. (a) Contour plot of the film height as function of radial position and time. The corresponding interface profiles are shown with $\Delta t = 0.1$ ms for (b1) the spreading stage up to 3.6 ms, and (b2) the contraction stage up to 8.6 ms. (c) Time evolution of the outer kink position, clearly showing the curling motion twice.

first kink reaches an equilibrium height above the substrate when it is regularized by surface tension [26]. When is this equilibrium film thickness sufficient to sustain the non-wetting situation - and allow the development of a second kink? It was demonstrated that the film breaks when its thickness decreases below ~ 200 nm, which gives an estimate for the critical Weber number. The equilibrium thickness can be expressed as $h_c = 5R\,Oh_g^{8/9}We^{-10/9}$ where $Oh_g = \mu_g(\sigma\rho R_0)^{-1/2}$ is the ratio between gas viscosity and surface tension (~ 10^{-4} for mm-sized water droplets). Hence, the film is expected to collapse when $We \gtrsim$ 4-6, in good agreement with our experimental observations. In that case, liquid-solid contact is formed within tens of microseconds after the first pressure-

induced deformation of the droplet interface. For smaller We numbers a second kink can develop, and reaches a minimal height above the substrate that is large enough for the air film to remain stable, i.e. 420 nm in Figure 17.

Subsequently, the squeezed air film starts contracting. One immediately observes that the profile of the air film during spreading and contraction of the drop is completely different. During the spreading phase the interface unfolds more and more outward, while the inner region remains almost unchanged, Figure 17(b1). The initial stagnation point in the center of the droplet interface expands into a larger and larger region, and the interface moves almost vertical outside this stagnation region. In contrast, during the contraction phase shown in Figure 17(b2), the kink moves towards the center of the drop while the minimum thickness gradually increases after some initial wiggles (Figure 17(c)) that are presumably caused by the higher modes that are excited during the contact phase (*cf.* Figure 13). Note, that the air film thickness inside the kink still decreases while it increases outside the kink as the drop 'peels off' the substrate. This pronounced asymmetry between the spreading and the receding phase shown in Figure 17(b) turns out to be crucial for the understanding of the bouncing process, as we will see in the next section.

For the following bounces the overall behavior is very similar: the confined air film spreads and contracts while developing several kinks. However, the number thereof does vary without showing a trend with the bouncing sequence, see Chapter 4. To compare the complex dimple shapes they are described by a few characteristic parameters, *e.g.* 'contact' radius r_{sq}, volume of the air film V_{sq}, average height of the film $\overline{h}$ and the minimum film thickness h_{min} which determines whether the squeezed air layer is stable against formation of liquid-solid contact. Figure 18 shows the time evolution of these parameters, which were calculated as discussed in section 5.3.2. For each bounce all quantities peak at approximately the same instant. The average height shows a similar trend as the minimum film thickness, but smoothened. For successive bounces, the maximum radius decreases from ~ 0.8 mm in the first bounce to ~ 0.4 mm in the hover stage. This corresponds in a continuous decrease of trapped air volume from typically 3 to 0.2 nL. Empirically, we find $\tilde{V}_{sq} \sim We^{0.83} \sim St^{-1.65}$ as shown in Figure 19(c) which is a slightly stronger dependence than theoretically predicted for the large St regime where capillarity smoothens the dimple ($\tilde{V}_{sq} \sim St^{-1}$) [27]. Although the minimum film height during the bounce does not show a decreasing trend, on average the droplet interface does approach the substrate closer and closer with each bounce.

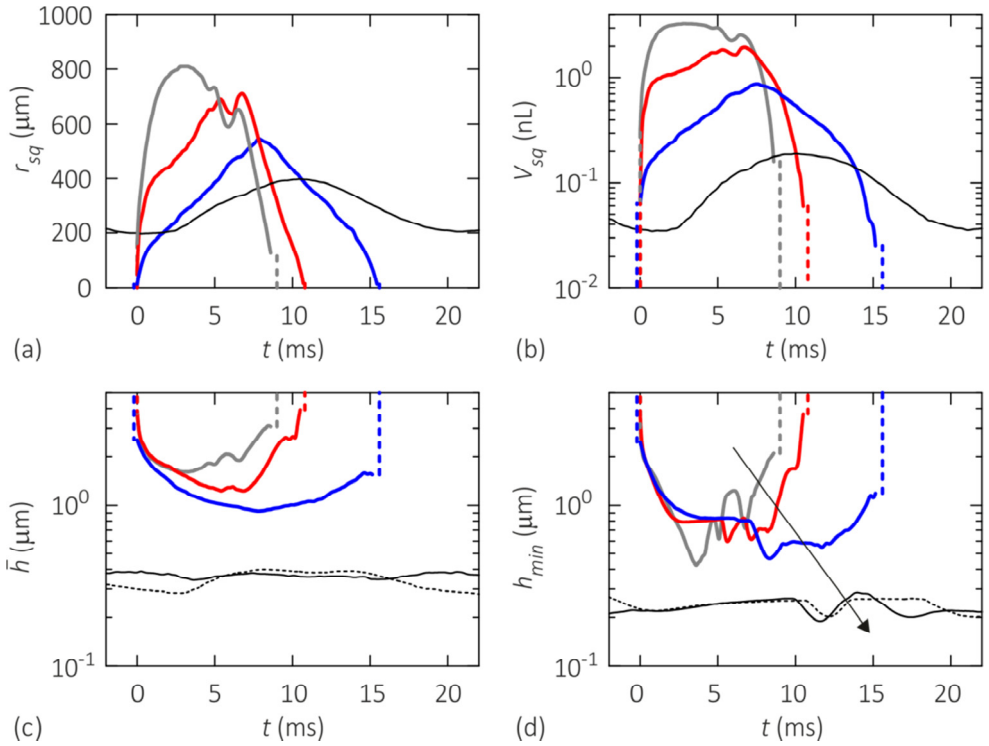

Figure 18. Time evolution for successive bounces of (a) 'contact' radius, (b) volume, (c) average and (d) minimum film thickness. three bounces are shown of the experiment from Figure 19: $We = 0.76$, 0.26, 0.05 (bounce no. 1: grey, 5: red, 12: blue) and one hover oscillation: $We = 0.007$ (no. 10: solid (dashed) black for trailing (leading) dimple side).

Figure 18(d) shows the minimum film thickness for a few selected bounces. For each bounce the film thickness diverges at $t = 0$ and at the end of the bounce; outside this interval the droplet is not interacting with the substrate. In contrast during the hover stage each oscillation continuously passes into the next one as the droplet interface is permanently deformed. For each bounce the minimum film thickness shows several oscillations in time, indicating that the kink comes down repeatedly or new kinks are formed. For the absolute stability we are only interested in the minimum value that is obtained during each bounce. The corresponding dimple profiles that approach the substrate most closely during each bounce, are shown in Figure 19(a). No clear trend is observed in the minimum film thickness during the bouncing stage, which is confirmed for all subsequent bounces in Figure 19(c): it varies between 300 and 900 nm depending on

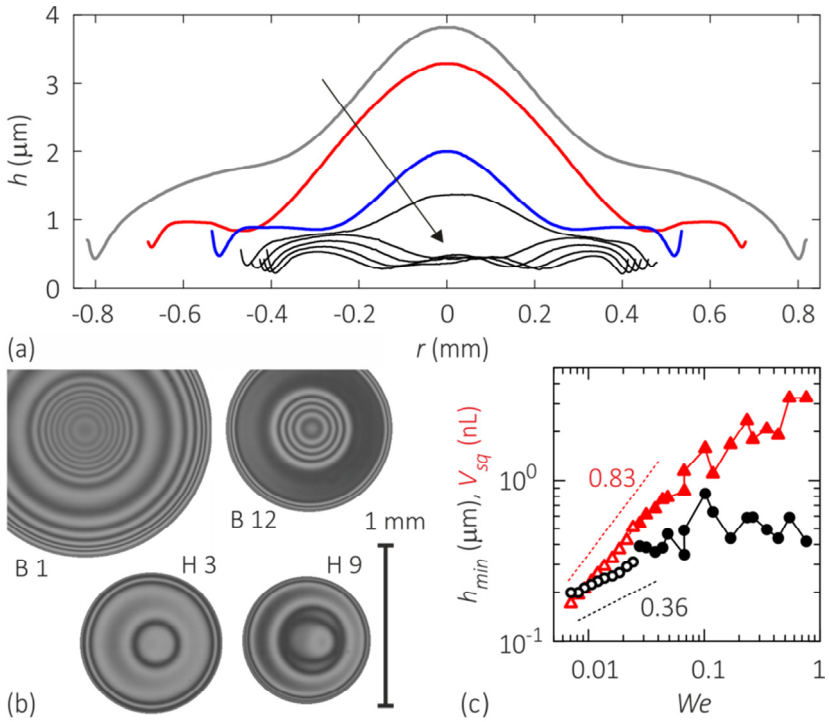

Figure 19. Interference signals and shape of the air film at minimum thickness for successive bounces. (a) The same bounces as in Figure 18 are shown, as well as hover oscillations no. 1, 3, 5, 7, and 9 ($We = 0.02$ … 0.008). (b) Snapshots of the film at maximum lateral extension. (c) Absolute minimum of the film thickness (black circles) with accompanying dimple volume (red triangles) for all bounces and hover oscillations (closed and open symbols respectively).

the details of the squeeze out. This is larger than 200 nm and thus the film is thick enough to prevent solid-liquid contact.

The dynamics in the hover stage is different. With decreasing We the influence of surface tension becomes more and more prominent and the droplet interface shows smaller fluctuations, see Figures 18(d) and 19(a). In fact the vertical impulse on the droplet is too low to replenish the air film and the center of the dimple suddenly collapses to a height of, here, approximately 500 nm. From here on the center of the dimple is more or less stationary and the droplet hovers on a micrometric layer. The outer kink gradually approaches the substrate more closely with each oscillation until the critical film height of $\sim$ 200 nm is reached and liquid-solid contact is established. Figure 19(c) shows clearly this transition between the bouncing and the hover phase: the minimum film thickness now

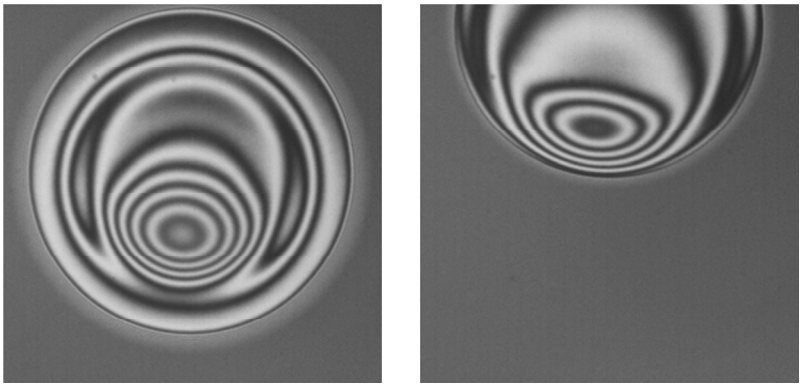

Figure 20. Asymmetry of the squeezed air layer during the hover phase. The snapshots shows the eighth and fourteenth (last) hover oscillation of an $R_0 = 1.04$ mm 90% wt. propanol droplet with initial velocity 0.22 m/s. The droplet moves laterally towards the upper side of the field of view.

shows a clear trend with We; empirically we find $\tilde{h}_{min} \sim We^{0.36} \sim St^{-0.72}$. The squeeze out of air in the hover stage sets the lower We limit $\mathcal{O}(10^{-3})$ for bouncing; and it shows a very slow dynamics compared to the fast formation of solid-liquid contact at $We \gg 1$. The slowing down of the film dynamics has another effect that can be observed in Figure 19(b) and more pronounced in Figure 20: the squeezed air layer loses its radial symmetry. The slight lateral velocity of the droplet of about 3 mm/s (caused by a small but unavoidable substrate tilt) becomes significant with respect to the near-zero vertical velocity of the droplet interface. As a result we observe that the interface always tilts backward as in a fluid-dynamic bearing: the dimple "center" moves towards the trailing edge of the supporting film where also the lower film thickness is obtained. Thus solid-liquid contact is preferentially formed at the trailing edge of the squeezed film. The effect greatly increases for propanol droplets that have a lower surface tension and thus deform more easily, see Figure 20.

5.4.3.3. Dissipation and momentum transfer

To understand the bouncing process, we need to understand the momentum transfer and the energy dissipation due to the air film during each bounce. The contribution of the air to the dissipation intuitively may seem small as the viscosity of the air is two orders of magnitude smaller than that of water. However, the shear rate diverges if the height of the air gap is small and yet decreases sufficiently fast; this would lead to significant viscous dissipation in the air. Indeed we find significant less bounces than the maximum of 1000

that can be obtained in a Leidenfrost situation where the air film is about 100 μm thick [3]. This suggest that air film dissipation should be considered.

As a first approach we notice that the squeezed air film has an extreme r/h aspect ratio, thus we assume a completely flat disk with radius $r_{dimple}(t)$ and radially invariant height. The height is chosen as shown in Figure 4(c): $h_{min}(t)$ gives an upper limit to the dissipation that diverges at low film height, *i.e.* at the kink, Equation (19), while $\bar{h}(t)$ provides a lower limit. The dissipation is obtained *via* Equation (19); the force and impulse follow from Equation (21). The flat disk approximation fails as the force on the droplet per definition becomes attractive as soon as it starts lifting off and air flows radially inward. From the CM motion in Figure 8 we know that this is not a physical solution; within the resolution of the side-view the force remains repulsive at all times. Using the flat disk approximation the attractive force can only be minimized (leading to a positive impulse on the droplet) if the 'contact' area is negligible during the contraction phase, which is experimentally not the case. As the interaction force is repulsive at all times, the interface should always exhibit a downward motion - at least locally.

We will show that an effective momentum transfer indeed originates from the fact that *the air film is not flat*! The details of the kink motion as described in Figure 17 are in fact critical to capture the physics of the air cushioning correctly. Figure 21 shows a sketch of the interface evolution; it is generic for all our experiments as shown in *e.g.* Figure 17. We see that *the net air flow can be continuously directed outward, thus providing a positive force at all times*. During the spreading phase in panel (a) the interface unfolds more and more outward, while the inner region remains almost unchanged (except from the decreasing center that corresponds to a negligible volume of air). Thus the air trapped within the kink is stationary (see blue shaded region), while around the kink the air flow is radially outward as the interface comes down (see red arrow). There is only one contribution to the flow field, which is radially outward, Δp is positive everywhere, and the squeeze force is repulsive, *cf.* the force peak in Figure 8. For symmetry reason, if the air film would contract in the same way the squeeze force would be attractive during the subsequent contraction. However, panel (b) shows that the outer kink rather starts moving inward instead of up, as shown in Figure 17. Now, we have two contributions to the flow field: outside the kink the interface moves back up, thus the flow is radially inward, and Δp is negative. In addition the region inside the kink is shrinking, still leading to an effectively downward motion of the interface and thus leading to a radially outward flow. This mechanism does allow for a net repulsive force; but is this also likely? A rough estimation shows that the kink is locally symmetric and moves horizontally. Thus we

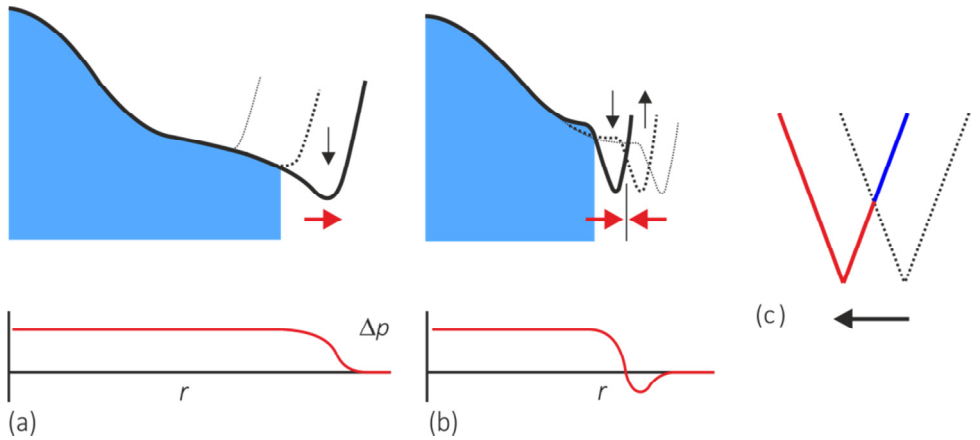

Figure 21. Sketch of the asymmetry in the spreading and contraction of the squeezed air layer: (a) spreading phase, and (b) contraction phase with zoom on the kink shown in (c). The red arrows indicate the direction of the air flow, while the blue shaded region indicates a stationary region. The corresponding pressure profile is shown below. In (c), red and blue indicate the region where the interface height decreases and increases, respectively.

sketch a zoom of the kink in Figure 21(c) and observe that the layer thickness $h(r,t)$ is on average smaller for the region where the interface comes down. As the force scales with $h(r,t)^{-3}$ we expect a net repulsive result, *cf.* the second force peak in Figure 8.

To calculate the force and dissipation we should thus use the full shape information that we obtain from the bottom view, *e.g.* Figure 17(b) and (c). Unfortunately, we miss crucial shape information outside the kink due to the steepness of the interface compared to the lateral resolution of the recording. Thus, the squeeze force (impulse) cannot be determined as it relies on the unknown reference pressure just outside the measurable region. Yet, we are able to determine the local dissipation in the measurable region up to R_{max}. First, we determine the local average velocity $\bar{v}$, which is shown in Appendix 5.5. Local outward velocities up to ~ 100 mm/s are obtained, in particular near the outer kink during both the spreading and contraction phase. Local inward velocities are observed as well in the inner region, but their maximum is at least an order of magnitude smaller. This allows a net outward directed flow. The local dissipation rate $\dot{w}_p$ (J/s), *i.e.* Equation (19), is shown in a contour plot *vs.* radial position and time in Figure 22. For several bounces the absolute values of the total dissipation and the percentage of the CM energy loss is shown in Table 2. As expected the total squeeze dissipation increases with increasing We;

Aqueous solution	Fig. 22	We (-)	W_p (lower estimate) ($\cdot 10^{-9}$J)	(%)
water	(a)	3.79	33.5	10
	(b)	0.76	1.0	3
		0.26	0.65	7
		0.05	0.35	27
		0.02	0.40	75
	(c)	0.007	0.06	$\sim$ 100
90% wt. propanol	(d)	1.48	1.2	8
85% wt. glycerol		0.84	3.4	1

Table 2. Squeeze dissipation in various bounces: total dissipation in confined region, and percentage of CM energy loss.

however, the percentages vary widely. We attribute this to two factors; the first is a real effect, while the second is due to experimental limitations. First, the percentage of squeeze dissipation is expected to increase with decreasing We as the internal dissipation strongly decreases. Indeed, in the last bounces and the hover phase the droplet oscillation is negligible and we attribute 75-100% of the total energy loss to squeeze dissipation. For a glycerol droplet the percentage of squeeze dissipation is low compared to a water droplet of similar We. This is due to the high internal dissipation, though the absolute value is high due to the small air film thickness obtained during the bounce. This is caused by the 'stiffer' droplet shape on short time scales due to the higher droplet viscosity.

The second important factor is the restricted measurable region. In all cases, a large dissipation is observed locally around the kink clearly shown in Figure 22. We fit a parabola to the kink in the interface profile and extend it to the region that we cannot observe with RIM. Although a very rough approach it shows that the region of locally high dissipation extends to just outside the kink, and then decreases radially (not shown here). This is expected as the vertical interface velocity $\dot{h}$ is very small in the region inside the kink, but outside the kink the interface is still continuing its motion. Thus, the percentages

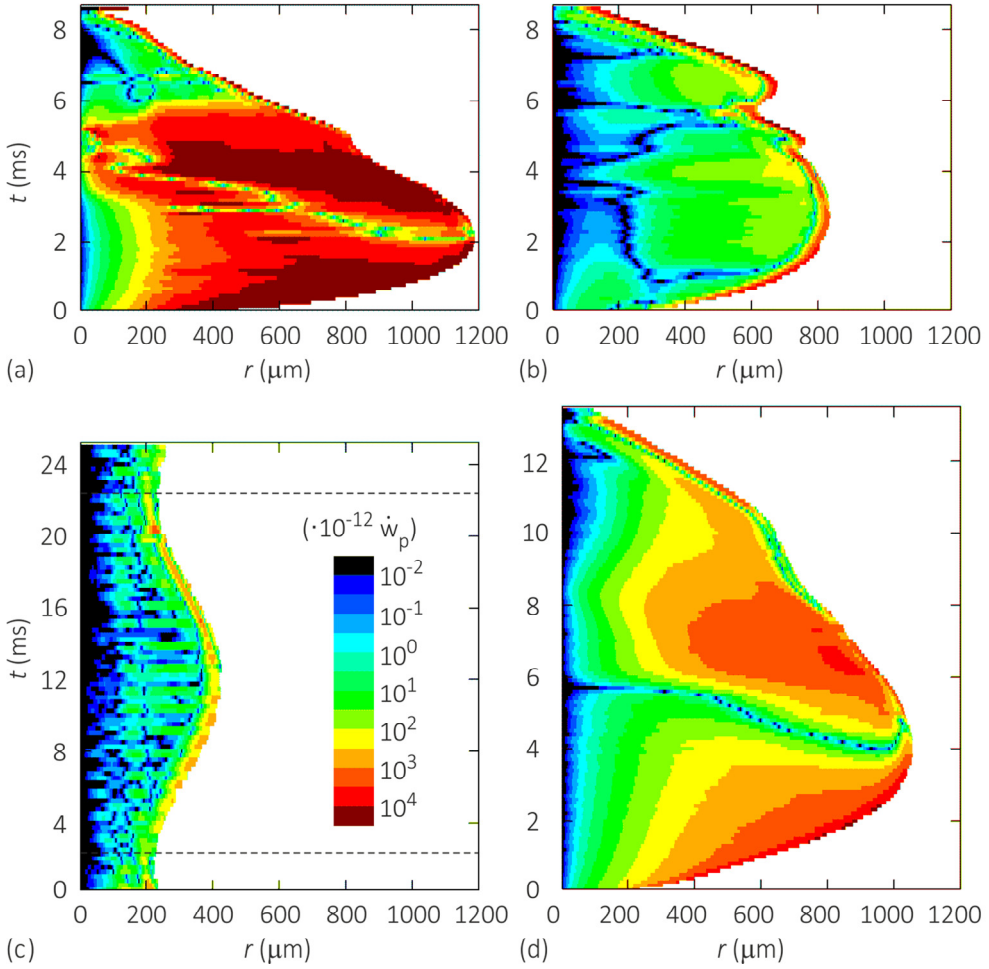

Figure 22. Local dissipation rate in the air film. The local dissipation rate $\dot{w}_p$ (J/s) is plotted versus radial position and time for (a, b, c) the impact of an $R_0 = 1.03$ mm droplet with $We = 3.79$, 0.76, 0.007, and (d) the impact of an $R_0 = 1.04$ mm 90% wt. propanol droplet with $We = 1.48$. The color scale is logarithmic. The time axis in panel (c) is compressed by a factor 2.

shown in Table 2 are lower limits. The underestimation is largest for bounces where dissipation in the center of the air film is low, and the slope outside the kink is steep, *i.e.* for intermediate We as in Figure 22(b). Based on the outer We limits we estimate that several tens of percent of the energy loss can be attributed to squeeze dissipation for $We \sim 1$ impacts.

5.4.4. A single oscillation mode model

To explain the mechanism of bouncing on a purely dissipative squeeze force we model an impacting droplet as a deformable cylindrical pill box The droplet has with radius a and height $2b$. The minimal energy surface then demands $a = b = R_c$ where $2\pi R_c^3 = V$ is the volume of the droplet. The mass is given by $M = 2\pi R_c^3 \rho$, and the relative height by $\beta = b/R_c$, see Figure 23(a). The flow field within the drop is given by $\dot{z} = \dot{\varepsilon} z$ and $\dot{r} = -\frac{1}{2}\dot{\varepsilon} r$, where $\dot{\varepsilon} = \dot{b}/b$, $0 \le r \le a = \sqrt{R_c^3/b}$ and $-b \le z \le b$. For a bouncing drop we find the following expressions for the kinetic energy K, the potential energy U, and the dissipation rate $\dot{W}$, in terms of the vertical droplet length $2b$ and the height z of the center of mass (CM):

$$K = \frac{1}{2}M\dot{b}^2\left(\frac{1}{3}+\frac{1}{8}\beta^{-3}\right) + \frac{1}{2}M\dot{z}^2 \quad (22)$$

$$U = 2\pi\sigma R_c^2\left(\beta^{-1}+2\beta^{1/2}-3\right) + Mgz \quad (23)$$

$$\dot{W} = -6\pi\mu R_c \dot{b}^2\beta^{-2} + \left(\dot{z}-\dot{b}\right)\, F_{sq}\left(b,\dot{b},z,\dot{z}\right) \quad (24)$$

where the first terms on the right-hand sides denote the internal contribution of the droplet oscillation (see Appendix 5.3). The internal kinetic energy and dissipation are calculated from the internal extensional flow, while the internal potential energy is just the interfacial energy due to the deformation of the pill box droplet. The second energy term denotes the contribution of the CM motion, while the second dissipation term denotes the rate of work done on the droplet by the squeeze force $\dot{h}F_{sq}$ where $h = z - b$ is the air film thickness.

In our pill box model the bottom of the droplet is a flat disk, thus the squeeze force F_{sq} is given by:

$$F_{sq}\left(b,\dot{b},z,\dot{z}\right) = -\frac{3}{2}\pi\mu a_{sq}^4(b)\frac{\dot{z}-\dot{b}}{(z-b)^3} \quad (25)$$

Where the radius of the squeezed layer $a_{sq}(b)$ in principle is given by the radius $a(b) = \sqrt{R_c^3/b}$ of the pill box. The flat interface assures that the pressure increases rapidly enough to sustain a micrometer-thick air layer, in contrast to a spheroid droplet where $\Delta p \sim h^{-1}$ only. This simple flat disk shape has obviously its limitations in capturing the exact mechanism of momentum transfer: we demonstrated experimentally that the asymmetric down- and inward motion of the kink is critical to sustain a repulsive force.

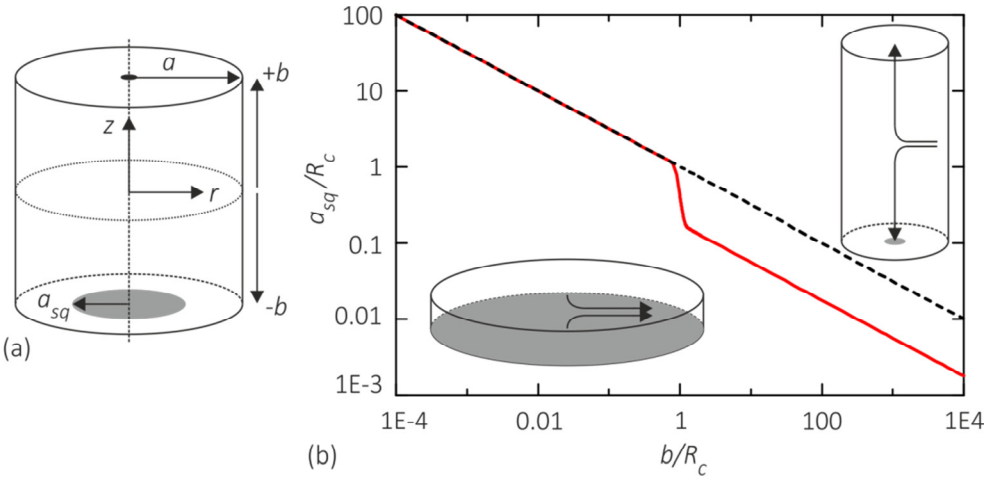

Figure 23. Properties of the "pill box" droplet with height $2b$ and radius a. (a) Sketch of the equilibrium droplet with the radius of the squeezed layer a_{sq} shaded in grey. (b) a (black dashed) and a_{sq} according to Equation (26) (red solid) versus b. Insets: compressed and elongated droplet.

However, in the model the asymmetry will be induced *via* an asymmetry of the 'contact' radius during approach and take-off. A completely symmetric bounce would lead to a zero momentum transfer; bouncing can only be achieved if the 'contact' area is on average larger during the approach phase. That is, there should be a phase difference between the start of the droplet contraction (first) and the return of the bottom droplet interface (second) to obtain an asymmetry in the squeeze force [9]. The attractive forces in the take-off stage are thus minimized rather than eliminated. Under the proper starting conditions this is indeed achieved, but we implemented an additional asymmetry to improve the agreement with the experiments: $a_{sq}(b) = f(b/R_c)\sqrt{R_c^3/b}$ where

$$f(\beta) = \left\{\epsilon + \frac{1-\epsilon}{1+c\,\beta^{25}}\right\}^{1/4} \tag{26}$$

where $\epsilon = 0.001$ and $c = 32.38$. Although an awkward expression at first glance it guarantees a more realistic 'contact' area in the initial approach and also in the last phase of the bounce when the drop elongates in vertical direction, see Figure 23(b).

As long as the drop makes no direct contact to the substrate, the squeeze force is, besides gravity, the only external force acting on the droplet. Hence, the momentum equation reads:

$$F_{sq} = M(\ddot{z} + g) \tag{27}$$

Because $\partial_t(K + U) = \dot{W}$ we obtain a second differential equation which together with Equation (27) describes the behavior of both the CM height z and the deformation of the droplet in terms of b, see Appendix 5.3 for details:

$$\alpha M\ddot{b} = -F_{sq} - 6\pi\mu R_c\dot{b} - 3\pi\sigma R_c\,\frac{2}{3}\left(\beta^{-1/2} - \beta^{-2}\right) \tag{28}$$

where $\alpha \approx \frac{11}{24} = 0.46$. In free flight when $F_{sq} = 0$, and for small deviations of β from unity, Equation (28) reduces to a damped harmonic oscillator equation, see Appendix 5.3. The resonance frequency is given by $\omega_{ff} = (3\pi\sigma/\alpha M)^{1/2}$ and the quality factor $Q = (3\pi\sigma\alpha M)^{1/2}/6\pi\mu R_c$. In the hovering state when $z = b$, it again reduces to a damped harmonic oscillator equation, now with $\omega_{ho} = (3\pi\sigma/(1+\alpha)M)^{1/2}$ and $Q = (3\pi\sigma(1+\alpha)M)^{1/2}/6\pi\mu R_c$. So the ratio between the oscillation frequencies in the flight and hovering phase is equal to $\omega_{ff}/\omega_{ho} = \sqrt{1/\alpha + 1} = 1.8$ which is in reasonable agreement with the observed ratio $T_{ho}/T_{ff} = 2.3$ (*cf.* Figure 13). Based on this ratio we should estimate $\alpha = 0.23$ instead of $\alpha = 0.46$.

The momentum equation (27) and the equation of motion (28) can be written in dimensionless form where the dimensionless heights Z, H, B are obtained by scaling with R_c and the time τ by scaling with $t_0 = \sqrt{R_c/g}$:

$$\ddot{Z} = -\lambda_A\frac{\dot{H}}{B^2H^3} - 1 \qquad \text{and} \qquad \alpha\ddot{B} = \lambda_A\frac{\dot{H}}{B^2H^3} - \lambda\dot{B} - \kappa\frac{2}{3}\left(B^{-1/2} - B^{-2}\right)$$

which depend on the four parameters α, κ, λ and λ_A. Here, $\kappa = 3\sigma/(2\rho g R_c^2) = 3/(2Bo_c)$ represents the stiffness of the liquid spring, $\lambda = (3\mu/\rho)(gR_c^3)^{-1/2}$ the damping coefficient in the droplet and $\lambda_A = (3\mu_{air}/4\rho)(gR_c^3)^{-1/2} = 1.58{\cdot}10^{-4}$ the damping coefficient in the air.

To get a better agreement with the experiments, the parameters α, κ and λ are optimized as follows. The restitution of the bounce is largely determined by the effective mass in vibration; α is adapted using the effective mass in the potential flow assumption: $\alpha = 3/(2n^2 + n)$. We choose $n = 3$, *i.e.* the lowest mode resulting in a flattened

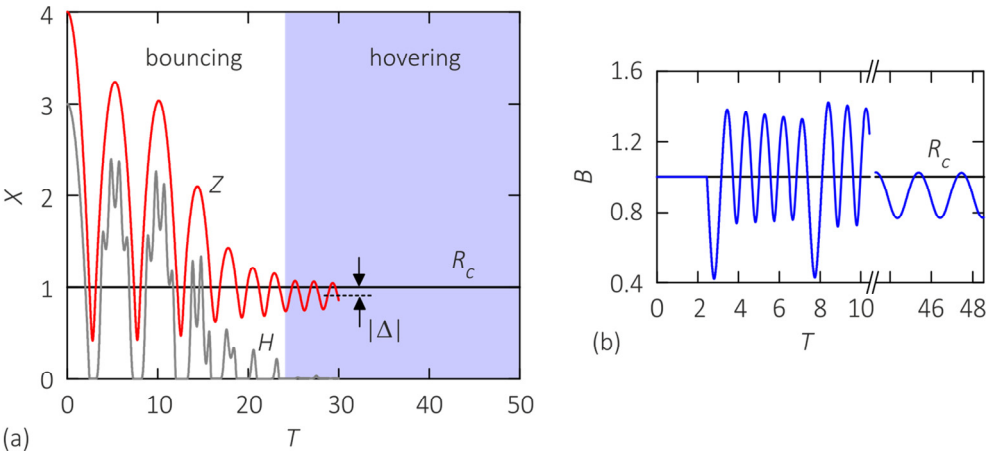

Figure 24. Calculated bouncing series for a pill box droplet. (a) Time evolution of CM height Z (red) and air layer thickness H (grey). The bouncing series can be subdivided into a bouncing phase and a hovering phase (shaded blue) that shows an equilibrium sag $|\Delta|$. This particular simulation extends to only $T = 30$, but more hover oscillations can be obtained afterwards. (b) Half droplet height B. The first two bounces are shown, as well as a few hover oscillations with equilibrated gravitational sag. The time axis has been scaled on $t_0 = 10.2$ ms and corresponds to that of Figure 7 and 12.

interface, leading to $\alpha = 1/7$. Both σ and μ are optimized to obtain the observed resonance frequency and quality factor. This yields estimations for λ and κ, *i.e.* $\lambda = \alpha(\omega_0 t_0)/Q$ and $\kappa = \alpha(\omega_0 t_0)^2$. Experimentally we measure the oscillation and damping times of the second mode and find that $\omega_0 t_0 = 6.61$ and $Q = 97$. This leads to $\lambda = 1.01{\cdot}10^{-2}$ and $\kappa = 6.24$.

5.4.4.1. Modeling results

We have solved Equations (27) and (28) for z and b numerically, while we scaled the distances on the droplet radius R_c ($B = b/R_c$, $Z = z/R_c$, while $H = Z - B$) and the time on $t_0 = (R_c/g)^{1/2} \approx 10.2$ ms for a millimeter sized droplet ($T = t/t_0$). The result for an initial height $z_0/R_c = 4$ is given in Figure 24(a). The calculations show six bounces before the droplet starts hovering (the hover phase extends infinitely as wetting is not implemented). However, as we can observe from Figure 24(b), the oscillation amplitude during the flight phases is considerably larger than observed in the experiments, while in the hovering phase the amplitude is more realistic.

.

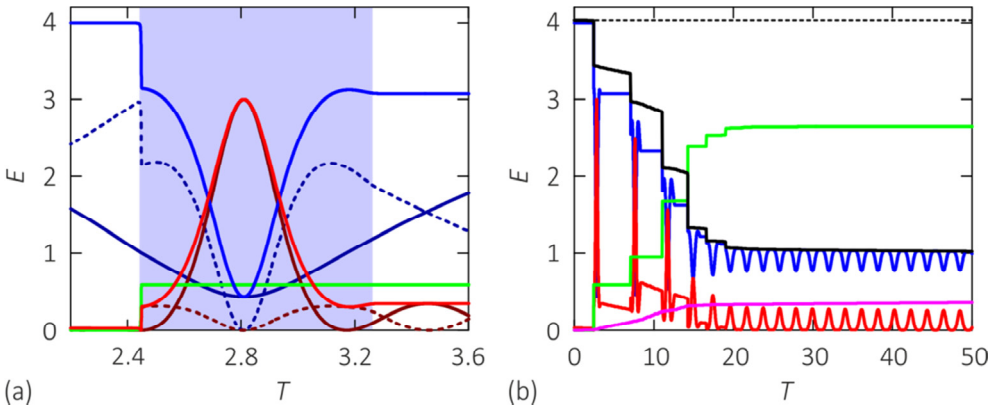

Figure 25. Energy during the calculated bouncing series: (a) details of the first bounce (blue shaded region), and (b) full series. The different colors indicate (blue) CM energy and (red) internal energy: (dark dashed) kinetic, (dark solid) potential, and (light) total energy. Further: (black) total energy, (green) squeeze dissipation, and (pink) internal dissipation.

5.4.4.2. Energy and dissipation

Also for the calculated bouncing we have investigated the energy transfer from the CM to internal and backwards. The results are given in Figure 25; panel (b) shows the whole bouncing series. Similar to the experiments, the total droplet energy (black) shows a step decrease during each contact phase, and a gradual decrease during each flight. Here, the internal energy dissipation (pink) is fully localized during the flight due to the large free oscillations, and amounts to 12% of the total energy loss. The 88% energy loss during contact is fully attributed to squeeze dissipation (green). The details of the first bounce in Figure 25(a) show that this squeeze dissipation is fully localized at the droplet approach.

5.4.4.3. Dynamics of the squeezed air layer

The sudden conversion and dissipation of kinetic CM energy (red dashed) at the approach is due to the diverging build-up of pressure and thus a repulsive force, see Figure 26 at $T \sim 2.4$ (black line), that is associated with the impact of a flat plate. The strong force decelerates the droplet interface that then keeps an almost constant height and the force suddenly drops preluding a gradual squeeze out phase. In the experiment the droplet interface flattens from the initial spherical shape during the approach, which smoothens the transition. Indeed in the experiments the dissipation is more gradual as shown in Figure 22, and the interaction force has a broader peak as shown in Figure 8. After the

maximum stretch of the pill box droplet at $T \sim 2.8$ the center of mass height Z increases before the air film height H does; this is the asymmetry needed to obtain a net upward

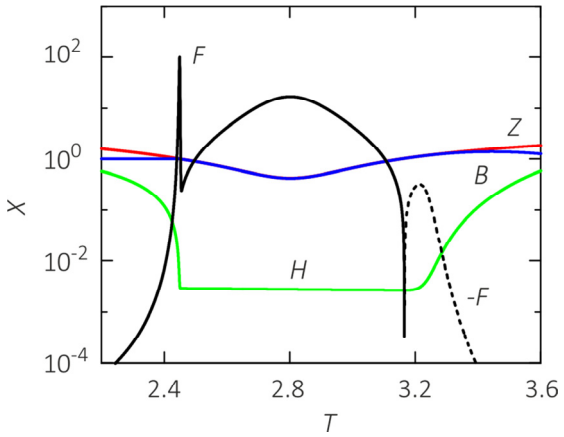

Figure 26. Zoom of the first bounce of the calculated series. Time evolution of the air film thickness H (green), center of mass height Z (red), half drop height B (blue) and squeeze force F (black). The squeeze force becomes attractive in the final stage and $-F$ is plotted instead (dashed).

impulse acting on the droplet: the droplet continuous to squeeze out air while the contact area is already reducing. When the interface reverses direction at $T \sim 3.2$ an attractive force (black dashed line) acts on the droplet, whose value depends on the asymmetry function for the 'contact' area, Equation (26). The residual attractive force causes the droplet to stretch out, converting CM energy to internal energy as indicated at $T \sim 3.2$ in Figure 25(a), thereby increasing the free oscillation amplitude. In the experiment a (negligible) attractive force is not expected until the final lift-off, thus the free oscillations are smaller and the restitution is higher.

5.5. Conclusions

We have demonstrated that millimeter-sized droplets are able to bounce multiple times on hydrophilic flat solid substrates. The independence of wettability suggests that a squeezed air film is present, which has been confirmed using reflection interferometry. This micrometer-thick air film provides a non-wetting situation in the regime $0.006 \lesssim We < 4$. Yet, we show that the air layer - and in particular its asymmetric spreading and

contraction - also plays a crucial role in the momentum transfer of the droplet, a role that was often overlooked or neglected in previous work. In the low Weber number regime investigated ($We \sim 1$) the local air film velocity reaches values up to order 100 mm/s thus the air film is incompressible, making the reaction force purely dissipative. Making the seemingly obvious assumption of a flat interface based on its extreme r/h aspect ratio leads to an attractive force when the interface moves back up. This problem was also encountered by Gilet *et al*. [9]. In a numerical model it can be solved by introducing an asymmetry of the contact area, yet the details of the interface evolution show a completely different asymmetry: namely in the motion of the outer kink entrapping the air film. The kink moves downward in the approach phase, but more inward instead of upward in the contraction phase, see Figure 17. This assures that the net movement of the interface is downward at all times as sketched in Figure 21, leading to a net outward air flow and an upwards force, also during retraction.

The corresponding dissipation in the air film is strongly localized around the kink region that we can only partially observe. However, for both low and high We a significant contribution is also located in the inner region, and we can attribute 10-100% of the total energy loss during the bounce to air film lubrication, which is in line with our estimate of the internal droplet dissipation during the bounce. In particular in the hover stage, where the amplitude of droplet oscillation and thus internal dissipation is extremely small, we indeed observe an almost 100% dissipation in the air film. Moreover, only 20% of the total energy loss is dissipated during the flight stage, yielding a significant contribution of air film dissipation to the overall bouncing dynamics.

References

[1] Y. Couder, E. Fort, C.H. Gautier and A. Boudaoud, From bouncing to floating: Noncoalescence of drops on a fluid bath, *Phys. Rev. Lett.* **94** (2005), 177801.

[2] A. Yarin, Drop impact dynamics: splashing, spreading, receding, bouncing…, *Annu. Rev. Fluid Mech.* **38** (2006), 159-192.

[3] A.-L. Biance, F. Chevy, C. Clanet, G. Lagubeau and D. Quéré, On the elasticity of an inertial liquid shock, *J. Fluid Mech.* **554** (2006), 47-66.

[4] D. Richard and D. Quere, Bouncing water drops, *Europhysics Letters* **50** (2000), 769-775.

[5] S. Chandra and C. Avedisian, On the collision of a droplet with a solid surface, *Proc. R. Soc. Lond. A* **432** (1991), 13-41.

[6] T. Tran, H.J.J. Staat, A. Prosperetti, C. Sun and D. Lohse, Drop impact on superheated surfaces, *Phys. Rev. Lett.* **108** (2012), 036101.

[7] C. Antonini, I. Bernagozzi, S. Jung, D. Poulikakos and M. Marengo, Water drops dancing on ice: how sublimation leads to drop rebound, *Phys. Rev. Lett.* **111** (2013), 014501.

[8] D. Terwagne, N. Vandewalle and S. Dorbolo, Lifetime of a bouncing droplet, *Phys. Rev. E* **76** (2007), 056311.

[9] T. Gilet, D. Terwagne, N. Vandewalle and S. Dorbolo, Dynamics of a bouncing droplet onto a vertically vibrated interface, *Phys. Rev. Lett.* **100** (2008), 167802.

[10] T. Gilet and J.W. Bush, The fluid trampoline: droplets bouncing on a soap film, *J. Fluid Mech.* **625** (2009), 167-203.

[11] J. Moláček and J.W. Bush, A quasi-static model of drop impact, *Phys. Fluids* **24** (2012), 127103.

[12] D. Terwagne, F. Ludewig, N. Vandewalle and S. Dorbolo, The role of the droplet deformations in the bouncing droplet dynamics, *Phys. Fluids* **25** (2013), 122101.

[13] D. Terwagne, T. Gilet, N. Vandewalle and S. Dorbolo, Metastable bouncing droplets, *Phys. Fluids* **21** (2009), 54103.

[14] R. Arayanarakool, L.L. Shui, A. Van Den Berg and J.C.T. Eijkel, A new method of UV-patternable hydrophobization of micro- and nanofluidic networks, *Lab on a Chip* **11** (2011), 4260-4266.

[15] K. Tsougeni, N. Vourdas, A. Tserepi, E. Gogolides and C. Cardinaud, Mechanisms of oxygen plasma nanotexturing of organic polymer surfaces: from stable super hydrophilic to super hydrophobic surfaces, *Langmuir* **25** (2009), 11748-11759.

[16] J.B. Segur and H.E. Oberstar, Viscosity of glycerol and its aqueous solutions, *Ind. Eng. Chem.* **43** (1951), 2117-2120.

[17] S. Mikhail and W. Kimel, Densities and viscosities of 1-propanol-water mixtures, *J. Chem. Eng. Data* **8** (1963), 323-328.

[18] J.M. Oh, S.H. Ko and K.H. Kang, Shape oscillation of a drop in ac electrowetting, *Langmuir* **24** (2008), 8379-8386.

[19] J. Oh, D. Legendre and F. Mugele, Shaken not stirred—On internal flow patterns in oscillating sessile drops, *Europhysics Letters* **98** (2012), 34003.

[20] E. Becker, W. Hiller and T. Kowalewski, Experimental and theoretical investigation of large-amplitude oscillations of liquid droplets, *J. Fluid Mech.* **231** (1991), 189-210.

[21] A.K. Chesters, The modeling of coalescence processes in fluid liquid dispersion - A review of current understanding, *Chem. Eng. Res. Des.* **69** (1991), 259-270.

[22] F.T. Smith, L. Li and G.X. Wu, Air cushioning with a lubrication/inviscid balance, *J. Fluid Mech.* **482** (2003), 291-318.

[23] P.D. Hicks and R. Purvis, Air cushioning and bubble entrapment in three-dimensional droplet impacts, *J. Fluid Mech.* **649** (2010), 135-163.

[24] M. Mani, S. Mandre and M.P. Brenner, Events before droplet splashing on a solid surface, *J. Fluid Mech.* **647** (2010), 163-185.

[25] K. Okumura, F. Chevy, D. Richard, D. Quéré and C. Clanet, Water spring: A model for bouncing drops, *Europhysics Letters* **62** (2003), 237.

[26] J. De Ruiter, J.M. Oh, D. Van Den Ende and F. Mugele, Dynamics of collapse of air films in drop impact, *Phys. Rev. Lett.* **108** (2012), 074505.

[27] W. Bouwhuis, R.C.A. Van Der Veen, T. Tran, D.L. Keij, K.G. Winkels, I.R. Peters, D. Van Der Meer, C. Sun, J.H. Snoeijer and D. Lohse, Maximal air bubble entrainment at liquid-drop impact, *Phys. Rev. Lett.* **109** (2012), 264501.

[28] R.C. Van Der Veen, T. Tran, D. Lohse and C. Sun, Direct measurements of air layer profiles under impacting droplets using high-speed color interferometry, *Phys. Rev. E* **85** (2012), 026315.

Appendix 5.1. Determination of internal energy and dissipation in the droplet

(A) Properties of the Legendre polynomials

The Legendre polynomials are azimuthally symmetric solutions to the Legendre differential equation occurring when solving Laplace's equation in spherical coordinates:

$$\frac{d}{dx}\left((1-x^2)\frac{d}{dx}P_n\right)+n(n+1)P_n(x)=0 \qquad \text{where } x=\cos\theta$$

Each Legendre polynomial $P_n(x)$ is an *n*th-degree polynomial, that can be expressed as follows:

$$P_n(x)=\frac{1}{2^n n!}\frac{d^n}{dx^n}[(x^2-1)^n]$$

Figure S1 shows the Legendre polynomials up to $n=5$ on the interval $-1\le x\le 1$, and the interface shape obtained for a single mode distortion: $\tilde{r}=1+\tilde{c}_n P_n(x)$ where $\tilde{c}_n$ is set to 0.25 to show a clear deformation. The Legendre polynomials are symmetric (even modes) or antisymmetric (odd modes). In the description of the droplet contour the *n*th-degree mode leads to *n* lobes on the droplet surface.

An important property of the Legendre polynomials is their orthogonality on the interval $-1\le x\le 1$:

$$\int_{-1}^{1} P_m(x)P_n(x)dx=\frac{2}{2n+1}\delta_{mn}$$

where δ_{mn} is the Kronecker delta (*i.e.* equal to 1 if $m=n$ and 0 otherwise).

Because $P_0(x)=1$, the orthogonality relation implies that for $n\neq 0$:

$$\int_{-1}^{1} P_n(x)dx=\int_{-1}^{1} P_n(x)P_0(x)dx=0$$

(B) Determination of internal potential energy

The oscillation potential energy is given by the surface energy of the deformed droplet interface. When deforming the droplet interface away from its spherical equilibrium shape, surface tension tends to contract the interface - thus acting as a liquid spring. The oscillation potential energy $U_{int}=\sigma A_{surf}$ is linear in the amount of surface area:

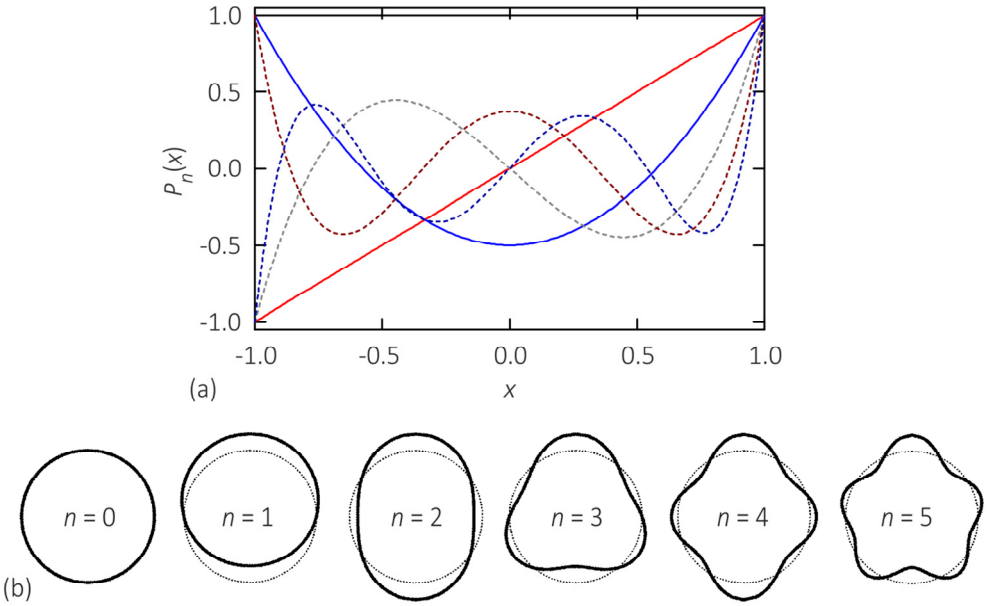

Figure S1. Legendre polynomials used for spherical decomposition of an interface. (a) $P_n(x)$ for orders $0 \leq n \leq 5$ on the interval $-1 \leq x \leq 1$ (colors with increasing n: black, red, blue, grey dashed, dark red dashed, dark blue dashed). (b) The higher modes are imposed onto the undisturbed droplet: $\tilde{r} = 1 + \tilde{c}_n P_n(x)$.

$$U_{int} = 2\pi\sigma \int_0^\pi R \sin\theta \sqrt{R^2 + (\partial_\theta R)^2}\, d\theta$$

(in spherical coordinates) with R the angle-dependent radius of the droplet. In the limit of small deformations from spherical this expression reduces to $U_{int} \simeq 2\pi\sigma \int_{-1}^{1} \left\{R^2 + \frac{1}{2}(\partial_\theta R)^2\right\} dx$, where it is used that $x = \cos\theta$. The potential energy can now be expressed in terms of the spherical interface decomposition $R(t,\theta) = R_0 + \sum_{n=0}^{\infty} c_n(t) P_n(x)$ that was obtained from analyzing the side-view recordings. The energy for each mode $n = 2 \ldots \infty$ can be calculated separately and then linearly superposed as the modes are independent for small amplitudes. Thus, the summation sign is temporarily dropped for convenience: we describe a single mode n imposed on the undisturbed droplet, i.e. $R = (R_0 + c_0) + c_n P_n(x)$ with a correction c_0 to account for volume conservation. The surface area integral is evaluated using the properties of the Legendre polynomials, see Appendix 5.1(A):

$$U_{int} = 2\pi\sigma\left(2(R_0 + c_0)^2 + c_n^2\,\frac{n(n+1)+2}{2n+1}\right) \tag{S1}$$

To find the potential energy apart from a constant $4\pi\sigma R_0^2$ for the equilibrium spherical shape, we need to take into account that $c_0 \neq 0$. To calculate the correction we start from volume conservation:

$$V = \frac{4}{3}\pi R_0^3 = 2\pi\int_0^{\pi}\int_0^{R(\theta)} r^2 \sin\theta\, dr\, d\theta = \frac{2}{3}\pi\int_{-1}^{1} R^3\, dx$$

Substituting $R^3 = ((R_0 + c_0) + c_n P_n)^3$ up to second order, and exploiting the properties of the Legendre polynomials described in Appendix 5.1(A) one gets:

$$V = \frac{2}{3}\pi\int_{-1}^{1}[(R_0 + c_0)^3 + 3(R_0 + c_0)^2(c_n P_n) + 3(R_0 + c_0)(c_n P_n)^2]\, dx$$

$$= \frac{2}{3}\pi\left[2(R_0 + c_0)^3 + 0 + 3(R_0 + c_0)c_n^2\frac{2}{2n+1}\right] = \frac{4}{3}\pi\left[(R_0 + c_0)^3 + \frac{3(R_0+c_0)c_n^2}{2n+1}\right]$$

Defining $(R_0 + c_0)/R_0 = 1 + \delta$ and dividing by $\frac{4}{3}\pi R_0^3$ last equation can be rewritten as:

$$1 = (1 + \delta)^3 + 3(1 + \delta)\frac{(c_n/R_0)^2}{2n+1}$$

Evaluating this expression for small δ and c_n (up to second order) one obtains:

$$\delta \simeq -\frac{(c_n/R_0)^2}{2n+1}$$

which yield the final expression for $(R_0 + c_0)$

$$(R_0 + c_0)^2 = \left(R_0 - \frac{c_n^2}{R_0(2n+1)}\right)^2 \simeq R_0^2 - 2\frac{c_n^2}{2n+1}$$

that is accurate up to second order and can be substituted back into the expression for the potential energy, Equation (S1). This yields apart from the constant contribution:

$$U_{int} = 2\pi\sigma\frac{(n-1)(n+2)}{2n+1}c_n^2 \tag{S2}$$

The potential energy for each individual mode $n \geq 1$ can be written in the usual form as $U_{int} = \frac{1}{2}k_{eff,n}c_n^2$ with the effective spring constant given by $k_{eff,n} = 4\pi\sigma(n-1)(n+2)/(2n+1)$. For the $n = 1$ mode describing the linear motion this reduces to zero, while for the $n \geq 2$ modes describing the oscillation the effective spring constant quickly

converges to $k_{eff,n} = 2n\pi\sigma$, thus increasing approximately linearly with increasing mode number. Higher frequency modes are logically stiffer as their creation causes a large increase of surface area. To calculate the total potential energy in second order accuracy of c_0 we sum Equation (S2) over the individual modes.

(C) Determination of internal kinetic energy

Given the velocity potential, $\varphi(r,\theta) = \sum_{n=2}^{\infty} A_n r^n P_n(x)$, we calculate the kinetic energy $K_{int} = \frac{1}{2}\rho \int \nabla\phi \cdot \nabla\phi \, dV$. Using the relation $\nabla \cdot (\phi\nabla\phi) = \nabla\phi \cdot \nabla\phi + \phi\nabla^2\phi = \nabla\phi \cdot \nabla\phi$ and the divergence theorem, the integral over the volume of the droplet is converted to a surface integral:

$$K_{int} = \frac{1}{2}\rho \int \phi\left(\underline{\mathrm{n}} \cdot \nabla\phi\right) dA$$

In the small deformation limit the surface integral can be simply evaluated over a sphere with mean radius R_0, allowing to substitute the normal vector $\underline{n}$ by the radial unit vector $\underline{e_r}$; the expression then reads:

$$K_{int} = \pi\rho R_0^2 \int_0^{\pi} (\varphi \, \partial_r\varphi)|_{R_0} \, \sin\theta \, d\theta$$

The latter expression can be evaluated for each individual mode describing the velocity field. We substitute the radial velocity $\partial_r\varphi = A_n n r^{n-1} P_n(x)$ at the boundary $r = R_0$, and use the properties of the Legendre polynomials in Appendix 5.1(A):

$$K_{osc} = \pi\rho {R_0}^2 \int_{-1}^{1} n A_n^2 R_0^{2n-1} {P_n}^2(x) \, dx = 2\pi\rho {R_0}^{2n+1} A_n^2 \frac{n}{2n+1}$$

Given the relation between c_n and A_n in the limit of small deformation, $\dot{c}_n = n A_n R_0^{n-1}$, the final expression for the kinetic energy is:

$$K_{int} = 2\pi\rho R_0^3 \frac{1}{n(2n+1)} \dot{c}_n^2$$

which can again be summed over the individual modes. The kinetic energy can be written in the usual form as $K_{int} = \sum_{n=2}^{\infty} \frac{1}{2} m_{eff,n} \dot{c}_n^2$ with the effective mass for oscillation given by $m_{eff,n} = 3M/(2n^2 + n)$ where *M* is the total mass of the droplet. The effective mass decreases with increasing mode number as the flow field gets more localized towards the surface region for higher frequency oscillations.

(D) Determination of dissipation in the droplet

Although potential flow assumes that the fluid is inviscid, we can calculate the dissipation in the flow field in the limit of low fluid viscosity, i.e. small Oh number. The internal dissipation rate is given in terms of the rate of strain tensor $\overline{\overline{D}}$ by $\dot{W}_{drop} = \int \left(2\mu \overline{\overline{D}} : \overline{\overline{D}}\right) dV$ where $\overline{\overline{D}}$ in case of rotational symmetry is given by:

$$\overline{\overline{D}} = (\partial_r u_r)\hat{e}_r\hat{e}_r + \left(\frac{1}{r}\partial_\theta u_\theta + \frac{u_r}{r}\right)\hat{e}_\theta\hat{e}_\theta + \left(\frac{u_r}{r} + \cot\theta\,\frac{u_\theta}{r}\right)\hat{e}_\phi\hat{e}_\phi$$

$$+\frac{1}{2}\left(r\partial_r\left(\frac{u_\theta}{r}\right) + \frac{1}{r}\partial_\theta u_r\right)(\hat{e}_r\hat{e}_\theta + \hat{e}_\theta\hat{e}_r)$$

It can be derived that [11]:

$$\dot{W}_{drop} = 8\pi\mu R_0 \sum_n \frac{n-1}{n}\dot{c}_n^2$$

Appendix 5.2. Dissipation and pressure distribution in the air film

The local dissipation in the film is given by $\dot{\varepsilon}(r,z) = 2\mu\overline{\overline{D}} : \overline{\overline{D}} = \mu(\partial_z v)^2$, where $\overline{\overline{D}} = \frac{1}{2}\partial_z v\,(\hat{e}_r\hat{e}_z + \hat{e}_z\hat{e}_r)$ is the rate of strain tensor. Given the velocity profile,

$$v(r,z) = \frac{\beta(\alpha)\dot{Q}(r)}{2\pi r h(r)}\left\{\left(\frac{z}{\alpha h(r)}\right) - \left(\frac{z}{\alpha h(r)}\right)^2\right\} \tag{S3}$$

it follows that

$$\dot{\varepsilon}(r,z) = \mu\left[\frac{\beta(\alpha)\dot{Q}(r)}{\pi r h(r) z}\left\{\frac{1}{2}\left(\frac{z}{\alpha h(r)}\right) - \left(\frac{z}{\alpha h(r)}\right)^2\right\}\right]^2$$

The total dissipation rate $\dot{W}_{sq}$ for a film with maximum lateral extension R_{max} is given by:

$$\dot{W}_{sq} = \int \dot{\varepsilon}(r,z)dV = 2\pi\int_0^{R_{max}} r dr \int_0^{h(r)} \dot{\varepsilon}(r,z)dz$$

$$\dot{W}_{sq} = \frac{2\mu\beta^2(\alpha)}{\pi}\int_0^{R_{max}} \frac{\dot{Q}^2(r)}{r h^2(r)} dr \int_0^{h(r)} \frac{1}{z^2}\left[\left\{\frac{1}{2}\left(\frac{z}{\alpha h(r)}\right) - \left(\frac{z}{\alpha h(r)}\right)^2\right\}\right]^2 dz$$

Evaluating the latter integral yields $\frac{1}{h(r)}(3\alpha^2 - 6\alpha + 4)/(12\alpha^4)$ which leads to the final expression for the total dissipation rate:

$$\dot{W}_{sq} = \frac{6\mu}{\pi}\left[\frac{3\alpha^2-6\alpha+4}{(3\alpha-2)^2}\right]\int_0^{R_{max}} \frac{\dot{Q}^2(r)}{rh^3(r)}dr$$

The partial slip pre-factor decreases from 1 to 1/4 when the boundary condition changes from no-slip to full slip at the droplet interface. For a parallel plate geometry $\partial_r \dot{h} = 0$ with no-slip condition this reduces to the classical solution $\dot{W}_{sq} = (3/2)\pi\mu\dot{h}^2h^{-3}R^4$.

Equivalently, we can calculate the pressure field in the squeeze flow and determine the squeeze force. By substitution of Equation (S3) in the Stokes equation $\partial_r p = \mu\partial_z^2 v$ we find the pressure gradient:

$$\frac{\partial p}{\partial r} = -\frac{6\mu}{\pi(3\alpha-2)}\frac{\dot{Q}(r)}{rh(r)^3}$$

This is integrated to obtain the radial pressure distribution. To determine the absolute pressure a reference value is needed. At $r \to \infty$, i.e. at outside the squeezed layer, the ambient pressure should be retrieved. Using this as boundary condition in the integration yields:

$$\Delta p(r) = p(r) - p_\infty = \frac{6\mu}{\pi(3\alpha-2)}\int_r^\infty \frac{\dot{Q}(s)}{sh^3(s)}ds$$

where $\Delta p(r)$ is the excess pressure in the air film. The squeeze force can be determined by integrating the pressure over the film area:

$$F_{sq} = \int_0^\infty 2\pi r\Delta p(r)dr = \frac{12\mu}{(3\alpha-2)}\int_0^\infty \left\{\int_r^\infty \frac{\dot{Q}(s)}{sh^3(s)}ds\right\}rdr$$

This can be transformed to:

$$F_{sq} = \int_0^\infty 2\pi r\Delta p(r)dr = \frac{12\mu}{(3\alpha-2)}\int_0^\infty \left\{\int_0^s rdr\right\}\frac{\dot{Q}(s)}{sh^3(s)}ds$$

Which leads to the final expression for the squeeze force:

$$F_{sq} = \frac{6\mu}{(3\alpha-2)}\int_0^\infty \frac{s\dot{Q}(s)}{h^3(s)}ds$$

Appendix 5.3. Details of the "single oscillation mode" model

The flow field within the drop is given by $\dot{z} = \dot{\varepsilon}z$ and $\dot{r} = -\frac{1}{2}\dot{\varepsilon}r$, where $0 \le r \le \sqrt{R_c^3/b}$, $-b \le z \le b$ and $\dot{\varepsilon} = \dot{b}/b$. So the internal kinetic energy is given by:

$$K = \tfrac{1}{2}\rho \int_0^a \int_{-b}^{b} (\dot{z}^2 + \dot{r}^2) dz\, 2\pi r dr = \tfrac{1}{2}\rho V \dot{b}^2 \left(\tfrac{1}{3} + \tfrac{1}{8}\beta^{-3}\right)$$

where $\beta = b/R_c$. The internal dissipation becomes:

$$\dot{W} = \int_0^a \int_{-b}^{b} (-3\mu \dot{\varepsilon}^2) dz\, 2\pi r dr = -6\pi\mu R_c\, \dot{b}^2\, \beta^{-2}$$

The potential energy is given by the excess surface of the drop: $U = \sigma(2\pi a^2 + 4\pi ab - 6\pi R_c^2)$, where $a = (R_c^3/b)^{1/2}$. Hence we obtain for the total kinetic energy K, the total potential energy U, and the dissipation rate:

$$K = \tfrac{1}{2} M \dot{b}^2 \left(\tfrac{1}{3} + \tfrac{1}{8}\beta^{-3}\right) + \tfrac{1}{2} M \dot{z}^2 \quad \text{(S4)}$$

$$U = 2\pi\sigma R_c^2 \left(\beta^{-1} + 2\beta^{1/2} - 3\right) + Mgz \quad \text{(S5)}$$

$$\dot{W} = -6\pi\mu R_c \dot{b}^2 \beta^{-2} + \left(\dot{z} - \dot{b}\right)\, F_{sq}\left(b, \dot{b}, z, \dot{z}\right) \quad \text{(S6)}$$

Because $\dot{W} = \partial_t (K + U)$ we obtain the following differential equation:

$$-6\pi\mu R_c \dot{b}^2 \beta^{-2} + \left(\dot{z} - \dot{b}\right) F_{sq} =$$
$$\left(\tfrac{1}{3} + \tfrac{1}{8}\beta^{-3}\right) M \ddot{b} \dot{b} + \tfrac{3M}{16R_c} \beta^{-4} \dot{b}^3 + M \ddot{z} \dot{z} + 3\pi\sigma R_c \tfrac{2}{3} \left(\beta^{-\frac{1}{2}} - \beta^{-2}\right) \dot{b} + Mg\dot{z}$$

Because $F_{sq} = M(\ddot{z} + g)$ the terms with $\dot{z}$ cancel and the equation reduces to:

$$-6\pi\mu R_c \dot{b} \beta^{-2} - F_{sq} = \left(\tfrac{1}{3} + \tfrac{1}{8}\beta^{-3}\right) M \ddot{b} + \tfrac{3M\beta^{-4}}{16R_c} \dot{b}^2 + 3\pi\sigma R_c \tfrac{2}{3} \left(\beta^{-\frac{1}{2}} - \beta^{-2}\right)$$

Neglecting the higher order terms, except for the interfacial tension contribution because otherwise the droplet height becomes negative, this results in

$$\alpha M \ddot{b} = -F_{sq} - 6\pi\mu R_c \dot{b} - 3\pi\sigma R_c \tfrac{2}{3} \left(\beta^{-1/2} - \beta^{-2}\right) \quad \text{(S7)}$$

where for small deviations of $\beta = 1 + \delta$ from 1 we get using the Taylor series:

$$(1 + \delta)^q = 1 + q\delta + \frac{1}{2} q(q-1)\delta^2 + \cdots$$

for the internal potential energy:

$$\tfrac{2}{3} \left(\beta^{-1/2} - \beta^{-2}\right) = \tfrac{2}{3} \left((1+\delta)^{-1/2} - (1+\delta)^{-2}\right) = \delta - \tfrac{7}{4}\delta^2 = (\beta - 1) + \cdots$$

So for small deviations and no interaction with the substrate, $F_{sq} = 0$, we get for Equation (S7) the damped harmonic oscillator equation:

$$\ddot{b} + \frac{6\pi\mu R_c}{\alpha M}\dot{b} + \frac{3\pi\sigma}{\alpha M}(b - R_c) = 0$$

The resonance frequency is given by $\omega_0 = (3\pi\sigma/\alpha M)^{1/2}$ and damping time $\tau = \alpha M/6\pi\mu R_c$. So the quality factor of the resonator is: $Q = (3\pi\sigma\alpha M)^{1/2}/6\pi\mu R_c$. When the drop is in contact with the substrate b is equal to z. Hence:

$$\ddot{b} + \frac{6\pi\mu R_c}{\alpha M}\dot{b} + \frac{3\pi\sigma}{\alpha M}(b - R_c) = -\frac{M(\dot{b}+g)}{\alpha M}$$

In this case the resonance frequency is given by $\omega_0 = (3\pi\sigma/(1+\alpha)M)^{1/2}$ and the quality factor by $Q = (3\pi\sigma(1+\alpha)M)^{1/2}/6\pi\mu R_c$, indicating that in the hover phase the dissipation is lower.

Appendix 5.4. Details of the observed droplet oscillation

Figure S2 shows the full time evolution of the half droplet height B to demonstrate the gradual decrease in droplet deformation with each bounce, and the transformation to a single oscillation pattern rather than separated bounce and flight phases.

Figure S3 shows the full time evolution of the c_n coefficients up to $n = 4$. Here we demonstrate the amplitude decrease of the modes with subsequent bounces, and the gradual synchronization of modes. Most clearly, the double peak of the $n = 3$ mode vanishes.

Figure S4 shows the corresponding time evolution of $\dot{c}_n$. The higher modes, *i.e.* $n = 3$ and 4 are clearly present in $\dot{c}_n$. As the kinetic energy and dissipation in the fluid increase with $\dot{c}_n$ they have significant contributions from the higher modes. For example, the damping time during the flight phase for the $n = 3$ mode is 0.037 ± 0.006 s, which is of the order of the free fall time of the first bounce. In contrast, the damping time of the $n = 2$ mode is significantly longer: 0.14 ± 0.05 s.

Figure S5 shows two selected bounces of Figure S4 to demonstrate the influence of phase mismatching. If the phase of the free oscillation does not match the phase imposed by the interaction, the amplitude of the respective mode is significantly smaller after the contact phase, as indicated by the arrows first for mode $n = 3$ (blue) and then for $n = 2$ (red).

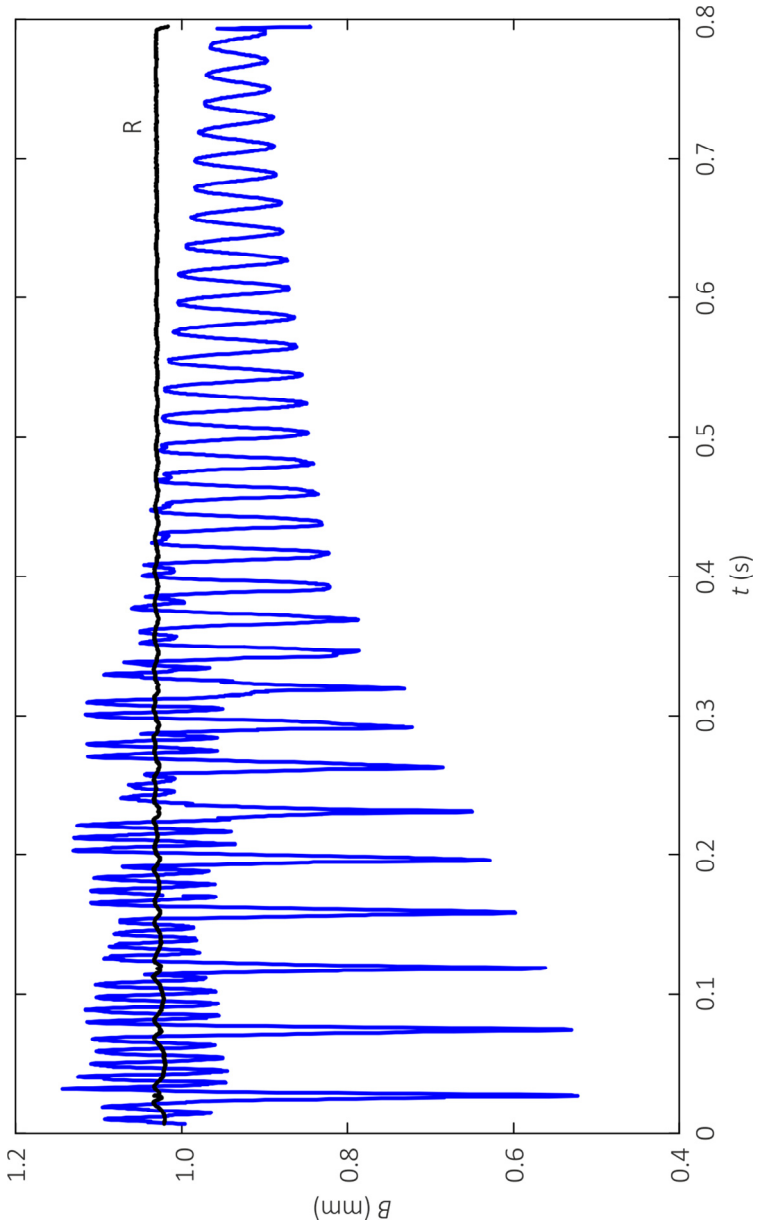

Figure S2. Droplet deformations during a bouncing series. Full time span for the bouncing series shown in Figure 7.

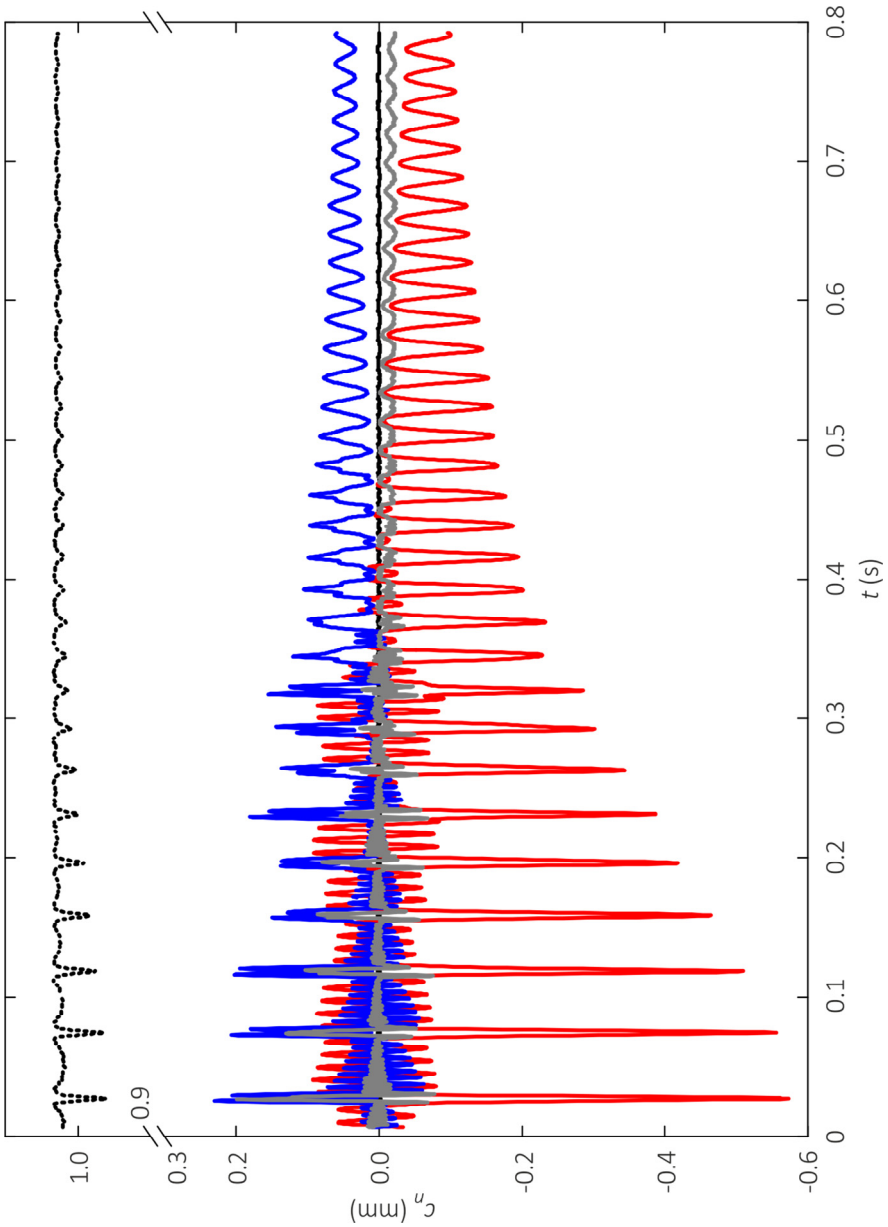

Figure S3. Shape mode decomposition using Legendre polynomials for the bouncing series shown in Figure 7, for $n = 0$ (black dotted line; shifted by R_0), $n = 1$ (black solid), $n = 2$ (red), $n = 3$ (blue), and $n = 4$ (grey) versus time. Full time span.

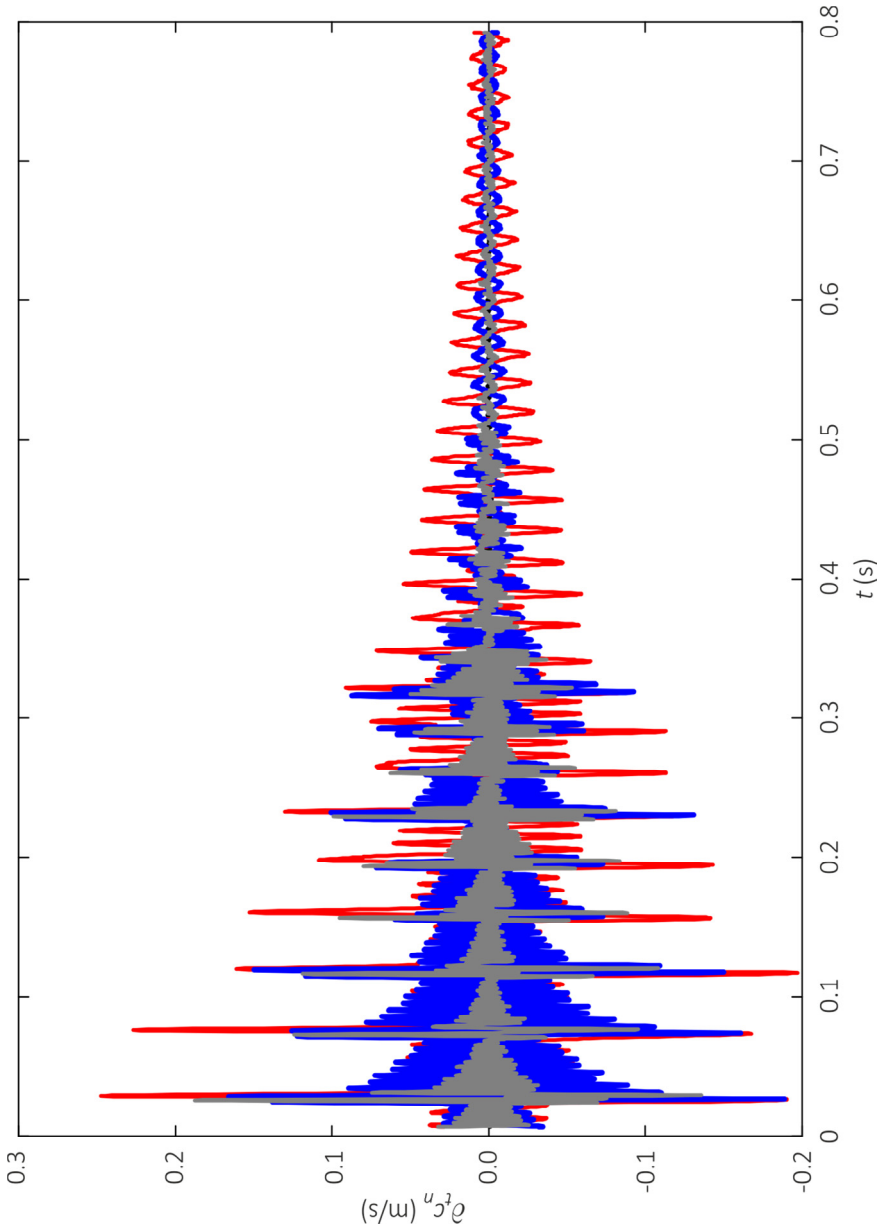

Figure S4. Time derivative of the shape mode coefficients for the bouncing series shown in Figure 7, for $n = 0$ (black dotted line; shifted by R_0), $n = 1$ (black solid), $n = 2$ (red), $n = 3$ (blue), and $n = 4$ (grey) versus time. Full time span.

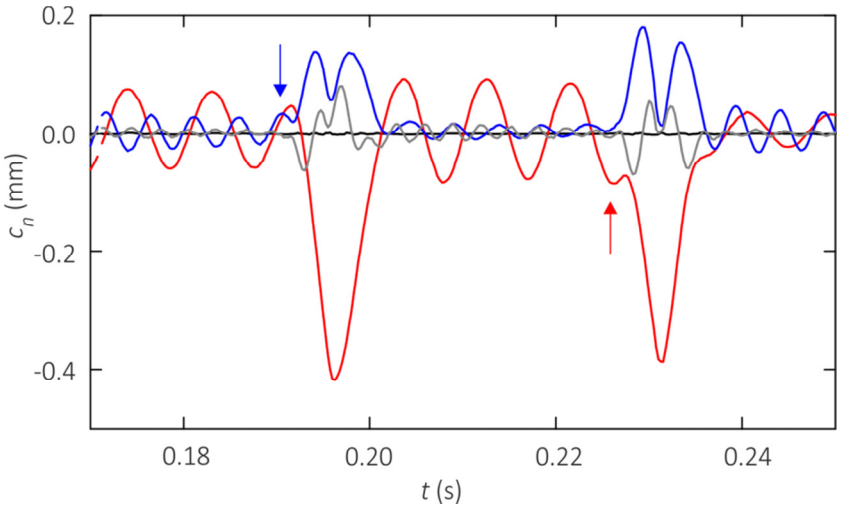

Figure S5. Example of synchronization of modes during the contact phase. The arrows indicate where mode $n = 2$ (red) and $n = 3$ (blue) are clearly forced into phase, leading to a decreased free oscillation amplitude afterwards. (Same experiment as in Figure 13).

Appendix 5.5. Local velocities in the air film

To calculate the force and dissipation we should thus use the full shape information that we obtain from the bottom view. Unfortunately, we miss the shape information outside the kink due to the steepness of the interface compared to the lateral resolution of the recording. Thus, the squeeze force (impulse) cannot be determined as it relies on the unknown reference pressure just outside the measurable region. Yet, we are able to determine the local dissipation in the measurable region up to R_{max}. First we determine the velocity field in this region. The local (average) velocity $\bar{v}$ in the air film is calculated and shown in a contour plot *vs.* radial position and time in Figure S6. Velocities are obtained up to ~ 100 mm/s, indeed much smaller than the speed of sound, thus the air film is compressible. The velocity is not monotonically increasing in the direction of the kink as previously shown in Ref. [28]. Instead, after formation of the first kink we also observe regions of moderately negative velocity in the inner region of the squeezed air film. However, the highest velocities are observed at the kink and are positive. This allows a continuously outward directed flow.

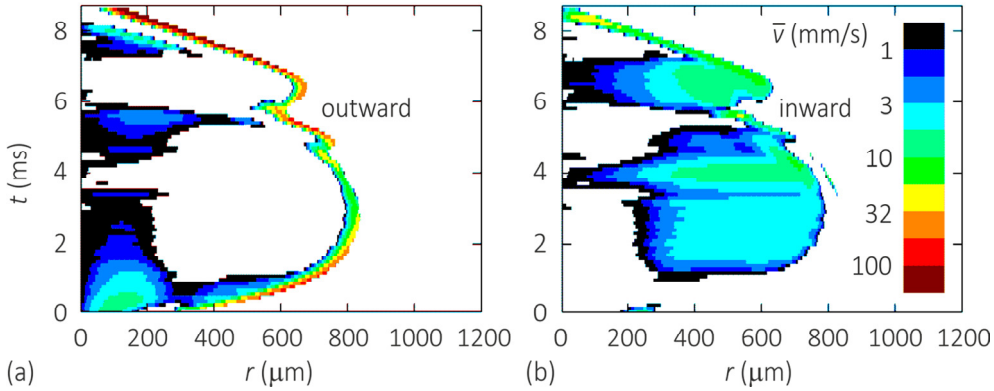

Figure S6. Average velocity in the air film. $\bar{v}$ (mm/s) is plotted versus radial position and time for the impact of an $R_0 = 1.03$ mm droplet with We= 0.76. The color scale is logarithmic with (a) showing regions of positive (outward) velocity and (b) showing regions of negative (inward) velocity.

Chapter 6

Living on the edge!

Controlling air film collapse using micro-textures

We use micro-textures like step profiles with sharp vertical edges to control formation of liquid-solid contact in an air-cushioned impact. Contact is formed where the ring of minimum film thickness is closest to the edge, provided that the latter is sufficiently high. The air gap thins to a minimum film thickness of 60 ± 40 nm, showing that collapse happens significantly later than on a flat substrate (~ 200 nm). We use a simple parameterization of the interface to predict the step height required to force contact. When the single step edge is replaced by a narrow ridge or pillar, the interface deflection is suppressed and liquid-solid contact is facilitated.

6.1. Introduction

It is of interest to study the influence of a micro-textured substrate on the air cushioning in low We droplet impact. It is of practical importance for inkjet printing applications on rough surfaces like the inkjet printing of electrical contact lines on a solar cell for which micro-textured silicon wafers are used (as described in the Chapter 1). The shape of this micro-texture might influence the formation of liquid-solid contact *via* local thinning of the air film. Here, we consider both the timing and location of the initial wetting spot. In particular the substrate micro-texture might be an interesting path for active control, especially since surface wettability has no influence on the initiation of liquid-solid contact (Chapter 4). We address questions like: Can we actively 'puncture' the air layer to eliminate bouncing? Can we control the location of the initial wetting spot, and eliminate air bubble inclusion?

Hicks and Purvis [1] studied this problem numerically for steps, ridges, and chasms that are small compared to the droplet size. They find that away from the structure the free surface profile remains undisturbed, and the air flow is radially outward. However, close to rapid changes in surface topography the flow becomes fully three-dimensional over relatively short azimuthal distances. At a protrusion, the air gap narrows faster which generates a pressure spike, and a deflection of the free surface away from the protrusion. The reduction of the air gap has two consequences: the time until impact is reduced, and the initial impact may occur at specific places rather than on a coherent ring.

To our knowledge this problem has not been studied experimentally. Most related are the studies of impact on superhydrophobic micropillar substrates and single textures with a typical size similar to the droplet diameter. For the first, the focus has been on both the impalement transition from Cassie-Baxter to Wenzel [2-4] (the latter Ref. using interferometry to visualize interface deformation and depinning), and the subsequent imbibition of the structure [5, 6]. For the second, the focus has been on spreading and rim destabilization leading to splashing, *e.g.* within a slot [7], or on top of a disk [8, 9] or a sphere [10]. In contrast to these two classes of experiments, our interest is focused to (i) the squeeze-out of the air and the initial formation of liquid-solid contact, in case of (ii) impacts onto single micro-textures located *within* the impact region. To understand the influence of shape properties of the micro-texture we use a wide range of structures with varying height and shape: microspheres, steps with sharp edges, and ridges with varying width.

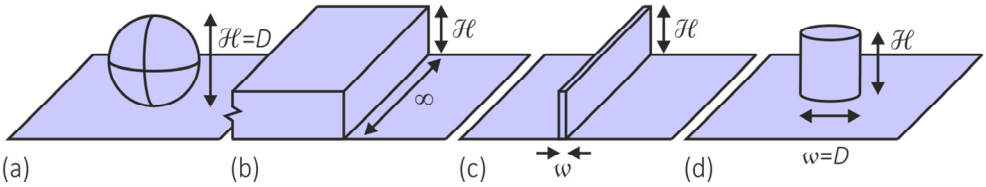

Figure 1. Micro-textures: (a) microspheres, (b) step edge, (c) ridge, and (d) pillar. Indicated are the height $\mathcal{H}$, width w, and diameter D.

6.2. Experimental set-up

Experiments are performed with millimetric aqueous droplets, quasistatically dispensed from a syringe needle to obtain a uniform radius $R = 1.03$ mm. The impact velocity $v \sim 0.22$ m/s is set by the falling height. Details of the experimental set-up can be found in Chapter 4. We create a micro-texture topography by either microsphere deposition or lithographic fabrication. Polystyrene microspheres with a diameter $D = 0.02$-15 μm are spin-coated onto a smooth glass substrate from a 10^{-7}-10^{-2} wt.% dispersion in ethanol. This results in a sparse coverage of several microspheres in the impact area such that isolated objects can be studied, see Figure 1(a). The microspheres are either hydrophobic (2.0 and 15 μm) or hydrophilic (carboxylated, 0.2 and 10 μm). Micro-textures with a step edge are produced by lithography. We use plasma-enhanced chemical vapor deposition (PECVD) to grow a SiO_x layer ($x \approx 2$) onto a carefully cleaned glass wafer by a chemical reaction of SiH_4 with N_2O. The SiO_x layer is grown to a final layer thickness ranging from 20-1300 nm. Using a mask the micro-texture pattern is covered with photoresist, after which the surrounding regions are etched with CHF_3 to remove the deposited top-layer of SiO_x around the micro-texture. Due to small pinholes in the SiO_x layer we obtain a relatively low surface roughness during the etching process. The microstructures thus obtained are shown in Figure 1(b-d). We use step edges with height $\mathcal{H}$, and ridges (pillars) with an additional width w ($w = D$). In this work, $\mathcal{H}$ ranges from 20-1300 nm, while $w \geq 2$ μm. Atomic force microscopy shows that the edges are relatively sharp with an edge region smaller than 1 μm, in contrast to the 'soft' edges implemented by Hicks and Purvis [1] that are ~ 20 μm wide if rescaled to our experimental situation. The height of the structures is measured by profilometry (Veeco Dektak) with an accuracy of 20 nm.

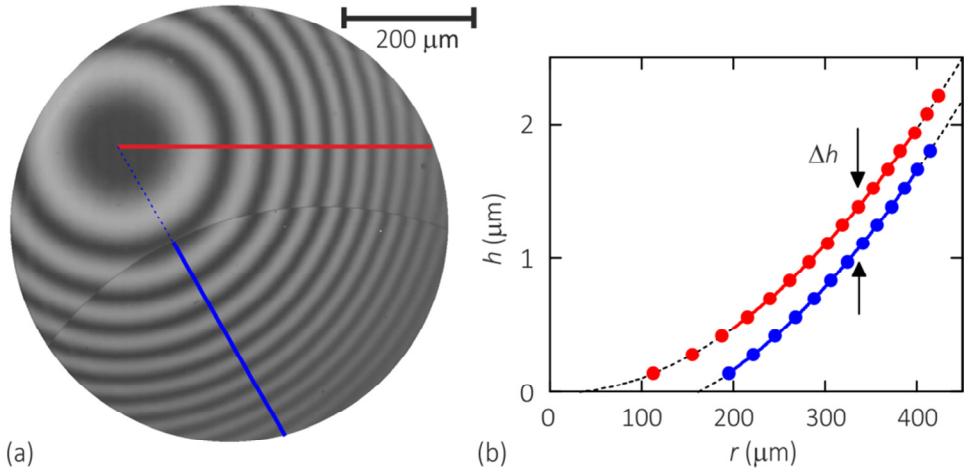

Figure 2. Absence of edge effects on the fringe pattern, and verification of texture height. (a) Fringe pattern below a lens, with a $\mathcal{H} = 332$ nm pillar in the thin film region in the lower-right corner of the field-of-view. The red line indicates the intensity scan on the flat region, the blue line on the pillar. (b) Corresponding air film profiles: (dots) interference peaks, (dashed black lines) fitted spherical lens profile, (solid lines) compared region to calculate Δh.

6.2.1. Interferometry near micro-textures

The air film beneath the droplet is visualized through the transparent, micro-textured, substrate using the interferometry technique described in Chapter 3. Near the micro-texture the radial symmetry is broken and we observe a distortion of the fringe pattern. Apart from the air film thickness variations we aim to measure, it is to be verified that the near-vertical step edge (and the associated discontinuous jump in film thickness) does not influence the fringe pattern. Therefore, a lens of known curvature is placed on top of a microstructure step edge, *i.e.* a pillar in Figure 2(a). We observe a *radial shift* of the fringes due to the presence of the pillar as expected. However no other distortion is observed around the pillar edge within our pixel resolution. Secondly, Figure 2(b) determines the pillar height from the fringe shift. A circle fit to the radial position of the interference peaks on both the flat region and the pillar show that the off-set $\Delta h = 320 \pm 20$ nm, in full correspondence with the atomic force microscopy measurement of 332 ± 2 nm for the same pillar. The absence of fringe distortions other than a radial shift indicates that for a deformable (*i.e.* droplet) interface this radial shift due to the edge height can be subtracted from the interference pattern, and the remaining distortion is due to the air film variation near the edge. In other words, at each side of the edge separately, the distortion is fully due to variation in air film thickness.

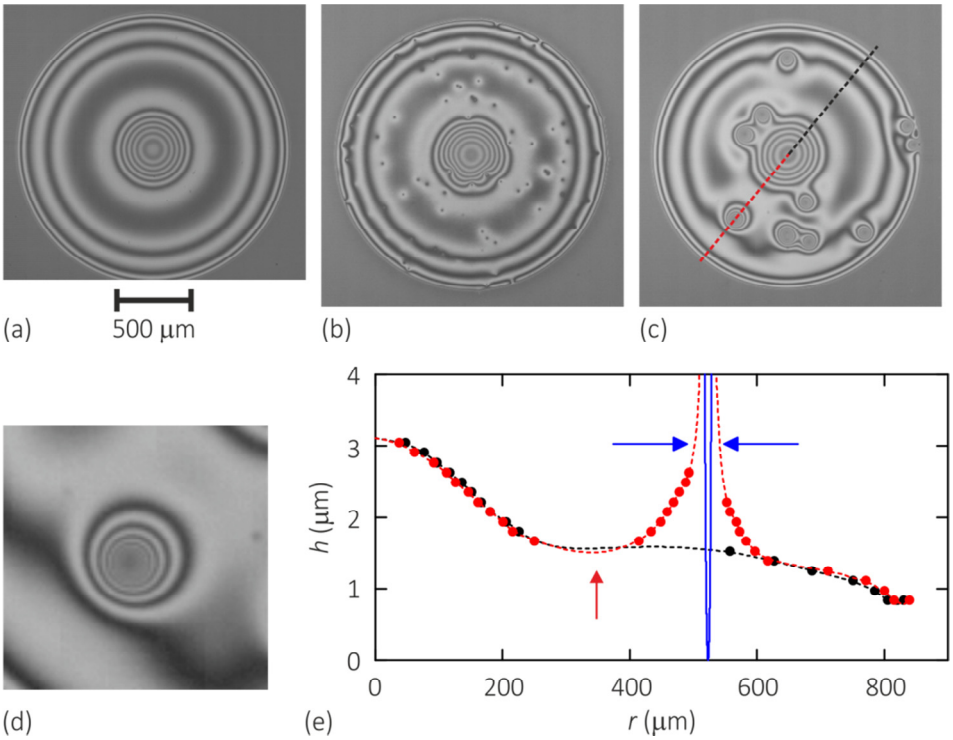

Figure 3. Interface deflection upon air cushioning in the presence of microspheres. Different microsphere diameters are used: (a) reference case, (b) 2 µm, (c-d) 10 µm. (e) Interface shape for the flat (black) region and the region with sphere (red) as shown in (c-d). The microsphere itself is indicated in blue (note the large x/y scale ratio).

6.3. Results and discussion

6.3.1. Microspheres

We first consider the impact on substrates with microspheres of which examples are shown in Figure 3 (a-c). All tested spheres ranging from 0.2 to 15 µm do not induce liquid-solid contact, even those with a diameter significantly larger than the air film thickness. We tested this also for higher impact velocities up to $We \sim 10$ where contact is formed at r_1, but specifically *not* at the microspheres located there. Instead, the droplet interface is deflected upward around the microsphere, while far away from deposited spheres the surface profile is undisturbed. Figure 3 (d-e) show a zoom on the microsphere region and the corresponding droplet interface profile compared to the flat region. Laterally inward

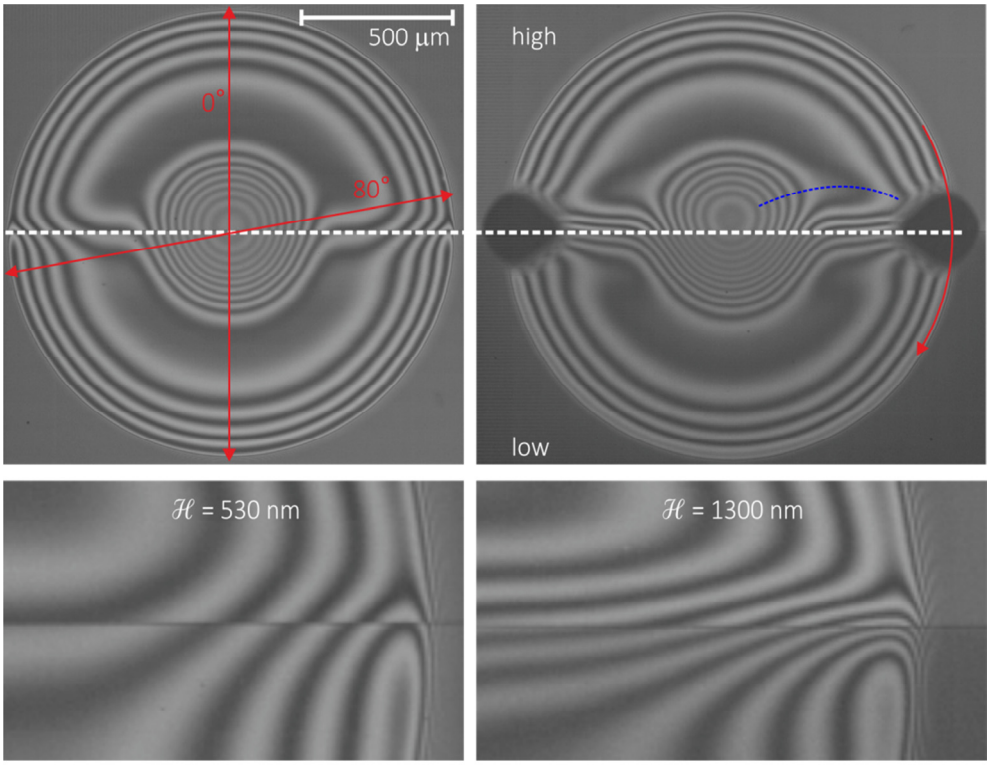

Figure 4. Interface deflection in the presence of a step edge. Edge (white dashed) with $\mathcal{H} =$ (a) 530 nm, and (b) 1300 nm at $t = 3.0$ ms. The lower panels show a zoom on the intersection between the ring of minimum film thickness and the edge, 0.1 ms earlier. The red arrows indicate the intensity scan in the (a) radial (selection: $\theta = 0°$ and 80°) and (b) azimuthal (φ) directions. The blue dashed line indicates a region of relative upwards deflection before the interface bends down near the edge.

(and to the sides) the interface shows a small depression (*i.e.* red arrow) but then steeply rises close to the particle. A region of 50 μm around the 10 μm sphere (indicated in blue) cannot be resolved due to the steep slope of the interface, but it is clear that the interface should rise to a minimum of 10 μm. We conclude that on a gradual topography such as a microsphere the droplet interface is sufficiently deflected to inhibit texture-induced contact formation. Accordingly, we next study sharp step edges which have the added benefit that fringes can be resolved at all flat sections except at the edge itself.

6.3.2. Step edges

The interface deflection above a step edge as sketched in Figure 1(b) is shown in Figure 4 for two different step heights. The impact is centered on the edge as well as possible such that the unperturbed air flow near the edge would be parallel to the step edge. (Off-center impacts are briefly discussed in Appendix 6.1.) In accordance to Hicks and Purvis [1] we find that the fringes, and thus the surface isopleths, are concentric away from the edge. Close to the edge, the fringe pattern along the step is distorted. We note four observations: (i) the center of the dimple shifts to the higher flat side of the step edge and (ii) the interface shows a local opposite deflection (dashed blue line) before finally (iii) deflecting up/ down at the edge. The relatively flat region around r_1 clearly visualizes the deflection at the edge with almost parallel fringes: the number of fringes is roughly two times higher for the higher step. However, (iv) the strongest gradients are observed at the intersection with the ring of minimum air film thickness, close to the outer rim of the profile, which is shown in the bottom row zooms. It is at *this* location that liquid-solid contact is formed if the step is high enough. If not, the droplet bounces as described in Chapter 5. (Note that liquid-solid contact may be formed at the lower flat side of the edge that is slightly roughened due to the etching procedure.) In the following we study the interface deflection near the edge, and the edge height required to force contact.

6.3.2.1. Distorted region around the edge

To determine the range of the distorted region around the edge we analyze the film height profile perpendicular to it - see the red arrows at 0° in Figure 4(a) - and compare the profile of the lower and higher flat sides of the step. The results are shown in Figure 5. Panel (a) demonstrates that for step heights of 530, 720 and 1300 nm the film thickness profiles fully collapse (solid lines) *i.e.* when measured with respect to the underlying substrate. (The film thickness on the lower flat side of the 1300 nm step edge could not be determined accurately due to its roughness.) The range of the distortion around the edge can be determined by folding both sides of the profile on top of each other. We determine this not only for the perpendicular scan at 0°, but take scans in steps of 10° up to 80°, see Figure 4(a). In this way the distortion perpendicular to the edge can be determined along the length of the step up to the radial position r_2. The results are shown in Figure 5 (b) for subsequent times. The distorted region is 100-200 μm wide at each side of the step edge. Under the influence of surface tension the distorted region grows perpendicular to the step while the deflection gets smoothened, *i.e.* the distorted region grows in time, and is largest at the center of the dimple.

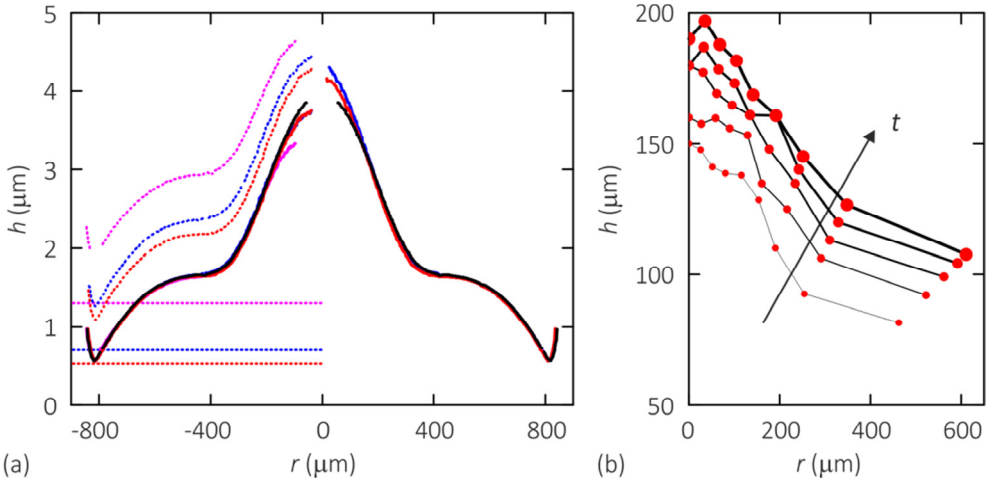

Figure 5. Interface profile in the radial perpendicular direction. (a) Profiles at the higher (left) and lower (right) side of the edge obtained at $t = 3.0$ ms. Different colors indicate different edge height: (black) reference, (red) 530 nm, (blue) 720 nm, and (magenta) 1300 nm. The dotted lines show the profiles shifted upwards with the height of the step. (b) Lateral range of interface distortion, measured perpendicular to the step edge *vs.* radial position. The step height shown is $\mathcal{H} = 530$ nm and $t = 0.8 \ldots 3.6$ ms in steps of 0.7 ms.

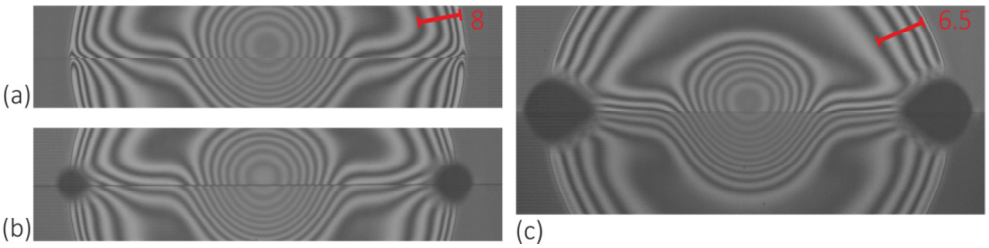

Figure 6. Transition to contact formation, and earlier onset. (a) $\mathcal{H} = 720$ nm at $t = 3.7$ ms, (b) $\mathcal{H} = 900$ nm at $t = 3.7$ ms, and (c) $\mathcal{H} = 1300$ nm at $t = 3.0$ ms. In the latter case the outer air film is less developed when contact is formed.

6.3.2.2. Edge height for contact formation

We showed in Figure 4 that contact is formed at the intersection between the step edge and the ring of minimum air film thickness. In the current experiments the latter is always located at the position r_2, but the same is valid for r_1 at higher We. For the minimum film thickness $h_2 = 440$ nm obtained in the current experiments we search for the critical edge height $\mathcal{H}^*$ required to form liquid-solid contact. Figure 6(a) shows that at an edge with $\mathcal{H} = 720$ nm the droplet bounces, while $\mathcal{H} = 900$ nm in panel (b) forces contact at both

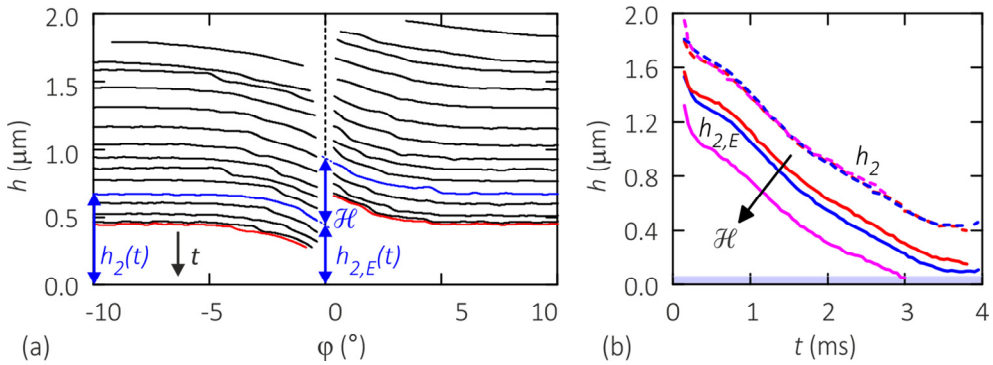

Figure 7. Interface profile under the kink (r_2) in the azimuthal direction. (a) Time evolution of the interface near the edge (located at $\varphi = 0°$) for $\mathcal{H} = 530$ nm and $t = 0.25$ … 3.5 ms in steps of 0.25 ms. The blue profiles at the higher (left) and lower (right) side of the step edge belong together, and show the measurements of $\mathcal{H}$, h_2, and $h_{2,E}$. The red profiles indicate the lowest h_2 obtained. (b) Height of the air gap above the flat region h_2 (dashed) and the edge $h_{2,E}$ (solid) for (red) $\mathcal{H} = 530$ nm , (blue) 720 nm, and (magenta) 1300 nm. The shaded region indicates the range of air film instability.

crossings when the interface kink is at its lowest point ($t = 3.7$ ms after appearance of the first fringes). When the height is further increased to *e.g.* 1300 nm in panel (c), contact is formed already at $t = 3.0$ ms while the air film is still thicker near the kink.

An analysis of the film profile in the azimuthal direction along r_2 up to $\varphi = \pm 10°$, see the red arrow in Figure 4(b), yields the droplet interfacial profile across the edge. An example is shown in Figure 7(a) for $\mathcal{H} = 530$ nm. Note that the air film thickness is measured with respect to the underlying substrate; as a result corresponding profiles at the left and right side differ a height $\mathcal{H}$ at the edge (*e.g.* blue indicated profiles). The influence of the edge is already observed from the beginning of the impact when the interface shows its initial deflection. This is because at the higher flat side of the step edge H^* is obtained earlier as the gas pressure grows more rapidly, see Chapter 4. In particular the droplet interface approaches the edge with an almost fixed shape. We measure the film thickness both away from the kink, i.e. h_2 (measured at the smooth higher flat side), and at the edge $h_{2,E}$. The latter must be extrapolated over a lateral distance ~ 5 µm due to missing intensity information at the edge itself. This induces a significant additional inaccuracy in its measurement. The time evolution of h_2 and $h_{2,E}$ is plotted in Figure 7(b) for several edge heights. As expected h_2 collapses for all edges (reaching a minimum value of 440 nm).

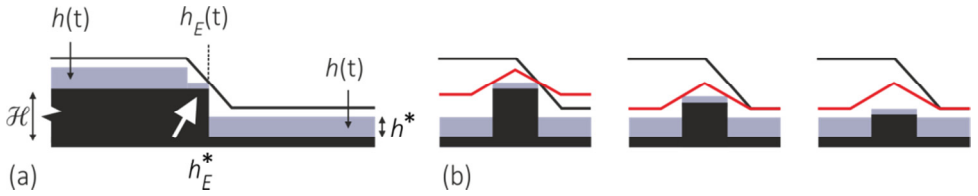

Figure 8. Contact formation scenario at (a) a step edge and (b) narrow ridges of varying height $\mathcal{H}$. The structure is indicated in black, while the instability regions $h < h^*$ at the flat parts and $h_E < h_E^* < h^*$ at the edge are shaded in grey. The black solid line shows the deflected interface that is approaching the substrate. In (b) three scenarios can be discerned: (left) if $\mathcal{H} > \mathcal{H}^*$ contact is forced earlier when the ridge width is smaller; (middle) if $\mathcal{H} \lesssim \mathcal{H}^*$ a transition from no contact to contact is observed; (right) if $\mathcal{H} < h_2 - h_E^*$ contact is never obtained irrespective of a smaller interface deflection. Red line: deflected interface for a narrow ridge; the curvature is smaller.

$h_{2,E}$ has the same slope but its absolute value depends strongly on the edge height $\mathcal{H}$. We determined the critical height for liquid-solid contact formation at step edges of 900 and 1300 nm, and find that $h_E^* = 60 \pm 40$ nm. Irrespective of the large uncertainty mentioned above, this is significantly lower than the 200 nm we observed for flat substrates in Chapters 2 and 4.

Based on the azimuthal interface profile, which derivative according to Figure 7(a) is symmetric around the step edge, a simple expression for the film thickness at the edge h_E is given by, see Figure 8(a):

$$h_E = [h + (\mathcal{H} + h)]/2 - \mathcal{H} = h - \mathcal{H}/2 \tag{1}$$

where both h and h_E are obtained at r_2 in the current experiments. However, the expression is independent of the exact shape near the edge. The liquid-air interface approaches the substrate until either the critical height $h_E^* \sim 60$ nm at the edge or $h^* \sim$ 200 nm away from the edge is obtained. The step height required to force contact at the edge can be determined from Equation (1):

$$\mathcal{H}^* = 2(h - h_E^*) \qquad (h > h^*) \tag{2}$$

where the latter condition is needed to exclude earlier contact formation away from the edge. For the current experiments with $h \geq 440$ nm we find $\mathcal{H}^* = 760$ which is indeed confirmed by the experiments shown in Figure 6 and the profilometer measurements. Caution is needed here due to the large uncertainty in h_E^*, but the simple expression does

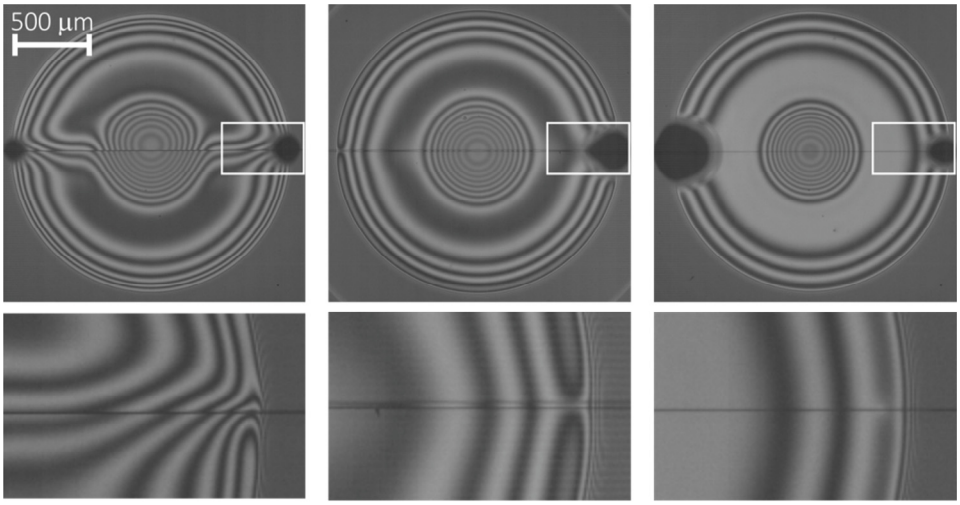

Figure 9. Interface deflection in the presence of a narrow ridge with $\mathcal{H} = 900$ nm. The time to contact formation (and air film development) decreases with decreasing ridge width: (a) $t = 3.7$ ms for $w = \infty$, (b) $t = 2.5$ ms for $w = 10$ μm, and (c) $t = 2.0$ ms for $w = 2$ μm. The lower panels show a zoom near the edge just before contact formation.

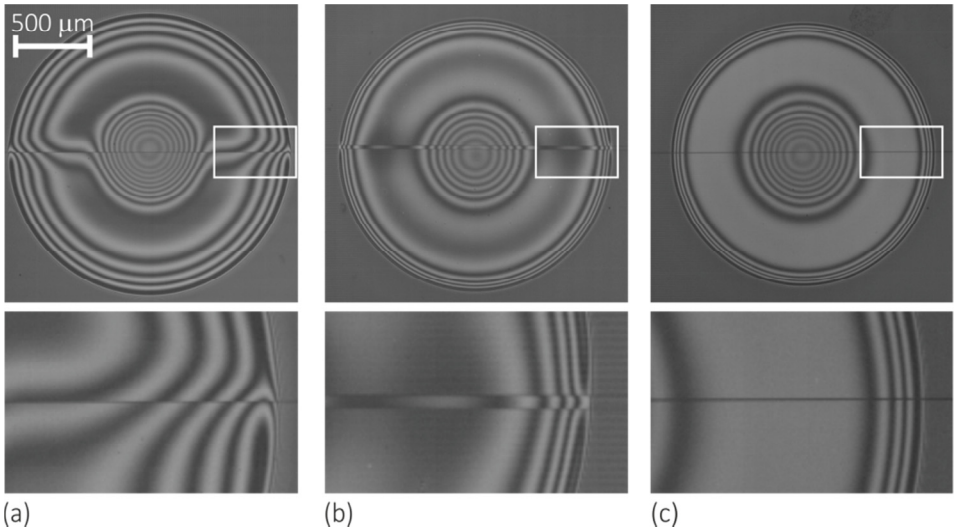

Figure 10. Interface deflection in the presence of a narrow ridge with $\mathcal{H} = 480$ nm. No contact is obtained but the deflection near the edge decreases with decreasing ridge width: (a) $w = \infty$, (b) 20 μm, and (c) 2 μm. The snapshots are taken at closest approach to the substrate, with the lower panels showing a zoom near the edge.

describe the air film narrowing at the edge very well. Close to the critical height $\mathcal{H}^*$ the experiments suffer from a distribution in impact results (forced contact or not). This can be explained by the fact that the film height away from the edge (h_2) varies with slight variations in impact velocity, especially around $v \sim 0.22$ m/s. This will be shown in Figure 1 of Chapter 7. For steps significantly higher than $\mathcal{H}^*$, the critical height for formation at the edge h_E^* is obtained earlier in the cushioning process thus cutting off the spreading of the air film as shown in Figure 6(c). In the next section we show that this effect can be amplified by using a narrow ridge instead of a step edge.

6.3.3. Narrow ridges

When the step edge is replaced by a ridge with finite width w, the droplet interface is now deflected at both sides of the texture. For small w the two distorted regions overlap, and the upwards deflection on top of the ridge cannot be sustained as shown by the red lines in Figure 8(b): we schematically indicate here that the curvature of the liquid-air interface is decreased at the overlap region due to surface tension. Depending on the ridge height $\mathcal{H}$ three different scenarios exist. First, if the step edge has a height large enough to force contact, *i.e.* $\mathcal{H} > \mathcal{H}^*$, successively narrower ridges will also force contact, yet at an earlier time. This is shown in Figure 9: for narrower ridges the deflection near the edge is strongly reduced (bottom row) and contact is formed while the air film is less developed, *i.e.* h_2 is still larger. In contrast, at the limit of a very low step edge, $\mathcal{H} < h_2 - h_E^*$, the flat interface above an extremely narrow ridge still does not induce contact. Indeed in Figure 10 we observe again a strong decrease of the interfacial deflection with decreasing ridge width, but no contact formation. Finally, for intermediate height there should thus a be critical ridge width below which a transition is observed from no contact formation to contact formation. This is shown in Figure 11 for pillars with $\mathcal{H} = 720$ nm: at a 100 μm wide pillar no contact is formed, while a 10 μm pillar does force contact. Thus we conclude that “sharp” structures with both a large height-to-width ratio and a minimum height are able to “puncture” the air layer.

6.4. Conclusion

Micro-textures can influence the formation of liquid-solid contact in an air-cushioned impact, on the condition that the protrusion is sufficiently steep and high. We have demonstrated this for the ideal case of a step edge. With such an edge the location of the initial wetting spot can be carefully controlled - *i.e.* at the intersections of the step edge with the ring of minimum film thickness - as well as the time of nucleation by varying the

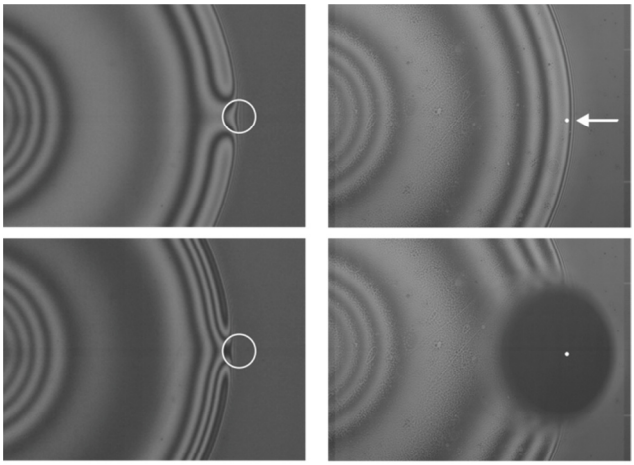

Figure 11. Interface deflection in the presence of a pillar with $\mathcal{H} = 720$ nm. A transition from no contact to contact is observed while decreasing the pillar diameter: (a) $w =$100 μm and (b) 10 μm. The upper snapshots are taken at $t = 3.1$ ms, while the lower snapshots are taken at (a) 4.3 ms and (b) just after contact formation.

step height. Moreover, ridges or pillars can be used to force earlier contact, owing to the suppression of the interface deflection by surface tension near the narrow texture.

These observations may have interesting applications in the control of droplet deposition and bubble inclusion. Although Chapter 4 shows that initial wetting is mainly in the cushioned area, for higher liquid viscosity the initial wetting is much slower and is less pronounced in a preferred direction. As a result the center of the deposited droplet shifts up to $R_0/4$ with respect to the impact center, which might be critical in droplet deposition accuracy. Micro-textures can here control the wetting center. Additionally, as nucleation is forced earlier on higher structures, we expect that step edges much higher than the air film thickness (not studied here) will force fast contact nucleation, such that a ring impact and thus air bubble inclusion can be inhibited.

References

[1] P.D. Hicks and R. Purvis, Air cushioning and bubble entrapment in three-dimensional droplet impacts, *J. Fluid Mech.* **649** (2010), 135-163.

[2] M. Reyssat, A. Pépin, F. Marty, Y. Chen and D. Quéré, Bouncing transitions on microtextured materials, *Europhysics Letters* **74** (2006), 306.

[3] D. Bartolo, F. Bouamrirene, É. Verneuil, A. Buguin, P. Silberzan and S. Moulinet, Bouncing or sticky droplets: Impalement transitions on superhydrophobic micropatterned surfaces, *Europhysics Letters* **74** (2006), 299.

[4] G. Manukyan, J.M. Oh, D. Van Den Ende, R.G.H. Lammertink and F. Mugele, Electrical switching of wetting states on superhydrophobic surfaces: A route towards reversible Cassie-to-Wenzel transitions, *Phys. Rev. Lett.* **106** (2011), 014501.

[5] C. Ishino, M. Reyssat, E. Reyssat, K. Okumura and D. Quéré, Wicking within forests of micropillars, *Europhysics Letters* **79** (2007), 56005.

[6] L. Courbin, E. Denieul, E. Dressaire, M. Roper, A. Ajdari and H.A. Stone, Imbibition by polygonal spreading on microdecorated surfaces, *Nat. Mater.* **6** (2007), 661-664.

[7] H.J. Subramani, T. Al-Housseiny, A.U. Chen, M. Li and O.A. Basaran, Dynamics of drop impact on a rectangular slot, *Ind. Eng. Chem. Res.* **46** (2007), 6105-6112.

[8] A. Rozhkov, B. Prunet-Foch and M. Vignes-Adler, Impact of water drops on small targets, *Phys. Fluids* **14** (2002), 3485.

[9] G. Juarez, T. Gastopoulos, Y. Zhang, M.L. Siegel and P.E. Arratia, Splash control of drop impacts with geometric targets, *Phys. Rev. E* **85** (2012), 026319.

[10] Y. Hardalupas, A. Taylor and J. Wilkins, Experimental investigation of sub-millimetre droplet impingement on to spherical surfaces, *Int. J. Heat Fluid Flow* **20** (1999), 477-485.

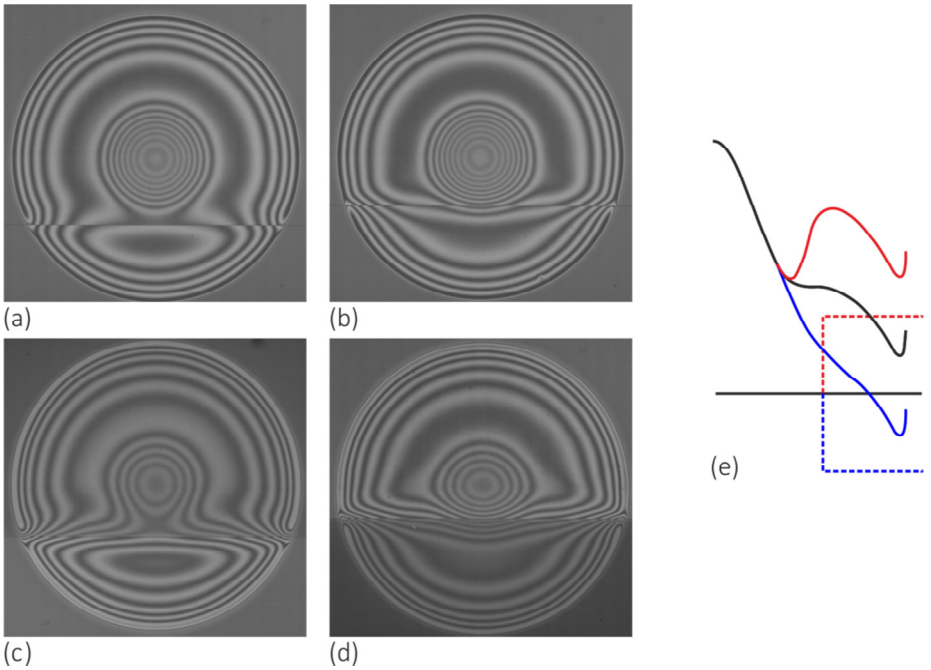

Figure S1. Interface deflection in the presence of an off-center step edge. Step with $\mathcal{H}$ = (a-b) 530 nm, and (c-d) 1300 nm. The impact is centered either at the (a, c) lower or (b, d) higher flat side of the step edge. (e) Sketch of interface deflection for a downward (blue) and upward (red) step edge.

Appendix 6.1. Off-center impacts on a step edge

In off-center impacts on a step edge, the combination of the global shape of the air film with the edge location and height lead to strong asymmetric profiles. For a downward step, the interface has merely an additional deflection downward, while an upwards step induces the formation of an "airbag" near the edge, see Figure S1. However, the local deflection at the intersection between edge and r_2 is not affected, and the scenario for forced contact described in this Chapter still holds.

Chapter 7

Conclusions and outlook

In this thesis we studied the lubricating air film below a droplet impacting on a solid substrate. The air acts as an airbag cushioning the fall of the droplet as the air pressure below it is building up. To visualize and quantitatively measure the air film thickness we developed in Chapter 3 a high-speed reflection interference microscopy technique with a depth of view of 8 μm, a height accuracy better than 30 nm and a time resolution better than 50 μs. Using this technique we studied different cushioning scenarios that can be collected in a single "cushioning map" as function of Weber number ($We \sim 0.001 \ldots 10$). We summarize the formation or inhibition of liquid-solid contact, *i.e.* wetting or bouncing, and the size (variability) of trapped air bubbles solely by the shape evolution of the droplet interface.

7.1. Conclusions

The "cushioning map" is shown in Figure 1. The air film thickness develops one or two local minima with a height h_1 (inner kink at r_1) and h_2 (outer kink at r_2) as shown in Chapter 2. For relatively high $We > 4$ (regime III) the inner kink approaches the substrate to a distance smaller than $h^* = 200$ nm within microseconds ('fast'), leading to numerous discrete impact points at r_1 that form a ring and entrap a small air bubble. Others have shown that in this regime the air bubble size increases with decreasing We [1, 2]. Our results conclusively demonstrate that this is due to suppression of the first kink by surface tension. We are particularly interested in its influence for $We < 4$ (regime II) and observe a strong increase of h_1 with decreasing We as demonstrated in Figure 1 and Chapters 2 and 4. In particular, we confirm that h_1 follows the scaling of the 'skating layer height' at which the locally diverging capillary force at the kink exceeds the local maximum gas pressure [3]. Simultaneously, suppression of the inner kink to $h_1 > 200$ nm allows a second local minimum h_2 to develop in the air film, whose height varies between 400-900 nm as shown in Figure 1 and Chapters 4 and 5. On a completely flat substrate this leads to a repeatedly bouncing droplet (IIb) as described in Chapter 5. Hovering (IIa) starts when the air film keeps its micrometric film thickness throughout the full oscillation. The height h_2 then systematically decreases with each oscillation until it reaches the critical height $h^* = 200$ nm and contact is formed under the outer kink at r_2. This is the transition to regime I in Figure 1, at $We < 0.006$, where gradual squeeze out of air also leads to formation of liquid-solid contact, yet on timescales of tens of milliseconds ('slow'). In

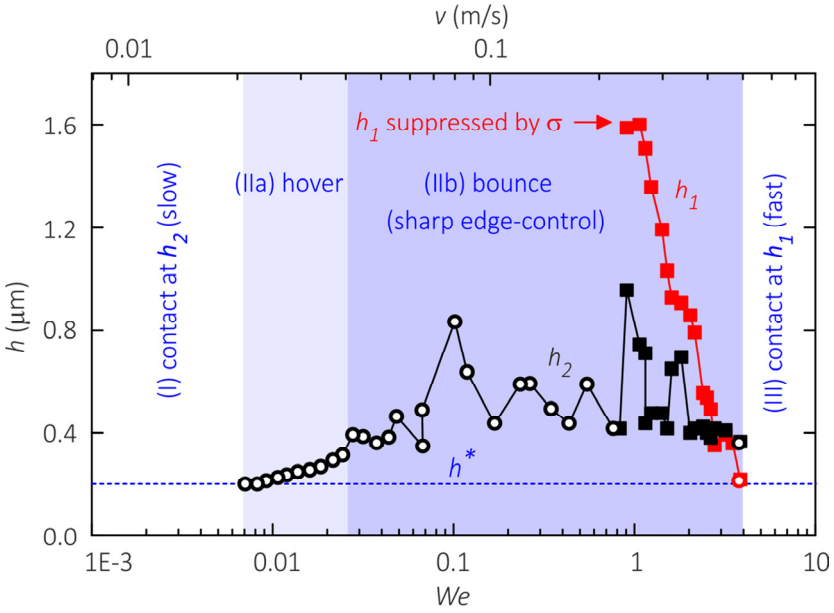

Figure 1. Map of cushioning scenarios at low We. The scenarios are, with increasing We: slow contact at h_2, non-contact, and fast contact at h_1. The height for contact formation h^* is indicated with the blue dashed line, while the film thicknesses h_1 (red symbols) and h_2 (black symbols) are plotted for two data series with $R = 1$ mm water droplets: the low-We bouncing series from Chapter 5 (open circles), and the individual higher-We experiments from Chapter 4 (closed squares).

regime II liquid-solid contact can be forced by the presence of a micro-texture. From Chapter 6 we conclude that sharp vertical step edges locally decrease the air film thickness, which is followed by liquid-solid contact when the air film thickness decreases below 60 nm at the edge. This may offer control of droplet positioning and elimination of air bubble inclusion, for example in inkjet printing. It also explains some experimental variability, *i.e.* premature formation of liquid-solid contact. In particular in regime II we expect that this is the mechanism of contact formation which happens at one or a few isolated locations. The isolated wetting spots and the variation in subsequent contact line propagation (Chapters 2 and 4) explain the large variability in air bubble volumes observed before for low We [4, 5], instead of complete entrapment of the squeezed air film into a bubble as proposed in Ref. [6].

Irrespective of the mechanism of contact formation we have studied the subsequent contact line propagation. Chapters 2 and 4 demonstrate that the initial spreading is

inertial and extremely fast: the thin air film geometry leads to fast preferential spreading within the cushioned region with a velocity that outweighs the velocity in a spherical approach situation [7-9]. For high liquid viscosities this asymmetry in spreading directions is smaller and the initial off-center wetting spot relocates the droplet position, as was briefly touched upon in Chapter 6. We thus conclude that the forcing of contact and subsequent initial wetting stage may influence both bubble inclusion and the accuracy of droplet positioning - the latter especially when spreading is restricted due to *e.g.* solidification effects of molten inks.

Finally, we studied the mechanism of droplet bouncing on a sustained air film (regime II) in Chapter 5. In the absence of a contact line, and thus contact angle hysteresis, a high restitution can be obtained due to low dissipation rates. 80% of the energy dissipation is obtained during the actual bounce (*vs.* flight) while only a fraction thereof is located in internal fluid motion due to droplet oscillations. We conclude that a significant part is dissipated in the strong shear field within the air film, based on a lubrication analysis of the measured time evolution of the film. This dissipative squeeze force is responsible for momentum reversal of the droplet. Here the crucial observation is the asymmetry in the air film development in the spreading and receding phase of the bouncing process. This allows for a permanently *repulsive* force as required for an effective momentum transfer. The shape evolution of the droplet interface is thus not only critical for the dynamics of liquid-solid contact formation and air bubble inclusion, but also for the bouncing process.

7.2. Outlook

7.2.1. Extension to inkjet droplets

Although we have used millimeter sized droplets as a model system, we believe that our conclusions are generic for all $We \sim 1$, in particular also for impacts of inkjet droplets. In previous experiments, Van Dam & Le Clerc [5] observed trapped air bubbles of variable size and number for low We impacts of inkjet droplet with a diameter of about 40-80 μm, while finding a significantly smaller, more reproducible air bubble size for higher We. This is fully consistent with the air film thickness evolution and contact formation scenarios described in this thesis for millimeter-sized droplets. We studied the interface evolution for inkjet droplets numerically using the theory by Brenner and co-workers [3, 10] and find that the same suppression of the kink(s) is observed, although at lower film thicknesses and shorter timescales, see Figure 2. Is the film thickness still sufficient to sustain non-

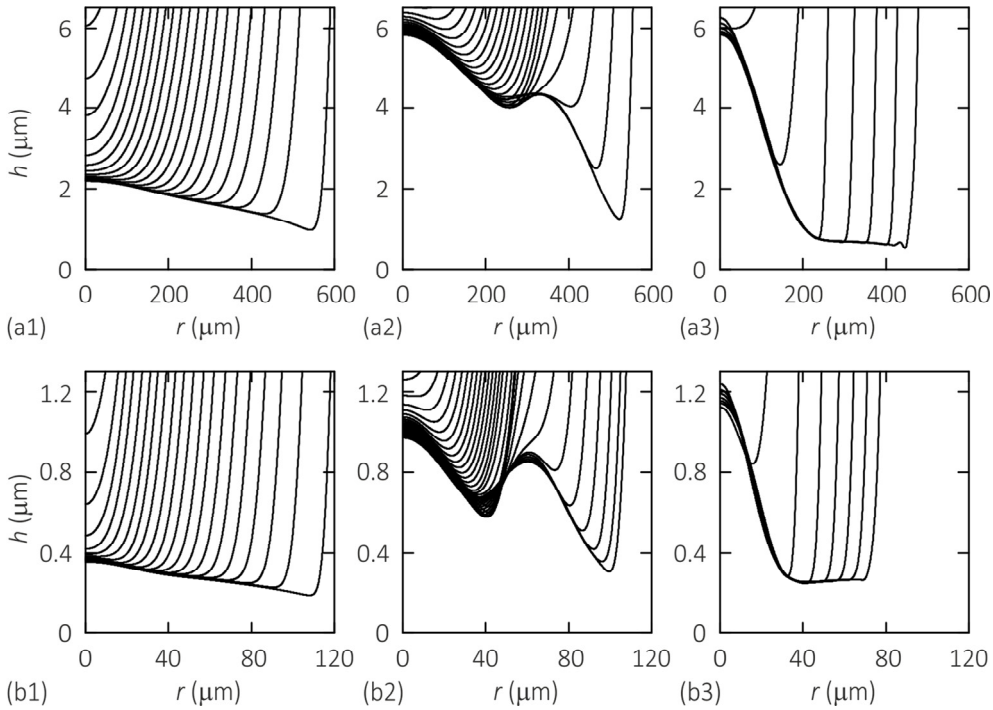

Figure 2. Air film development for large *vs.* small droplets at equal We. Numerical results for (1) $We \sim 0.001$, (2) $We \sim 0.1$ and (3) $We \sim 1$ for droplets of (a) $R = 1$mm and (b) $R = 100$ μm. Note that the relative time step with respect to (a1) decreases by a factor (a2-3) 100, (b1) 10, (b1-2) 1000.

wetting and allow the air film to expand? Let us consider a droplet with $R =$ 10-30 nm and $We \sim 1$. Using the scaling for $H^* \sim St^{-1/2}$ in the capillary regime [6] as described in Chapter 4 and 5 we obtain an air film thickness of one hundred to a few hundred nanometer that indeed allows the air film to expand. It would be interesting to study the development of this air film using total internal reflection [2] to obtain a better resolution for this range of film thicknesses, provided that the temporal resolution is sufficient.

7.2.2. Fundamental aspects

The smallest stable air film thickness we measured at both sides of regime II in Figure 1 is 200 nm, which is remarkably high. Although dust particles may occasionally force contact, we never measured a film thickness lower than 200 nm on thoroughly cleaned flat substrates (rms $<$ 3 nm). Remarkably, the critical air film thickness at a micro-texture edge is consistently smaller, *i.e.* $\sim$ 60 nm as found in Chapter 6. It is conceivable that the gas

pressure at the edge peaks strongly, so that the critical thickness is indeed smaller [11]. However, the final dynamical rupture mechanism of the air film is still an open question. Various effects have been proposed: surface interaction, interface fluctuations and/or substrate roughness, and rarefied gas effects upon approaching the mean free path ($\sim$ 60 nm) [12]. We studied here the influence of substrate micro-texture. Next, it would be interesting to study the influence of surface interactions on the air film rupture, in particular electrostatic forces [13, 14] that are longer-ranged than Van der Waals forces [15] (up to several hundred nm *vs.* 50 nm). This type of instability yields a typical wavelength able to explain the occurrence of many isolated contact points in regime III. (In regime I the tilt of the dimple, see Chapter 5, favors one single contact point.) It would be interesting to exert a linear stability analysis assuming a long-range electrostatic force, and calculate the instability wavelength and growth time for the squeezed air film.

We observed some interesting phenomena during the initial wetting stages that deserve further study; we established a simple inertial-capillary wetting scenario at early times, but also observed a strong influence of liquid viscosity (Chapter 2) and substrate wettability (Chapter 4) on the shape of the wetted area. On non-perfectly wetting substrates the characteristic cusps in the wetted area at the position of the minimum film thickness promote air bubble incorporation. Thus it would be interesting to study the effects of viscosity and wettability; they for example influence the dynamic contact angle and thus the Laplace pressure driving the spreading.

Regarding droplet bouncing, knowing that the region *just* outside the outer kink in the droplet interface is critical in the bouncing mechanism, it would be particularly useful to determine the shape of the interface outside the kink more carefully. This can be implemented by employing the radial symmetry of the air film, and zoom in on the edge of the squeezed air film. A larger lateral resolution allows to observe the air film up to a (slightly) higher thickness, and determine the full dissipation in the squeezed air film using lubrication theory. More importantly, this may also yield unambiguous direct confirmation that the force on the droplet is repulsive at all times.

In this study we varied the liquid properties, but not the properties of the surrounding gas. The latter would be in particular interesting in terms of ambient pressure and gas viscosity, since they influence the dimple height and the squeeze force. In particular it is plausible that the squeeze force decreases with gas viscosity rather than increases, due to the strong negative dependence on layer thickness that itself increases with gas viscosity.

References

[1] H. Fujimoto, H. Shiraishi and N. Hatta, Evolution of liquid/solid contact area of a drop impinging on a solid surface, *Int. J. Heat Mass Transfer* **43** (2000), 1673-1677.

[2] J.M. Kolinski, S.M. Rubinstein, S. Mandre, M.P. Brenner, D.A. Weitz and L. Mahadevan, Skating on a film of air: drops impacting on a surface, *Phys. Rev. Lett.* **108** (2012), 074503.

[3] S. Mandre, M. Mani and M.P. Brenner, Precursors to splashing of liquid droplets on a solid surface, *Phys. Rev. Lett.* **102** (2009), 134502.

[4] S.T. Thoroddsen, T.G. Etoh and K. Takehara, Air entrapment under an impacting drop, *J. Fluid Mech.* **478** (2003), 125-134.

[5] D. Van Dam and C. Le Clerc, Experimental study of the impact of an ink-jet printed droplet on a solid substrate, *Phys. Fluids* **16** (2004), 3403.

[6] W. Bouwhuis, R.C.A. Van Der Veen, T. Tran, D.L. Keij, K.G. Winkels, I.R. Peters, D. Van Der Meer, C. Sun, J.H. Snoeijer and D. Lohse, Maximal air bubble entrainment at liquid-drop impact, *Phys. Rev. Lett.* **109** (2012), 264501.

[7] A.L. Biance, C. Clanet and D. Quere, First steps in the spreading of a liquid droplet, *Phys. Rev. E* **69** (2004), 016301.

[8] J.C. Bird, S. Mandre and H.A. Stone, Short-time dynamics of partial wetting, *Phys. Rev. Lett.* **100** (2008), 234501.

[9] K.G. Winkels, J.H. Weijs, A. Eddi and J.H. Snoeijer, Initial spreading of low-viscosity drops on partially wetting surfaces, *Phys. Rev. E* **85** (2012), 055301(R).

[10] M. Mani, S. Mandre and M.P. Brenner, Events before droplet splashing on a solid surface, *J. Fluid Mech.* **647** (2010), 163-185.

[11] P.D. Hicks and R. Purvis, Air cushioning and bubble entrapment in three-dimensional droplet impacts, *J. Fluid Mech.* **649** (2010), 135-163.

[12] L. Duchemin and C. Josserand, Rarefied gas correction for the bubble entrapment singularity in drop impacts, *C. R. Mecanique* **340** (2012), 797-803.

[13] D. Michael and M. O'neill, Electrohydrodynamic instability in plane layers of fluid, *J. Fluid Mech.* **41** (1970), 571-580.

[14] A. Staicu and F. Mugele, Electrowetting-induced oil film entrapment and instability, *Phys. Rev. Lett.* **97** (2006), 167801.

[15] A. Vrij, Possible mechanism for the spontaneous rupture of thin, free liquid films, *Discuss. Faraday Soc.* **42** (1966), 23-33.

Acknowledgements

First of all I would like to thank Frieder who accepted me as a PhD-student in his group. I got the freedom to explore, and focus on the most promising directions what lead us unexpectedly to air cushioning of droplets and (on the side) drop-on-a-fiber studies. At times I struggled a bit with sharply formulating the main message of a paper, but you always tried to push this. In this respect I appreciate initiatives like Dimple Day and Toulouse that forced me to focus again on the basic ideas of my research.

Dirk, I really enjoyed working with you as my daily supervisor. I have the habit of postponing meetings until I have a (seemingly) complete, coherent story to present. Fortunately you took the initiative to discuss more regularly than that. I greatly appreciate your down-to-earth approach and solid knowledge, and always walked out of your office with new insights or tangible suggestions for further work or analysis! You actively helped me with ideas for experiments, suggestions for analysis, and the modeling and numerical implementation of the bouncing process. Also, your confidence in my work pushed me ahead many times, in particular during the last months of writing.

I would like to thank my committee members for kindly agreeing to be in my thesis committee and taking the effort to critically read this thesis. Also I highly appreciate that several of you will speak at the mini-symposium following my thesis defense.

This research is part of the project “High Precision Inkjet Printing System (HIPRINS)” with the industrial partners Holst Center, Océ, Roth & Rau, Thales, and NTS. Although my work on air cushioning for gi-gan-tic (millimeter-sized) droplets may have been a bit too fundamental, I appreciate the valuable input I got, ranging from industrial inks (Holst Center) and ideas for micro-textured substrates, to insights about industrial printing. Aart Polderman, thank you for the project coordination and your kind interest in my research.

I spent my time in the Physics of Complex Fluids group together with the a large number of colleagues: Aditya, Agata, Alberto, Andrea, Annelies, Aram, Arjen, Armando, Arun B., Arun G., Bijoy, Burak, Chandra, Cunlu, Daniel E., Daniel H., Daniel W., Davood, Dhirendra, Dieter, Dileep, Dirk, Edith, Fei, Gor, Hao, Huub, Igor, Ivo, Jane, Jorick, Jung, Kartikeya, Lei, Lisette, Mariska, Martien, Mathijs, Michel, Naveen, Olga, Omkar, Pablo, Riëlle, Sietske, Sissi, Somnath, Tarun, Willem, and a number of visiting BSc students and interns of which I (co)supervised Karina, Florian, Astrid, Pim and Rudy. I enjoyed being part of PCF and sharing experimental results, support and discussions. Thanks to Annelies, Lisette, and

Edith for the administrative aid, and Mariska and Daniël H. for the organization of the labs! Of course I cannot forget to mention the great times I had with many of my colleagues during group outings and celebrations, but also our game nights, Big Bang Theory sessions, plenty of shared Wednesday dinners, and lunch break-Frisbee playing.

I would like to thank a few PCF colleagues specifically. With Burak and Riëlle I formed the experimental half of the “drop-on-a-fiber” team. Burak, you are always full of ideas and enthusiastic to try them out, while Riëlle and I pushed for very accurate experiments. Together we formed a strong team that spent many weekends playing around with this toy project, which ultimately resulted in two very nice publications.

“Thanks for the papers! We think we have a really interesting topic here…” I sent this email a year into my PhD to Omkar, who attended me to the recent theoretical papers about droplet cushioning after I presented curious air films observed in the early stages of my droplet *spreading* experiments. It marked the start of three years of air cushioning and bouncing, a gradual change of topic that I certainly do not regret. Chandra was our valuable “optics expert” that ordered optical components for the interferometry set-up, and was always willing to help solving problems. I really benefitted from your help! Jung, I highly appreciate your numerical work within this project. Your implementation of Brenner’s theory not only allowed us to compare many experimental measurements to the theory - also outside the range of numerical results presented in the original paper -, but you also provided me with more insights into the theory itself. Finally, I would like to thank Rudy who was looking for a “baantje” in between his BSc and MSc. From previous experiments I had some interesting observations of droplets bouncing on an air layer. Rudy, with your good experimental skills, independent work attitude, and the careful cleaning and coating procedures you developed with help of Dhirendra, you obtained all the experimental data I needed for Chapter 5!

I greatly appreciate the technical support from Mariska, Daniel W., Daniel H., and Klaas. Klaas, it was really nice to work with you and see your inventiveness and the beautiful equipment you can make in the workshop. You were always willing to bend numerous fibers in the correct shapes, but you also designed a useful cuvet for me and a beautiful drop impact pressure chamber. It is really unfortunate that I did not have the time to do the experiments I planned with it, and hopefully it will be used in the future! Mariska, thanks for the help with my set-up and all “small things” in the lab. Daniel W., thanks for the cleanroom work and production of micro-textured substrates. Daniel H., thanks for your immediate help with any kind of pc and software troubles.

I would like to thank Ciro Semprebon and Martin Brinkmann from the Max Planck Institute in Göttingen for their numerical work within the drop-on-a-fiber project. You provided so many ideas to test experimentally that we often could not keep up with everything you calculated! Thanks for the nice collaboration.

One of the highlights of my PhD career: the Les Houches summerschool “Soft Interfaces”. Nearly a month with fifty dedicated PhD students from all over the world, confined to our “little village” and the surrounding mountains, with lectures by the best professors in our field. A high-intensity workshop like this is a recommendation to each student!

Then, it cannot have slipped any colleague’s attention that I have been actively participation in the Lindy Hop association Swing Out Loud. Irene, thank you so much for introducing Lindy Hop in Enschede! After picking up enthusiasm for Lindy Hop during my MSc internship in Boston, this new scene has been a major addition to my life here in Enschede. Erik G., thanks for teaching us many years and our discussions ranging from Lindy Hop to PhD life. Everyone else who has been part of it, thanks for our dances and practices, your enthusiasm, our shared trips all across the Netherlands, Germany and Sweden, and very important: the distraction from work stress.

I would like to thank my paranymphs, Huub and Erik L., for supporting me during my thesis defense. Huub, while advocating for the “dark side of the world” a.k.a. industry, you have been patiently listening to all my worries and complaints, and supporting me throughout. Thanks also for all dinners, longboard trips, and vacations! Erik L., thanks for sharing many, many Lindy Hop activities with me and the good times we had with them! Our “paranymph quartet” is not complete without Bijoy and Dieter. Bijoy, we had great times at the Les Houches summerschool! Dieter, thanks for all the fun times we shared, both at PCF and during all our dance, sport, and game activities and trips.

Many people are surprised the first time they find out that we are both colleagues and twin sisters, but for me it feels so familiar. We may be too alike to form a synergistic team, but we do add up perfectly… which from my experience is exceptionally good. Riëlle, thanks for ALL!

Tenslotte, papa en mama, dank jullie wel voor jullie steun, interesse, en geloof in ons kunnen, en de gezellige weekends als welkome afleiding!

List of publications

Publications from this thesis research:

J. de Ruiter, J.M. Oh, H.T.M van den Ende & F. Mugele. Dynamics of collapse of air films in drop impact. *Physical Review Letters* **108** (2012), 074505.

In preparation:

J. de Ruiter, R. Lagraauw, H.T.M. van den Ende & F. Mugele. The role of air film asymmetry on non-contact droplet bouncing. In preparation (2014).

J. de Ruiter, F. Mugele & H.T.M van den Ende. Dynamics of thin films studied by dual wavelength Reflection Interference Microscopy: cushioning in droplet impact. In preparation (2014).

Other publications: (* equal contributions)

R. de Ruiter*, J. de Ruiter*, H.B. Eral, C. Semprebon, M. Brinkmann & F. Mugele. Buoyant droplets on functional fibers. *Langmuir* **28** (2012), 13300-13306.

H.B. Eral*, J. de Ruiter*, R. de Ruiter*, J.M. Oh, C. Semprebon, M. Brinkmann & F. Mugele. Drops on functional fibers: from barrels to clamshells and back. *Soft Matter* **7** (2011), 5138-5143.

J. de Ruiter, R.E. Pepper & H.A. Stone. Thickness of the rim of an expanding lamella near the splash threshold. *Physics of Fluids* **22** (2010), 022104.

M.L.J. Steegmans, J. de Ruiter, C.G.P.H. Schroën & R.M. Boom. A descriptive force-balance model for droplet formation at microfluidic Y-junctions. *American Institute of Chemical Engineers Journal* **56** (2010), 2641-2649.

L.M.C. Sagis, R. de Ruiter, F. Rossier Miranda, J. de Ruiter, C.G.P.H. Schroën, A.C. van Aelst, R.M. Boom & E. van der Linden. Polymer microcapsules with a fiber-reinforced nanocomposite shell. *Langmuir* **24** (2008), 1608-1612.

Conference presentations:

FLOW 14: 1st International conference on micro & nanofluidics. Fundamentals and applications, Enschede (18-21 May 2014). The role of air film asymmetry on non-contact droplet bouncing. Co-authors: H.T.M. van den Ende & F. Mugele. Poster presentation.

555th WE-Heraeus-Seminar: Wetting of structures with complex geometries, Bad Honnef (16-19 March 2014). The role of air film asymmetry on non-contact droplet bouncing. Co-authors: H.T.M. van den Ende & F. Mugele. Poster presentation.

Droplets 2013: 1st International workshop on wetting and evaporation: droplets of pure and complex fluids, Marseille (17-20 June 2013). Living on the edge: air film collapse in drop impact on microstructures. Co-authors: H.T.M. van den Ende & F. Mugele. Oral presentation.

APS Division of Fluid Dynamics meeting, San Diego (18-20 Nov 2012). Living on the edge: air film collapse in drop impact on microstructures. Co-authors: H.T.M. van den Ende & F. Mugele. Oral presentation.

MESA+ colloquium, Enschede (10 April 2012). On the collapse dynamics of air films in drop impact. Co-authors: J.M. Oh, H.T.M. van den Ende & F. Mugele. F. Oral presentation.

Physics @ FOM, Veldhoven (17-18 Jan 2012). On the collapse dynamics of air films in drop impact. Co-authors: J.M. Oh, H.T.M. van den Ende & F. Mugele. Oral presentation.

APS Division of Fluid Dynamics meeting, Baltimore (20-22 Nov 2011). Evolution of the contact area of a cushioned droplet hitting a solid surface. Co-authors: J.M. Oh, H.T.M. van den Ende & F. Mugele. Poster presentation: Gallery of Fluid Motion.

APS Division of Fluid Dynamics meeting, Baltimore (20-22 Nov 2011). On the collapse dynamics of air films in drop impact. Co-authors: J.M. Oh, H.T.M. van den Ende & F. Mugele. Oral presentation.

Liquid Matter Conference, Vienna (6-10 Sept 2011). Drops on functional fibers: from barrels to clamshells and back. Co-authors: H.B. Eral, R. de Ruiter, J.M. Oh, C. Semprebon, M. Brinkmann & F. Mugele. Oral presentation.

Liquid Matter Conference, Vienna (6-10 Sept 2011). Roughness-enhanced acceleration of spreading of completely wetting fluids. Co-authors: H.T.M. van den Ende & F. Mugele. Poster presentation.

18th Ostwald Kolloquium, Mainz (16-18 May 2011). Drops on functional fibers: from barrels to clamshells and back. Co-authors: H.B. Eral, R. de Ruiter, J.M. Oh, C. Semprebon, M. Brinkmann & F. Mugele. Poster presentation.

18th Ostwald Kolloquium, Mainz (16-18 May 2011). Roughness-enhanced acceleration of spreading of completely wetting fluids. Co-authors: H.T.M. van den Ende & F. Mugele. Poster presentation.

Physics @ FOM 2011, Veldhoven (18-19 Jan 2011). Roughness-enhanced spreading of completely wetting fluids. Co-authors: H.T.M. van den Ende & F. Mugele. Poster presentation.

FERMAT-IMPACT-GIMFus meeting, Sevilla (20-22 October 2010). Drops on functional fibers: from barrels to clamshells and back. Co-authors: H.B. Eral, R. de Ruiter, J.M. Oh, C. Semprebon, M. Brinkmann & F. Mugele. Oral presentation.

About the author

Jolet de Ruiter was born on the 5th of April 1985 in Tiel, the Netherlands. She grew up in Geldermalsen, and completed her secondary education at RSG Lingecollege in Tiel in 2003. After obtaining her propaedeutic diplomas in Applied Physics and Applied Mathematics at the Technical University of Eindhoven, she started her studies in Food Technology at Wageningen University in 2004. Her BSc research focused on the production of microcapsules with composite shells using electrostatic layer-by-layer deposition of polymers and microspheres. As part of the MSc program she did an internship at Harvard University, Cambridge (USA), in the group of prof. Howard Stone. Here she studied both the formation of water-filled colloidosomes from microsphere-coated gas bubbles under the influence of surfactants, as well as the lamella expansion of impacting droplets near the splash threshold. She completed her studies in Wageningen in 2009 with an MSc research under supervision of dr. Karin Schroën in the group of prof. Remko Boom. This research focused on emulsification in microfluidic channels, in particular the influence of continuous and dispersed phase viscosity on droplet formation at a Y-shaped junction.

In August 2009 she started her PhD research under supervision of dr. Dirk van de Ende in the Physics of Complex Fluids group of prof. dr. Frieder Mugele at the University of Twente. The results of this PhD research are presented in this thesis.

ISBN: 978-90-365-3638-7